

**Structure-property relationships in an Al matrix Ca nanofilamentary composite  
conductor with potential application in high-voltage power transmission**

by

**Liang Tian**

A dissertation submitted to the graduate faculty  
in partial fulfillment of the requirements for the degree of

DOCTOR OF PHILOSOPHY

Major: Materials Science and Engineering

Program of Study Committee:  
Alan Russell, Co-Major Professor  
Iver Anderson, Co-Major Professor  
Richard Lesar  
Scott Chumbley  
Frank Peters

Iowa State University

Ames, Iowa

2015

Copyright © Liang Tian, 2015. All rights reserved.

## TABLE OF CONTENTS

ACKNOWLEDGMENTS .....	iii
ABSTRACT.....	v
CHAPTER 1    GENERAL INTRODUCTION.....	1
CHAPTER 2    THE MICROSTRUCTURE-STRENGTH RELATIONSHIP IN A DEFORMATION PROCESSED AL-CA COMPOSITE .....	9
CHAPTER 3    A DISLOCATION-BASED, STRAIN-GRADIENT-PLASTICITY STRENGTHENING MODEL FOR DEFORMATION PROCESSED METAL- METAL COMPOSITES.....	32
CHAPTER 4    MODELING THE ELECTRICAL RESISTIVITY OF DEFORMATION PROCESSED METAL/METAL COMPOSITES .....	52
CHAPTER 5    PRODUCTION OF FINE CA POWDERS BY CENTRIFUGAL ATOMIZATION WITH ROTATING QUENCH BATH .....	86
CHAPTER 6    PROSPECTS FOR NOVEL DEFORMATION PROCESSED AL/CA COMPOSITE CONDUCTORS FOR OVERHEAD HIGH VOLTAGE DIRECT CURRENT (HVDC) POWER TRANSMISSION .....	116
CHAPTER 7    A LIGHTWEIGHT, HIGH STRENGTH, HIGH ELECTRICAL CONDUCTIVITY DEFORMATION PROCESSED AL MATRIX CA NANOFILAMENTARY COMPOSITE.....	149
CHAPTER 8    PHASE FIELD STUDY OF INTERFACIAL DIFFUSION- DRIVEN SPHEROIDIZATION IN A COMPOSITE COMPRISED OF TWO MUTUALLY INSOLUBLE PHASES .....	170
CHAPTER 9    GENERAL CONCLUSIONS.....	192
APPENDIX A   A PRELIMINARY STUDY OF THE AL/CA INTERFACE AT ELEVATED TEMPERATURE.....	200
APPENDIX B   GUIDELINE TO USE LAMMPS MOLECULAR DYNAMIC PACKAGE WITH REAXX FORCE FIELD .....	214

## ACKNOWLEDGMENTS

I would like to thank my major professors, Alan Russell and Iver Anderson, for their guidance and encouragement on my way to becoming an independent scientific researcher through this Ph.D research project, their support in giving me the freedom to develop my own ideas, allowing me to participate in writing grant proposals and funding reports, teaching undergraduate level materials science courses, presenting research results in professional conferences, and acting as the corresponding author for published journal articles.

I would also like to thank my committee members Prof. Richard Lesar for permission to audit his amazing computational materials science course, Prof. Scott Chumbley for his expertise and help in scanning electron microscopy, and Prof. Frank Peters for his willingness to join the POS committee and to review my dissertation. Furthermore, I would like to thank the staff of the Iowa State University Preparing for Future Faculty (PFF) program for designing a wonderful course to help me prepare for a future career in academia.

In addition, I would also like to thank Prof Mirzaeifar from Virginia Tech on discussing questions about LAMMPS, colleagues Trevor Riedemann, Hongjune Kim and Austin Shaw for their various technical contributions to this research project. The financial support from ISU's Electric Power Research Center, Iowa State University Research Foundation, U.S. Department of Energy Office of Electricity, and Summit Technology Group LLC is also gratefully appreciated.

Finally, I would like to thank the department faculty/staff, Ames Laboratory staff, various wonderful invited speakers for helping me gain a good learning experience at Iowa

State University. I want to also offer my appreciation to friends and family supporting my decision to become a scientific scholar. Without assistance from all these helpful people, this dissertation would not have been possible.

## ABSTRACT

This study investigated the processing-structure-properties relationships in an Al/Ca composites using both experiments and modeling/simulation. A particular focus of the project was understanding how the strength and electrical conductivity of the composite are related to its microstructure in the hope that a conducting material with light weight, high strength, and high electrical conductivity can be developed to produce overhead high-voltage power transmission cables. The current power transmission cables (e.g., Aluminum Conductor Steel Reinforced (ACSR)) have acceptable performance for high-voltage AC transmission, but are less well suited for high-voltage DC transmission due to the poorly conducting core materials that support the cable weight. This Al/Ca composite was produced by powder metallurgy and severe plastic deformation by extrusion and swaging. The fine Ca metal powders have been produced by centrifugal atomization with rotating liquid oil quench bath, and a detailed study about the atomization process and powder characteristics has been conducted. The microstructure of Al/Ca composite was characterized by electron microscopy. Microstructure changes at elevated temperature were characterized by thermal analysis and indirect resistivity tests. The strength and electrical conductivity were measured by tensile tests and four-point probe resistivity tests. Predicting the strength and electrical conductivity of the composite was done by micro-mechanics-based analytical modeling. Microstructure evolution was studied by mesoscale-thermodynamics-based phase field modeling and a preliminary atomistic molecular dynamics simulation. The application prospects of this composite was studied by an economic analysis. This study suggests that the Al/Ca (20 vol. %) composite shows promise for use as overhead power transmission

cables. Further studies are needed to measure the corrosion resistance, fatigue properties and energized field performance of this composite.

## CHAPTER 1 GENERAL INTRODUCTION

### Background

The purpose of this research is to study the processing-microstructure-properties relationship in a deformation processed Al matrix Ca filament metal metal composites with intended application as high-voltage power transmission cables. Light weight, high strength, and high electrical conductivity are highly desired properties for overhead conductor materials. If these three properties could be combined in one material, it would decrease transmission tower construction costs, increase power transmission efficiency and increase system reliability against ice, wind, and emergency loading. However, it is difficult to produce a material that possess both high strength and high conductivity. Conventional strengthening methods like strain hardening, solid solution hardening, precipitate hardening, and second phase hardening tend to decrease the electrical conductivity due to the electron scattering effect of these microstructure features. In this research, a type of materials called deformation processed metal metal composites (DMMCs) has been proposed as a potential candidate to deliver both high strength and high conductivity.

There has been 40 years of research [1] on various DMMCs, beginning with Cu-Nb DMMCs first reported by Bevk et al [2] to have an extraordinary combination of high strength 2.2 GPa (substantially higher than the rule of mixture (ROM) predictions) and high electrical conductivity 70% IACS (close to the ROM predictions). Nb filaments only tens of nanometers in diameter act as barrier to dislocation motion and conductive pathways to electrons with minimal interphase boundary scattering. However, the Cu-Nb DMMCs are not suited for high-voltage power transmission cables because they are too heavy and

expensive. Therefore, in this study, we decided to adapt the concept of DMMCs to other metal-metal combinations. Al and Ca are the most promising choices considering electrical conductivity, ductility, density and price. Since both Al and Ca are highly ductile fcc metals, the Al/Ca composite should be able to tolerate a large deformation true strain (as high as 14) without intermediate annealing, which reduces the processing costs of this composite. The principal initial concern of Al-Ca composite is that Ca is a reactive metal that forms a non-protective oxide or hydroxide when exposed to air, particularly humid air. This problem can be circumvented by encapsulating Ca metal filaments inside an Al metal matrix. The Ca filaments are thus embedded in protective Al and isolated from moisture and air. Furthermore, though Al and Ca metals are very weak metal with yield strength around 80 MPa [3], the strength of Al-Ca DMMCs can still be as high as 600 MPa as long as the Ca filaments size can be a few hundred nanometers or smaller [4]. This is because the strength of DMMCs does not comes from the strength of their constituent metals predicted by the rule of mixture, but from the major strengthening from interfaces that make the strength of DMMCs much higher than the rule of mixture prediction [2], based on previous research on Cu-Nb DMMCs. Therefore, the concept of designing an Al-Ca DMMC seems plausible. But first, we need to study the processing-structure-properties relationship in Al-Ca DMMCs to verify this concept experimentally and to develop theoretical understanding of this relationship to explain experiments that can help us design future Al-Ca DMMCs with tailored properties to meet the requirement of high-voltage power transmission purposes.



## Topics Review

### High-voltage power transmission direct currents (DC) vs alternating currents (AC)

As global energy dependency gradually shifts from fossil fuel combustion to renewable energy resources (i.e., wind, solar energy, tidal energy etc.), long distance electric power transmission is necessary to transmit electric power efficiently from remote areas with rich renewable energy resources to populated cities. For the same amount of transmitted power, higher-voltage power reduces the current in power cables, which reduces the energy losses associated with long-distance transmission. For long-range power transmission, overhead conductor cables are the mostly widely used. High-voltage alternating current (HVAC) transmission is widely adopted in power grid system due to the ease of converting high voltage to low voltage by transformer technology. For high-voltage direct current (HVDC) transmission, the DC has to be converted to AC first and then decrease voltage for end users by transformer. This converter technology is expensive for DC transmission. Another advantage of AC transmission relative to DC transmission is that designing overhead conductors for AC can be very practical due to the skin effect of AC currents. However, HVDC has been proven to be more energy-efficient than HVAC, which results in substantial cost saving when the power transmission distance is several thousand kilometers or more. With recent development of new affordable converter technology, the economic benefits of HVDC for long-distance transmission have been enhanced, making HVDC an attractive future power transmission technology. However, there is no conductor that has been expressly designed for HVDC transmissions though several optimal designs of transmission conductors exist for HVAC. It is thought that Al/Ca composites may be suitable conductor materials for HVDC transmission.

### Current power transmission conductor materials

All currently available power transmission conductors are designed for HVAC, not optimized for HVDC. The most widely used conductor is Aluminum Conductor Steel Reinforced (ACSR), which is comprised of pure or nearly pure Al outer strands around a steel core. Since pure Al is weak, the steel core provides the strength needed to hold the conductor aloft. Due to the skin effect of alternating current flow, most AC flows near the surfaces of the outer Al strands so that the conductivity of ACSR for AC power is nearly the same as pure Al. The strong but poorly conductive steel core allows the conductor to be suspended on transmission towers without sagging near the ground as pure Al conductor would do. This conductor design can satisfy the requirement of high conductivity for AC currents and high strength by combining the advantages of the high conductivity of pure Al with the high strength of the steel core. The ACSR design works less well for DC currents because the DC flows uniformly across the entire cross section of the conductor, rendering the poorly conductive steel core to be a “dead zone” for DC current flows.

In addition, the large mismatch of thermal expansion coefficients between Al and steel can cause “bird caging” and thermal fatigue problems for both HVAC and HVDC use [4]. Other power transmission conductors have similar design limitations. All Aluminum Alloy Conductor (AAAC) uses Mg, Si, and other alloying elements to increase conductor strength by precipitation hardening, but these impurities degrade AAAC’s conductivity to 52.5–53% IACS. Aluminum Conductor Alloy Reinforced (ACAR) uses the middle Al alloy strands instead of a steel core to reinforce the conductor to get desired strength and better AC conductivity, but for HVDC this material suffers to some degree from the same poor DC

conductivity effects seen in ACSR due to the poorly conductive Al alloy core. Aluminum Conductor Composite Reinforced (ACCR) invented by 3M uses a composite core comprised of 50 vol. % aluminum oxide fibers embedded inside Al matrix to reinforce the conductor. This material has excellent sag resistance when used at temperatures as high as 200 °C, but the composite core has poor DC conductivity. Similarly, Aluminum Conductor Composite Core (ACCC) invented by CTC cable used a poorly conductive polymer matrix carbon and glass fiber reinforced composite core to strengthen pure Al strands. Thus, while there are several conductor materials on the market, none is ideal for HVDC power transmission.

#### Deformation processed metal-metal composites (DMMCs)

To develop a conductor material for HVDC, it requires a single type of material to possess high conductivity for DC currents and high strength at the same time because there is no skin effect for DC currents. However, it is inherently difficult for a single material to achieve high strength and high conductivity at the same time because most strengthening methods (e.g. precipitation hardening, solid solution hardening, 2<sup>nd</sup> phase hardening, work hardening) decrease the conductivity.

DMMCs can possess both high strength and high conductivity due to their unique microstructure. Cu-Nb DMMCs studied by Bevk et al [2] were found to have a 2.2 GPa ultimate tensile strength and conductivity of 70% IACS. They are comprised of two pure ductile metal phases with one phase being the matrix and the other phase being the filaments. DMMCs can be produced by either (1) co-melting two metals that are miscible in liquid but immiscible in solid or (2) powder metallurgy, then subjecting the material to severe plastic deformation (e.g. extrusion, swaging, drawing or rolling) to narrow and elongate the two

metal phases [1]. The ductility of the metal phases allows the composite to be deformed substantially without any intermediate annealing to reduce the filament thickness and spacing to tens to hundreds of nanometers [1]. This nanoscale microstructure gives the composite high strength due to the large interface area acting as barriers to matrix dislocation motion. The strength of the second-phase metal filaments makes only a secondary contribution to the high strength of DMMCs [2]. Therefore, the strength of DMMCs due to these interface barrier follows a Hall-Petch relation, similar to the strengthening effect of grain boundaries acting as barriers to dislocation motion [2]. DMMCs are essentially nanoscale bundles of two pure metals that provide conductive pathways for electrons so that their electrical conductivity is usually high unless the filament thickness and spacing become extremely small (a few tens of nanometers or less). When filament thickness and spacing reach a size that is comparable with the mean free path of electrons, the electron scattering from interfaces becomes substantial, and the electrical conductivity decreases [5]. Based on the above description, it seems that there is a trade-off between strength and electrical conductivity for DMMCs. However, the reality is that the strength of DMMCs increases rapidly when the filament thickness becomes smaller than about 1  $\mu\text{m}$  [6], while the electrical conductivity won't decrease until the filament thickness decreases below a few tens of nanometers for most metals. Thus, there is a "sweet spot" in the filament size range between tens of nanometers and several hundreds of nanometers where DMMCs typically have both high strength and high conductivity. Based on specific applications, we can also tune the properties of DMMCs to meet the requirements of these applications by designing the DMMCs with a particular filament size to optimize their characteristics for a particular application.

## Dissertation Organization

The organization of the dissertation is as follows:

Chapter 2 of this dissertation describes experimental studies of the processing-microstructure-strength relationship in Al/Ca (9 vol. %) composite. In this chapter, a review of past DMMC systems and strengthening mechanisms in DMMCs is presented. Chapter 3 presents a dislocation density based, strain gradient strengthening model for DMMCs to guide the design of next-generation Al/Ca composites. Chapter 4 presents a size-dependent electrical resistivity model for DMMCs based on five scattering mechanisms by Boltzmann transport equation to understand the possible deviation of the conductivity of DMMCs from ROM predictions. Chapter 5 presents findings from development of a centrifugal atomization system with rotating quench bath in inert gas atmosphere to produce small quantities (~100 g) of fine Ca metal powders with average diameters around 200  $\mu\text{m}$ . The powders were characterized and found to satisfy the requirement for the production of 2<sup>nd</sup> generation Al/Ca (20 vol. %) composite for higher strength. Chapter 6 presents an analysis of the application prospects of Al/Ca composites as overhead high-voltage power transmission conducting cables and compares them with the conductors now in use. Chapter 7 presents the results of an experimental study of the processing-microstructure-strength/conductivity relationship in 2<sup>nd</sup> generation Al/Ca (20 vol. %) composite with a comparison to identically processed pure Al. Chapter 8 presents a simulation of the interfacial-diffusion driven phase morphological change in a two-phase composite at elevated temperature by diffuse interface phase field approach. Chapter 9 presents the general conclusions of this research project and proposes possible future research work. Appendix A

presents preliminary findings on Al/Ca interface at elevated temperature by Al/Ca diffusion couple experiments, physical properties measurements made on Al<sub>2</sub>Ca intermetallic compound and molecular dynamics simulations to evaluate the elevated temperature performance of the Al/Ca composite. Appendix B presents a short guide on how to build LAMMPS with reax package and library, and the input script codes for equilibrium lattice constant and cohesive energy calculations for Al<sub>2</sub>Ca and codes for Al/Ca bicrystal interface simulation.

### References

1. Russell AM, Chumbley LS, Tian Y. Adv Eng Mater 2000;2:11.
2. Bevk J, Harbison JP, Bell JL. J Appl Phys 1978;49:6031.
3. ASM International Handbook Committee. Metals Handbook 10 ed. Metals Park, Ohio: ASM International; 1990.
4. Tian L, Anderson I, Riedemann T, Russell A, Kim H. Electr Pow Syst Res 2013;105:105.
5. Sondheimer EH. Adv Phys 2001;50:499.
6. Xu K, Russell AM, Chumbley LS, Laabs FC, Gantovnik VB, Tian Y. J Mater Sci 1999;34:5955.

## CHAPTER 2 THE MICROSTRUCTURE-STRENGTH RELATIONSHIP IN A DEFORMATION PROCESSED AL–CA COMPOSITE

A paper published in Materials Science and Engineering: A

Liang Tian<sup>1</sup>, Hyongjune Kim<sup>2</sup>, Iver Anderson<sup>3</sup>, Alan Russell<sup>3</sup>

1. Primary author and corresponding author 2. Experimentalist 3. Project principal  
investigators

### Abstract

An Al-9 vol. % Ca composite was produced by powder metallurgy and deformation processing. The Al–Ca composite was extruded, swaged and wire drawn to a deformation true strain of 13.8. Both Al and Ca are face-centered cubic, so the Ca second phase deformed into continuous, nearly cylindrical filaments in the Al matrix. The formation of intermetallic compounds, filament coarsening, and spheroidization at elevated temperature was observed by scanning electron microscopy, differential scanning calorimetry, and X-ray diffraction. Both the thickness and spacing of the Ca filaments decreased exponentially with increasing deformation. The ultimate tensile strength of the composite increased rapidly with increased deformation, especially at high deformation processing strains. The relation between deformation true strain and ultimate tensile strength is underestimated by the rule of mixtures; a modified Hall–Petch barrier strengthening model was found to fit the data better.

### Introduction

Deformation processed metal–metal composites (DMMCs) are a class of composites developed by severe mechanical deformation (i.e., extruding or rolling, swaging, and wire

drawing) of two ductile metal phases [1]. They are also sometimes referred to as in-situ composites because their filamentary microstructure is formed during deformation [2]. DMMC processing can begin by blended elemental powder consolidation, a powder metallurgy route, or by solidification of a liquid solution of two elements that are mutually insoluble in the solid state [1–3]; in both cases extensive deformation is used to deform the second phase into lamellae (rolling) or filaments (axisymmetric deformation). After the first report of a Cu–Nb DMMC by Bevk et al. [2], DMMCs received considerable study in subsequent years because many of them display an extraordinary combination of high strength and high electrical conductivity [1, 3–5]. When two highly ductile metal phases are used to make the composite, deformation true strains as high as 16 have been reported. Filament thicknesses below 50 nm are observed commonly after such extreme deformation. DMMCs are essentially metallurgically bonded nano-scale bundles of two pure metal continuous phases. This microstructure promotes high electrical conductivity in DMMCs because they act much like parallel conductive pathways that display minimal interphase boundary scattering of electrons traveling parallel to the wire axis or in the plane of rolled sheet [1].

Previous studies showed that the rule of mixture (or volumetric weighted average) model under-predicts the strength of DMMCs [2–14, 17–28]. For example, a Cu-18 vol% Nb DMMC was reported with an ultimate tensile strength of 2200 MPa at a deformation true strain of 11.5, which is higher by a factor of 4 than values predicted by rule of mixtures for Cu and Nb [2]. Bevk et al. first explained the anomalous strength of Cu–Nb composites by the hypothesis that the filaments act as barriers to the motion of matrix dislocation. They emphasized that despite the low volume fraction of Nb filaments, the Cu–Nb DMMC can



still achieve a strength comparable to the best strengths of copper whiskers. Trybus and Spitzig [6] studied rolled Cu–Nb sheet and found that the Nb second phase appeared in a ribbon-like shape parallel to the sheet surface in both transverse and longitudinal directions. The strengths in rolled and wire drawn Cu–Nb both increase as the amount of deformation increases. Wire-drawn Cu–Nb followed the Hall–Petch relationship, but rolled Cu–Nb showed a weaker strength dependence on filament spacing. The strengthening in rolled Cu–Nb correlated well with a modified rule of mixtures model, which takes the strength of Cu–Nb at an equivalent deformation of the composite. The weaker dependence of strength on filament spacing in rolled Cu–Nb could be a consequence of the aligned planar filament morphology presenting less effective barriers to dislocation motion than the curled and convoluted filaments in wire drawn Cu–Nb. The highly kinked Nb filaments in wire drawn Cu–Nb are thought to make slip and plastic flow between the Cu and Nb phases more difficult. Trybus et al. also pointed out that some sub-structural features (i.e. dislocation cell walls and deformation twins) may be responsible for the weaker strengthening effect in rolled Cu–Nb DMMC. Later, Verhoeven, Spitzig and their colleagues studied a series of Cu–matrix-refractory-metal composites similar to the Cu–Nb prototype [7,8,9]. The chosen refractory metals all had bcc crystal structures: Ta [7,9,11], Fe [5,12], V [5,7], and Cr [8,11]. However, none of those combinations improved upon the strength and conductivity of Cu–20% Nb DMMC [1,3–5,7–9,11–13]. The effects of elevated temperature on the microstructure and mechanical properties of Cu refractory metal composite were also investigated [13–16]. Three microstructure evolution mechanisms have been proposed [14,15].

The Cu–Fe system was particularly attractive to many investigators due to the low cost of iron compared with other bcc metals that are insoluble in Cu [17–20]. However, Fe has some limited solid solubility in Cu at elevated temperature and some precipitation of dissolved Fe during deformation reduces the electrical conductivity of Cu–Fe composites [18,19]. Hong et al. [17] and Gao et al. [18,19] investigated the effect of adding third elements on the microstructure and physical properties of Cu–Fe system. The addition of Ag could refine the microstructure of Fe dendrites, reduce filament spacing and promote precipitation of dissolved Fe at high temperature, to achieve an improved combination of strength and conductivity in Cu–Fe composites.

Besides fcc–bcc DMMCs, other combinations of metal phases of DMMC were also developed. An fcc–fcc Cu–Ag DMMC was developed for high-field pulsed magnet use due to its ultrahigh strength and conductivity [21–24]. More recently Al-matrix DMMCs have been explored to see the potential to produce lighter and stronger composite materials. Russell et al. did systematic studies on Al–Ti [25], Al–Mg [26], Al–Sn [27] DMMCs and confirmed that the anomalously high strength also develops in these materials as convoluted, ribbon shape hexagonal close-packed (hcp) and body centered tetragonal (bct) filaments are reduced in size by the deformation. They exhibited high specific strength and high conductivity making them potential candidates for structural and electrical conductor applications.

The strengthening mechanism of various DMMCs is still being debated [10, 28-33]. Studies on Cu–X DMMCs (where X is a bcc metal) showed that the bcc phase is constrained to deform in plane strain due to texturing effects. In contrast, Cu–Ag DMMCs [23] have shown that the fcc Ag second phase is free to deform in the fcc matrix into a cylindrical

filament morphology that is somewhat less effective at blocking dislocation motion than is the convoluted, ribbon-like filamentary morphology observed in Cu-X systems. The strengthening mechanism in Cu-Ag DMMC was attributed to its extremely fine microstructure rather than to effects related to dislocation generation and glide [21]. At high reductions of cross-sectional area, the fiber became so thin (i.e. 50 nm-100 nm) that a Frank-Read source becomes difficult to operate to generate new dislocations. At the same time, the large interface area of the fine filaments act as possible sinks for dislocations. Frommeyer et al [21] and Hong et al [23] observed surprisingly low dislocation densities at large deformations by TEM in Cu-Ag. This experimental evidence supported the Hall-Petch barrier model proposed by Spitzig et al [10], which described the interphase boundary as an effective barrier for dislocation motion. A geometrically necessary dislocation (or work hardening) model was developed by Funkenbusch et al [29, 30] to explain the incremental strength above the rule of mixtures as a consequence of extra dislocation generation to accommodate the additional strain across the interphase boundary. This model also predicted a Hall-Petch dependence of strength on interphase spacing. The controversy about these two models was debated in the literature [28, 32-34] and is still not resolved.

The degradation of strength properties at elevated temperature has been explained as: filament coarsening by the Hall-Petch barrier model [13, 35] or recovery and recrystallization by the work hardening model [31]. The Hall-Petch barrier model failed to explain the increased strength observed in cold-worked, two-phase materials relative to single phase metals with similar filament (i.e., grain) thickness and spacing [29, 31], and the weaker strengthening effect of rolled Cu-Nb sheet compared to wire drawn Cu-Nb rod [6]. The work hardening model does not incorporate the morphology evolution of substructure and was

criticized as only a qualitative prediction because it contains more than one adjustable parameters, which makes this model applicable to only some DMMC systems [31]. However, these two models are not mutually exclusive [30, 31]. Interphase boundaries play a dominating strengthening role and act as sinks for dislocations at very fine interphase spacing due to large true strain (above 10 or so) while substructural development (i.e. dislocation generation) is inhibited [2, 21, 30]. The substructural development may play a strong role in DMMCs of two different crystal structure components at moderate deformation strain, where large strain accommodation between two phases across the boundary is necessary [2, 21, 30].

In this study, an Al-9 vol. % Ca DMMC was produced and characterized. This composition was chosen because the high conductivity and very low density of Ca were thought to hold potential value to produce strong, highly conductive, low-density conducting wires. All three of these characteristics are important for optimizing the performance of high-voltage, overhead power transmission lines. The current study focused on the quantitative relation among deformation true strain  $\eta$ , thickness  $t$  or spacing  $\lambda$  of the reinforcing Ca filaments and ultimate tensile strength of Al-Ca DMMC. This investigation would enhance our understanding of the strengthening mechanism in a similar fcc-fcc DMMC system.

### Experimental Procedure

An Al-9% vol Ca DMMC was produced by a powder metallurgy approach that involves blending fine metal powders, compaction and sintering [37]. High-purity (99.99%, 20-45  $\mu\text{m}$ ) Al powder was produced by the Ames Laboratory gas atomization reaction

synthesis (GARS) process and blended with commercially available high purity (99.5%) Ca powder with an average particle size 1.2 mm. A commercial purity 1100 Al alloy can (Outside diameter 88.9mm, inside diameter 81.2mm) was prepared to hold the blended powder mixture of 91 vol.% Al and 9 vol.% Ca during compaction (by a loose fitting punch) with a pressure of 6.55 to 8.73 MPa. The powder-filled Al can was sealed by electron beam welding in a vacuum chamber at a pressure of  $3.2 \times 10^{-5}$  Pa to protect the specimen from atmospheric contamination during subsequent hot extrusion and room temperature swaging operations. The hot extrusion was performed near 285°C at the SAPA, Inc. facility in Portland, Oregon. A pressure of 26.2 MPa was used to extrude the powder mixture compact through a conical die with a 81.23 mm diameter inlet and 22.1 mm outlet diameter, following by water cooling to room temperature. The extrusion temperature was selected to be high enough for recovery and recrystallization of Al and Ca (0.4  $T_m$ ), but low enough to avoid formation of Al-Ca intermetallic compounds (see Fig. 1).

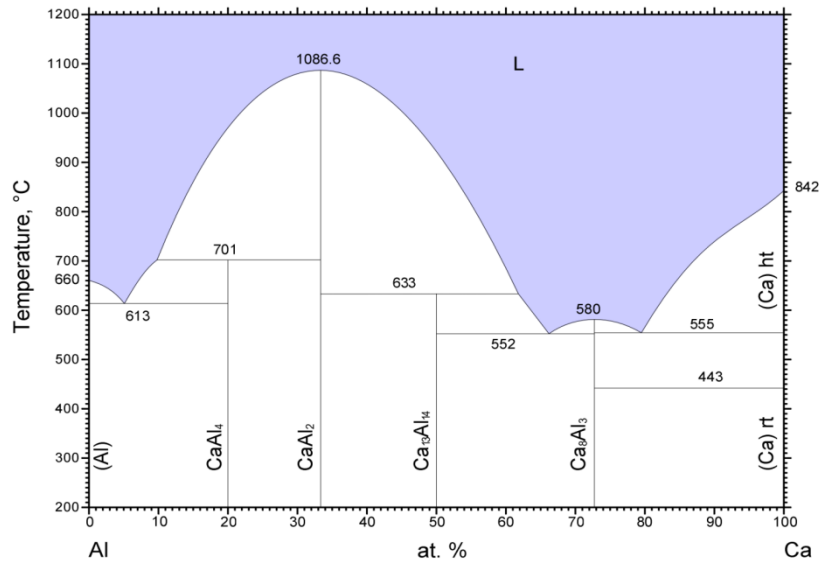


Fig. 1. Al-Ca phase diagram [36]

The deformation true strain  $\eta$  of the specimen was calculated as  $\eta = 2 \ln \frac{d_0}{d_f}$ , where  $d_0$  and  $d_f$  are the initial and final specimen diameters, respectively. A correction was added to account for the fact that collapsing the initial 30% porosity of the compacted powders does not contribute to total true strain. The extruded rod specimens were swaged to a diameter of 6.35mm ( $\eta=4.86$ ) at room temperature and then wire drawn to a diameter of 1mm ( $\eta=8.55$ ). Wires were cut to 35mm lengths at  $\eta=8.55$  so they could be bundled and packed into a fully annealed Cu tube with an inside diameter 25.4 mm. The bundled specimens were then swaged to a diameter of 6.8 mm and wire drawn to a diameter of 1.7mm ( $\eta=13.76$ ). The true strains of the bundled specimens were calculated by measuring the wire diameter under the transverse cross section images of a JEOL JSM-606LV scanning electron microscope. The true strains of the available specimens used for further analysis were 6.27, 8.55, 10.34, 12.45, and 13.76.

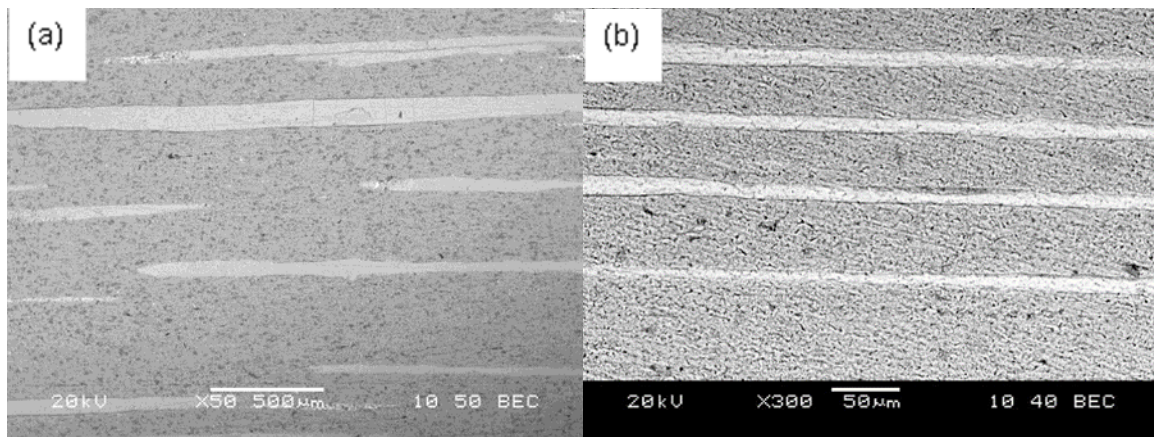
Microstructure images of specimens with  $\eta=2.25, 4.89, 6.27, 8.55, 12.45$  and 13.76 were taken with a JEOL JSM-606LV scanning electron microscope (SEM). Every specimen was prepared by dry grinding with silicon carbide grinding paper: grit size of 600 [38]. Conventional polishing fluids are avoided in order to prevent reaction with Ca. Both polished transverse and longitudinal cross sections were prepared for microstructural analysis. X-ray diffraction (XRD) patterns of Al-9vol% Ca with  $\eta=6.27$  after various heat treatment were obtained from 1-BM beamline (wavelength=0.6066 Å, energy=8-22 keV) at the Advanced Photon Source (APS) at Argonne National Laboratory. Each specimen was exposed to X-rays at room temperature for 200 sec in order to provide a baseline for the possible microstructure evolution of pure Al and Ca into Al-Ca intermetallic compounds after initial hot extrusion and after each step of heat treatment at elevated temperatures. The

formation of intermetallic compounds was further identified by differential scanning calorimetry (DSC). The temperature scanned ranged from 50°C to 535°C at a heating rate of 10°C/min. Tensile tests were performed for specimens with  $\eta=6.27, 8.55, 12.45, 13.76$  for Al-9 vol.% Ca. Ultimate tensile strength (UTS) of every specimen was determined from the average value from at least two tensile tests. Due to the small specimen size of Al-Ca DMMC, UTS is more reproducible and reliable than yield strength. The UTS for  $\eta>10$  is estimated by Vickers microhardness test data under a 100g load because the bundled wires were not consolidated well enough for tensile testing. Four-point resistivity measurements were performed for Al-9 vol.% Ca specimens with  $\eta=8.55$  after heat treatments of various durations at 300°C.

## Results and Discussion

### Microstructure characterization

Fig 2 shows the microstructure of Al-9 vol.% Ca DMMC in the longitudinal direction at four different deformation true strains without heat treatment. The Ca second phase developed a long continuous filament morphology with a uniform thickness.



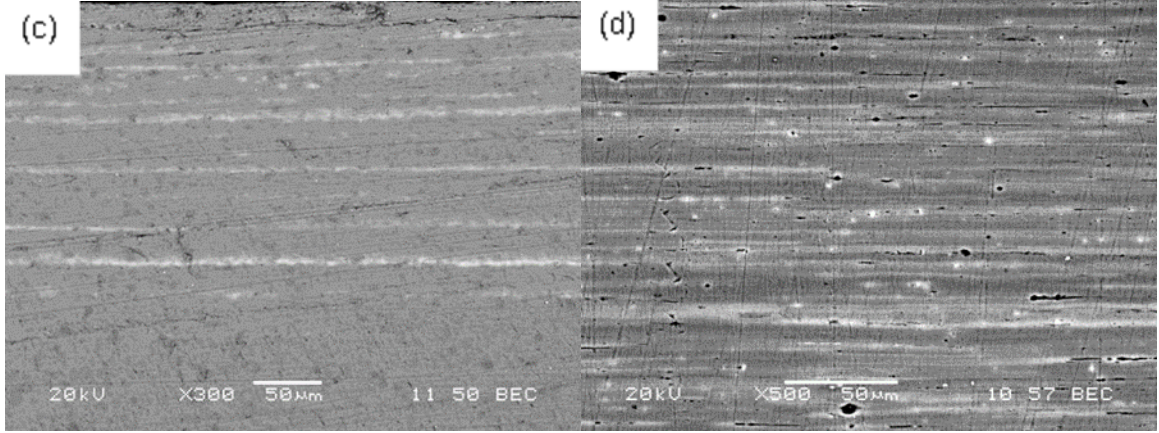


Fig. 2. Back-scattered electron SEM (Scanning Electron Microscopy) micrograph of Al-9 vol.% Ca in longitudinal direction (specimen rod axis parallel to the plane of the micrograph: (a)  $\eta=2.25$ , (b)  $\eta=4.89$ , (c)  $\eta=7.32$ , (d)  $\eta=13.76$ . The Al matrix is dark gray, and the Ca filament is light gray in these images. Some degree of reaction occurs in the Ca phase on contact with the humidity of normal room air, as manifested by the voids visible in image (d).

The relationship between filament thickness and deformation true strain is plotted in Fig. 3. The filament thickness is measured from the SEM micrographs in Fig. 2. The filament thickness decreases sharply with deformation processing. As expected, the filament thickness shows an exponential dependence on deformation true strain. The filament spacing should also exponentially depend on deformation true strain because it is directly proportional to the filament thickness, as described in Ref [25].

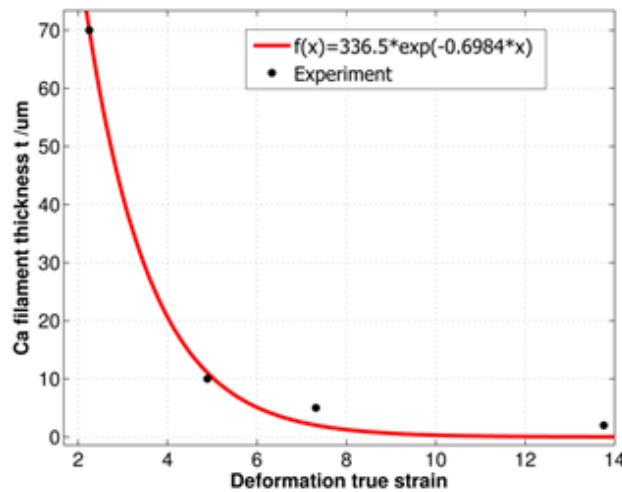
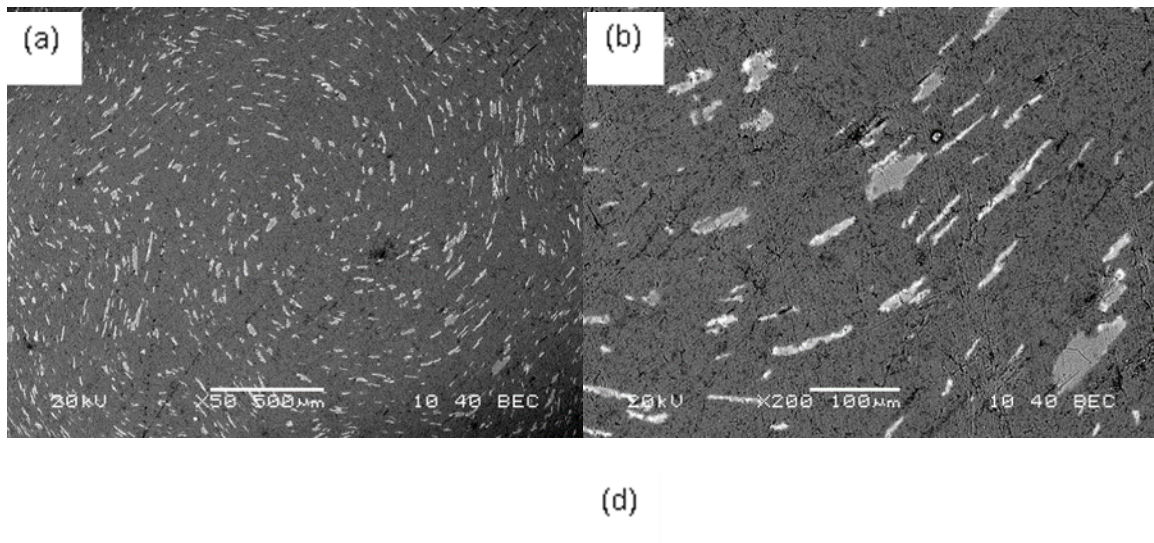




Fig. 3. Ca filament thickness as a function of deformation true strain for Al-9 vol. %Ca.

Fig. 4 shows the microstructure of transverse section of Al-9 vol.% Ca heat treated at three different temperatures for 1 hour. The Ca filament did not display an ideal cylindrical rod morphology, which should be expected from a fcc-fcc DMMC [21]. The lamellar shape of Ca filaments formed a whorl pattern around the deformation axis, which indicates a certain degree of plane-strain deformation. Previous studies [2, 4, 21, 25, 26, 39, 40] found that the morphology of the microstructure was dependent on the crystal structure of the two phases. In a fcc metal matrix, the body centered cubic (bcc) second phase develops a  $\langle 110 \rangle$  fiber texture parallel to the deformation direction and results in a plane-strain deformation mode, forming ribbon-shaped filaments that curl around the deformation axis [2]. A hexagonal close-packed (hcp) second phase adopts  $\langle 101\bar{0} \rangle$  texture and a similar convoluted, ribbon-like filament when deformed axisymmetrically [25, 26]. In contrast, the fcc second phase is free to deform without plane-strain constraints since an fcc matrix provides adequate slip systems to develop a continuous and cylindrical filament morphology [21].



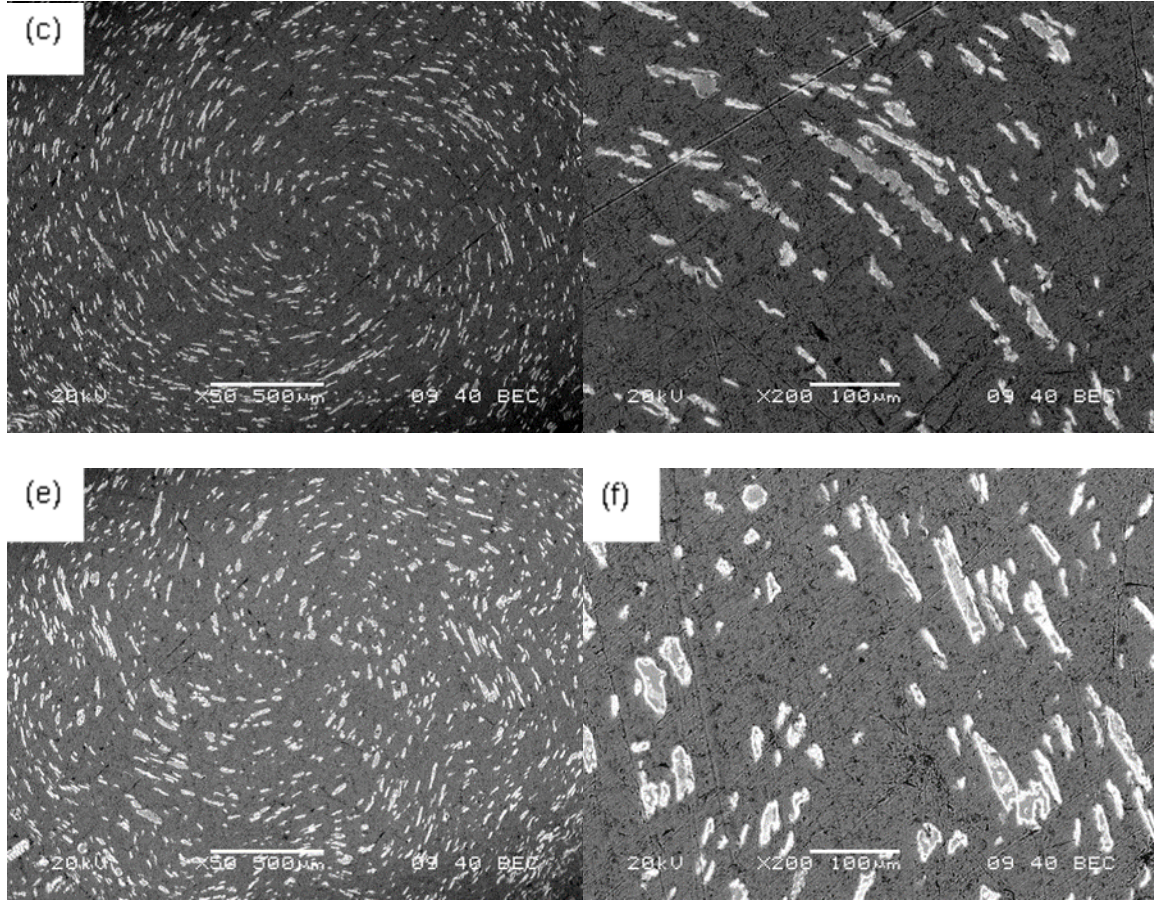


Fig. 4. Back-scattered electron SEM (Scanning Electron Microscopy) micrographs of transverse sections of Al-9 vol.% Ca ( $\eta=6.27$ ) with different heat treatment temperature for 1 hour: (a) and (b) heat treated at 225°C (c) and (d) heat treated at 275°C, (e) and (f) heat treated at 325°C. The Al matrix is dark gray, and the Ca filaments are light gray.

A possible explanation of the apparent plane-strain deformation mode in the Ca filaments is that the stress during deformation induced a temporary phase transformation from fcc to bcc during deformation processing [41, 42]. The Al-Ca phase diagram (Fig. 1), shows a fcc-bcc transformation at 728K for Ca, which is substantially higher than the extrusion temperature. However, the high stress and heat generated during deformation may cause a fcc-bcc transformation during the 285°C extrusion. This hypothesis seems to be supported by the fact that the Ca filaments close to the extrudate's centerline are nearly cylindrical, while the outside edges of the sample are more ribbon-shaped. This is consistent

with the fact that a greater shear stress occurs near the surface of the sample than at the center of the sample. The outside edges of the sample should exhibit more plane-strain deformation features (long ribbons) than the center of the sample, which would be expected to display more nearly cylindrical rods.

Filament coarsening and spheroidization were observed with increased heat treatment temperature from 225°C to 325°C in Fig 4. (b), (d), (f). Spitzig et al [13] suggested that the kinetic driving force for filament coarsening is the tendency to reduce the surface-area-to-volume ratio. This diffusion-controlled process should be thermally activated and associated with an activation energy. This could explain why filament coarsening and spheroidization are more obvious at the higher heat treatment temperature in Fig 4.(f). An empirical rule suggests that the activation energy generally scales with the melting temperature. In ref [13], Ta has a higher melting point (2950°C) than Nb (2468°C) [43], so that kinetic transformation of filament coarsening and spheroidization is more prominent in Nb than in Ta. Since the filament coarsening and spheroidization degrade the strength of the composite, Cu-Ta DMMC exhibited better elevated temperature performance than Cu-Nb [13].

The white regions surrounding the light gray Ca filament in Fig. 4 (f) are  $Al_xCa_y$  intermetallic compounds. At high heat treatment temperature 325°C in Fig. 4 (f), the white area is obviously larger than that at lower temperature in Fig. 4 (b) or (d). The Al-Ca intermetallic compounds were identified by Differential Scanning Calorimetry (DSC) and X-Ray Diffraction (XRD) as  $Al_4Ca$  and  $Al_2Ca$ . Two transformation events were detected by DSC tests, as shown in Fig. 5. Each event corresponds to the formation of a specific Al-Ca intermetallic compound. The lower temperature event occurred at 295°C, and the higher temperature event occurred at 345°C. The XRD tests in Fig. 6 clearly indicated that the

lower temperature transformation is the formation of  $\text{Al}_4\text{Ca}$  and the higher temperature transformation is the formation of  $\text{Al}_2\text{Ca}$ . In Fig. 6. (b), the intensity of the Ca peak decreases with increasing heat treatment temperature, which indicated that Ca filaments were partially consumed to form Al-Ca intermetallic compounds.  $\text{Al}_2\text{Ca}$  has a higher melting temperature ( $1075^\circ\text{C}$  [44]) than either Al ( $660^\circ\text{C}$ ) or Ca ( $842^\circ\text{C}$ ) [43]. Therefore,  $\text{Al}_2\text{Ca}$  may be a more stable reinforcement phase than pure Ca at elevated temperature. Further XRD studies are needed to investigate the kinetics of this reaction.

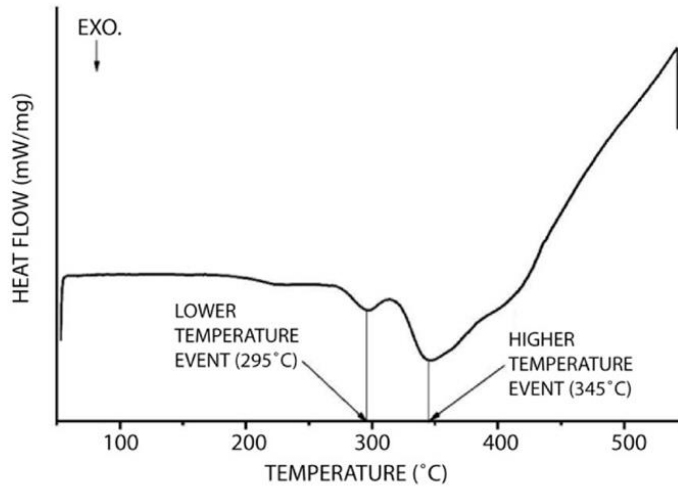


Fig. 5. DSC (Differential Scanning Calorimetry) measurement for Al-9 Vol.% Ca at  $\eta=8.55$ .

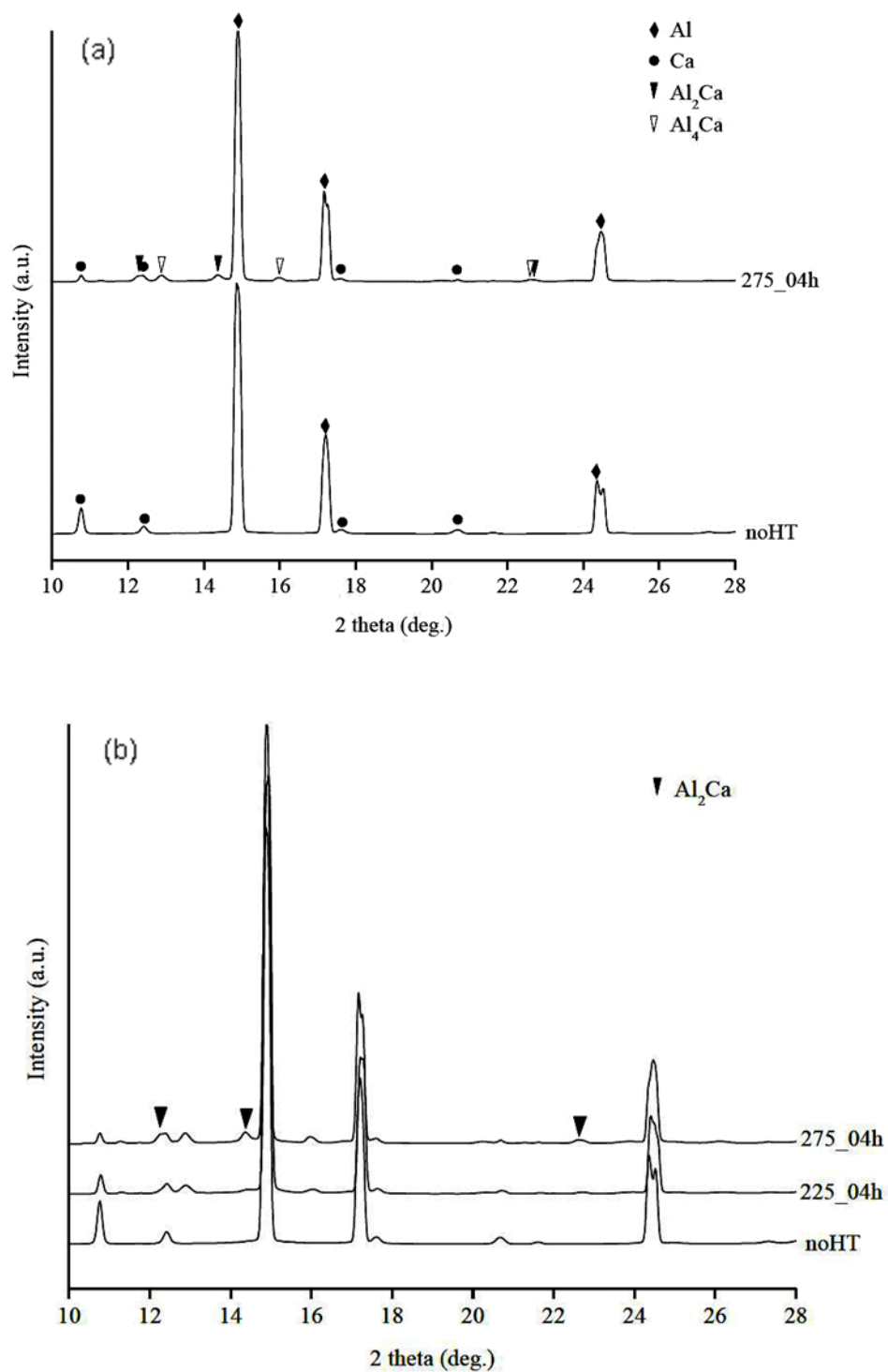


Fig. 6. X-ray diffraction patterns obtained at APS (Advanced Photon Source) of specimens with  $\eta=6.27$ : (a) One sample was non heat treated (noHT) and the other one was heat treated at 275°C for 4 hours (275\_04h). (b) The three samples were non-heat treated (noHT), heat treated at 225°C for 4 hours (225\_04h) and 275°C for 4 hours (275\_04h).



The ultimate tensile strength of Al-9 Vol.% Ca composite wire

Table 1 shows the ultimate tensile strength of unheat-treated Al-9vol.% Ca composite specimens at different deformation true strains. As deformation true strain increased from 6.27 to 13.76, the strength of the composite more than doubled.

Table 1. Average values of ultimate tensile strength and maximum strain for Al-9 vol.%Ca specimens without heat treatment at  $\eta=6.27, 8.55, 12.45$  and  $13.76$ .

Specimens with different true strain $\eta$	Ultimate tensile strength (MPa)	Maximum strain at fracture (%)
6.27	93	13
8.55	145	18
12.45	179	16
13.76	197	16

Previous investigators confirmed that a simple rule-of-mixture model failed to predict the strength of DMMCs [2, 10, 29]. The two mathematical models proposed by Spitzig et al [10] and Funkenbusch et al [29] each have their strengths and weaknesses. The primary difference between these two models is the role of interphase boundaries. The Hall-Petch barrier model proposed by Spitzig et al described the interphase boundary as a barrier to dislocation motion. Funkenbusch's model proposed that interphase boundaries emitted new geometrically necessary dislocations to accommodate strain incompatibility at the boundary. In this study, the Hall-Petch barrier model was chosen to describe the strengthening behavior of Al-9 vol.% Ca DMMC that had not received any heat treatment. Fcc Ca filaments were free to deform in the fcc Al matrix during axisymmetrical deformation.

The strength and ductility of Ca are similar to those of Al, except that Ca's Young's modulus is considerably lower than that of Al. Unlike the case of a softer matrix containing

a hard, rigid reinforcing phase, the Al/Ca composite deformation should be nearly uniform throughout the specimen. Therefore, the strain incompatibility and geometrically necessary dislocations might be expected to be less important factors in Al/Ca composites. However, there may be some extra dislocations emitted by interphase boundaries near the ribbon-shaped Ca filaments, which may have deformed in a plane strain deformation mode. As previously mentioned, a stress-induced phase transformation from fcc to bcc in Ca filament may be responsible for the plane strain deformation, if plane strain did, indeed, occur. The relatively low number of geometrically necessary dislocations expected in Al/Ca should contribute less to the strength increase observed in Al-Ca DMMCs. However, a greater contribution to the strength increase is expected from the large amount of interphase boundaries acting as barriers to dislocation glide in the confined volumes of Al between fine Ca filaments. Since the extrusion temperature was above the recovery and recrystallization temperatures of pure Al and pure Ca, development of substructure (and work hardening) was unlikely to occur during extrusion.

Resistivity measurements for Al-9vol. % Ca at  $\eta=8.55$  seem to support the absence of sub-structural development. Table 2 shows that resistivity remained nearly constant before and after a 300°C heat treatment. This suggests that the dislocation density in the Al-9vol.% Ca composite was relatively low before and after heat treatment. If the dislocation density had been high (as Funkenbusch's model suggests), the heat treatment should decrease dislocation density substantially and therefore reduce dislocation scattering to electrons and decrease resistivity. However, that was not seen in the resistivity measurements. The resistivity increase with heat treatment time was due to the formation of intermetallic compounds, which has higher electrical resistivity than pure Al or Ca.

Table 2. Electrical resistivity for Al-9vol.% Ca at  $\eta=8.55$  heat treated at 300°C for various times. For comparison, the electrical resistivity of pure Al is  $0.0263 \mu\Omega \cdot m$ .

Heat treatment time (min)	Resistivity ( $\mu\Omega \cdot m$ )
0	0.027
10	0.027
30	0.029
60	0.030
180	0.030
300	0.030
720	0.030

The strengthening of Al-Ca DMMC at elevated temperature is complicated by the formation of intermetallic compounds and by filament coarsening. The intermetallic compound  $Al_2Ca$  surrounding the Ca filaments is a hard and stable phase at high temperature. This intermetallic phase formation (as a shell around the Ca) is expected to immobilize dislocations and improve the high temperature strength. On the other hand, filament coarsening degrades the strength of the composite and reduces the inter-phase boundary area. The combined (opposite) effects of intermetallic compound formation and filament coarsening make it difficult to determine which effect is the dominant strengthening (or weakening) mechanism. Further studies are needed to investigate the strength of Al-Ca composite at elevated temperature.

Fig. 7 shows the relationship between ultimate tensile strength (UTS) of Al-9vol % Ca and the tensile deformation true strain  $\eta$ . The ultimate tensile strength increased rapidly with increasing deformation true strain  $\eta$ . The experimental data fit reasonably well to a modified Hall-Petch model, which suggests that UTS is exponentially dependent on deformation true strain  $\eta$ . This modified Hall-Petch model was also found to model well the relation between strength and deformation true strain in Al-Ti [25], Al-Mg [26], and Al-Sn



[27]. In the Al-9 vol. % Ca of this study, the relation between UTS and deformation true strain is  $UTS=51.4\exp(0.01\eta)$ . The exponential dependence index 0.01 is lower than 0.2 observed in Al-Sn [27]. The weaker strengthening effect with increasing deformation true strain in Al-9vol. % Ca may be related to the fcc crystal structure of Al and Ca. A cylindrical Ca filament has a smaller surface-to-volume ratio than a ribbon-shaped Ca filament. Fcc Ca filaments tend to form a mixture of cylinders and ribbons in the fcc Al matrix and therefore have less interphase boundary area than fcc-hcp or fcc-bct DMMC with plane-strain, ribbon-shaped filaments (i.e., Al-Ti, Al-Mg, Al-Sn). However, the inter-phase boundaries always act as effective barriers to dislocation motion, regardless of the type of crystal structure matching. Therefore, a reduced strengthening (due to the decreased surface area generated) with increased deformation true strain should be expected in Al-9vol.% Ca compared to the interfacial boundary strengthening of other DMMCs of two different crystal structure phases. At very large true strain, the ultrafine filaments (of all types of crystal structure pairs) create a substantial amount interphase boundary area that acts as a barrier to dislocation motion, and thus the strengthening is greater at high true strains. It can also be expected that Al-Ca DMMC with larger Ca fraction will exhibit a larger strengthening effect with increased deformation true strain. Future studies are needed to address this topic to see the ultimate extent of this strengthening effect.

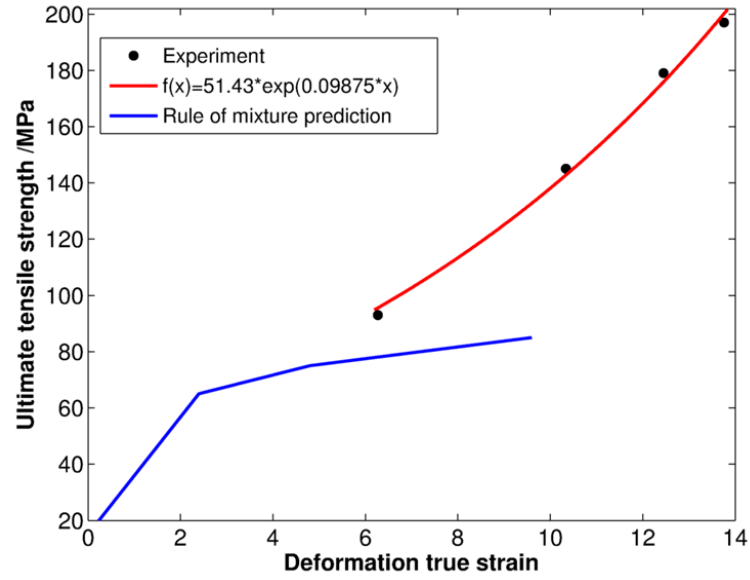


Fig. 7. The relationship between ultimate tensile strength (UTS) and deformation true strain  $\eta$  in Al-9vol.% Ca.  $\eta$  is the deformation true strain of the specimen before tensile testing. The UTS shows an exponential relation to deformation true strain. The simple rule-of-mixture model (Data estimated from [45, 46]) underestimates the strength of Al-9vol% Ca composite, especially at high deformation true strain.

### Conclusions

1. An Al-9 vol. % Ca composite was produced by powder metallurgy and deformation processing to a maximum true strain of 13.8.
2. Most Ca filaments adopted a nearly cylindrical rod shape after deformation processing. However, Ca filaments close to the outside edges of the specimen developed a ribbon-shaped morphology, which may be the result of stress-induced phase transformation from fcc to bcc Ca during deformation.
3. Filament thickness decreased sharply as deformation progressed, producing a fine, uniform microstructure. The interphase boundaries acted as barriers to dislocation motion, strengthening the composite as deformation progressed.

4. Filament coarsening and spheroidization were observed by SEM after heat treatment at 325°C. Two intermetallic compounds Al<sub>2</sub>Ca and Al<sub>4</sub>Ca formed at elevated temperature (275° to 350°C), as determined by SEM, DSC, and XRD.

5. The ultimate tensile strength of Al-9 vol. % Ca composite increased substantially as deformation true strain increased. A modified Hall-Petch barrier model was utilized to quantify the relationship between UTS and deformation true strain. The results of resistivity measurements not only showed the high electrical conductivity of the composite, but also provided evidence for the validity of Hall-Petch barrier model in the Al-9 vol. % Ca composite.

#### References

- [1]. A.M. Russell, L.S. Chumbley, and Y. Tian, *Adv. Eng. Mater.* 2 (2000) 11-22.
- [2]. J Bevk, J.P. Harbison, and J.L. Bell, *J. Appl. Phys.* 49 (1978) 6031-6038.
- [3]. J.D. Verhoeven, W.A. Spitzig, F.A. Schmidt, and C.L. Trybus, *Mater. Manuf. Processes* 4 (1989) 197-209.
- [4]. J.D. Verhoeven, E.D. Gibson, T.W. Ellis, *Key Eng. Mater.* 104-107 (1995) 483-492.
- [5]. J. Bevk, and W.A. Sunder, in: F.D. Lemkey, H.E. Cline, M.McLean (Eds.), *In Situ Composites IV*, Elsevier Science Publishing Co., Inc. New York, 1982, pp.121-133.
- [6]. C.L. Trybus, W.A. Spitzig, *Acta Metall.*, 37 (1989) 1971-1981.
- [7]. J.D. Verhoeven, F.A. Schmidt, E.D. Gibson, W.A. Spitzig, *J.Met.* 38 (1986) 20-24.
- [8]. M.A. Morris, and D.G. Morris, *Mater. Sci. Eng., A* 111 (1989) 115-127.
- [9]. W.A. Spitzig and P.D. Krotz, *Acta metal.* 36 (1988) 1709-1715.
- [10]. W.A. Spitzig, A.R. Pelton and F.C. Laabs, *Acta metal.* 35 (1987) 2427-2442.
- [11]. J.D. Verhoeven, W.A. Spitzig, L.L. Jones, H.L. Downing, C.L. Trybus, E.D. Gibson, L.S. Chumbley, L.G. Fritzmeier, G.D. Schnittgrund, *J. Mater. Eng.* 12 (1990) 127-139.

- [12]. C. Biselli and D.G. Morris, *Acta metal. Mater.* 42 (1994) 163-176.
- [13]. W.A. Spitzig, P.D. Krotz, L.S. Chumbley, H.L. Downing, J.D. Verhoeven, *Mater. Res. Soc. Symp. Proc.* 120 (1988) 45-50.
- [14]. J. Bevk, K.R. Karasek, in: D.Kuhlmann-Wilsdorf, W.C. Harrigan, Jr. (Eds.), *New Developments and application in Composites*, Met. Soc. of AIME, Warrendale, PA, 1979, pp. 101-113.
- [15]. J.C. Malzahn Kampe, T.H. Courtney, Y. Leng, *Acta metal.* 37 (1989) 1735-1745.
- [16]. T.H. Courtney and J.C. Malzahn Kampe, *Acta metal.* 37 (1989) 1747-1758.
- [17]. S.I. Hong, *Adv. Eng. Mater.* 7 (2001) 475-479.
- [18]. H.Y. Gao, J. Wang, D. Shu, B.D. Sun, *Scr. Mater.*, 53 (2005) 1105-1109.
- [19]. H.Y. Gao, J. Wang, D. Shu, B.D. Sun, *Mater. Sci. Eng., A*, 452-453 (2007) 367-373.
- [20]. J.S. Song, S.I. Hong, Y.G. Park, *J. Alloys Compd.*, 388 (2005) 69-74.
- [21]. G. Frommeyer and G. Wassermann, *Acta Metal.* 23 (1975) 1353-1360.
- [22]. Y. Sakai, H.J. Schneider-Muntau, *Acta mater.* 45 (1997) 1017-1023.
- [23]. S.I. Hong, M.A. Hill, Y. Sakai, J.T. Wood, J.D. Embury, *Acta metal. Mater.* 43 (1995) 3313-3323.
- [24]. Y. Sakai, K. Inoue, T. Asano, H. Wada, and H. Maeda, *Appl. Phys. Lett.* 59 (1991) 2965-2967.
- [25]. A.M. Russell, T. Lund, L.S. Chumbley, F.A. Laabs, L.L. Keehner, J.L. Harringa, *Composites: Part A*, 30 (1999) 239-247.
- [26]. K. Xu, A.M. Russell, L.S. Chumbley, F.C. Laabs, *J. Mater. Sci.*, 34 (1999) 5955-5959.
- [27]. K. Xu, A.M. Russell, *Mater. Sci. Eng., A*, 373 (2004) 99-106.
- [28]. W.A. Spitzig, J.D. Verhoeven, C.L. Trybus and L.S. Chumbley, *Scr. Metall.*, 24 (1990) 1171-1174.
- [29]. P.D. Funkenbusch and T.H. Courtney, *Acta metall.* 33 (1985) 913-922.
- [30]. P.D. Funkenbusch, J.K. Lee and T.H. Courtney, *Met. Trans. A.*, 18A (1987) 1249-1255.

- [31]. P.D. Funkenbusch and T.H. Courtney, *Scr. Metall.*, 23 (1989) 1719-1724.
- [32]. P.D. Funkenbusch and T.H. Courtney, *Scr. Metall.*, 24 (1990) 1175-1180.
- [33]. P.D. Funkenbusch and T.H. Courtney, *Scr. Metall.*, 24 (1990) 1183-1184.
- [34]. W.A. Spitzig, J.D. Verhoeven, C.L. Trybus, L.S. Chumbley L.S., *Scr. Metall.*, 24 (1990) 1181-1182.
- [35]. L.S. Chumbley, H.L. Downing, W.A. Spitzig, and J.D. Verhoeven, *Mater. Sci. Eng., A*, 117 (1989) 59-65.
- [36]. <http://www1.asminternational.org/asmenterprise/apd/>, ASM International, Materials Park, OH, USA, 2006-2012.
- [37]. American Society for Metals, *Metals Handbook*, Desk ed., Metals Park, Ohio, 1985.
- [38]. H. Kim, Ph.D thesis, Iowa State University, 2011.
- [39]. A.M. Russell, L.S. Chumbley, T.W. Ellis, F.C. Laabs, B. Norris, and G.E. Donizetti, *J. Mater. Sci.*, 30 (1995) 4249-4262.
- [40]. W.F. Hosford, *Trans. Met. Soc. AIME*, 230 (1964) 12-15.
- [41]. W. Steurer, in: R.W. Cahn and P. Haasen (Eds.), *Physical Metallurgy*, fourth ed., Elsevier, The Netherland, 1996, pp. 17.
- [42]. A. Jayaraman, W. Klement, Jr., and G. C. Kennedy, *Phys. Rev.*, 132 (1963) 1620-1624.
- [43]. R.B. Ross, *Metallic Materials Specification Handbook*, third Edition, E.&F.N. Spon Ltd, New York, 1980.
- [44]. K. Ozturk, Y. Zhong, A.A. Luo, and Z.K. Liu, *JOM*, 55 (2003) 40-44.
- [45]. American Society for Metals, *Metals Handbook*, tenth ed., Metals Park, Ohio, 1990.
- [46]. K. Rodak, K. Radwański and R. Molak, *Solid State Phenom.* 176 (2011) 21-28.

CHAPTER 3 A DISLOCATION-BASED, STRAIN-GRADIENT-PLASTICITY  
STRENGTHENING MODEL FOR DEFORMATION PROCESSED METAL-METAL  
COMPOSITES

A paper published in Journal of Materials Science

Liang Tian<sup>1</sup>, Alan Russell<sup>2</sup>, Iver Anderson<sup>2</sup>

1. Primary researcher and author 2. Project principal investigators

Abstract

Deformation processed metal-metal composites (DMMCs) are high strength, high electrical conductivity composites developed by severe plastic deformation of two ductile metal phases. The extraordinarily high strength of DMMCs is underestimated by the rule of mixture (or volumetric weighted average) of conventionally work-hardened metals. In this paper, a dislocation-density-based, strain-gradient-plasticity model is proposed to relate the strain gradient effect with the geometrically necessary dislocations emanating from the interface to better predict the strength of DMMCs. The model prediction was compared with the experimental findings of Cu-Nb, Cu-Ta, Al-Ti DMMC systems to verify the applicability of the new model. The results show that this model predicts the strength of DMMCs better than the rule-of-mixture model. The strain gradient effect, responsible for the exceptionally high strength of heavily cold worked DMMCs, is dominant at large deformation strain since its characteristic microstructure length is comparable with the intrinsic material length.

## Introduction

Deformation processed metal-metal composites (DMMCs) are composites with an excellent combination of high strength and high conductivity. This combination of characteristics makes them candidates for numerous engineering applications, including high-voltage power transmission conductors, high-field pulsed magnets, fly-by-wire flight control system, electric motor armature windings, etc. [1]. The production of DMMCs begins with powder metallurgy or solidification of a liquid solution of two metal elements that are mutually insoluble in the solid state [1]. The mixture of two ductile metal phases is then subjected to plastic deformation processing (i.e., extruding/swaging/wire drawing or rolling) to deform the minor phase into elongated nano-scale (cross-section) filaments or lamellae with nanometer scale spacings [1]. The strength of DMMCs increases greatly with the deformation true strain [2-8], deviating substantially from the conventional rule of mixture model [2]. Bevk et al. [2] observed the exceptionally high strength of Cu-Nb with relatively small amounts of filamentary Nb (with moderate strength) and confirmed that the strength and volume fraction of the filament phase was insignificant to achieve the high strength of DMMCs. However, they also found that the strength of Cu-Nb composites could be predicted well by the rule-of-mixtures model at small deformation true strains (~5 or less).

Various strengthening mechanisms or models have been proposed to explain the extraordinarily high strength of DMMCs subjected to a large deformation true strain [9-13]. Bevk et al. [2], Spitzig et al. [3] and other investigators [4-8] have confirmed that the high strength of DMMCs was underestimated by a simple rule-of-mixtures (ROM) model for several different DMMC compositions. Spitzig et al. [9] suggested a Hall-Petch barrier model, which attributed the strengthening effect to the role of the interface as a barrier to

dislocation motion. This model described the dependence of the strength of a composite on the filamentary spacing by a Hall-Petch relationship. Funkenbusch et al. [10] proposed a work hardening model, which explained the incremental strength above the ROM prediction as a consequence of geometrically necessary dislocations emitted from the interface to accommodate the strain incompatibility across the interphase boundary. However, these two mechanisms are not completely exclusive. One mechanism will dominate over the other depending on the deformation processing and crystal structure of the two metal phases. Interphase boundaries appear to be the major strengthening mechanism at large deformation strain (above 10) because they act as sinks for dislocations and inhibit the development of Frank-Read dislocation sources due to the fine interphase spacing [11]. The geometrically necessary dislocations (GNDs) are mainly responsible for the incremental strength when two metal phases with different crystal structure are deformed to a moderate strain so that strain accommodation by GNDs between two phases is necessary. These two models are not perfect. The Hall-Petch barrier model failed to explain the high strength of cold-worked two phase materials relative to single phase material with similar filament (i.e. grain) spacing [10]. The work hardening model was assessed only as a semi-quantitative model because it contains many adjustable parameters, making it applicable to some specific DMMC systems [12]. Raabe et al. [13] brought up a modified linear rule of mixture model to include a Hall-Petch contribution from phase boundaries for simulating the strength of fcc/bcc type DMMCs. However, this model requires mathematical assumptions to explain the origin of the Hall-Petch contribution from the interface, which casts some doubt over the universality of the model. Therefore, opportunities exist to further refine models addressing the physical origin of the anomalously high strength of DMMCs.



Strain-gradient-plasticity theories interpret size-dependent deformation behavior of metals at the micrometer scale [14, 15]. Previous experiments on micro-torsion [15], micro-bending [16] and micro-indentation [17] confirmed the size effect present in the deformation response of metals. For example, Fleck et al. [15] observed that the shear strength of twisted thin copper wires increased by a factor of three as the wire diameter decreases from 170 to 12  $\mu\text{m}$ . A similar bending hardening effect was observed by Stolken and Evans [16] as the Ni foil thickness decreased from 50 to 12.5  $\mu\text{m}$ . De Guzman et al. [17] conducted micro-indentation tests on Ni and Cu samples and showed that the measured hardness increased with decreasing penetration depth from 2000 to 200nm. Lloyd et al. observed a substantial strength increase for SiC-particle-reinforced composite when the particle diameter decreased from 16 $\mu\text{m}$  to 7.5 $\mu\text{m}$  with a fixed particle volume fraction of 15% [18]. The conventional plasticity theories cannot explain this size-dependent material behavior at the micro-scale, because no internal material length scale was implemented in their constitutive models [19, 20, 21]. In strain gradient plasticity theories, a material length scale was introduced to compare with the characteristic microstructure dimension to determine the strain-gradient effect [14, 19, 20]. The strain gradient effect can also be used to interpret the grain-size-dependent flow stress of polycrystalline materials—the Hall-Petch relation [19]. How the plasticity behavior of metals is affected by the strain gradient is determined by dislocation motion, which has long been known to be the most important mechanism of plastic deformation [14, 19, 20]. Strain gradients are accommodated by the geometrically necessary dislocations (GNDs) to distort the crystalline lattice structure [22, 23]. An increased density of GNDs will work harden crystals like that of statistically stored dislocations (SSDs) by Taylor's hardening law [24].

Various strain gradient plasticity continuum models have been put forward to describe the collective behavior of material defects and to predict the size-dependent mechanical behavior of materials due to the difficulty to perform atomistic simulation and discrete dislocation dynamics calculations [19, 20]. Fleck and Hutchinson developed a higher order couple stress theory to relate strain gradients with the effective measure of a curvature tensor [15] and later with both rotation and stretch gradients [25]. A higher order stress was defined as the work conjugate of strain gradient to satisfy the Clausius-Duhem thermodynamic inequality. It requires additional boundary conditions for finite element implementation. The phenomenological nature of Fleck-Hutchinson theories requires many fitting parameters, which are difficult to test fully by limited strain-gradient dominated experiments. A mechanism-based strain gradient theory proposed by Gao et al. distinguished the micro-scale at which dislocation interaction follows the Taylor's hardening law from the meso-scale where high-order strain-gradient plasticity is established. An effective strain gradient measure was derived from three deformation modes to be linked with geometrically necessary dislocations [20]. This model used Taylor's hardening law as the foundation so that it can predict the linear dependence of the square of plastic flow stress on strain gradient that was observed experimentally by Nix and Gao [26]. It has fewer adjustable parameters than Fleck-Hutchinson theory, and it interpreted the experiments of size-dependent plasticity well. Gao et al. [27] presented another way to link Taylor's hardening law with continuum theories without resorting to the high-order stresses at the meso-scale cell in mechanism-based strain-gradient theory. The essential idea is to calculate the density of GNDs as nonlocal variables expressed in terms of plastic strain by representing strain gradients as a non-local integral of strains. The constitutive equations of this theory resemble those of

conventional plasticity theory and are much simpler than high-order theory of Fleck-Hutchinson and mechanism-based strain-gradient theory.

In this paper we present a dislocation-density-based strain-gradient model for the strengthening effect of deformation processed metal-metal composites (DMMCs). The motivation to incorporate the strain gradient effect into the deformation behavior of DMMCs comes from the fact that the sub-micron size (as low as 20nm [2]) filamentary microstructure in DMMCs is obviously comparable with a common intrinsic material length scale from a fraction of a micron to tens of microns. In addition, the interfaces between fiber and matrix are provided as a realistic source to generate the geometrically necessary dislocations to accommodate a strain gradient. Instead of a continuum formulation, an effective strain gradient is proposed to be directly proportional with the deformation true strain during severe plastic deformation of DMMCs and inversely proportional to the characteristic microstructure length [15, 19, 20]. This assumption should be plausible for DMMCs due to the uniaxial deformation mode during deformation processing and taken by Gao et al. [20] as an argument to discuss the strain gradient effect. A material-dependent parameter is introduced in this assumption to average the effect of different orientations of the slip systems, which is hard to implement in continuum models [14]. An analytic expression of the yield strength of DMMCs was derived in the following section to compare with the experimental results to test the effectiveness of this model.

### Model Formulation

In the section, a physically based strain-gradient plasticity strengthening model for DMMCs is presented based on a modified rule of mixtures. The yield strength of each metal

phase in DMMCs obeys Taylor's dislocation hardening law with an additional GNDs density term from the interface. An explicit relation between SSDs (or GNDs) and deformation true strain is established to show the predominant strain gradient effect at large deformation true strain and hence predict the extraordinarily high strength of heavily deformed DMMCs. The internal material length scale for each phase can be totally derived from physical parameters of the material as in the mechanism-based strain-gradient theory [20]. This model eliminates the mathematical complexity of previously developed continuum strain gradient models due to the uniaxial deformation mode of DMMCs, but captures all the essential features of strain-gradient plasticity theory to make it physically plausible.

Plastic deformation in monolithic metallic materials comes from the collective motion of numerous dislocations. A dislocation density concept was found to be useful as the average treatment of dislocation processes to be linked with the macroscopic stress and strain. The plastic hardening originates from the interaction of mobile dislocations with immobile dislocations or other crystal microstructures (e.g. precipitates, solute atoms, grain boundaries) that act as obstacles to dislocation motion. A critical shear stress, known as shear strength, is required to untangle the interaction between dislocations and obstacles and hence to initiate plastic deformation. Taylor's hardening law relates the shear strength to the dislocation density by

$$\tau = \tau_0 + \alpha G b \sqrt{\rho_t} = \tau_0 + \alpha G b \sqrt{\rho_s + \rho_G} \quad (1)$$

where  $\tau_0$  is the extrapolated shear strength at zero dislocation density,  $\alpha$  is a material constant ranging from 0.1 to 0.5 [23],  $G$  is the shear modulus,  $b$  is the Burgers vector length,  $\rho_t$  is the total dislocation density,  $\rho_s$  is the density of statistically stored dislocations,  $\rho_G$  is the density of geometrically necessary dislocations. By taking a direct sum of SSDs and GNDs into the

strain hardening relation, we make no distinction between SSDs and GNDs in the effectiveness of blocking the motion of mobile dislocations [27]. For crystalline materials, the tensile yield strength is related to the shear strength by a Taylor factor  $m$  as

$$\sigma = \sigma_0 + m\alpha Gb\sqrt{\rho_S + \rho_G} \quad (2)$$

where  $\sigma_0 = m\tau_0$  is the extrapolated yield strength at zero dislocation density. The Taylor factor  $m$  reflects the degree of crystalline anisotropy at the continuum level [19]. For a perfectly isotropic solid,  $m = \sqrt{3}$ . For face-centered cubic (fcc) polycrystalline metals,  $m = 3.08$  [19].

GNDs are used to accommodate the strain gradient and the curvature of a crystal lattice [22]. The effective density of GNDs is given as [20]

$$\rho_G = \frac{\eta}{b} \quad (3)$$

where  $\eta$  is the effective strain gradient. Without the strain-gradient effect, the strain hardening relation (2) can be rewritten as

$$\sigma = \sigma_0 + m\alpha Gb\sqrt{\rho_S} = \sigma_0 + (\sigma_Y - \sigma_0)f(\varepsilon) \quad (4)$$

where  $f(\varepsilon)$  is a function satisfying  $f(0)=1$  that can be obtained from uniaxial tension testing,  $\sigma_Y$  is the yield strength without any strain hardening ( $\varepsilon=0$ ). For ductile metals, the yield strain  $\varepsilon_Y$  is taken as 0.2% so that the elastic strain is negligible during severe plastic deformation processing of metal phases. A common power hardening law is chosen as  $f(\varepsilon)=1+\varepsilon^n$ , where  $n$  is the work hardening exponent for the metal [21]. The density of SSDs can be derived from eq. (4) as

$$\rho_S = \left[ \frac{(\sigma_Y - \sigma_0)f(\varepsilon)}{m\alpha Gb} \right]^2 \quad (5)$$

With  $\rho_S$  and  $\rho_G$  given by eq. (5) and (3), respectively, we can rewrite eq. (2) as

$$\sigma = \sigma_0 + (\sigma_Y - \sigma_0)\sqrt{f(\varepsilon)^2 + l\eta} \quad (6)$$

where  $l = m^2 \alpha^2 (\frac{G}{\sigma_Y - \sigma_0})^2 b$  is identified as the intrinsic material length scale defined by Gao et al. [20]. The intrinsic material length totally hinges on the structure and properties of the monolithic metal phase. The strength of DMMCs follows a modified rule of mixture relation [13] as

$$\sigma_c = \sigma_A V_A + \sigma_B V_B \quad (7)$$

where  $\sigma_c$  is the yield strength of metal-metal composites,  $V_A$  and  $V_B$  are the volume fraction of metal phase A and B, respectively.  $\sigma_A, \sigma_B$  are the yield strength of metal phase A and B considering the work hardening effect from both SSDs and GNDs, given by eq.(2) and (6) as

$$\begin{aligned} \sigma_A &= \sigma_{A0} + m_A \alpha_A G_A b_A \sqrt{\rho_{SA} + \rho_{GA}} = \sigma_{A0} + (\sigma_{AY} - \sigma_{A0}) \sqrt{f(\varepsilon)^2 + l_A \eta_A} \\ \sigma_B &= \sigma_{B0} + m_B \alpha_B G_B b_B \sqrt{\rho_{SB} + \rho_{GB}} = \sigma_{B0} + (\sigma_{BY} - \sigma_{B0}) \sqrt{f(\varepsilon)^2 + l_B \eta_B} \end{aligned} \quad (8)$$

where  $\rho_S$  and  $\rho_G$  for metal phases A and B are given by eq (5) and (3), respectively. The effective strain gradient  $\eta$  can be taken to be proportional to the deformation true strain  $\varepsilon$  and inversely proportional to the characteristic length of the microstructure [20]. When the characteristic microstructure length is much larger than the intrinsic material length, the strain gradient hardening effect by GNDs become negligible in comparison with the strain hardening by SSDs, and the strain gradient plasticity model eq. (6) will degenerate to the conventional work-hardening model eq. (4). In DMMCs, the cross-section thicknesses of fiber and matrix are chosen as the characteristic length (see Fig. 1.). So we get  $\eta_A = k_A \frac{\varepsilon}{t_A}$ ,  $\eta_B = k_B \frac{\varepsilon}{t_B}$ , where  $k_A, k_B$  are the material-dependent parameters introduced for metal phases A and B, respectively. The thickness of metal phase A and B should satisfy  $t_A/t_B = V_A/V_B$  from previous work on Al/Ti DMMCs [6]. The deformation true strain  $\varepsilon$  is calculated as  $\varepsilon = 2 \ln(t_0/t_B)$ , where  $t_0$  is the initial thickness of fiber phase B [1]. So we have  $t_B = t_0 \exp(-\varepsilon/2)$ .

From the above relations, the effective strain gradient can be directly related to the deformation true strain as

$$\eta_A = k_A \frac{V_B \varepsilon \exp(\frac{\varepsilon}{2})}{V_A t_0}$$

$$\eta_B = k_B \frac{\varepsilon \exp(\frac{\varepsilon}{2})}{t_0} \quad (9)$$

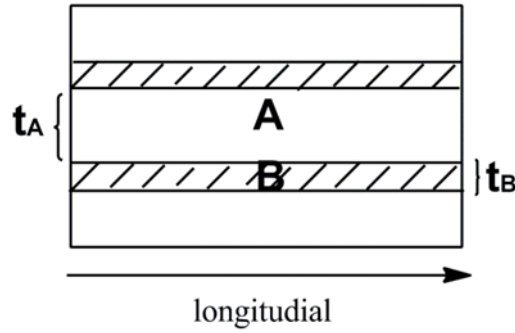


Fig.1 A schematic of metal-metal composite with A being the matrix metal phase, B being the fiber metal phase.

Combining eqs. (7), (8) and (9), the yield strength of DMMCs will be given by

$$\sigma_c = \sigma_{A0} V_A + \sigma_{B0} V_B + V_A (\sigma_{AY} - \sigma_{A0}) \sqrt{f(\varepsilon)^2 + l_A k_A \frac{V_B \varepsilon \exp(\frac{\varepsilon}{2})}{V_A t_0}} + V_B (\sigma_{BY} - \sigma_{B0}) \sqrt{f(\varepsilon)^2 + l_B k_B \frac{\varepsilon \exp(\frac{\varepsilon}{2})}{t_0}} \quad (10)$$

Eq. (10) gives the yield strength of DMMCs,  $\sigma_c$ , as a function of the deformation true strain  $\varepsilon$  and the volume fraction, the initial dimension, the physical properties and the strain hardening behavior of two metal phases. It clearly explains why strain gradient effects are predominating at large deformation true strain and heavily cold-worked DMMCs have extraordinarily high strengths. Both the strain gradient effects and the strength of DMMCs increase exponentially with deformation true strain. The volume fraction and strength of each phase have less impact on strength of DMMCs than deformation true strain, especially at large deformation true strain, which was observed experimentally by Bevk et al. [2]. This strengthening model for DMMCs captures the essential feature of strain gradient effects by

establishing a link between the density of GNDs and the effective strain gradient while maintaining a simple mathematical structure due to the uniaxial deformation processing model of DMMCs. This model can be easily modified to more accurately predict the strength of DMMCs by representing the intrinsic material length as a function of strain, strain rate, grain size and temperature, etc. [19]. The purpose of this paper is to show a physically plausible method to incorporate the strain gradient effects into the strengthening behavior of DMMCs, which has not been done in previous studies [9, 12, 13].

### Model Predictions versus Experimental Results

In this section, the model prediction of the strength of Cu/Nb, Cu/Ta and Al/Ti DMMCs will be compared with the corresponding experimental results. The upper bound of rule of mixtures prediction is also given to confirm the strain gradient effects that are responsible for the extraordinarily high strength at large deformation true strain. The physically plausible link between the effective strain gradient and the density of GNDs makes the model predict the experimental results quite well.

#### Cu/Nb and Cu/Ta DMMCs

The strength of Cu/Nb DMMCs has been investigated extensively in the past [2, 3, 28, 29]. The two phase Cu/Nb composites were produced by rapid cooling of the homogeneous liquid of two elements into two-phase solid eutectics to minimize the crucible contamination and to ensure clean interphase boundaries [2]. The Cu/20 vol% Nb composites with two different initial Nb dendrite sizes due to different melting procedures in ref. [3] are taken as the experimental results for us to compare with the strain-gradient-based model.



The input parameters for the model are set up as follows: the power hardening law for the strength of Cu is given by  $103+(210-103)(1+\epsilon^{0.54})$  MPa [30]. For Nb, it is  $240+(300-240)(1+\epsilon^{0.29})$  MPa [31]. The heavily deformed fcc-Cu and bcc-Nb exhibited crystallographic  $\langle 111 \rangle$  and  $\langle 110 \rangle$  texture parallel to the wire axis, respectively. The Taylor factors for heavily deformed fcc-phase and bcc-phase are taken as 3.16 and 2.15, respectively from ref. [13]. The constant  $\alpha$  is estimated as 0.3. The shear modulus for Cu is 46 GPa and for Nb, 37.5 GPa [32]. The Burgers vectors for Cu and Nb can be estimated by the interatomic spacing, which is twice the atomic radius in the close-packed slip systems. So we get  $b_{Cu}=0.256\text{nm}$  and  $b_{Nb}=0.292\text{nm}$ . Therefore, the intrinsic material lengths for Cu and Nb can be calculated to be  $l_{Cu}=42.52\text{ }\mu\text{m}$  and  $l_{Nb} = 47.45\text{ }\mu\text{m}$ , which are on the order of microns. The two initial Nb dendritic sizes are  $t_0=6.2\text{ }\mu\text{m}$  and  $t_0=3.8\text{ }\mu\text{m}$  in ref. [3]. The prediction of the strain-gradient strengthening model is compared with the experimental results and the rule of mixtures prediction in Fig. 2(a). The strain-gradient strengthening model matches well with the experimental data over the entire strain range, while rule of mixtures predicts the strength accurately only at low deformation strain. The fitting material parameters  $k$  for Cu is 0.01 and for Nb is 0.201 for  $t_0=6.2\text{ }\mu\text{m}$ . For  $t_0=3.8\text{ }\mu\text{m}$ ,  $k_{Cu}$  and  $k_{Nb}$  are 0.01 and 0.213, respectively. The values of fitted material parameters  $k$  for Cu and Nb are quite close, which indicates that  $k$  may be a material-related parameter.

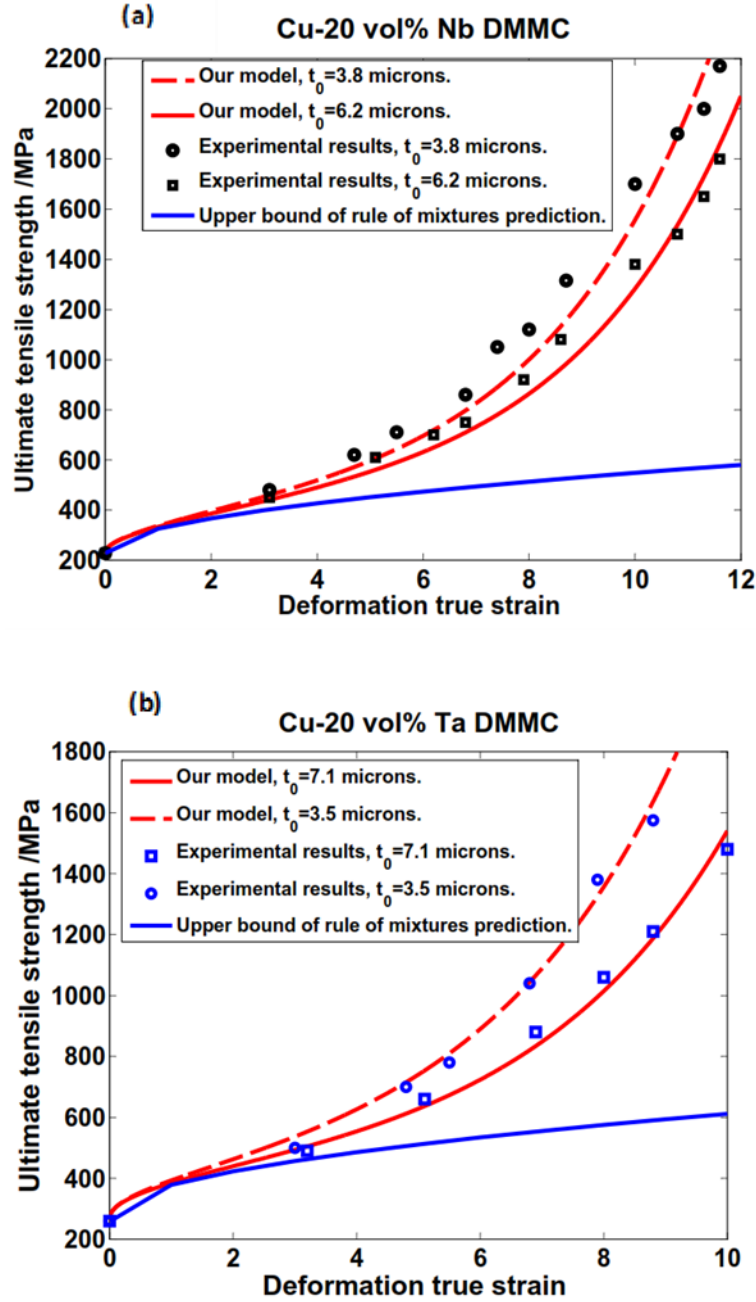


Fig. 2 (a) Comparison of the tensile strength of Cu-20 vol% Nb DMMC between experimental results [3] and our strain gradient hardening model. Two different initial Nb dendritic sizes were analyzed to show the size effect. (b) Comparison of the tensile strength of Cu-20 vol% Ta DMMC between experimental results [3] and our strain gradient hardening model. Two different initial Ta dendritic sizes were analyzed to show the size effect. An upper bound of rule of mixtures prediction is given for comparison purposes.

Similar comparison between our model and experimental results is made for Cu/20 vol % Ta DMMC. The Cu/20 vol% Ta with two different initial Ta dendritic sizes (7.1 $\mu\text{m}$  and 3.5 $\mu\text{m}$ ) were used to produce DMMCs for the strength test [3]. The parameters for Ta are as follows: the power hardening law for Ta is given by  $275+(450-275)(1+\varepsilon^{0.21})$  MPa [33]. The Taylor factor for heavily deformed bcc Ta is estimated to be 2.15 [3]. The constant  $\alpha$  is 0.3. The shear modulus for Ta is 69 GPa [32]. The Burgers vector of Ta is estimated by 0.292 nm. Therefore, the intrinsic material length of Ta can be calculated to be 18.89  $\mu\text{m}$ . The comparison between the prediction of the strain gradient strengthening model and the experimental results is given in Fig 2(b). The fitted material parameters for Cu and Ta are  $k_{\text{Cu}}=0.01$ ,  $k_{\text{Ta}}=0.1465$  for  $t_0=7.1\mu\text{m}$ . For  $t_0=3.5\mu\text{m}$ ,  $k_{\text{Cu}}=0.01$  and  $k_{\text{Ta}}=0.1926$ . The two  $k$  values for Ta are close, which suggests that  $k$  is material dependent.

The rule of mixtures is obviously unable to predict the high strength at large deformation true strain (greater than 5) because it neglects the contribution of GNDs as an immobile dislocation forest blocking dislocation motion. The number of GNDs increased substantially to accommodate the strain gradient due to non-uniform deformation of two phases at the interface, work-hardening the composite to diverge from the rule of mixtures prediction. At low deformation true strain, the strain gradient is negligible mainly due to the relatively large characteristic microstructure length, so that the strain gradient hardening effect is weak, and our model coincides with the rule of mixtures.

The initial dendritic size effect on the strength of DMMCs is explained by different physical mechanisms in our strain gradient hardening model and Hall-Petch barrier model, although they both give an inverse-square-root relation. The Hall-Petch barrier model attributed this size effect to the increased interface area that acts as a barrier to dislocation

motion for fine filaments. In contrast, our strain gradient hardening model proposed that at the same deformation true strain, the initial finer dendritic size will lead to finer filament thickness, which will increase the strain gradient. The increased strain gradient has to be accommodated by an increased density of GNDs that work-harden the composite. The increased dislocation density is experimentally observed by Trybus et al. [34]. Therefore, the strain gradient hardening model should be more physically plausible than the Hall-Petch barrier model that considers only the hardening from the impeded dislocation motion.

#### Al/Ti DMMC

Several Al matrix DMMCs have been investigated to produce lighter and stronger composite materials [6-8, 35]. Al/20 vol% Ti DMMC, produced by powder metallurgy and deformation processing, is taken as our test material to compare the strain gradient hardening model with experimental results. The initial Ti powder size was roughly around 60  $\mu\text{m}$ , close to that of Al powders [6]. The high ductility of two metal phases allows severe plastic deformation to proceed without any intermediate annealing. A Ti filament thickness of 50 nm can be obtained after a deformation true strain of 12.1. The strain gradient effect is intensive for such fine characteristic microstructure length. The parameters for the strain gradient hardening model are set up as follows: the power hardening law for Al is  $\sigma_{\text{Al}} = 6.81 + (45 - 6.81)(1 + \epsilon^{0.297})$  fitted by the experimental data in ref [36]. For Ti, the power law is  $\sigma_{\text{Ti}} = 87 + (215 - 87)(1 + \epsilon^{0.13})$  [37]. The Taylor factors for heavily deformed fcc-Al and hcp-Ti are estimated to be 3.16 and 2.16, respectively because Ti exhibited a curled filament morphology similar to that of Nb. The shear moduli for Al and Ti are 25 GPa and 43 GPa, respectively. Constant  $\alpha$  is still taken as 0.3. The Burgers vectors for Al and Ti are 0.286 nm

and 0.294 nm. The intrinsic material length can be calculated as  $l_{Al}=110.14 \mu\text{m}$  and  $l_{Ti}=13.93 \mu\text{m}$ . The comparison between our strain gradient hardening model and the experimental results is given in Fig. 3. The fitted  $k$  values for Al and Ti are 0.053 and 0.04. The strain gradient hardening model shows a good fit with experimental results during the entire strain range while rule of mixtures can predict the strength of Al-Ti composite only at low true strain levels.

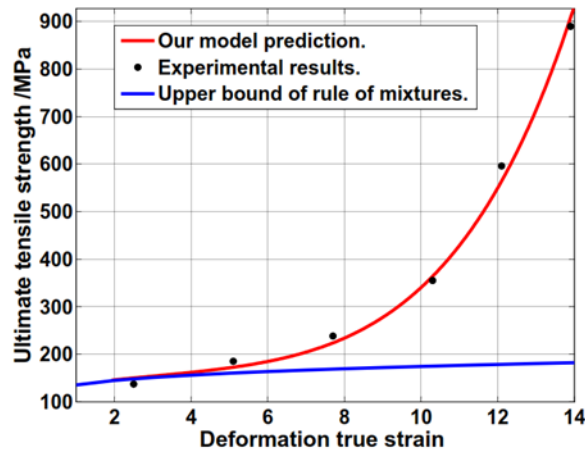


Fig. 3 The comparison of the strength of Al-20 vol % Ti DMMCs between our strain gradient hardening model prediction and the experimental results. The upper bound of rule of mixtures is given to illustrate the intense strain gradient effect at large deformation true strain

For these three test cases, the strain-gradient hardening model predicts the strength of DMMCs regardless of the crystallographic structures of the two metal phases and the production methods. The microstructure of DMMC has a crucial effect on its strength. A fine microstructure requires a large strain gradient to accommodate at the interface, generating a large amount of GNDs to strengthen the composite. The model can be easily extended to include other effects like grain size, strain rate, temperature by modifying the corresponding material length scale.

## Conclusions

In this paper, a dislocation-density-based strain gradient hardening model is presented to predict the strength of DMMCs. This model is based on the modified rule of mixtures in which the strength of each phase obeys the Taylor's dislocation hardening law with additional contribution from GNDs emitted from the interface to accommodate the strain gradient. A physical link between the density of GNDs and the effective strain gradient has been established to incorporate the strain gradient hardening effect. The strain gradient effect can be strongly affected by the deformation true strain, the type of composite constituent phases, and the characteristic microstructure length scale. An intrinsic material length scale was introduced to compare with the characteristic microstructure length scale to evaluate the extent of the strain gradient effect. Large deformation true strain leads to a small characteristic microstructure length, causing a strong strain-gradient effect when it is comparable with relatively large intrinsic material length. Our strain-gradient hardening model can predict the experimental strengths of Cu/Nb, Cu/Ta and Al/Ti DMMCs well over the entire deformation strain range. The dominating strain gradient effect at large deformation true strain is responsible for the anomalous high strength of heavily cold-worked DMMCs, which deviates from the rule of mixtures prediction. The rule of mixtures can fit with experimental results only at low strains. The strain gradient model can also account for the initial dendritic size effect on the strength of DMMCs. This hardening model is more physically plausible than the modified rule of mixtures model by Raabe et al. [13] by providing the GNDs as the physical origin of strain gradient. It requires fewer fitting parameters than the work-hardening model proposed by Funkenbusch et al. [10]. The experimentally observed increased dislocation density [34] also makes our model superior to

the Hall-Petch barrier model, which assumes that the interfaces only block dislocation motion and have no effect on increasing dislocation density. In addition, the strain gradient hardening model has the flexibility to incorporate various physical conditions (e.g. temperature, grain size, strain rate, etc.) to be easily extended to match various experimental conditions, an advantage compared with previous models.

### References

- [1]. Russell AM, Chumbley LS, and Tian Y (2000) Deformation Processed Metal–Metal Composites, *Adv. Eng. Mater.* 2: 11-22.
- [2]. Bevk J, Harbison JP and Bell JL (1978) Anomalous increase in strength of in situ formed Cu-Nb multifilamentary composites, *J. Appl. Phys.* 49: 6031-6038.
- [3]. Spitzig WA and Krotz PD (1988) Comparison of the strengths and microstructures of Cu-20% Ta and Cu-20% Nb in situ composites, *Acta metall.* 36: 1709-1715.
- [4]. Biselli C and Morris DG (1994) Microstructure and strength of Cu-Fe in situ composites obtained from prealloyed Cu-Fe powders, *Acta metal. Mater.* 42: 163-176.
- [5]. Frommeyer G and Wassermann G (1975) Microstructure and anomalous mechanical properties of in situ-produced silver-copper composite wires, *Acta Metall.* 23: 1353-1360.
- [6]. Russell AM, Lund T, Chumbley LS, Laabs FA, Keehner LL, Harringa JL (1999) A high-strength, high-conductivity Al–Ti deformation processed metal metal matrix composite, *Composites: Part A*, 30: 239-247.
- [7]. Xu K, Russell AM, Chumbley LS, Laabs FC et al (1999) Characterization of strength and microstructure in deformation processed Al-Mg composites, *J. Mater. Sci.* 34: 5955-5959.
- [8]. Xu K, Russell AM (2004) Texture–strength relationships in a deformation processed Al–Sn metal–metal composite, *Mater. Sci. Eng., A*, 373: 99-106.
- [9]. Spitzig WA, Pelton AR and Laabs FC (1987) Characterization of the strength and microstructure of heavily cold worked Cu-Nb composites, *Acta metall.* 35: 2427-2442.

- [10]. Funkenbusch PD, Courtney TH (1985) On the strength of heavily cold worked in situ composites, *Acta metall.* 33: 913-922.
- [11]. Funkenbusch PD, Lee JK, Courtney TH (1987) Ductile two-phase alloys: Prediction of strengthening at high strains, *Met. Trans. A*, 18: 1249-1256.
- [12]. Funkenbusch PD, Courtney TH (1989) On the role of interphase barrier and substructural strengthening in deformation processed composite materials, *Scr. Metall.* 23: 1719-1724.
- [13]. Raabe D, Hangen U (1995) Introduction of a modified linear rule of mixtures for the modeling of the yield strength of heavily wire drawn in-situ composites, *Comp Sci Tech.* 55: 57-61.
- [14]. Brinckmann S, Siegmund T, Huang Y (2006) A dislocation density based strain gradient model, *Int. J. Plast.* 22: 1784-1797.
- [15]. Fleck NA, Muller GM, Ashby MF, Hutchinson JW (1994) Strain gradient plasticity: Theory and experiment, *Acta Metall. Mater.* 42: 475-487.
- [16]. Stolken JS, Evans AG (1998) A microbend test method for measuring the plasticity length scale, *Acta Mater.* 46: 5109-5115.
- [17]. De Guzmana MS, Neubauer G, Flinn P, Nix WD (1993) The Role of Indentation Depth on the Measured Hardness of Materials, *Mater. Res. Symp. Proc.* 308: 613-618.
- [18]. Lloyd DJ (1994) Particle reinforced aluminium and magnesium matrix composites, *Int. Mater. Rev.* 39: 1-23.
- [19]. Abu Al-Rub RK, Voyiadjis GZ (2006) A physically based gradient plasticity theory, *Int. J. Plast.* 22: 654-684.
- [20]. Gao H, Huang Y, Nix WD, Hutchinson JW (1999) Mechanism-based strain gradient plasticity— I. Theory, *J. Mech. Phys. Solids*, 47: 1239-1263.
- [21]. Lubliner J (1990) *Plasticity theory* 1st edn. Macmillan Publishing Company, New York.
- [22]. Nye J (1953) Some geometrical relations in dislocated crystals, *Acta Metall.* 1: 153-162.
- [23]. Ashby MF (1970) The deformation of plastically non-homogeneous materials, *Philos. Mag.* 21: 399-424.
- [24]. Taylor GI (1938) Plastic Strain in Metals, *J. Inst. Met.* 62: 307-324.



- [25]. Fleck NA, Hutchinson JW (2001) A reformulation of strain gradient plasticity, *J. Mech. Phys. Solids*, 49: 2245-2271.
- [26]. Nix WD, Gao H (1998) Indentation size effects in crystalline materials: A law for strain gradient plasticity, *J. Mech. Phys. Solids*, 46: 411-425.
- [27]. Gao H, Huang Y (2001) Taylor-based nonlocal theory of plasticity, *Int. J. Solid Struct.* 38: 2615-2637.
- [28]. Trybus CL, Spitzig WA (1989) Characterization of the strength and microstructural evolution of a heavily cold rolled Cu-20% Nb composite, *Acta Metall.* 37: 1971-1981.
- [29]. Spitzig WA, Krotz PD, Chumbley LS, Downing HL, Verhoeven JD (1988) Effect of temperature on the mechanical properties and microstructures of in-situ formed Cu-Nb and Cu-Ta composites, *Mater. Res. Soc. Symp. Proc.* 120: 45-50.
- [30]. Dieter GE, Kuhn HA, Semiatin SL (2003) *Handbook of workability and process design* 2nd edn. ASM International, Materials Park, OH.
- [31]. Zamiri A et al (2006) On mechanical properties of the superconducting niobium, *Mater. Sci. Eng., A*, 435-436: 658–665.
- [32]. <http://www.matweb.com/>
- [33]. Bechtold JH (1955) Tensile properties of annealed tantalum at low temperatures, *Acta Metall.* 3: 249-254.
- [34]. Trybus CL, Chumbley LS, Spitzig WA, Verhoeven JD (1989) Problems in evaluating the dislocation densities in heavily deformed Cu-Nb composites, *Ultramicroscopy*, 30: 315-320.
- [35]. Tian L, Kim H, Anderson I, Russell AM (2013) The microstructure-strength relationship in a deformation processed Al–Ca composite, *Mater. Sci. Eng., A*, 570: 106–113.
- [36]. Rodak K, Radwański K, Molak R (2011) Microstructure and mechanical properties of aluminum processed by multi-axial compression, *Solid State Phenom.* 176: 21-28.
- [37]. Welsch G, Boyer RF, Collings EW (1994) *Materials properties Handbook: Titanium Alloys* 1st edn. ASM International, Materials Park, OH.

## CHAPTER 4 MODELING THE ELECTRICAL RESISTIVITY OF DEFORMATION PROCESSED METAL/METAL COMPOSITES

A paper published in *Acta Materialia*

Liang Tian<sup>1</sup>, Iver Anderson<sup>2</sup>, Trevor Riedemann<sup>3</sup>, Alan Russell<sup>2</sup>

1. Primary researcher and author 2. Principal investigators 3. Reviser

### Abstract

Deformation processed metal/metal (matrix/reinforcement) composites (DMMCs) are high-strength, high-conductivity in-situ composites produced by severe plastic deformation. The electrical resistivity of DMMCs is rarely investigated mechanistically and tends to be slightly higher than the rule-of-mixtures prediction. In this paper, we analyze several possible physical mechanisms (i.e. phonons, interfaces, mutual solution, grain boundaries, dislocations) responsible for electrical resistivity of DMMC systems and how these mechanisms could be affected by processing conditions (i.e. temperature, deformation processing). As an innovation, we identified and assembled the major scattering mechanisms for specific DMMC systems and modeled their electrical resistivity in combination. From this analysis, it appears that filament coarsening rather than dislocation annihilation is primarily responsible for the resistivity drop observed in these materials after annealing and that grain boundary scattering contributes to the resistivity at least at the same magnitude as does interface scattering.

## Introduction

Deformation processed metal/metal composites (DMMCs) are a class of in-situ composites that display high strength and high electrical and thermal conductivity [1]. They are produced by severe plastic deformation (i.e., rolling or extruding, swaging, and wire drawing) of two ductile phases [1]. The first Cu/Nb DMMCs were developed by Bevk et al [2], and other Cu refractory metal composites were studied by Verhoeven et al [3]. The strengthening mechanisms in DMMCs have been studied extensively [4-8], but only a few papers have attempted to explain the electrical conductivity of DMMCs [9, 10]. An early model of the electrical resistivity of DMMCs can be described by the rule of mixtures (ROM) [10]. However, the rule of mixtures considers only the resistivity and volume fractions of each constituent phase without accounting for any microstructural feature of the DMMCs.

Various resistivity models have been developed for macroscopic metal matrix composites to include the microstructural details (e.g. size, shape, orientation, and spacing of constituent phases, dislocations, mutual solution) [11-18]. Most of these are empirical models that do not consider the physical mechanisms for resistivity, and they depend on many phenomenological parameters to represent microstructural features. Thus, they are best described as fitting models. Moreover, these models are all based on various simplifying assumptions of composite microstructures and are therefore restricted by the difficulty of accurately capturing the complexity of real microstructural features. The spheroidal model developed by Ondracek [11] considers two-phase composites in which discontinuous spheroidal particles are embedded in the matrix phase. This model is capable of predicting the electrical conductivity of two-phase composites over a range of

compositions by considering the shape and orientation of both phases. However, this model doesn't account for formation of a continuous network of the inclusion phase at a sufficiently high volume fraction, which will increase the conductivity drastically when a conducting inclusion phase is interconnected in an insulating matrix phase [12]. This percolation concept is well described by the general effective media (GEM) equation developed by McLachlan et al [13]. Based on percolation theory [14], which is applicable only when the electrical conductivities of two phases differ substantially (conductivity of one phase tends to zero), the GEM equation incorporates the conductivities of both constituent phases, their volume fractions, and two free parameters to explain different experimental results over an entire composition range. The percolation effect (i.e., the formation of an interconnected network of highly conductive inclusion phase) in this model is described by an asymptotic S-shaped curve that shows the effective conductivity dependence on the volume fraction of the high-conductivity phase. However, the major drawback of the GEM model is that the free parameters do not have a direct correlation with the real microstructural features and serve only as fitting parameters, which limits the applicability of GEM to that of a fitting model relying on experimental inputs [15].

Fan [16] introduced a new approach to topologically transform a two-phase microstructure into a body with three well defined microstructural elements, which is microstructurally and electrically equivalent to the original microstructure. This model recovers the ROM for conductivity when both phases are perfectly aligned along the current direction (parallel configuration) and recovers the ROM for resistivity when both phases are alternately separated from each other along the current direction (serial configuration). The model considers the effects of the microstructural features (e.g., volume fraction, phase

arrangement, phase continuity, and phase resistivity ratio) on the electrical resistivity of two-phase composites, making it superior to ROM and Hashin and Shtrikman's bounds for electrical resistivity [17] that account only for the volume fraction and resistivity of constituent phases. The major drawback of Fan's model is that the two constants characterizing the phase topology are difficult to measure, rendering it phenomenological rather than physical. A comprehensive review on these macroscopic models was done by Fux [18].

In all the above resistivity models, the composites are comprised of a conducting metal inclusion phase and an insulating matrix phase, and the inclusion phase is comprised mostly of macroscopic particles. However, in DMMCs, both reinforcement and matrix phase are metals, and the reinforcement phase is comprised of long (extremely high aspect ratio), almost continuous filaments with thickness from tens to hundreds of nanometers. None of the above models would be able to predict the resistivity of DMMCs well for the following reason. It is well known that a size effect exists for the resistivity of thin metal films or wires when any one of the dimensions of metal specimens is comparable with the mean free path of free electrons in the bulk metal [19-25]. The mean free path of free electrons in most metals are in the range of several to tens of nanometers [9, 10, 26], thus the size effect on the resistivity should be considered in DMMCs. The size dependent resistivity can be attributed to the increasing restriction of the interface on the mean free path of electrons as film thickness decreases since the resistivity is inversely proportional to the mean free path of electrons. Thomson [19] first derived a formula for thickness-dependent resistivity of thin films by averaging all the free paths of a single free electron over all depths and all angles under the restriction that surfaces act as termination sites for the electron's free path. Fuchs

[20] pointed out that it is necessary to consider the mean of all the free paths of all the electrons in the metal in order to obtain an accurate mean free path. By solving Boltzmann's transport equation under the diffuse or partial diffuse scattering boundary condition, he obtained a rigorous formula for thickness-dependent resistivity of thin films and derived approximate formulas for thin and thick film limits. An interface scattering factor was introduced in his paper to characterize the probability of elastic scattering. According to Fuchs, the interface scattering factor is directly related to the surface roughness. A perfectly smooth mirror surface tends to scatter electrons elastically, making the conductivity of a perfectly smooth thin film the same as its bulk counterpart. In contrast, a jagged, rough surface tends to scatter electrons diffusely and increases the resistivity of a thin film.

Fuchs found a good agreement between the theory and experimental resistivity data of a cesium thin film. Soudheimer corrected the approximation formula in the thick film limit of Fuchs [21]. Dingle [22], MacDonald [23], and Chambers [24] extended the thin film work to circular, square, and arbitrary cross section thin wires with two dimensions confined, respectively. In the above theories, grain boundaries are believed to have negligible effect on the resistivity of the metals because the grain size is usually much larger than the electron mean free path in bulk metal so that the grain boundary contribution to resistivity is relatively small [25]. However, the average grain size in a polycrystalline thin film would be roughly equal to film thickness, which is comparable to the electron mean free path [25]. Therefore, grain boundary scattering also predicts a thickness-dependent resistivity similar to the Fuchs size effect caused by surface scattering. Mayadas and Shatzkes incorporated the grain boundaries as parallel, partially reflecting planes with delta scattering potential and solved the Boltzmann transport equation with the purely specular scattering at the external surface

(i.e. no Fuchs size effect in this model). They found that the grain boundary scattering can contribute to thickness-dependent resistivity in roughly the same manner as pure Fuchs size effect caused by diffuse surface scattering [25]. Thus, the grain boundary scattering of electrons can no longer be neglected. Ignoring the contribution of grain boundary scattering to resistivity can lead to misinterpretation of the higher resistivity of a polycrystalline thin film than that of a single crystal thin film with equal thickness as the smaller interface scattering factor in the polycrystalline film according to Fuchs size effect. Later, they extended this model to a more general theory including the combined effect of grain boundary scattering and Fuchs size effect (partially diffuse surface) [27]. The derived formula will degenerate into Fuchs' size-effect formula for a single-crystal thin film and the previous formula of pure grain boundary scattering for completely specular scattering surfaces, respectively. Grain boundary scattering has been concluded to contribute to a significant portion of the resistivity of polycrystalline thin films [27].

Few models are available to incorporate the size effect into the resistivity of DMMCs. Raabe [9] developed a resistivity model for deformation-processed Cu/Nb composites to attribute the decreased conductivity of the composite compared with the ROM prediction to the inelastic scattering of conduction electrons at internal phase boundaries (i.e. size effect) as primary and scattering at dislocations as secondary. The heavy deformation processing resulted in very fine filament spacing and substantial increase of interphase boundaries. When the filament thickness/spacing is comparable with the mean free path of conduction electrons, a drop in conductivity will occur in each metal phase. The resistivity of each phase was modified by additional dependence on filament diameter/spacing by Dingle's thin wire theory and increased dislocation density by a linear law. The final conductivity of the

composite would be the ROM of modified conductivity of each constituent phase due to the parallel configuration created during heavy deformation processing. This deviation from ROM primarily due to size effect has never been discussed in previous models because the two-phase composites in those models are macroscopic instead of microscopic. The incorporation of additional microstructural features (i.e. phase shape and phase arrangement) has been done by Heringhaus et al [10]. Their model considered the size effect on resistivity by Dingle's thin wire theory with arbitrary cross section shape. However, the parameters characterizing the interface scattering and phase arrangement were treated as fitting parameters, adding phenomenological nature to this model. It seems that none of the above models has considered the effect of grain boundary scattering. The possible formation of mutual solutions may also be an important contributor to resistivity in some cases.

In this paper, we analyze all the possible scattering mechanisms (i.e. interfaces, grain boundaries, impurities/mutual solutions, phonons, dislocations) in DMMCs. And for each specific DMMC system, we apply the mathematical models of each major scattering mechanism to obtain a tailored resistivity model. Since the processing conditions can significantly affect the dominating scattering mechanisms in DMMCs, two common processing parameters—temperature and deformation true strain have been used as examples to explain their effect on scattering mechanisms and the resistivity behavior of Cu-Nb, Au-Ag and Cu-Ag-Nb composites.



## Models for Scattering Mechanisms in DMMCs

### Interface scattering

In DMMCs, both matrix and reinforcement metal phases have thicknesses perpendicular to the direction of current flow in the tens to hundreds of nanometers size regime, which is roughly comparable to the bulk electron mean free path from several to tens of nanometers at room temperature. The interphase boundaries in DMMCs act as the surfaces in Fuchs size effect theory of thin metal films. The limitation of electron mean free path due to interface scattering is responsible for the observed size dependent resistivity behavior [10]. When metal wire size of each phase in DMMCs is larger than its bulk electron mean free path, a quantitative relation between the resistivity of each metal phase in DMMCs with arbitrary cross section shape and filament thickness/spacing is given by [10, 22]

$$\rho = \rho_0(T) \left[ 1 + \frac{3}{16} (1 - p) \lambda_0(T) \frac{P}{S} \right] \quad (1)$$

where  $\rho$  is the size dependent resistivity for each phase,  $\rho_0$  is the bulk resistivity that is different from intrinsic resistivity  $\rho_i$  contributed by phonons and defects due to the additional grain boundary scattering in fine grained polycrystalline wire, and  $p$  is the probability of elastic scattering at the interface. The term  $\lambda_0$  is the bulk mean free path of electrons, which is different from the mean free path  $\lambda_i$  from grain interiors (due to intrinsic scattering from phonons and defects) for fine grain polycrystalline phases due to the additional scattering at grain boundaries. Here  $T$  is temperature,  $P$  is perimeter, and  $S$  is cross section area of the phase. Both  $\rho_0$  and  $\lambda_0$  are primarily caused by phonon scattering and are therefore strongly temperature dependent. The term  $(1-p)$  is the probability of inelastic scattering at interfaces that is responsible for decreased conductivity.  $p$  is directly affected by the interface

morphology according to Fuchs. A rough interface tends to scatter inelastically and yields a low  $p$ . The ratio  $P/S$  stands for the interface area per unit volume of the phase. For circular reinforcement filaments,  $P/S=4/d$ , where  $d$  is the diameter. For ribbon-like reinforcement lamella,  $P/S=2/t$ , where  $t$  is the thickness.

The cross sectional shape of reinforcement phases after deformation is related to the crystal structures of both matrix and reinforcement phase according to classic co-deformed composite observations. DMMCs usually consist of bcc or fcc filaments inside an fcc matrix [1]. A bcc metal phase embedded inside an fcc matrix tends to develop a ribbon-like morphology during deformation processing, while a fcc phase inside an fcc matrix tends to develop a cylindrical morphology [28]. This difference is due to the texture development during deformation [1]. Bcc metal tends to develop a  $\langle 110 \rangle$  texture after axisymmetric deformation (e.g. extrusion, swaging, wire drawing), while fcc metal tends to develop a predominate  $\langle 111 \rangle$  fiber texture mixed with a weaker  $\langle 001 \rangle$  component [29-32]. The  $\langle 111 \rangle$  or  $\langle 001 \rangle$  texture in fcc metal can accommodate axisymmetric deformation by three or four slip systems [33]. For bcc metal, there are no exactly close-packed planes. The most closely packed planes are  $\{110\}$ , and other planes such as  $\{112\}$  and  $\{123\}$  are also relatively closely packed, though less so than the  $\{110\}$ . The development of  $\langle 110 \rangle$  texture in bcc metal would maximize Schmid factor for  $\langle 111 \rangle$  slip direction on these low index slip planes, which would favor the plain strain deformation mode [1]. Hosford [32] gave a quantitative explanation of why plain strain deformation is more energetically favorable than axisymmetric plastic flow for  $[011]$  fiber-textured bcc metals. Two of the four  $\langle 111 \rangle$  slip directions,  $[111]$  and  $[1\bar{1}1]$  are oriented to accommodate elongation in  $[011]$  and contraction in  $[100]$ , rendering no deformation in the  $[01\bar{1}]$  direction. Therefore, deformation is

confined in  $(01\bar{1})$  plane. The other two slip directions,  $[1\bar{1}\bar{1}]$  and  $[11\bar{1}]$ , are perpendicular to the  $[011]$  axis and are therefore hard to operate. Hosford showed that these two directions must be operated to accommodate axisymmetric deformation. He calculated that the tensile stress needed to produce axisymmetric deformation for each grain is  $3/2$  of that required for plain strain deformation. Therefore, grains in  $[011]$  textured bcc metals tends to deform in plain strain mode and to develop elliptical cross sections normal to the fiber axis [32]. Neighboring grains of bcc reinforcement phase would bend around each other to develop a curled ribbon bcc filament shape in an fcc matrix to accommodate overall axisymmetrical deformation of the composite. This means that the bcc phase in an fcc matrix should deform by an even mixture of plane-strain deformation mode and axisymmetrical deformation mode to achieve the overall axisymmetrical deformation. To conclude, bcc filaments in an fcc matrix tend to possess an elliptical cross sectional shape, while fcc filaments in an fcc matrix would have a circular cross section. Alternatively, hcp phases tend to behave similarly to bcc phases in an fcc matrix, since hcp metals have similar slip constraints to those observed in bcc metals [1].

The initial metal-metal composites prepared by powder metallurgy approach or by solidifying a liquid solution of two metals that are immiscible in the solid phases tend to have fairly equiaxed reinforcement phases with diameter  $d_0$  embedded uniformly inside the matrix. After a deformation true strain  $\eta$  in the axial direction, bcc filaments in an fcc matrix would have an elliptical cross section with one long major axis  $d_0/e^{\eta/4}$  (i.e.  $[0\bar{1}1]$  in Hosford's case) and one short minor axis  $d_0/e^{3/4\eta}$  (i.e.  $[100]$  in Hosford's case) under a combined plane strain and axisymmetrical deformation mode and volume conservation constraint, where  $e$  is the mathematical constant 2.718. For deformation true strain  $\eta > 2$  (the major experimentally

studied strain range), the bcc filaments can be approximated as thin films with thickness  $\frac{d_0}{e^{\frac{3}{4}\eta}}$ .

Fcc reinforcement filaments in an fcc matrix would develop a circular cross section with diameter  $\frac{d_0}{e^{\frac{\eta}{2}}}$  [8]. Regardless of the cross section shape of filaments, the matrix phase will

always be approximated as a thin wire with diameter  $d_m$  equal to the filament spacing according to Verhoeven's work (J. Appl. Phys. 65 (3), 1989). The filament spacing can be estimated by  $(1-V_f)/V_f * d_{eff}$  [34], where  $V_f$  is the volume fraction of the filaments,  $d_{eff}$  is the effective radius of a circle whose area is equal to the cross section area of the filaments.

Then we can calculate  $d_m = (1-V_f)/V_f * d_0 / e^{\eta/2}$ . With all the above geometrical information, we can get size dependent resistivities for bcc or fcc filaments and matrix from eq. (1) as

$$\rho_{bccf} = \rho_{bcc0}(T) \left[ 1 + \frac{3}{8} (1-p) \lambda_{bcc0}(T) \frac{e^{\frac{3}{4}\eta}}{d_0} \right] \quad (2)$$

$$\rho_{fccf} = \rho_{fcc0}(T) \left[ 1 + \frac{3}{4} (1-p) \lambda_{fcc0}(T) \frac{e^{\frac{\eta}{2}}}{d_0} \right] \quad (3)$$

$$\rho_m = \rho_{m0}(T) \left[ 1 + \frac{3}{4} (1-p) \lambda_{m0}(T) \frac{V_f e^{\frac{\eta}{2}}}{(1-V_f) d_0} \right] \quad (4)$$

where  $\rho_{bccf}, \rho_{fccf}, \rho_m$  are size dependent resistivities for bcc filaments, fcc filaments and matrix, respectively.  $\rho_{bcc0}, \rho_{fcc0}, \rho_{m0}$  are their bulk resistivities, which should include grain boundary scattering for fine-grain polycrystalline phases.  $\lambda_{bcc0}, \lambda_{fcc0}, \lambda_{m0}$  are their bulk electron mean free paths. The  $\rho_0(T)$  and  $\lambda_0(T)$  for each phase is not independent. The electrical resistivity  $\rho_0(T)$  and the corresponding  $\lambda_0(T)$  in metallic materials is given by [26]

$$\rho_0(T) = \frac{m}{ne^2 \tau(T)} \quad (5)$$

$$\lambda_0(T) = v_F \tau(T) \quad (6)$$

where  $m$  is the mass of an electron,  $e$  is the charge of an electron,  $n$  is the concentration of electrons that are insensitive to temperature for an ideal free electron gas,  $\tau(T)$  is the relaxation time between two collision or scattering events that can be temperature dependent for phonon dominated scattering, and  $v_F$  is Fermi velocity that depends on electron concentration by  $v_F = \frac{\hbar}{m} (3\pi^2 n)^{1/3}$  [26], where  $\hbar$  is the reduced Planck constant. From eqs. (5) and (6), we have

$$\rho_0(T)\lambda_0(T) = \frac{(3\pi^2)^{\frac{1}{3}}\hbar}{e^2} n^{-\frac{2}{3}} \quad (7)$$

$\rho_0(T)\lambda_0(T)$  depends only on electron concentration and is a temperature-insensitive constant for each metal. A list of electron concentrations for various metals at room temperature are given in Ref [26]. By inserting eq. (7) into eqs. (2-4), we can obtain the resistivity purely attributable to interface scattering as

$$\rho_{bccf}^{int} = \rho_{bccf} - \rho_{bcc0} = \frac{3(3\pi^2)^{\frac{1}{3}}\hbar}{8e^2} (1-p) \frac{e^{\frac{3}{4}\eta}}{d_0} n_{bcc}^{-\frac{2}{3}} \quad (8)$$

$$\rho_{fccf}^{int} = \rho_{fccf} - \rho_{fcc0} = \frac{3(3\pi^2)^{\frac{1}{3}}\hbar}{4e^2} (1-p) \frac{e^{\frac{\eta}{2}}}{d_0} n_{fcc}^{-\frac{2}{3}} \quad (9)$$

$$\rho_m^{int} = \rho_m - \rho_{m0} = \frac{3(3\pi^2)^{\frac{1}{3}}\hbar}{4e^2} (1-p) \frac{V_f e^{\frac{\eta}{2}}}{(1-V_f)d_0} n_m^{-\frac{2}{3}} \quad (10)$$

where  $\rho_{bccf}^{int}, \rho_{fccf}^{int}, \rho_m^{int}$  are the increased resistivities due to interface scattering for bcc filaments, fcc filaments and matrix, respectively. Eqs. (8-10) showed that the interface scattering in DMMCs depends on the interface nature by interfacial scattering factor  $p$ , deformation true strain  $\eta$ , initial size and volume fraction of the second phase  $d_0$  and  $V_f$ ,

metal type by electron concentration  $n$  and its crystal structure. The fact that  $\rho_0(T)\lambda_0(T)$  is a constant decouples the interface scattering from the bulk resistivity  $\rho_0(T)$ .

### Grain boundary scattering

The contribution of grain boundary scattering to resistivity is not negligible when the grain size is comparable with the electron mean free path inside the grain interior [27]. In a thin polycrystalline film, the grain size is roughly equal to the film thickness, which is comparable to the bulk mean free path [27]. So  $\rho_0(T)$  would increase with reduced film thickness. This thickness dependent resistivity contributed by grain boundaries can be as strong as that from Fuchs size effect [27]. As pointed out by Mayadas and Shatzkes [27], it can be seductive to mistakenly take the bulk resistivity  $\rho_0(T)$  and mean free path  $\lambda_0(T)$  which includes the grain boundary scattering, as the intrinsic resistivity  $\rho_i(T)$  and mean free path  $\lambda_i(T)$  that comes only from phonon and intrinsic defects so that  $\rho_0(T)$  and  $\lambda_0(T)$  are independent of thickness [35]. Though the decoupling of interface scattering from bulk resistivity  $\rho_0(T)$  (i.e.,  $\rho_0(T)\lambda_0(T) = \rho_i(T)\lambda_i(T)$ ) makes no difference in obtaining the correct interface scattering, it is necessary to derive the correct thickness-dependent bulk resistivity  $\rho_0(T)$  including the grain boundary scattering effect for fine grained polycrystalline phases. By modeling grain boundaries as parallel partially reflecting planes located perpendicular to electric field with delta scattering potential and external surfaces as purely specular reflecting surfaces, Mayadas et al [25] solved the Boltzmann transport equation and obtained the bulk resistivity  $\rho_0(T)$  including grain boundary scattering as

$$\rho_0(T) = \rho_b(T) \left\{ 3 \left[ \frac{1}{3} - \frac{\alpha}{2} + \alpha^2 - \alpha^3 \ln \left( 1 + \frac{1}{\alpha} \right) \right] \right\}^{-1} \quad (11)$$

where  $\rho_b(T)$  is the bulk resistivity without grain boundary scattering,  $\alpha = \frac{\lambda_b(T)}{d} \frac{R}{1-R}$ ,  $\lambda_b(T)$  is the electron mean free path in the grain interior,  $d$  is the average grain size,  $R$  is called the reflection coefficient of grain boundaries, representing the mean probability of an electron to be reflected by the grain boundaries [36].  $\rho_b(T)$  mainly consists of intrinsic resistivity  $\rho_i(T)$  that is contributed by phonons and intrinsic defects (e.g. bulk equilibrium concentrations of vacancies and dislocations before deformation) and may include other contributions from increased dislocation density during severe deformation and impurity scattering. The product of  $\rho_b(T)$  and the corresponding mean free path  $\lambda_b(T)$  satisfies the relation in eq. (7). If the reflection coefficient  $R$  is 1, electrons would be completely trapped inside individual grains, and the bulk resistivity  $\rho_0(T)$  would be infinity by the large  $\alpha$  approximation  $\frac{\rho_0(T)}{\rho_b(T)} = \frac{4}{3} \alpha$  [27]. For  $R=0$ , the grain boundaries have no effect on scattering electrons, and the bulk resistivity  $\rho_0(T)$  would be equal to  $\rho_b(T)$  by the small  $\alpha$  approximation  $\frac{\rho_0(T)}{\rho_b(T)} = 1 + \frac{3}{2} \alpha$  [27, 37]. Therefore, the resistivity caused by pure grain boundary scattering can be obtained as

$$\rho_{GB} = \rho_0(T) - \rho_b(T) = \rho_b(T) \left\{ \left\{ 3 \left[ \frac{1}{3} - \frac{\alpha}{2} + \alpha^2 - \alpha^3 \ln \left( 1 + \frac{1}{\alpha} \right) \right] \right\}^{-1} - 1 \right\} \quad (12)$$

In DMMCs,  $d$  is comparable with  $\lambda_b$ , but is still larger than  $\lambda_b$ . Most metals have  $R$  around 0.2 [35-37]. So in the small  $\alpha$  regime, eq. (12) can be approximated as

$$\rho_{GB} = \frac{3}{2} \rho_b(T) \alpha = \frac{3(3\pi^2)^{\frac{1}{3}} \hbar}{2e^2} n^{-\frac{2}{3}} \frac{R}{1-R} \frac{1}{d} \quad (13)$$

Eq. (13) shows that  $\rho_{GB}$  increases with increasing  $R$  and decreasing  $d$ . In the small  $\alpha$  regime applied for DMMCs,  $\rho_{GB}$  decouples from  $\rho_b(T)$  so that the grain boundary scattering totally hinges on the electrons concentration of metals  $n$ , the grain boundary reflection coefficient  $R$

and the inverse of average grain size  $\frac{1}{d}$  that characterizes the grain boundary area per unit volume. According to Ref [27], the average grain size would be roughly equal to the thickness of thin metal phases at least within the thickness range from 100 nm to 1  $\mu$ m. So

$$d = \frac{d_0}{\epsilon^{\frac{1}{2}} \eta} \text{ for bcc filaments, } d = \frac{d_0}{\epsilon^{\frac{1}{2}} \eta} \text{ for fcc filaments, } d = \frac{1-V_f}{V_f} \frac{d_0}{\epsilon^{\frac{1}{2}} \eta} \text{ for the matrix.}$$

This should be a good estimation for the fine metal phases in DMMCs considering the dynamic recrystallization and recovery effect [38] driven by the stored energy in the large dislocation density, increased nuclei number and sites, and heat generated during severe plastic deformation. This dynamic recrystallization and recovery effect also yields a high ductility of the metal phases and an intermediate level of the dislocation density so that deformation can proceed smoothly and the dislocations have a weak effect on scattering electrons [38]. The contribution of grain boundary scattering to the resistivity of DMMCs has not been considered by previous studies [9, 10, 38-40], which assume that each phase in DMMCs is a single crystal [39]. Furthermore, the observation that electrical conductivity, filament thickness and spacing decreased proportionally with reduced wire diameter in Ref [38] suggested that interface scattering was the major scattering mechanism contributing to the resistivity of the Cu-Nb DMMCs. This is not necessarily true because the grain boundary scattering has the same thickness dependence as the interface scattering, and its resultant conductivity is also proportional with filament thickness or spacing in our model (see eqs. (8-10) and (13)). In our model, the grain boundary effect was incorporated into each phase as a row of single crystals lying parallel to the wire axis with grain size equal to the thickness of each phase, which should be more reasonable than a single crystal assumption. This is because the growth of recrystallized grains in each phase can not be fast enough to remove



all grain boundaries to obtain a single crystal phase and would terminate at the interphase boundary [40] to have a grain size roughly equal to phase thickness.

### Mutual solution

In some DMMCs, the two fine metal phases may dissolve into each other and form mutual solid solutions, which could increase the resistivity of DMMCs significantly [39-41]. The effect of solid solution on resistivity is especially evident after annealing a chemically miscible system at high temperature because diffusion is a thermally activated process [39-41]. The intermixing of two metastable pure metal phases in DMMCs could lower the total free energy, which is the driving force for the diffusion-controlled intermixing process [41]. The diffusion coefficient depends on the activation energy by the Arrhenius relation. The various structural defects (e.g. dislocations, grain boundaries) in heavily deformed DMMCs and the small radius of curvature of the interface between filaments and matrix provide additional driving force for diffusion controlled processes and lower the activation energy so that the diffusion rate increases substantially [41, 42]. This additional driving force is responsible for the larger diffusion coefficient in DMMCs than that measured in single crystal planar diffusion couple experiments [41]. In addition, considering the fine thickness of metal phases in DMMCs, we would assume a uniformly distributed impurity content in each phase, as many previous studies did [39, 41]. Then the contribution of impurity atoms to the resistivity of each phase  $\rho_{imp}$  can be calculated as

$$\rho_{imp} = \int_0^x \left( \frac{d\rho}{dx} \right) dx = \left( \frac{d\rho}{dx} \right) x \quad (14)$$

where  $\frac{d\rho}{dx}$  is resistivity change per unit atomic percent of impurity atoms, taken to be a constant by previous studies [38, 39, 41],  $x$  is the solubility of the impurity atoms in the host phase. For example,  $\frac{d\rho}{dx}$  can be as high as  $10.4 \mu\Omega \cdot \text{cm}/\text{at\%}$  for Fe impurity atoms in Cu phase [39]. And Fe has a solubility close to 1 at% in Cu at annealing temperature 800 °C. So the formation of solid solution can contribute substantially to the resistivity of the composite. Measuring the resistivity change as a function of annealing time at different annealing temperature has been adopted to characterize the kinetics of transformation from two metastable phases to a homogenized solid solution [41]. Due to the rapid cooling that may be employed to form initial two-phase composites by solidification, the actual solubility of Fe [40] in Cu can be higher than equilibrium solubility so that conductivity can be degraded. For Cu-Fe DMMC, the slow kinetics of Fe precipitation at low temperature makes it difficult to achieve the equilibrium solubility. Verhoeven et al [43] showed that the conductivity of Cu-Fe DMMC could be increased by intermediate heat treatment and slow cooling to precipitate more Fe. However, in some DMMCs like Cu-Nb DMMC, the two phases have almost no solubility in each other (e.g., Nb has less than 0.02% solubility in Cu [38]) so that impurity scattering contributes little to the resistivity. The tiny impurity content of oxygen and other atoms from the atmosphere can be generally neglected [38]. Another important effect on solubility is that the heavy co-deformation processing can enhance chemical mixing and increase the mutual solubility of each phase [44-46]. Various mechanisms were proposed for this deformation induced chemical mixing. As previously discussed, the deformation induced structural defects and interface curvature in heavily deformed DMMCs allow chemical mixing to exceed the equilibrium mutual solubility by accelerating diffusion. Furthermore, Raabe et al [44] and Sauvage et al. [46] also proposed that the enhanced

diffusion can be attributed to the increase of the non-equilibrium vacancy density. Besides, Raabe et al [44] also brought up the following mechanisms. Instead of being diffusion pipe, dislocations can cause the excessive chemical mixing by attracting more solute atoms due to the high solubility of these atoms for dislocations. The deformation induced chemical mixing can occur via the dislocation shuffling mechanism, which creates small particles of one phase that would be dissolved into another phase due to the Gibbs-Thomson effect by multi-slip shear transfer across the heterogeneous interfaces. All these complex physical mechanisms make it extremely difficult to calculate the mutual solubility of each phase theoretically. Thus, in this paper, the contribution of mutual solution to resistivity is obtained from previous experimental resistivity measurements directly or indirectly through the experimental solubility data.

#### Dislocations and phonons

Dislocation densities in DMMCs have been estimated to be one to two orders of magnitude higher than that in heavily deformed single-phase material with the same deformation true strain [47, 48]. The effect of dislocations on the resistivity of DMMCs would be obvious only if the dislocation density is very large ( $10^{17}$  to  $10^{18} \text{ m}^{-2}$ ) [47, 48] because the dislocation scattering power is small (e.g. resistivity increase per unit dislocation density is  $2 \times 10^{-19} \mu\Omega \cdot \text{m}^3$  at 273K [47, 48]). The small dislocation scattering power is due to the fact that dislocations scatter electrons isotropically by the localized dislocation core instead of its long-range elastic stress field [48]. As a result, dislocation scattering power should be treated as a constant independent of the dislocation density if the dislocation density does not exceed  $10^{18} \text{ m}^{-2}$  so that the overlap of dislocation cores would not occur [48,

49]. Therefore, the resistivity due to dislocation scattering tends to be temperature insensitive and directly proportional to dislocation density [48, 49]. In fact, measuring the residual resistivity caused by dislocations becomes a viable and indirect approach to measure dislocation densities when measuring by TEM and the calorimetric method is not possible due to the limited measuring range of dislocation densities [49]. Since the dislocation densities in DMMCs would normally be less than  $10^{15} \text{ m}^{-2}$  [38], the resistivity increase due to dislocations can be calculated as [49]

$$\rho_{dis} = \mathfrak{R}_d N_d \quad (15)$$

where  $\mathfrak{R}_d$  is dislocation scattering power and  $N_d$  is dislocation density. Based on eq. (15), the contribution of dislocations to resistivity increase is usually around  $0.02 \mu\Omega\cdot\text{cm}$ , which is almost negligible compared with the effects of other scattering mechanisms [28, 49]. The effect of dislocations is evident only in heavily deformed, high-purity, bulk, coarse-grained, single-phase material at low temperature so that background scattering is minimized [49].

The relative role of dislocation scattering compared with interface scattering in the resistivity of DMMCs has been debated due to the difficulty of measuring dislocation densities accurately. Karasek and Bevk studied the relative contribution of interface and dislocation scattering to the total resistivity of Cu-Nb DMMCs by comparing the resistivity values of as-drawn and annealed composite specimens [47]. They believed that the resistivity drop after annealing was due only to the reduced dislocation density and therefore a dislocation density as high as  $10^{17} \text{ m}^{-2}$  was predicted. The high dislocation density was said to be consistent with qualitative TEM observations, the high strength of the composites, and the idea that Nb filaments inhibit the dynamic recovery. Verhoeven et al [38] did additional TEM studies on Cu-Nb DMMCs and found that the interface scattering made the major

contribution to the resistivity of Cu-Nb. The measured dislocation densities were at least two orders of magnitude smaller (i.e. less than  $10^{15}\text{m}^{-2}$ ) than Karasek and Bevk's prediction and roughly constant at deformation true strains larger than 4 due to the dynamic recovery and recrystallization of the Cu matrix. Therefore, the contribution of dislocations to resistivity is weak and maintains a constant value around  $0.1\ \mu\Omega\cdot\text{cm}$  according to their experimental data. They attributed the resistivity drop after annealing in Karasek and Bevk's work to the Nb filament coarsening, which reduced the contribution of interface scattering significantly. The measured dislocation densities in Cu-Nb DMMC by Verhoeven et al were confirmed by Trybus et al [50] to be roughly constant around  $10^{14}\sim 10^{15}\text{m}^{-2}$  at all deformation strain levels.

The contribution of phonon scattering to the metal resistivity is strongly temperature dependent [26, 35]. The electron scattering mechanism of lattice phonons results from the perturbation of band energy caused by lattice vibration [26]. At room temperature, phonon scattering is the major contributor to the resistivity even when other scattering mechanisms are active. For example, at 300K, a large contribution of phonon scattering, as high as 63% to the total resistivity of 75nm diameter copper wire was observed, while this phonon contribution decreased to 16% at 20K [35]. The temperature dependence of phonon scattering is proportional to the rate of electrons colliding with phonons. This collision rate is directly proportional to the concentration of phonons [35], which is proportional to the temperature when the temperature is above half of the Debye temperature [29]. The resistivity originating from phonons  $\rho_{pho}$  can be obtained from experimentally measured resistivity data at different temperatures of bulk pure metal samples, where other scattering mechanisms are negligible [28]. The experimentally measured  $\rho_{pho}$  should roughly satisfy the relation:  $\rho_{pho} = \alpha_t T + b$ , where  $\alpha_t$  is the temperature coefficient of resistivity, b is the

fitting parameter and  $T$  is the temperature in Kelvin [35]. The other intrinsic defects in undeformed pure bulk material such as vacancies and dislocations would contribute very little and are incorporated into  $\rho_{pho}$  after fitting with experimental resistivity data.

### Application of Scattering Models in Various DMMCs

In this section, analytic models for various scattering mechanisms introduced in section 2 will be applied to model the resistivity of different DMMCs systems. The major scattering mechanisms will be identified in a specific DMMC and adopted for calculation of the resistivity for each metal phase in the DMMCs. For the temperature and length scale in previous DMMCs studies [38, 39, 40], various scattering mechanisms can be treated as independent [37] and therefore the resistivity of each metal phase can be calculated by Matthiessen's rule as

$$\rho = \rho_{int} + \rho_{GB} + \rho_{imp} + \rho_{dis} + \rho_{pho} \quad (16)$$

where  $\rho_{int}, \rho_{GB}, \rho_{imp}, \rho_{dis}$  are given by eqs (8-10), 13, 14, 15, respectively.  $\rho_{pho}$  will be obtained from experimental data. Two metal phases in DMMCs are aligned parallel to each other after large deformation [38, 39]. Thus, the resistivity of DMMCs can be calculated by an inverse rule of mixtures for modified resistivity of each metal phase as

$$\frac{1}{\rho_{DMMC}} = \frac{V_f}{\rho_f} + \frac{1 - V_f}{\rho_m} \quad (17)$$

where  $\rho_{DMMC}$  is the resistivity of the DMMC,  $V_f$  is the volume fraction of filament metal phase,  $\rho_f$  and  $\rho_m$  are the modified resistivities of filament and matrix metal phases, respectively, which includes all major scattering mechanisms and can be calculated by eq. (16).

### Cu-Nb DMMCs

The resistivity of fcc Cu/bcc Nb DMMCs has been extensively studied in the past three decades [28, 38, 47, 48]. The fact that Nb has little solubility in Cu favors the high conductivity of the composite by avoiding forming solid solution, though Nb is a poor conductor (10 times less conductive than Cu). In this study, we modeled Karasek and Bevk's experimental resistivity data measured at different temperature for as-drawn and annealed samples, respectively [47, 48]. In their experiments, 7.6 mm diameter, as-cast Cu/Nb samples with 5.5  $\mu\text{m}$  average thickness Nb precipitates were deformation processed to 61  $\mu\text{m}$  diameter Cu-10% Nb DMMC wires. The samples were then heated from room temperature to 823K to measure their resistivities (see Fig. 1). The upper branch of the curves in Fig. 1 is obtained from the as-drawn samples. At elevated temperature, the as-drawn samples would be annealed so that its temperature resistivity curve would transit to the lower part of the curves. Upon cooling, the resistivity followed the lower branch of the curve for annealed samples. Once this cycle was completed, the resistivity data would follow the lower part of the curve repeatedly.

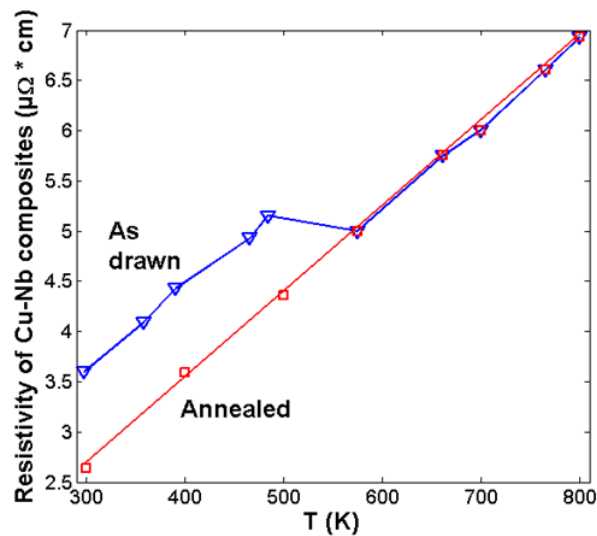


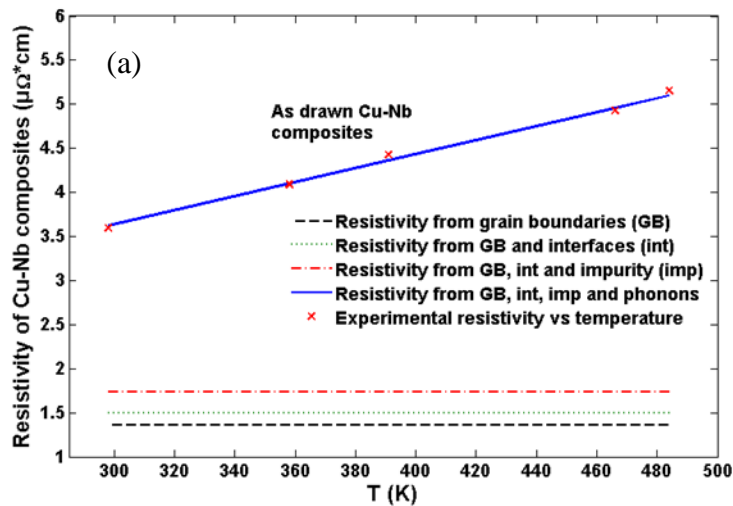
Fig. 1. The experimental temperature versus resistivity curves for as-drawn and annealed Cu/Nb samples with deformation true strain 9.6 [47, 48].

Various input parameters are needed to model the temperature vs. resistivity curve for as-drawn and annealed samples. For interface and grain boundary scattering, the free electron concentrations for Cu and Nb are taken to be  $8.45 \times 10^{28} / \text{m}^3$  and  $5.56 \times 10^{28} / \text{m}^3$ , respectively [51]. The bcc Nb filament thickness  $d$  can be calculated to be 4 nm by  $\frac{d_0}{\varepsilon^{\frac{1}{2}}}$ , and the filament spacing  $\frac{1-V_f}{V_f} \frac{d_0}{\varepsilon^{\frac{1}{2}}}$  is calculated to be 397 nm. The filament thickness 4 nm and spacing 397 nm are larger than the mean free path of Nb (2 nm at 293K) and Cu (40 nm at 293K), respectively [28]. So eq. (1) and (13) are valid for calculating interface and grain boundary scattering, respectively. The phonon contribution  $\rho_{pho}$  can be fitted by the undeformed pure bulk resistivity data in Ref [28] to be  $(0.0072 T(K) - 0.424) \mu\Omega \cdot \text{cm}$  for Cu and  $(0.062 T(K) - 2.747) \mu\Omega \cdot \text{cm}$  for Nb. The impurity contribution is  $0.21 \mu\Omega \cdot \text{cm}$  in as-drawn samples and  $0.03 \mu\Omega \cdot \text{cm}$  in annealed samples [38]. This is because the fast cooling rate used to prepare Cu/Nb alloy by a chill casting process in this case allows a higher solubility of Nb in Cu than the equilibrium solubility (i.e. less than 0.02 at.%) of Nb in Cu predicted by the phase diagram [38], which is responsible for the stronger impurity scattering in as-drawn samples. During annealing, the excessively dissolved Nb precipitated out of the supersaturated solid solution to reach the equilibrium solubility so that the impurity contribution decreased substantially. The role of dislocations would be negligible due to the low dislocation density (less than  $10^{15} \text{ m}^{-2}$ ) at all deformation true strains as a result of dynamic recovery and recrystallization during room temperature drawing, according to Verhoeven et al [38].



The modeling results fitting the experimental data of as-drawn and annealed samples in Fig. 1 are given in Fig. 2(a) and (b), respectively. The fitting results of as-drawn samples yield  $p \approx 0$ ,  $R_{\text{Cu}}=0.83$ ,  $R_{\text{Nb}}=0.45$ . Previous studies showed that the  $p$  value of Cu/Nb interface would be likely to be close to 0 [10, 38, 47]. The grain boundary reflection coefficient of Cu is high, which seems to match the previously reported high  $R$  value for Au that shares a similar electronic structure with Cu [36]. The Nb reflection coefficient between 0 and 0.5 is common. We used these parameters to fit the experimental resistivity data of annealed samples and obtained the Nb filament thickness to be 8.6 nm. This certainly matches the Verhoeven et al's [38] description qualitatively that as drawn Nb filaments of 5-7 nm coarsened to 30-50 nm after 0.5 h annealing at 550 °C. There is no clue of the heating rate and holding time in Karasek and Bevk's paper, so it is hard to compare quantitatively. Therefore, the decreased resistivity of annealed samples should be strongly related to the filament coarsening. The reduced dislocation densities in annealed samples may contribute slightly to the resistivity drop, but its effect should be minor and can not result in such a substantial resistivity drop. Raabe et al [52] also investigated the effect of annealing treatment on the resistivity of Cu-Nb at room temperature and found that the resistivity drop after heat treatment was due to the coarsening of Nb filaments, which occurred easily by interfacial diffusion at the Cu-Nb phase boundaries with a much lower activation energy than bulk diffusion due to the Gibbs-Thomson effect and various structural defects. They also confirmed that the increase of dislocation density had a minor effect on the resistivity of the composite. In order to further confirm this idea, we fitted the experimental data of both as-drawn and annealed samples with the filament thickness fixed and found that the resistivity contribution from dislocations in as-drawn samples has to be  $0.57 \mu\Omega\cdot\text{cm}$  to satisfy the

resistivity drop in annealed samples. This resistivity contribution from dislocations corresponds to a dislocation density as high as  $2.85 \times 10^{16} / \text{m}^2$ , which directly conflicts with Verhoeven's observation of dislocation density less than  $10^{15} / \text{m}^2$  at all deformation true strains. So the above calculations validated the idea that the filament coarsening is primarily responsible for the resistivity drop in annealed samples and the resistivity curve transition to the lower branch (Fig. 1) for as-drawn samples at elevated temperature. From Fig. 2, in both as-drawn and annealed samples, the phonon scattering is the major contributor to the resistivity of Cu/Nb DMMCs in the temperature range studied. Both the interface and grain boundary scattering decreased substantially in annealed samples due to the filament coarsening. It is worthwhile to note that the grain boundary scattering contributes strongly in both samples, which is different from previous studies assuming that both metal phases are single crystals [38-40]. The temperature dependence of resistivity in both as-drawn and annealed samples shows a roughly linear trend. This is because the Nb reinforcement filaments account for only 10% of the composite's volume, so the linear temperature dependent resistivity in the Cu matrix dominates the temperature dependence of the composites' resistivity.



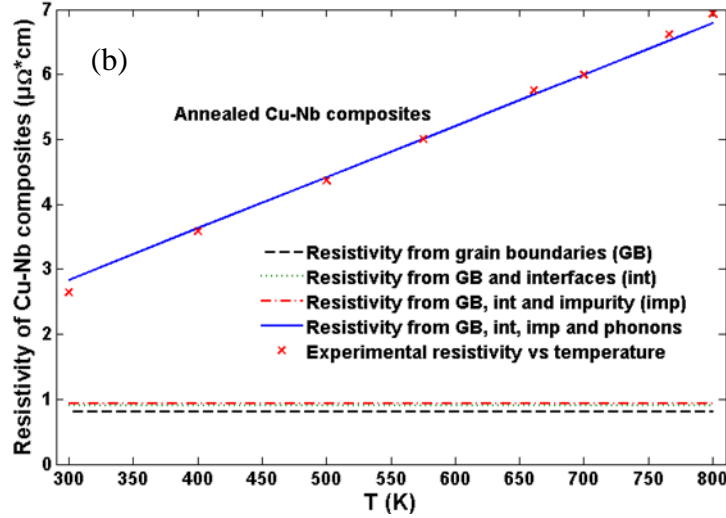


Fig. 2. A comparison between the experimental resistivity and calculated resistivity for Cu/10 vol. % Nb DMMC with deformation true strain  $\eta=9.6$  in the temperature range 293 to 823 K. The resistivity contributions from various scattering mechanisms have been specified. (a) as-drawn Cu/Nb DMMC; (b) annealed Cu/Nb DMMC.

#### Au-Ag DMMCs

The fcc Au/fcc Ag DMMCs have been widely used for interconnection wires in electronic industry. Extensive deformation processing is needed to convert micron-size equiaxed particles into fine nano-scale filaments to obtain the high strength. The effect of deformation processing on resistivity of the composites has to be studied. Wongpreedee and Russell [41] studied the resistivity of Au/14 vol.% Ag DMMCs as a function of deformation true strain. The room temperature resistivity of Au/Ag increases substantially with deformation true strain. This is consistent with the enhanced interface and grain boundary scattering due to the reduced filament thickness and spacing at high true strains. The impurity contribution to resistivity at room temperature can be neglected because experimental results in Ref [41] showed that the resistivity of Au/14%Ag increased by only 0.1% after 20 hours annealing at 175 °C, suggesting excellent thermal stability against mutual solid solution formation. The contribution from dislocations would be negligible in

most DMMCs according to Verhoeven et al [38]. Various parameters needed for model calculation are set up as follows. The initial equiaxed Ag particles are 5  $\mu\text{m}$ . The free electron concentrations in Au and Ag are taken to be  $5.9 \times 10^{28} \text{ /m}^3$  and  $5.86 \times 10^{28} \text{ /m}^3$ , respectively [51]. The resistivity from phonon contribution is taken to be  $2.2 \mu\Omega \cdot \text{cm}$  and  $1.61 \mu\Omega \cdot \text{cm}$  for Au and Ag, respectively [26].

The calculated resistivities are compared with the experimental data in Fig. 3. They showed a good fit with the following parameters  $R_{\text{Au}}=0.6$ ,  $R_{\text{Ag}}=0.97$ ,  $p=0.21$ . The Au reflection coefficient matched the range from 0.4 to 0.9 by previous study [36]. The high reflection coefficient of Ag seems consistent with the strong size dependence of the experimental resistivity. The high  $R_{\text{Ag}}$  may also be related to the fact that the Ag filaments account for only 14 % of the composite's volume, and any slight underestimation of resistivity in Au from interfaces and grain boundaries could lead to an evident overestimation. The interfacial factor  $p$  between 0 and 0.5 is common [27]. It can be seen from Fig. 3 that phonon scattering is still the major contributor in the resistivity of Au/Ag DMMCs at room temperature, and the grain boundary scattering contributes more to the size dependent part of resistivity than does interface scattering. The increasing resistivity with deformation true strain is attributed to the gradually reduced filament thickness and spacing, which increase the interface and grain boundary scattering.

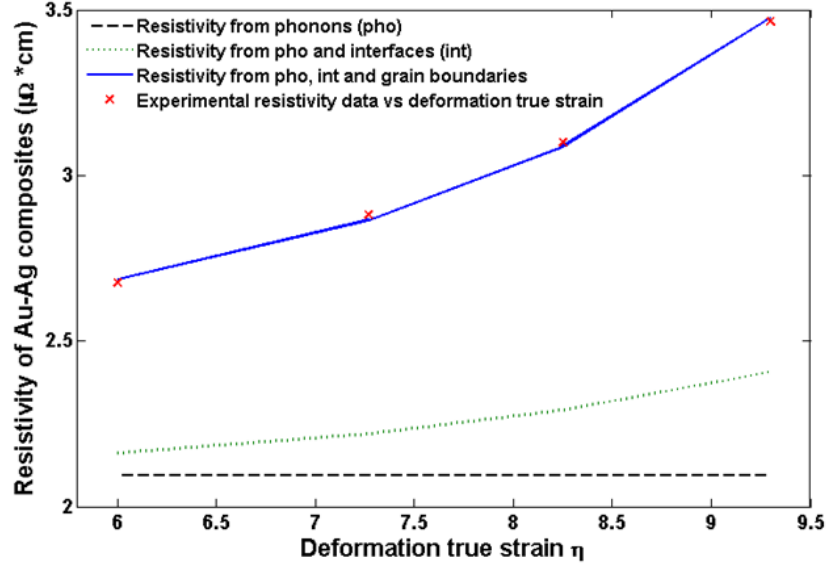


Fig. 3. A comparison between the experimental and calculated resistivities of Au/14 vol. % Ag DMMC at room temperature at deformation true strain values from 6 to 9.3. Experimental resistivities are from Ref [41].

#### Cu-Ag-Nb DMMCs

Mattissen, Raabe and Heringhaus [53] investigated the evolution of electrical resistivity of a ternary Cu-8.2wt. % Ag-4 wt. % Nb in situ composite as a function of deformation true strain at room temperature. The resistivity of this composite increased evidently with the degree of deformation, which is similar for previous binary DMMC systems. This ternary composite can be treated as a material made up of two primary phases, i.e., 95.82 vol. % Cu-Ag phase and 4.18 vol. % Nb phase. The Cu-Ag phase consists of two sub phases, which are 91.92 vol. % Cu and 8.08 vol. % Ag. Therefore, to model the resistivity of this composite, we apply eq. (17) to calculate the resistivity of Cu-Ag phase from its two sub phases first and then calculate the resistivity of the Cu-Ag-Nb composite by applying eq. (17) again to Cu-Ag phase and Nb phase.

The initial average phase diameters are 31767 nm for Cu, 2630 nm for Ag and 1386.6 nm for Nb [53]. The interfacial scattering factor  $p$  is 0.81 for Cu/Ag interface [10, 53] and 0

for Cu/Nb interface [10, 38]. The free electron concentrations of Cu, Ag and Nb can be obtained from previous sections. The phonon contributions to resistivity in Cu, Ag and Nb are 1.72, 1.61, 15.73  $\mu\Omega\cdot\text{cm}$ , respectively at room temperature [26, 51]. The impurity contributions to resistivity in Ag and Nb can be estimated as 0.38  $\mu\Omega\cdot\text{cm}$  [10] and 0.21  $\mu\Omega\cdot\text{cm}$  [38], respectively. The impurity contribution to resistivity in Cu comes from both Ag and Nb, and can be estimated as a sum of two contributions, i.e., 0.59  $\mu\Omega\cdot\text{cm}$ . The increase of dislocation density has negligible effect on the resistivity according to Verhoeven [38] and Raabe [52].

Fig. 4. shows a comparison between experimental resistivity data and our modeling results. Our modeling results have a very good fit with the experimental resistivities with the following parameters:  $R_{\text{Cu}}=0.68$ ,  $R_{\text{Ag}}=0.98$ ,  $R_{\text{Nb}}=0.51$ . The high reflection coefficient of Ag matches very well with the  $R_{\text{Ag}}$  value in section 3.2. The reflection coefficients of Cu and Nb are close to those in section 3.1, which certainly confirms the effectiveness of our model's prediction. To further demonstrate the quality of our model, we compared the simulated resistivities from Mattissen et al [53] with our modeling results in Fig. 4. It is clear that our model is superior to Mattissen's model in its predicting accuracy. However, both models are unable to explain the decreased resistivity when deformation true strain increases to the range between 8 and 9. As Mattissen et al suggested, this unusual resistivity at intermediate strains should be related to the change in precipitation state due to frictional heating during wire drawing [53], which could be difficult to model. The failure to incorporate this additional feature into our model does not obscure the overall effectiveness of our model. At high degree of deformation (i.e. strain above 9), the dominating interface and grain boundary scattering obscures this feature and increases the resistivity of the composite substantially. It

is also important to notice that with a reflection coefficient higher than 0.5, the resistivity contribution of grain boundary scattering would be at least 4 times that of interface scattering in our model, which confirms the significance of grain boundary scattering in contributing to the resistivity of heavily deformed metal-metal composites.

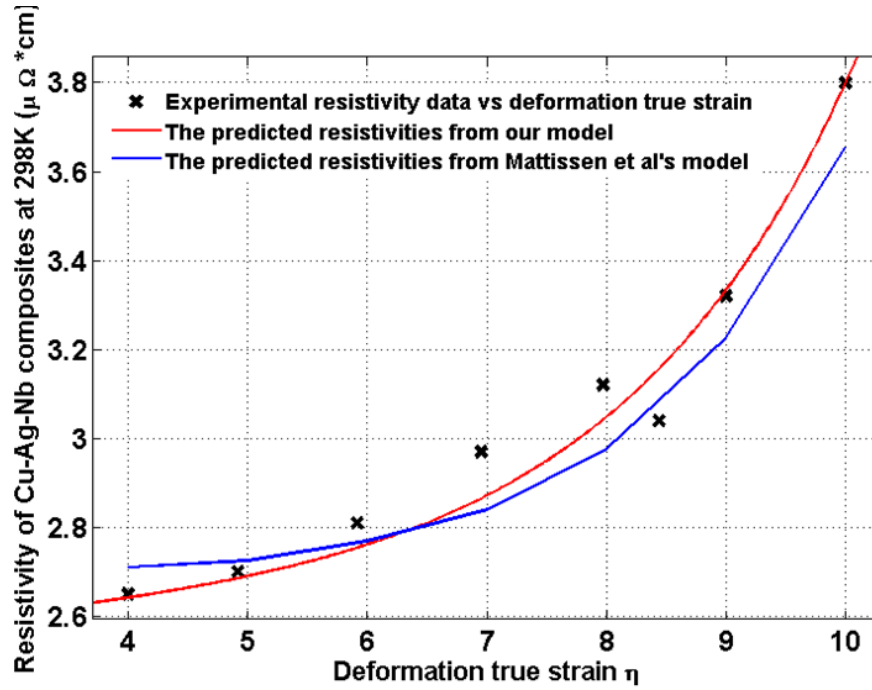


Fig. 4. A comparison of experimental resistivities, calculated resistivities from our model and Mattissen et al's model [53] for ternary Cu-8.2 wt. % Ag-4 wt. % Nb composites at room temperature 298 K as a function of deformation true strain.

## Conclusions

Deformation processed metal-metal composites (DMMCs) are high-strength, high-conductivity in-situ composites and although the high strength has been thoroughly studied, the electrical resistivities of DMMCs are seldom investigated mechanistically. In this paper, we proposed an approach to model the electrical resistivity of deformation processed metal-metal composites by a modified inverse rule of mixture that combines all the plausible scattering mechanisms such as interfaces, grain boundaries, impurities, phonons and

dislocations. We re-interpreted the models for interface and grain boundary scattering in DMMCs by considering filament morphological evolution during deformation processing. Instead of assuming that each metal phase is a single crystal, we incorporated the role of grain boundary scattering into our model by treating each metal phase as a single row of single crystals so that the grain boundary scattering would show a similar thickness dependence to interface scattering. This modeling approach has been successfully applied to the Cu-Nb, Au-Ag and Cu-Ag-Nb systems. With our new combined model, the linear temperature dependence of phonon scattering has been confirmed in Cu-10vol% Nb DMMC in which the resistivity is dominated by the Cu matrix whose temperature dependence is linear by phonon scattering. Filament coarsening instead of dislocation annihilation is primarily responsible for the resistivity drop after annealing treatment or high temperature resistivity measurement in Cu-Nb DMMC. The increasing resistivity with deformation true strain is due to the reduced filament thickness and spacing that would increase the interface and grain boundary scattering. Our results confirmed the evident contribution of grain boundary scattering to the resistivity of DMMCs. We also explained why these different scattering mechanisms can be modeled independently in a common microstructure of DMMCs, which has been misinterpreted by previous investigators.

## References

- [1] Russell AM, Chumbley LS, Tian Y. *Adv Eng Mater* 2000;2:11.
- [2] Bevk J, Harbison JP, Bell JL. *J Appl Phys* 1978;49:6031.
- [3] Verhoeven JD, Schmidt FA, Gibson ED, Spitzig WA. *Jom-J Min Met Mat S* 1986;38:20.
- [4] Spitzig WA, Pelton AR, Laabs FC. *Acta Metall Mater* 1987;35:2427.



- [5] Funkenbusch PD, Courtney TH. *Acta Metall Mater* 1985;33:913.
- [6] Funkenbusch PD, Lee JK, Courtney TH. *Metall Trans A* 1987;18:1249.
- [7] Raabe D, Hangen U. *Compos Sci Technol* 1995;55:57.
- [8] Tian L, Russell A, Anderson I. *J Mater Sci* 2014;49:2787.
- [9] Raabe D. *Computational materials science* 1995;3:402.
- [10] Heringhaus F, Schneider-Muntau HJ, Gottstein G. *Mat Sci Eng a-Struct* 2003;347:9.
- [11] Ondracek G. *Metall* 1982;36:523.
- [12] Boccaccini AR. *Scripta Mater* 1997;36:1195.
- [13] McLachlan DS, Blaszkiewicz M, Newnham RE. *J Am Ceram Soc* 1990;73:2187.
- [14] Stauffer D, Aharony A. *Introduction to percolation theory*: Taylor and Francis, 1994.
- [15] Kovacik J. *Scripta Mater* 1998;39:153.
- [16] Fan ZY. *Acta Metallurgica Et Materialia* 1995;43:43.
- [17] Hashin Z, Shtrikman S. *J Appl Phys* 1962;33:3125.
- [18] Lux F. *J Mater Sci* 1993;28:285.
- [19] Thomson J. On the theory of electric conduction through thin metallic films. *Proc. Cambridge Philos. Soc*, vol. 11, 1901. p.120.
- [20] Fuchs K. *P Camb Philos Soc* 1938;34:100.
- [21] Sondheimer EH. *Advances in Physics* 2001;50:499.
- [22] Dingle R. *Proceedings of the Royal Society of London. Series A. Mathematical and Physical Sciences* 1950;201:545.
- [23] MacDonald D, Sarginson K. *Proceedings of the Royal Society of London. Series A. Mathematical and Physical Sciences* 1950;203:223.
- [24] Chambers RG. *Proceedings of the Royal Society of London. Series A. Mathematical and Physical Sciences* 1950;202:378.
- [25] Mayadas AF, Shatzkes M, Janak JF. *Appl Phys Lett* 1969;14:345.

- [26] Kittel C. Introduction to solid state physics: John Wiley & Sons, Inc, 2005.
- [27] Mayadas AF, Shatzkes M. Phys Rev B 1970;1:1382.
- [28] Tian L, Kim H, Anderson I, Russell A. Mat Sci Eng a-Struct 2013;570:106.
- [29] Verhoeven JD, Spitzig WA, Jones LL, Downing HL, Trybus CL, Gibson ED, Chumbley LS, Fritzemeier LG, Schnittgrund GD. J Mater Eng 1990;12:127.
- [30] Trybus CL, Spitzig WA. Acta Metall Mater 1989;37:1971.
- [31] Biselli C, Morris DG. Acta Metallurgica Et Materialia 1994;42:163.
- [32] Hosford WF. T Metall Soc Aime 1964;230:12.
- [33] Frommeyer G, Wassermann G. Acta Metall Mater 1975;23:1353.
- [34] Russell AM, Lund T, Chumbley LS, Laabs FA, Keehner LL, Harringa JL. Compos Part a-Appl S 1999;30:239.
- [35] Plombon JJ, Andideh E, Dubin VM, Maiz J. Appl Phys Lett 2006;89.
- [36] Durkan C, Welland ME. Phys Rev B 2000;61:14215.
- [37] Thieme F, Kirstein W. Thin Solid Films 1975;30:371.
- [38] Verhoeven J, Downing H, Chumbley L, Gibson E. J Appl Phys 1989;65:1293.
- [39] Qu L, Wang EG, Han K, Zuo XW, Zhang L, Jia P, He JC. J Appl Phys 2013;113.
- [40] Hong SI. Adv Eng Mater 2001;3:475.
- [41] Wongpreedee K, Russell AM. Gold Bull 2004;37:174.
- [42] Xu K, Wongpreedee K, Russell AM. J Mater Sci 2002;37:5209.
- [43] Verhoeven JD, Chueh SC, Gibson ED. J Mater Sci 1989;24:1748.
- [44] Raabe D, Choi PP, Li YJ, Kostka A, Sauvage X, Lecouturier F, Hono K, Kirchheim R, Pippan R, Embury D. Mrs Bull 2010;35:982.
- [45] Raabe D, Ohsaki S, Hono K. Acta Mater 2009;57:5254.
- [46] Sauvage X, Jessner P, Vurpillot F, Pippan R. Scripta Mater 2008;58:1125.
- [47] Karasek KR, Bevk J. J Appl Phys 1981;52:1370.

- [48] Karasek KR, Bevk J. Scripta Metall Mater 1980;14:431.
- [49] Kocer M, Sachslehner F, Muller M, Schafler E, Zehetbauer M. Mater Sci Forum 1996;210-2:133.
- [50] Trybus CL, Chumbley LS, Spitzig WA, Verhoeven JD. Ultramicroscopy 1989;30:315.
- [51] Ashcroft NW, Mermin ND. Solid State Physics. Philadelphia: Saunders College, 1976.
- [52] Raabe D, Heringhaus F, Hangen U, Gottstein G. Z Metallkd 1995;86:416.
- [53] Mattissen D, Raabe D, Heringhaus F. Acta Mater 1999;47:1627.

## CHAPTER 5 PRODUCTION OF FINE CA POWDERS BY CENTRIFUGAL ATOMIZATION WITH ROTATING QUENCH BATH

A paper to be submitted to Powder technology

Liang Tian<sup>1</sup>, Trevor Riedemann<sup>2</sup>, Iver Anderson<sup>3</sup>, Alan Russell<sup>3</sup>

1. Primary researcher and author 2. Primary researcher 3. Principal investigators

### Abstract

Recently, a novel Al/Ca composite for possible use as a high-voltage power transmission conductor was produced by severe plastic deformation of Al powders and calcium granules. Since the strength of such composites is inversely proportional to the Ca filament size, fine Ca powders ( $\sim 200\text{ }\mu\text{m}$ ) are needed for the powder metallurgy production of an Al matrix composite reinforced by nano-scale Ca filaments to achieve the desired high strength for the composite conductor. However, fine Ca powders are not commercially available. Therefore, we have developed a method to produce fine Ca powders via centrifugal atomization to supply Ca powder for prototype development of Al/Ca composite conductor. A secondary goal of the project was to demonstrate that Ca powder can be safely prepared, stored, and handled and could potentially be scaled for commercial production. We report on our initial yield, mean particle size, particle size distribution, morphology, and surface reactivity of the atomized Ca powder. Our results showed that this method can yield as much as 83 vol. % Ca powder particles smaller than  $250\text{ }\mu\text{m}$ . The mean particle size obtained roughly matches and sometimes deviates largely from the predictions from the Champagne & Anger equation. The particle size distribution is typical for a ligament-disintegration atomization mode. Scanning electron micrographs showed that the

morphology of these Ca powders varied with powder size. Spark testing and thermal gravimetric tests indicated that the atomized powders were well passivated and difficult to ignite, providing confidence that this material can be safely utilized.

## Introduction

The authors are engaged in a long-term project to develop an Al/Ca metal-metal composite (MMC) for use as a next-generation high-voltage power conductor [1]. This composite is produced by powder metallurgy from blended Al and Ca powders. Fine Al powder is readily available from commercial vendors; however, fine Ca powders (a few hundred microns and smaller) are not available commercially. The strength of Al/Ca composite increases rapidly with decreasing Ca filament thickness by a Hall-Petch relation. For this reason, initial Ca powder particles with size below 200  $\mu\text{m}$  are necessary to achieve the desired high strength according to theoretical prediction. Once achieved, the Al/Ca composite could reduce the construction costs and increase the reliability and efficiency of high-voltage power transmission systems [2]. This paper reports on the development of a centrifugal atomization method to produce fine Ca powders, which could be scaled up to meet the future needs of commercial-scale manufacturing of Al/Ca composite conductors.

Centrifugal atomization is a well-established method to produce fine metal powders [3-5]. This method has been successfully used to produce various metal powders such as Sn, Pb, Al, Mg, Zn, Ti, Ni, and their alloys [4, 5]. Compared with liquid or gas atomization techniques, centrifugal atomization can produce spherical metal powders with lower impurity content, narrow particle size distributions, high production yields, and moderate production costs [4, 5]. Centrifugal atomization uses centrifugal force to disintegrate a molten metal

stream poured directly onto a rotating disk, cup, or wheel [3]. For rotating-disk centrifugal atomization, successful atomization can be achieved only if the molten metal forms a thin liquid film on the surface of the rotating disk [3-5]. This requires excellent wettability of the molten metal on the rotating disk so the metal will flow freely on the surface of the rotating disk [3, 5]. The melt is then accelerated tangentially by the friction between liquid metal and the rotating disk [6]. These processes lead to a thin liquid metal film on the disk surface to be atomized at the disk edge where the film disintegrates into fine droplets [6]. These fine droplets would be expected to solidify during flight by convective cooling before hitting the atomizer chamber wall or quenching medium [6].

#### Atomization disk characteristics

The design characteristics of the atomization disk in a rotating disk atomizer can have a significant impact on the performance of the atomizer [3-6]. Improper disk design can cause deviations from optimal atomization conditions, resulting in undesired powder characteristics such as large mean particle size, irregular, non-spherical particle shape, wide particle size distributions, and excessive chemical contamination [3]. An ideal atomization disk has the following characteristics: perfect wetting with the liquid metal, low heat capacity and thermal conductivity, resistance to chemical attack, and a smooth profile that redirects the liquid from vertical to horizontal motion [3].

The perfect wetting between rotating disk and molten metal ensures that the liquid metal spreads freely on the disk to form a thin liquid film that would be atomized at the disk edge as previously discussed [3, 5]. Poor wetting may result in a metal skull forming on the disk, which reduces the effective radius of the atomization disk since the atomization occurs

at the edge of the skull instead of the disk edge [7]. The skull may detach from the atomization disk during the operation, which could damage the device and degrade the atomizer performance [5]. Some investigators reported that a moderately rough surface finish on the atomization disk promoted physical bonding between the disk and skull, preventing skull detachment [3]. Wetting condition can be improved through design modifications of the disk. For example, a thin coating of other metals on the disk, such as Ta [3] and Sn [5], has been used to enhance wettability of a stainless steel atomization disk. Likewise, excellent wetting can be achieved between liquid metal and a coating with a composition similar to the molten metal [5]. The surface profile of an atomization disk can be designed to promote the wetting. Compared with flat disks, cup-shaped disks use centrifugal force to push the liquid metal against the disk surface to improve the wetting [5], reducing the mean particle size. In Ref [5], two methods other than achieving perfect wetting were taken to address the skull formation problem: a motor coupler was used to reduce heat conduction through the motor shaft, and a hot-air gun was used to preheat the atomization disk and maintain the disk at elevated temperature throughout the operation.

It is desirable for atomization disk to have low heat capacity and low thermal conductivity because this allows rapid heating of the thin disk, which aides in minimizing solid metal buildup [3]. Otherwise, a thick skull may form to change the effective atomization radius so that the mean particle size and particle size distribution would deviate from the expected results. The break-up of the solid film during atomization would change the particle size distribution and powder morphology [5, 6]. Therefore, in order to eliminate fractions of irregular particles, the thickness of this solid layer should be minimized [5, 6]. The chemical inertness of atomization disk to constituents of molten metal stream is

necessary to maintain high purity in the metal being atomized [3]. A smooth surface profile on the atomization disk would prevent liquid splashing and direct the molten metal stream evenly to form a uniform thickness liquid metal film, narrowing the particle size distribution [3].

#### Atomization modes

Three atomization modes are typically available at the disk as shown in Fig. 1: direct droplet formation, ligament disintegration, and film disintegration [3-6]. The transitions between these three modes depend on liquid metal flow rate, the liquid metal's physical properties, and the speed of rotation and diameter of the atomization disk [5]. Direct droplet formation is favored at low liquid flow rates and low disk rotating speeds. Increasing the flow rate or rotating speed continuously would lead to transition to the liquid disintegration mode first and then to film disintegration [5]. Champagne and Angers proposed an empirical formula to predict the critical flow rates of the melt corresponding to the transitions between three modes, though the mechanisms of the transitions are not clear [8]. Considering the complexity of melt flow on an atomization disk, the atomization mode on the disk edge is unable to be identified as a single mode and can be a mixture of the three modes [5]. Therefore, mathematical models based on the flow behavior of liquid melt should be used with caution and experimentally verified before they can be relied upon to predict particle shape and particle size distribution [5, 9].



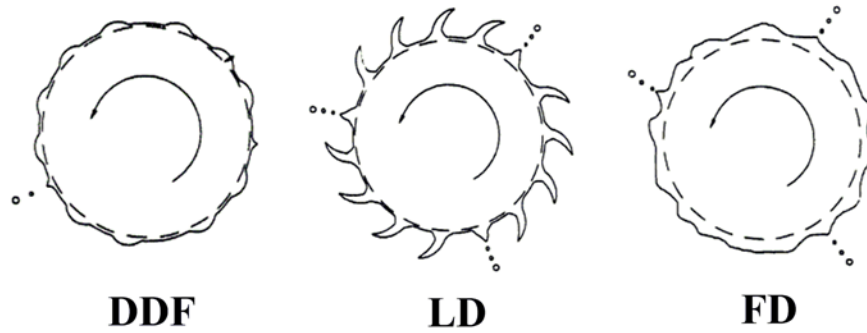


Fig.1. Three atomization modes at the edge of atomization disk: direct droplet formation (DDF); ligament disintegration (LD); film disintegration (FD) [3].

High quality centrifugally atomized powders tend to have a spherical shape. However, irregular particles have been frequently observed in centrifugally atomized Al and Mg alloy powders [10, 11]. Various factors cause these irregular morphologies. First, during flight, the fast cooling rate of fine droplets can prevent complete spheroidization before solidification [6]. The spheroidization of these droplets is caused by the intrinsic interface perturbation coming from gas and liquid interaction according to Lord Rayleigh's instability theory [12]. The growing of the most favorable single harmonic perturbation is a kinetic process [13]. It takes more time for large droplets to complete spheroidization than it does for smaller droplets [13]. Thus, large droplets tend to develop irregular shapes, while small droplets are spherical, which has been experimentally observed by Xie et al [5].

Second, if the atmosphere in the atomizer chamber contains oxygen, rapid oxidation of the liquid metal would form rigid oxide shells around droplets, preventing their spheroidization and further disintegration [3, 5, 6]. This leads to irregular particle morphologies and distorted particle size distributions. An inert gas atmosphere design has been adopted to produce spherical powders of oxide-forming metals with less chemical contamination [3].

Third, irregular powder morphologies can also be caused by secondary atomization via impingement on the chamber wall [5, 6]. Small droplets fully solidify before hitting the chamber wall, so their spherical shape is maintained. Large liquid droplets have relatively slower cooling rates due to its smaller surface to volume ratio than small liquid droplets. Thus, these large droplets would be partially liquid and break up into flake or splat shapes upon striking the chamber wall, which will also distort the particle size distribution [5]. Secondary atomization can be reduced by use of a high thermal conductivity gas as chamber atmosphere (e.g., He) [6]. Increasing the atomization disk's rotating speed promotes smaller particles, which favor the formation of spherical particles [6].

Finally, irregular particles can form from a small fraction of melt solidified into a thin film on the disk. This solid thin film would break up into small irregular particles during atomization and leave the disk free from residual metal [5, 6]. The solidification on the disk surface must be eliminated in order to reduce the proportion of these irregular particles. This can be done by preheating the disk, increasing the liquid metal's superheat, using a low heat capacity and low thermal conductivity disk, and improving the wetting between liquid metal and disk.

In this paper, a preliminary design of a Centrifugal Atomizer with Rotating Quench Bath (CARQB) has been completed for producing fine Ca powders. Funke and Anderson originally developed and built a system at Ames Laboratory to produce spherical metal powders such as Ag [7], and this was adapted later by Osborne and Anderson to produce powders of oxide-forming metals, such as rare earths [3]. These adaptations include using inert gas atmosphere to replace ambient atmosphere, Ta coated smooth cup shaped disk to replace flat disk, a more complex rotating quench bath design for quenchant introduction and

removal. This was later further modified to utilize a spray-quenching system [3]. The new design features of our CARQB will be introduced in the next section. The performance of our atomizer will be evaluated by the production yield, the mean particle size, the particle size distribution and the morphology of obtained Ca powders.

### Experimental Methods

The CARQB used to produce fine Ca powders (Fig. 2) is similar to the Ames Laboratory centrifugal atomizer with rotating quench bath developed in 1993 by Osborne and Anderson [3]. The atomization assembly (i.e. the melt supply system, atomization disk, and rotating quench bath) is housed in a mechanically pumped vacuum chamber, allowing backfilling of ultrahigh purity inert gas operated under a static or dynamic positive pressure ( $\leq 5$  psi). An externally mounted router motor is magnetically coupled to the atomization disk through the chamber floor, providing a rotational speed up to 24,000 RPM. Likewise, the quench bath is driven externally by an AMETEK Series MA34000 motor with integrated motor-drive controller, where coupling is via ferrofluidic feed-through. A rotation speed of 20,000 RPM is chosen to produce Ca powders with size ranging from 100 to 200  $\mu\text{m}$  according to the empirical formula proposed by Champagne and Angers [14].

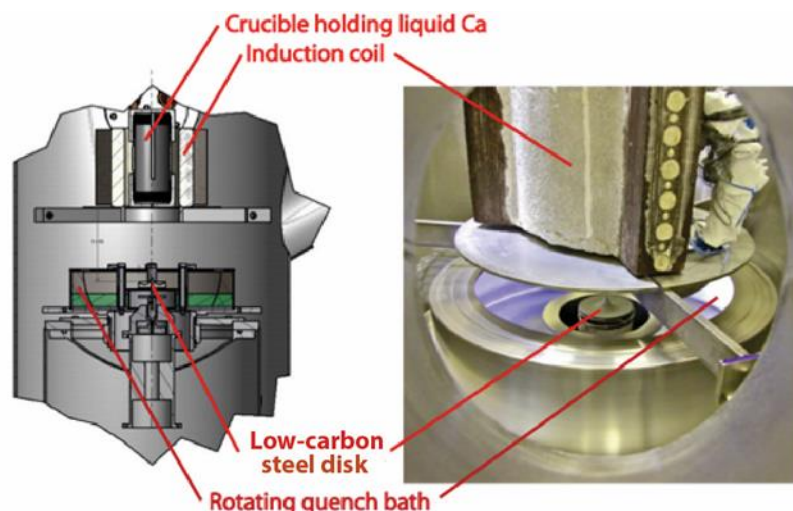


Fig. 2. Ames centrifugal atomizer for producing fine Ca metal powders: mechanical design drawing (left), photograph of the atomizer showing induction heating coil, atomization disk and rotating quench bath (right).

The melt supply system is comprised of a stainless steel crucible (Fig. 3) and induction heating system energized by a 9 KHz, 30 KW power supply. The crucible design by Osborne used a hollow stopper rod and embedded type R thermocouple to control the superheat of liquid metal before the liquid metal was ejected through the bottom hole of the alumina crucible by gravity. In our crucible design, pressurized inert gas is used to deliver a controlled liquid Ca stream through the bottom orifice when the desired superheat is achieved. This method was developed to overcome two problems: (1) the low static head of liquid Ca, which has a density only  $\sim 1/7$  that of Ag or  $\sim 1/5$  that of Sn, and (2) the high vapor pressure of Ca, which is 1.6 torr (mmHg) at its melting point [15]. Controlling the head pressure in the crucible allows control of the mass flow rate of the calcium and ensures delivery of a stable, continuous liquid stream. The closed crucible effectively eliminates vapor loss of the Ca metal, which would otherwise deposit on the chamber's interior surfaces during heating/melting and coat the observation port, blocking the operator's view of the process. Head pressure due to Ca vaporization and thermal expansion of trapped gas is

removed thru a 0.076mm hole near the top of the crucible to relieve the pressure. A thermocouple well with a Type K thermocouple is used to monitor melt temperature. Using water to simulate liquid Ca flow, tests showed that 69 kPa pressurized argon would give a proper liquid supply rate to ensure that the atomization can be completed in a suitable time period. Before the system was induction heated, the crucible was leveled by bullseye level, and the bottom orifice of the crucible was manually aligned with the tip of the atomization disk via a hypodermic tube and inspection mirror.

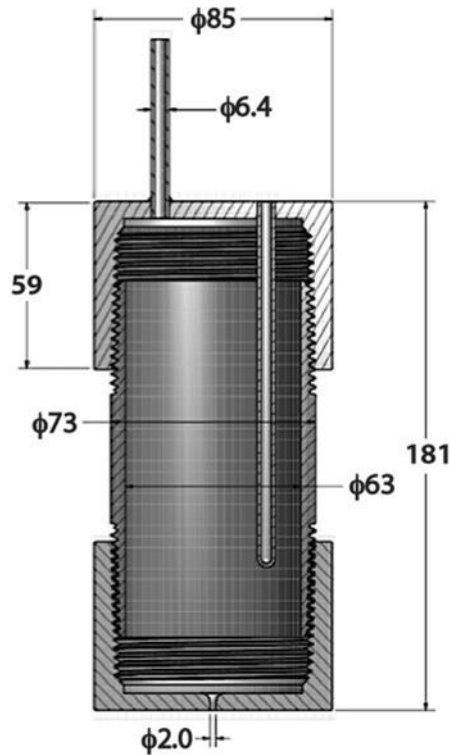


Fig. 3. A mechanical drawing of the crucible assembly. Dimensions are in mm.

The design of the atomization disk roughly follows Osborne's smooth cup shaped disk though several modifications are made. We utilized a 51mm diameter by 0.5 mm-thick cup shaped disk fabricated from a low carbon steel sheet, which is supported by a 25mm-thick ceramic substrate of equal diameter. The atomization disk secures the ceramic

substrate as its shaft penetrates the substrate and is secured into the hollow-center, magnetically coupled drive shaft by a pair of set screws. Additionally, the substrate is supported by a cup-shaped platen that is threaded on the end of the same drive shaft.

The upward angle at the disk edge is 45 degrees. The center tip of the soft steel disk has been blunted to promote the free flow of liquid metal on the disk. Our initial run used a pointed tip like Osborne, but the rest part below this tip acted as a heat sink that solidified the liquid calcium into a mushroom-head, torus-like mass, preventing liquid flow on the entire disk. Atomization took place at the edge of this solidified mass, which reduced the effective radius of atomization and produced larger powders than predicted. In preliminary runs, we did not use a Ta disk or Ta-coated disk; such modifications remain for future optimization.

Fisherbrand 19 mechanical pump oil was used as the quench medium. The quench basin has sufficient volume of oil to produce a 25mm-deep bath on the side while rotating. This amount of oil ensures that the heat transfer from 300 grams of liquid Ca does not raise the temperature of the oil above its flash point 212 °C. The rotating quench bath is a compact design due to a more efficient cooling of liquid droplets by spreading heat uniformly inside the liquid quenchant under rotation. The quench bath was co-rotated with atomization disk to minimize droplets splashing upon hitting the liquid quenchant. A rotational speed of 150 RPM was used.

155 grams of high purity (99.5%) Ca granules from Minteq (Minerals Technologies Inc.) were loaded into the crucible. The crucible and the loaded Ca granules were induction heated gradually to 940 °C in the Ar atmosphere; a 10 minute dwell was imposed just under the melting temperature of Ca 842 °C to ensure that the loosely loaded pellets were heated evenly. Even with the vent hole to relieve head pressure, calcium dripped from the orifice

prior to initiation of stream flow due to the static head. The rotation of the atomization disk cast off the solidified drips and continuous steady liquid flow was initiated by establishing 69 kPa pressurized Ar gas head. The atomization process was recorded by Canon EOS Rebel T3i digital camera to analyze the atomization mode at the disk edge. After atomization, the solidified Ca powders were collected and rinsed with hexane for seven times to remove the quench oil on the Ca powder surface. These rinsed hexane-covered Ca powders were placed in an antechamber of glove box for vacuum removal of the hexane, and the dried powder was moved into the glove box. A two-gram random powder sample was pulled from the batch to measure the particle size distribution via a Microtrac S3500 laser diffraction particle size analyzer. The remaining powders were mechanically sieved into different particle size ranges. The powders at different size ranges were collected, weighed and stored in air-tight jars in the glove box. Powder samples from four different size ranges below 250  $\mu\text{m}$  were sealed in air-tight argon filled vials and sent to scanning electron microscopes for morphology observations. Another set of powder samples from the same four size ranges were spark tested to inspect its flammability and any potential danger of handling fine Ca powders.

## Results and Discussions

### Atomization condition

The atomization disk assembly used in this study is shown in the upper left image of Fig. 4. The atomization process of liquid Ca was captured at a frame rate of 30 fps. Fig. 5 shows a continuous series of frames at the onset of atomization. The final frames in Fig. 5 appear to show that atomization was quickly established at the disk edge. Stream flow

terminated approximately 16 s after its initiation. At approximately 10 s into the atomization, the soft steel disk structurally failed and separated from the assembly, as seen in the lower left image of Fig. 4, though the welded blunted tip and shaft were still secured. Time of failure was measured by the captured video where a sudden rise of pitch from the router motor and mechanical impact noise were evident. A skull had formed on the metallic disk prior to failure. The partial skull was not uniform in thickness and it clearly showed that the atomization occurred at the disk edge. A Ca skull formed and covered the entire ceramic atomization disk as shown in the upper right image of Fig. 4. This certainly indicates that a satisfactory wetting existed between the ceramic atomization disk and the liquid Ca metal and that the atomization of liquid Ca metal occurred at the disk edge as expected. The blunted tip design appears to improve liquid Ca spreading freely on the disk surface. However, the skull is rather thick, indicating that the Ca melt had insufficient superheat to avoid solidification on the ceramic disk. This could be caused by the high thermal capacity of the alumina disk, which is roughly 5 times that of a Ta disk [16]. The non-uniform skull thickness may be due to the liquid splashing when the molten metal stream impinged on the blunted disk tip. This liquid splashing could also contribute to the uneven distribution of liquid Ca on the steel disk, which could lead to large unevenly distributed thermal stress inside the relatively weak soft steel disk causing the disk failure. In our future work, the soft steel atomization disk will be replaced by a plasma-sprayed refractory metal (e.g. Ta) coating on the ceramic disk [3]. It is anticipated that Ta coated disk would perform better because Ta has an excellent wettability with most liquid metal [3] and a low thermal capacity and conductivity to reduce skull formation.



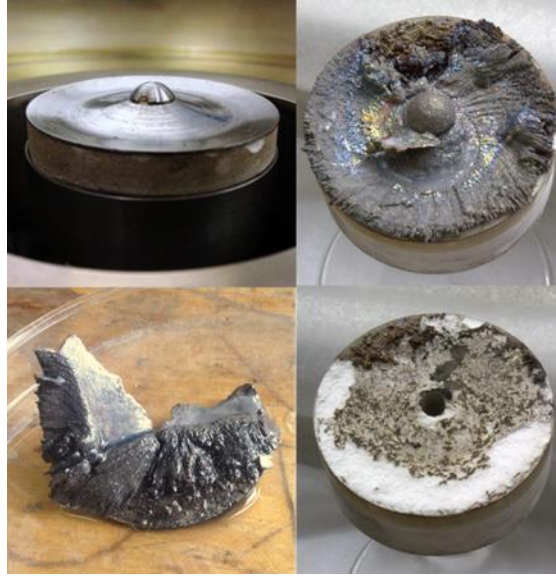


Fig. 4. The atomization disk before the experiment (upper left). The broken soft steel disk during the atomization (bottom left). The remaining solid Ca skull covered on the ceramic disk after the experiment (upper right). The ceramic disk after the skull removed (bottom right). Disk rotation was counterclockwise.

Despite the disk assembly failure, atomization was occurring at the disk edge as desired; under this condition, the particle size can be predicted by mathematical models. The nature of the skull in upper right picture of Fig. 4 indicated that the atomization mode at the disk edge seemed to be ligament disintegration as evidenced by solidified ligaments at disk edge.

Champagne and Angers brought up an empirical formula to calculate the critical flow rates of liquid melt  $Q_t$  in  $\text{m}^3/\text{s}$  corresponding to the transitions between three modes [5, 8]:

$$Q_t = \frac{K \gamma^{0.88} D^{0.68}}{\mu^{0.17} \omega^{0.6} \rho^{0.71}} \quad (1)$$

Where  $\gamma$  is the surface tension of the liquid metal in N/m,  $D$  is the diameter of atomization disk in m,  $\mu$  is the dynamic viscosity of the liquid metal in Pa·s,  $\omega$  is the rotating speed of atomization disk in rad/s,  $\rho$  is the density of liquid metal in  $\text{kg}/\text{m}^3$ .  $K$  is

0.07 for the transition from direct droplet formation to ligament disintegration and 1.33 for the transition from ligament disintegration to film disintegration. In our case, the surface tension of liquid Ca is 0.361 N/m [17, 18], the density of liquid Ca is  $1.33 \times 10^3 \text{ kg/m}^3$  [18], the dynamic viscosity of liquid Ca is  $1.012 \times 10^{-3} \text{ Pa}\cdot\text{s}$  [19]. Disk diameter is 0.0508 m. Disk rotating speed is 2094.4 rad/s. The calculated critical liquid flow rates according to eq. (1) are 1 g/s for direct droplet to ligament disintegration transition, 18.9 g/s for ligament to film disintegration transition. Around 134.6 grams of liquid Ca metal was ejected onto the disk during an approximate time period of 16 s, which gives the liquid flow rate 8.4 g/s in our experiment. This liquid flow rate is between the above calculated two critical flow rates, which means that the atomization mode at disk edge in our experiment should be ligament disintegration. The spiral ligaments around the disk edge in Fig. 5 seem to match the ligament disintegration atomization mechanism.

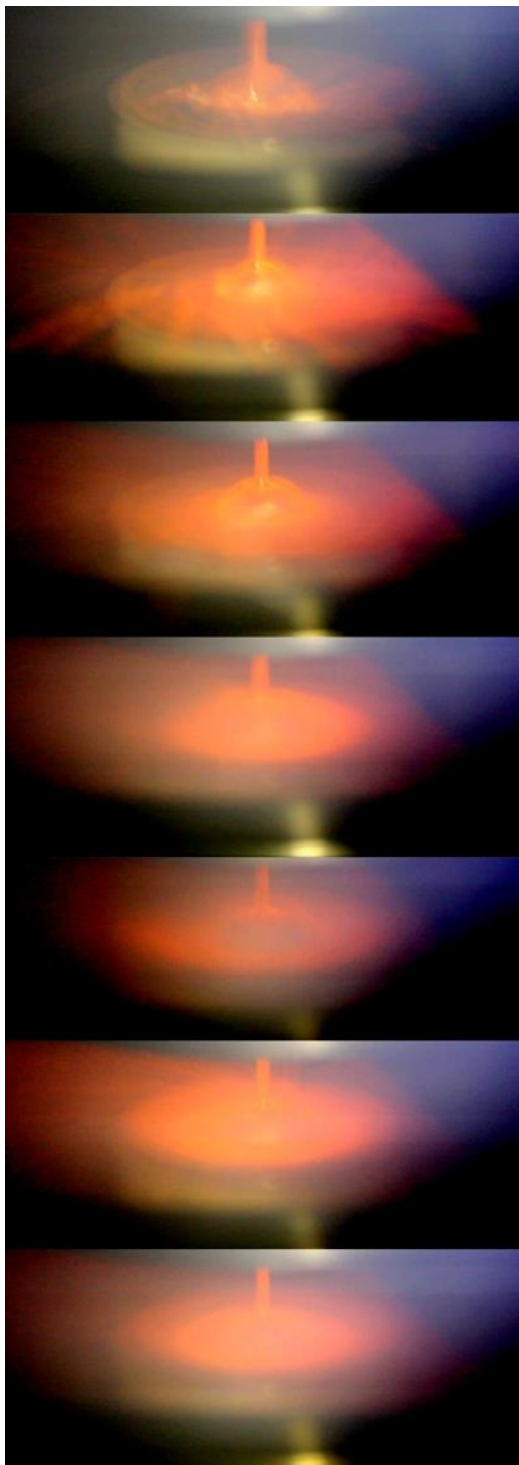


Fig. 5. Continuous frames of the initiation of liquid Ca metal atomizing with time progressing from the top to the bottom under Ar atmosphere at 30 fps.

### Particle size distribution and production yield

Particle size distribution is the most important characteristic of a powder sample and is commonly used to evaluate the performance of a centrifugal atomizer. Particle size distribution is strongly dependent on atomization mechanisms, which are determined by the operating parameters and the physical properties of the liquid metal being atomized [8]. The particle size distributions of 2 two-gram random clean Ca powder samples from each of the 2 atomization runs produced from our centrifugal atomizer is shown in Fig. 6. The mean particle size,  $d_{50}$ , for these two distributions is 126.1  $\mu\text{m}$  and 123.8  $\mu\text{m}$  for the 1st atomization run. The mean particle size,  $d_{50}$ , for these two distributions is 168.2  $\mu\text{m}$  and 181.8  $\mu\text{m}$  for the 2nd atomization run. Champagne and Angers proposed an empirical formula to predict the mean particle size  $d_{50}$  (meter) of centrifugally atomized powders [3, 14]:

$$d_{50} = \frac{3.65Q^{0.06}}{\omega D^{0.58}} \left(\frac{\gamma}{\rho}\right)^{0.46} \quad (2)$$

where  $Q$  is the liquid flow rate in  $\text{m}^3/\text{s}$ ,  $\omega$  is the disk rotational speed in  $\text{rad/s}$ ,  $D$  is the disk diameter in  $\text{m}$ ,  $\gamma$  is the surface tension of liquid metal in  $\text{N/m}$ ,  $\rho$  is the density of liquid metal in  $\text{kg/m}^3$ . In our experiment,  $Q=6.3 \times 10^{-6} \text{ m}^3/\text{s}$ ,  $\omega=2094.4 \text{ rad/s}$ ,  $D=0.0508 \text{ m}$ ,  $\gamma=0.361 \text{ N/m}$ ,  $\rho=1.33 \times 10^3 \text{ kg/m}^3$  [17-19]. According to eq. (2), the calculated mean particle size would be 109.5  $\mu\text{m}$ . The average of two mean particle sizes of 1st atomization run is 125  $\mu\text{m}$ , which is 14% larger but roughly matches the predicted mean particle size. The average of two mean particle sizes of 2nd atomization run is 175  $\mu\text{m}$ , which is 60% larger than predicted mean particle size. There are several possible reasons for this deviation of mean particle size from the predicted value. According to eq. (2), the mean particle size depends on rotating speed and diameter more strongly than other parameters. A 10% reduction in rotating speed would

change the mean particle size to 121.6  $\mu\text{m}$ . Though we have calibrated the continuous dial setting of the speed controller, it is possible that combination of measurement error from the tachometer, minor dial-setting error during operation, and liquid Ca load-induced reduction in rotating speed would contribute to the deviation of rotating speed from 20,000 RPM. It is also possible that a small fraction of liquid Ca atomized from the skull, which reduce the effective atomization radius and increase the mean particle size. Besides, the Champagne and Angers equation is an empirical equation based on the regression analysis. The ranges of various experimental parameters that is used to derive this equation is not applicable for our current atomization condition. For example, the density of liquid Ca metal is only 1330  $\text{kg/m}^3$ , outside of the density range 2000-8000  $\text{kg/m}^3$  in Champagne and Angers equation [14]. The disk rotating speed 2094  $\text{rad/s}$  is outside of the range 600-1600  $\text{rad/s}$  in Champagne and Angers equation. The atomization disk diameter 0.05 m is outside of the range 0.01-0.04 m. The surface tension 0.361  $\text{N/m}$  is outside of the range 0.7-1.8  $\text{N/m}$ . The liquid flow rate 6.3  $\text{cm}^3/\text{s}$  is outside of the range 0.06-0.8  $\text{cm}^3/\text{s}$  in Champagne and Anger equation. Furthermore, most experimental studies just investigated the effect of each processing parameter on the mean particle size without fitting by full Champagne and Anger equation [5, 6, 20]. Some studies showed a contradiction with Champagne and Anger equation, e.g. Plookphol et al [21] found out a strong dependence of the mean particle size on liquid flow rate. The effects of various operating parameters and physical properties of the liquid metal on the mean particle size could be studied in the future.

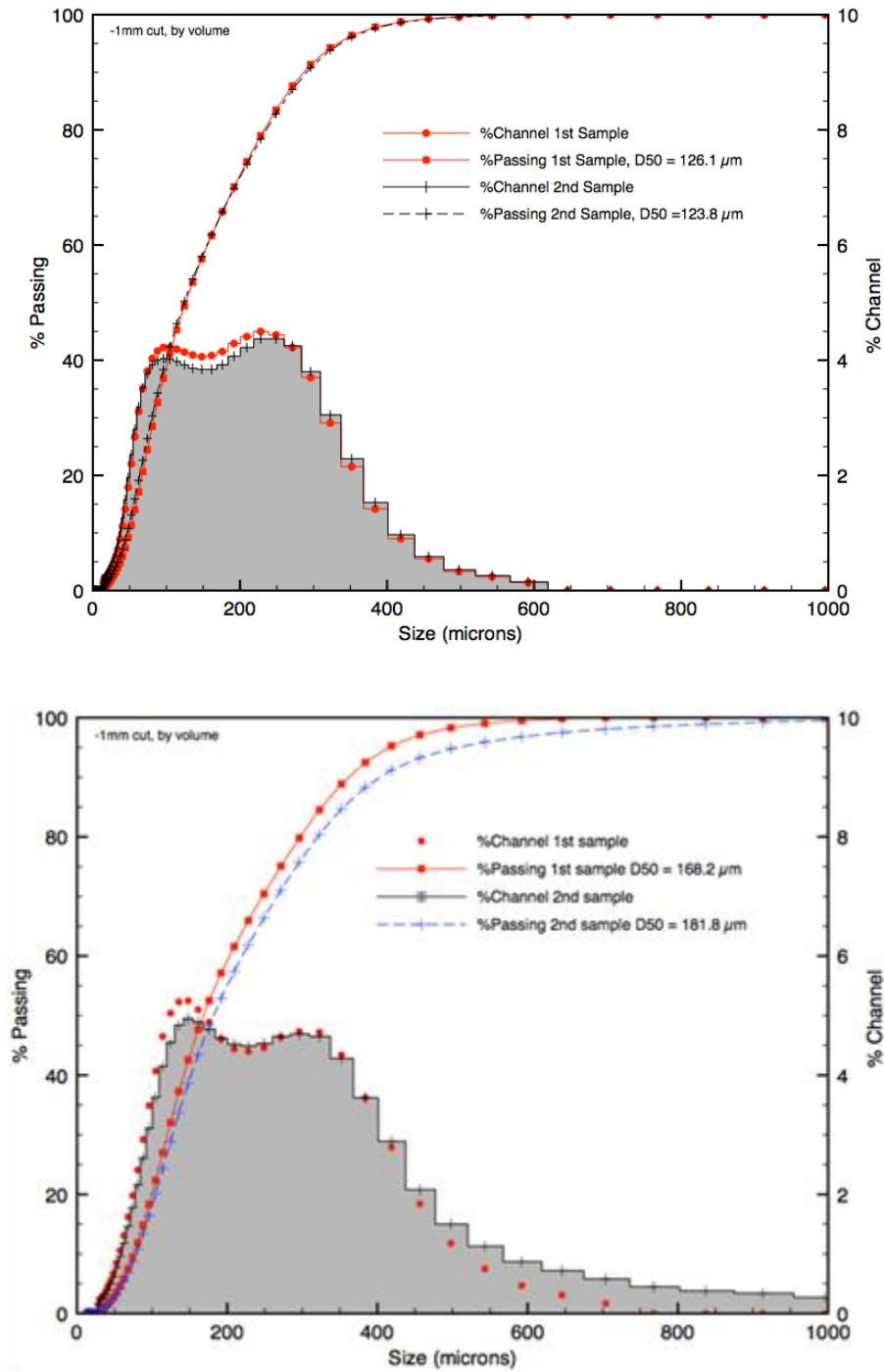


Fig. 6. The particle size distributions of 2 random clean atomized Ca powder samples for each of two atomization runs. The samples were run through a 1mm screen prior to analysis.

From Fig. 6, the majority powders sit in the size range from 60  $\mu\text{m}$  to 320  $\mu\text{m}$ , which is the desired size range needed to produce test samples for the proposed Al/Ca composite

conductor. This particle size distribution would not be expected if the direct droplet formation was the primary atomization mechanism. The direct droplet formation mechanism would generate an obvious bimodal particle size distribution with the main and secondary particles forming two different modes [8]. In addition, the mode from secondary particles should have much less volume fraction than that of the mode from main particles, considering the number of secondary particles is roughly equal to that of main particles [8]. The particle size distribution in Fig. 6 clearly deviates from the above description. Increasing the liquid flow rate would lead to the gradual transition of atomization mode from direct droplet formation to ligament disintegration. As discussed in section 3.1, the liquid flow rate in our experiment would be predicted by theory to operate in the liquid disintegration atomization mode. It has been observed that the proportion of secondary particles increases steadily with the liquid flow rate [8]. This can explain the fact that the volume fraction of the secondary particles is roughly equal to that of the main particles observed in Fig. 6. This feature of particle size distribution further indicated the ligament disintegration atomization mechanism in our experiment.

In addition to the atomization mode, the operating conditions and properties of the liquid metal can also affect particle size distribution by: (1) forming a thick skull that could shift the particle size to a coarser range; (2) the non-uniform skull thickness on the ceramic disk that could widen the particle size distribution. The particle morphology can further alter the particle size distribution as well. For example, non-spherical particles like flakes, splats, and rods could result in a bimodal particle size distribution as well since the Microtrac unit could mistakenly read the two different dimensions of these irregular particles as two different particle sizes [2].

Dry clean Ca powders produced from one run of our centrifugal atomizer were mechanically sieved into different particle size ranges and weighed, as shown in Table 1. About half of these Ca powders ranged from 74  $\mu\text{m}$  to 149  $\mu\text{m}$ , and 83 % of the Ca powders have particle size less than 250  $\mu\text{m}$ . This demonstrates that our centrifugal atomizer is capable of producing high yield percentage of desired fine Ca powders around 200  $\mu\text{m}$ .

Table 1. The powder production yields for different particle size ranges.

U.S. mesh size	Powder size	Powder weight (g)	Percentage of total mass collected
+18	>1 mm	8.920	8.7%
+30/-18	595 $\mu\text{m}$ -1 mm	1.562	1.5%
+60/-30	250-595 $\mu\text{m}$	6.794	6.6%
+80/-60	177-250 $\mu\text{m}$	11.045	10.7%
+100/-80	149-177 $\mu\text{m}$	10.622	10.3%
+150/-100	105-149 $\mu\text{m}$	23.820	23.1%
+200/-150	74-105 $\mu\text{m}$	26.819	26.0%
-200	< 74 $\mu\text{m}$	13.491	13.1%
		Total: 103.073	

### Particle morphology

Particle morphology is another important powder characteristic that indicates the quality of the centrifugally atomized powders. Ideally, spherical powders are expected for centrifugally atomized powder. However, irregular powder shapes are frequently observed in centrifugal atomization for various reasons [5, 6, 8, 20, 22]. In our experiment, SEM micrographs of Ca powders with four different particle size ranges were taken to examine their morphologies. As shown in Fig. 7, large Ca powders (i.e. 177  $\mu\text{m}$  ~ 250  $\mu\text{m}$ ) tend to have irregular ligamental, rodlike shapes, while smaller Ca powders (i.e. 74  $\mu\text{m}$  ~ 105  $\mu\text{m}$ )



are predominantly spherical. As the Ca powder size decreases, a gradual transition of particle shape is observed from irregular to spherical.

Various reasons can explain the change of particle morphology with particle size. First, liquid droplets atomized at the disk edge have sufficiently fast cooling rates to solidify during flight. Larger droplets may not have sufficient time to spheroidize before solidification so that ligament, rod, and teardrop shaped powders would be produced, while small droplets completed spheroidization before solidification to possess a spherical shape. If irregular shaped Ca powders were produced in this way, the surface of these Ca powders would be smooth due to a solidification process [6, 8], as can be seen in the smooth solidified surface of Ca powders of 74-105  $\mu\text{m}$  in Fig. 7. However, it is clear in Fig. 7 that a substantial fraction of Ca powders of 177-250  $\mu\text{m}$  have rough surfaces and tortured shapes other than ligament or spheroid. To explain these characteristics, we propose that secondary atomization was occurring as the partially liquid Ca droplets impinged on the quench bath. Due to a smaller surface to volume ratio, larger Ca liquid droplets have a slower cooling rate than smaller Ca liquid droplets so that larger Ca droplets may become semi-solid and not fully solidified before hitting the rotating quench bath. The impingement of partly liquid Ca droplets upon the quench bath would substantially distort the morphology of the droplets and create rough surfaces and tortured shapes, while small spheroidized Ca droplets would fully solidified before hitting the quench bath to become spherical powders with smooth surface.

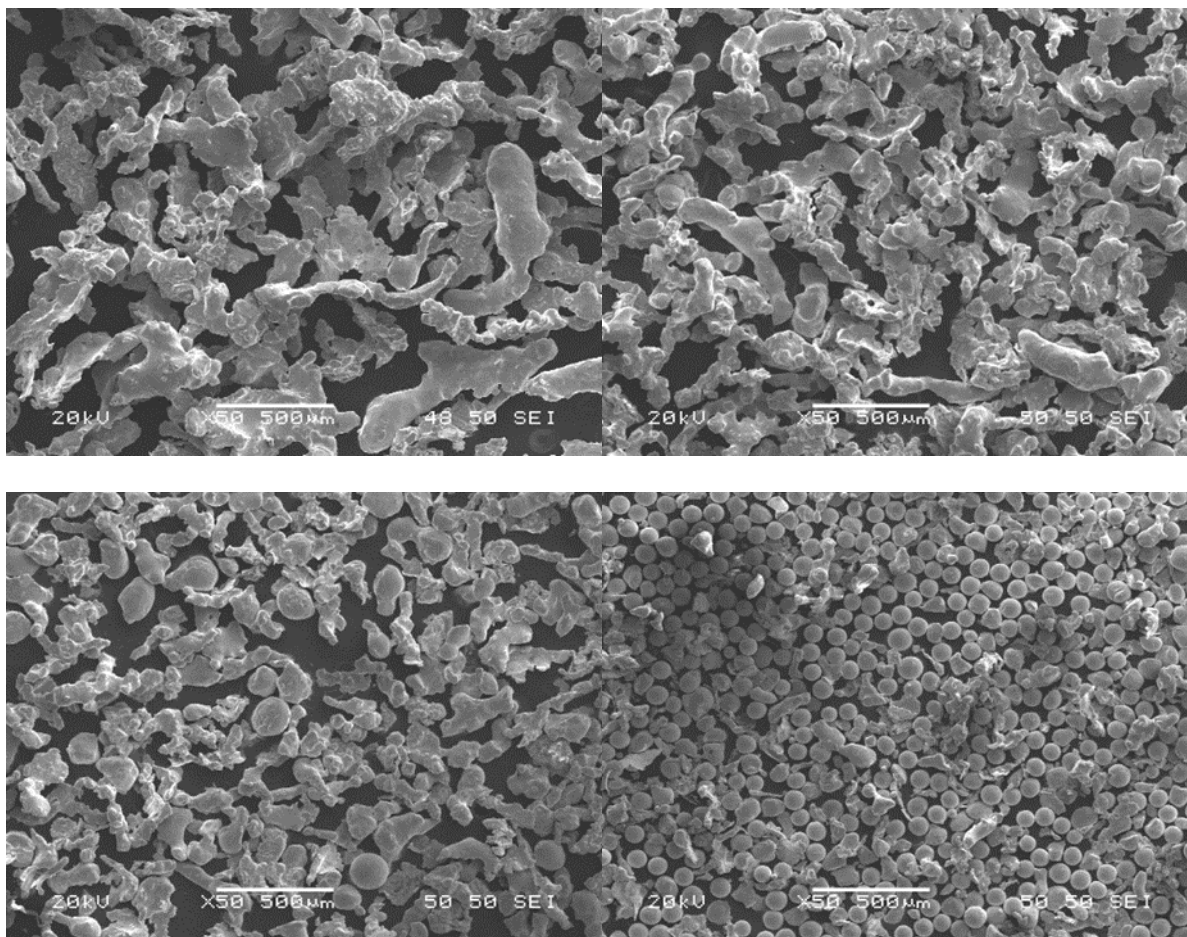


Fig. 7. Scanning electron microscope (SEM) images of centrifugally atomized Ca powders for four different size ranges: 177-250  $\mu\text{m}$  (upper left); 149-177  $\mu\text{m}$  (upper right); 105-149  $\mu\text{m}$  (lower left); 74-105  $\mu\text{m}$  (bottom right). The chamber was filled with Ar gas.

Confirmation of this mechanism has been done by filling the chamber with helium gas that has a higher thermal conductivity than Ar. Helium gas should rapidly cool the liquid Ca droplets during flight; thus, it would be expected that a larger portion of droplets will fully solidify before reaching the quench bath, increasing the fraction of spherical particles. Fig. 8 shows the SEM pictures on powder morphology of atomized Ca powders after filling the chamber with helium gas. It can be clearly seen that the transition from irregular particle shape to spherical particle shape occurred at 149-177  $\mu\text{m}$  for powders produced under helium gas atmosphere chamber, compared with 105-149  $\mu\text{m}$  for powders produced under Ar gas

atmosphere. The rapid cooling of helium gas allowed larger size powders to be fully solidified into spheres before hitting the quench bath while the slower cooling of Ar gas can only allow smaller powders to be fully solidified and spherical. All the above evidence confirmed that the irregular shape is caused by the secondary atomization when the partially solidified Ca droplets hit upon the liquid quench bath.

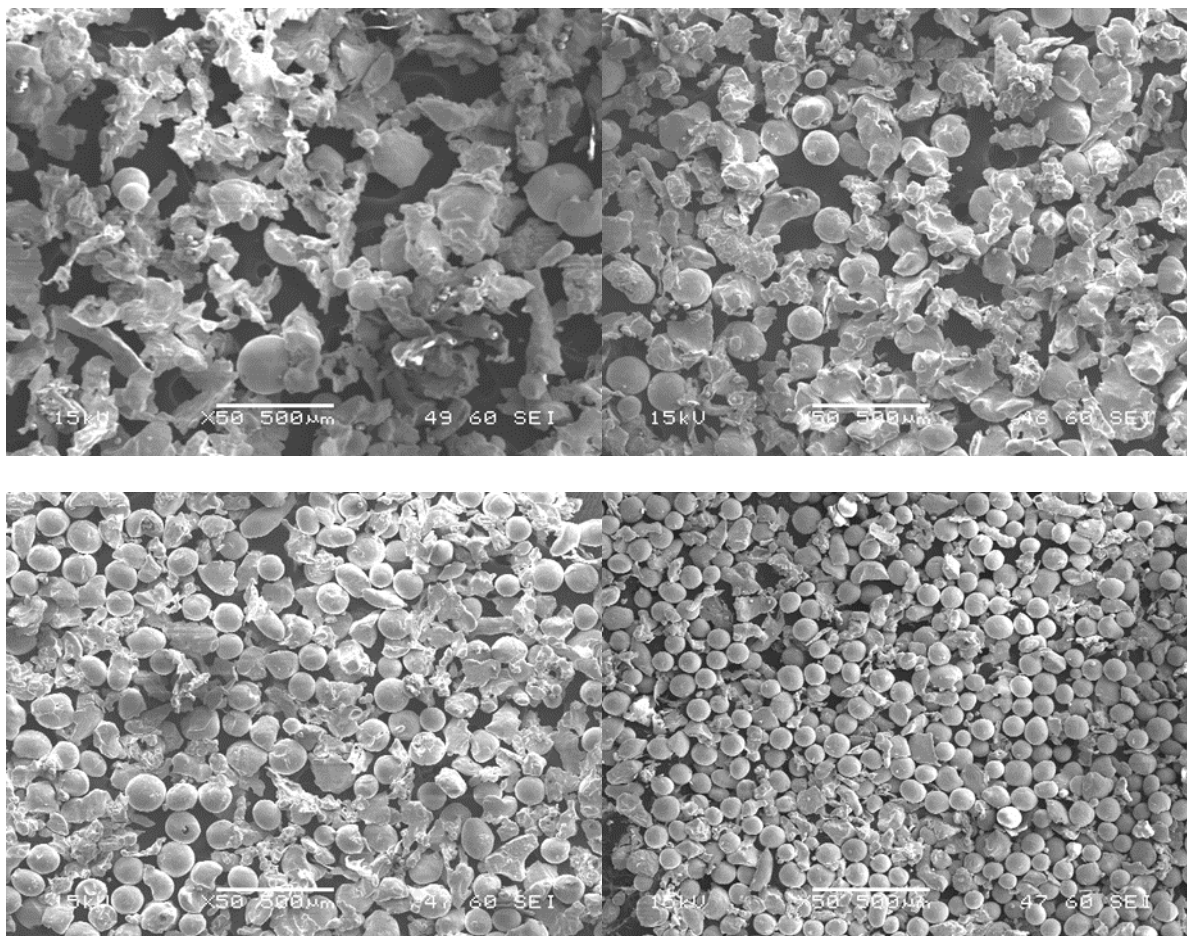


Fig. 8. Scanning electron microscope (SEM) images of centrifugally atomized Ca powders for four different size ranges: 177-250  $\mu\text{m}$  (upper left); 149-177  $\mu\text{m}$  (upper right); 105-149  $\mu\text{m}$  (lower left); 74-105  $\mu\text{m}$  (bottom right). The chamber was filled with He gas.

It is worth noting that a small fraction of these irregular powders probably comes from the break-up of a solidified thin film on the disk [5, 6]. Besides, any method that can

produce smaller liquid Ca droplets, such as increasing disk rotating speed and diameter, would increase the fraction of spherical powders.

#### Surface reactivity and safe handling

Throughout the development of CARQB, safe handling of calcium powders has been a major concern. Ca is a reactive metal that readily oxidizes in air and water. The spark testing of hand-filed fine Ca debris showed little reactivity and suggested that large quantities of fine Ca powders could be handled safely. To further verify this idea, four Ca powder samples from the particle size ranges shown in Fig. 7 were used for spark testing in air. Tesla coil was used to attempt to ignite each sample. Our results showed that powders with mesh size +80/-60 had no reaction; powders with mesh size +100/-80 had a little glow that was not sustained when the spark source was removed; powders with mesh size +150/-100 and +200/-150 would glow but with little propagation when the spark source was removed. These simple tests suggest that fine Ca powders quenched in oil pose no hazard to safe handling, similar to that of other metal powders already produced on a large scale such as Mg powders. The surface inertness of these fine Ca powders could originate from a passivation surface layer on these Ca powders due to the chemical reaction with the liquid quenchant or a partially oxidized surface.

To verify the surface passivation of atomized Ca powders, thermal gravimetric (TG) analysis were done on atomized Ca powders (177-250  $\mu\text{m}$ ) and Ames Lab distilled high purity Ca bulk piece as reference. The tests were conducted under a combined gas flow of room air at 40 mL/min and protective Argon gas at 20 mL/min. Fig. 8 shows the TG of two types of samples varying as a function of time/temperature with the temperature profile

indicated. The atomized Ca powders were clearly passivated until 825 °C and then the protective layer broke so that pure Ca were exposed in air to be oxidized rapidly. This TG trend of atomized Ca powders is very similar to that of pure Ca bulk piece, which has a slightly higher ignition temperature 835 °C and was protected by a thin layer of oxide and hydroxide [23]. A possible reason of slightly lower ignition temperature in atomized powders may be due to the larger pre-existing surface stress due to the small diameter of atomized powders, so that less thermal stress from thermal expansion mismatch between surface passivated layer and inside Ca would be needed to crack the surface. The higher percentage of TG increase in atomized powders should be related to the fact that powders have larger percentage of surface atoms than that in bulk form. The initial slightly decrease of TG in both sample could be due to the desorption of water molecules by breaking secondary bonds upon heating. To further understand the passivating layer on atomized Ca powders, surface sensitive characterization techniques such as Auger electron spectroscopy and X-ray photoelectron spectroscopy have been used to qualitative analyze the composition of passivating layer due to the non-flat nature of powders. These tests suggested a carbonaceous layer on the surface, which seems to be consistent with the measured carbon content 0.1% in atomized Ca powders (177-250  $\mu\text{m}$ ) and 0.0% carbon content in pure Ca pieces by the same CHN combustion tests. All the above tests suggested that our atomized Ca powders are well passivated and safe to handle.

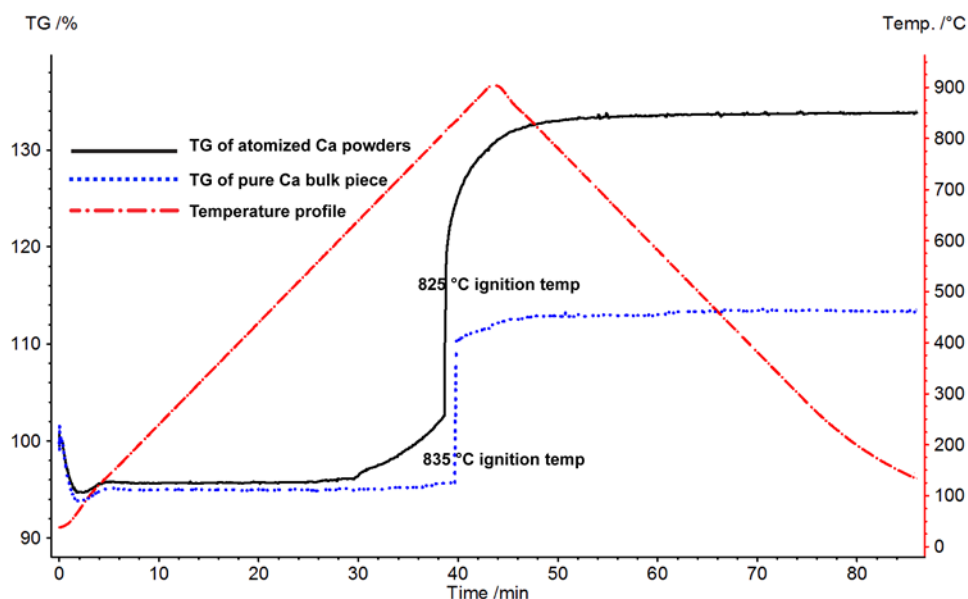


Fig. 8. Thermal gravimetric (TG) tests on atomized Ca powders (Mesh -80/+100) and pure Ca bulk piece under a combined gas flow of 40 mL/min room air and 20 mL/min protective argon gas.

### Conclusions

Fine Ca metal powders have been produced by rotating disk centrifugal atomizer with a rotating quench bath under an Ar atmosphere. The performance of the centrifugal atomizer was evaluated by the atomizing condition that can be reflected by solid skull thickness and uniformity, and various powder characteristics such as mean particle size, particle size distribution, production yield and particle morphology. Our results support the conclusion that the atomization of liquid Ca metal occurred at the edge of the atomization disk by a ligament disintegration atomization mode. The mean particle size of centrifugally atomized Ca powders roughly match and sometimes deviates from the empirical formula proposed by Champagne & Angers. The production yield of fine Ca powders less than 250  $\mu\text{m}$  is as high as 83% of the total powders produced by the centrifugal atomizer. SEM micrographs showed that the larger Ca powders (i.e. 177-250  $\mu\text{m}$ ) tend to have irregular shapes, and the

smaller Ca powders (i.e. 74-105  $\mu\text{m}$ ) tend to be spherical. This can be explained by a secondary atomization mechanism that distorted the particle morphology when partially liquid Ca droplets impinged upon the quench bath. Spark testing and thermal gravimetric (TG) tests showed that these fine Ca powders were passivated well and posed no greater hazard than powders of other metals, thus should be safe to handle. The effects of processing parameters (e.g. disk rotational speed and radius, liquid flow rate, type of inert gas atmosphere) on powder characteristics will be investigated in the future.

### References

- [1] L. Tian, H. Kim, I. Anderson, A. Russell, The microstructure-strength relationship in a deformation processed Al-Ca composite, *Mat Sci Eng a-Struct*, 570 (2013) 106-113.
- [2] L. Tian, I. Anderson, T. Riedemann, A. Russell, H. Kim, Prospects for novel deformation processed Al/Ca composite conductors for overhead high voltage direct current (HVDC) power transmission, *Electr Pow Syst Res*, 105 (2013) 105-114.
- [3] M.G. Osborne, Centrifugal atomization of lanthanide materials for cryogenic coolers, Other Information: TH: Thesis (M.S.); PBD: 4 Jan 1994, 1994, pp. Medium: ED; Size: 106 p.
- [4] T.P. Phairote Sungkhaphaitoon, and Sirikul Wisutmethangoon, Design and Development of a Centrifugal Atomizer for Producing Zinc Metal Powder, *International Journal of Applied Physics and Mathematics*, 2 (2012).
- [5] J.W. Xie, Y.Y. Zhao, J.J. Dunkley, Effects of processing conditions on powder particle size and morphology in centrifugal atomisation of tin, *Powder Metall*, 47 (2004) 168-172.
- [6] R. Angers, R. Tremblay, D. Dube, Formation of irregular particles during centrifugal atomization of AZ91 alloy, *Mater Lett*, 33 (1997) 13-18.
- [7] K. Funke, Development of a centrifugal atomization process for the production of large spherical metal powders, Ames Lab., IA (United States), 1991.
- [8] B. Champagne, R. Angers, Rep Atomization Mechanisms, *Powder Metall Int*, 16 (1984) 125-128.

- [9] Y.Y. Zhao, M.H. Jacobs, A.L. Dowson, Liquid flow on a rotating disk prior to centrifugal atomization and spray deposition, *Metall Mater Trans B*, 29 (1998) 1357-1369.
- [10] R. Angers, C. Dube, R. Tremblay, Inverted disk centrifugal atomization of 2024, *Int J Powder Metall*, 30 (1994) 429-434.
- [11] C. Labrecque, R. Angers, R. Tremblay, D. Dube, Inverted disk centrifugal atomization of AZ91 magnesium alloy, *Canadian metallurgical quarterly*, 36 (1997) 169-175.
- [12] J.W. Strutt, L. Rayleigh, On the instability of jets, *Proc. R. Soc. London A*, 1879, pp. 4-13.
- [13] L. Tian, A. Russell, Phase field study of interfacial diffusion-driven spheroidization in a composite comprised of two mutually insoluble phases, *The Journal of Chemical Physics*, 140 (2014).
- [14] B. Champagne, R. Angers, Size distribution of powders atomized by the rotating electrode process, *Modern Development in Powder Metallurgy*, 12 (1980) 83-104.
- [15] R.E. Honig, Vapor Pressure Data for the Solid and Liquid Elements, *Rca Rev*, 23 (1962) 567-586.
- [16] <http://www.matweb.com/>, May 19, 2014.
- [17] B.J. Keene, Review of Data for the Surface-Tension of Pure Metals, *Int Mater Rev*, 38 (1993) 157-192.
- [18] Bohdansk.J, H.E.J. Schins, Surface Tension and Density of Liquid Earth Alkaline Metals Mg Ca Sr Ba, *J Inorg Nucl Chem*, 30 (1968) 2331-&.
- [19] M.F. Culpin, The Viscosity of Liquid Magnesium and Liquid Calcium, *P Phys Soc Lond B*, 70 (1957) 1079-1086.
- [20] S. Ozturk, F. Arslan, B. Ozturk, Effect of process parameters on production of metal powders by water jet cooled rotating disc atomisation, *Powder Metall*, 48 (2005) 163-170.
- [21] T. Plookphol, S. Wisutmethangoon, S. Gonsrang, Influence of process parameters on SAC305 lead-free solder powder produced by centrifugal atomization, *Powder Technology*, 214 (2011) 506-512.
- [22] P. Sungkhaphaitoon, W. Likhidkan, S. Kitjaidiaw, S. Wisutmethangoon, T. Plookphol, Effect of Atomizer Disc Geometry on Zinc Metal Powder Production by Centrifugal Atomization, *Appl Mech Mater*, 271-272 (2013) 232-236.



- [23] N.M. Laurendeau, I. Glassman, Ignition Temperatures of Metals in Oxygen Atmospheres, *Combustion Science and Technology*, 3 (1971) 77-82.

CHAPTER 6 PROSPECTS FOR NOVEL DEFORMATION PROCESSED AL/CA  
COMPOSITE CONDUCTORS FOR OVERHEAD HIGH VOLTAGE DIRECT CURRENT  
(HVDC) POWER TRANSMISSION

A paper published in Electric Power Systems Research

Liang Tian<sup>1</sup>, Iver Anderson<sup>2</sup>, Trevor Riedemann<sup>3</sup>, Alan Russell<sup>2</sup>, Hyongjune Kim<sup>3</sup>

1. Primary researcher and author 2. Principal investigators 3. Experimentalists

Abstract

In the quest for more efficient long-distance power transmission, High Voltage Direct Current (HVDC) transmission offers a reliable, cost-effective alternative to HVAC for long distance overhead transmission. Development of stronger, more conductive, and lighter conductor materials could lower HVDC construction costs, reduce energy losses, and increase reliability. In this paper, we describe a new deformation processed Al/Ca composite conductor now in development that has the potential to offer substantially lower density, higher strength, and higher conductivity for HVDC than today's conductor materials. This Al/Ca composite has shown promising early corrosion and elevated temperature performance test results, but additional research is needed to determine its fatigue and creep strengths, as well as its susceptibility to electrotransport phenomena and other factors. The design process, production methods, and physical properties of the new composite conductor are discussed. An economic and thermal analysis of this conductor material is also presented.

## Introduction

## HVDC power transmission technology

More efficient long-distance, high-voltage power transmission technologies will be required in the 21st century to support a transition from predominant fossil fuel combustion to a mix of nuclear fission and greatly expanded renewable energy sources (i.e., solar, wind, tidal, etc.)[1]. High voltage direct current (HVDC) transmission technology is more energy efficient than high voltage alternating current (HVAC) technology. A thousand-mile HVDC line carrying thousands of megawatts might only lose 6 to 8 percent of its power, compared with 12 to 25 percent loss for a similar HVAC line [2]. Fig. 1 shows schematically the variation of costs and power transfer capacity for DC and AC as a function of transmission distance. HVDC is cost-effective for long distance (~500 km) overhead transmission because the reduced cost of energy losses more than matches the high cost of converter stations for long-distance transmission [3]. The distance at which HVDC technology cost equals HVAC cost is called the break-even distance. The break-even distance varies with transmission medium, route, and the amount of power to be transmitted [4].

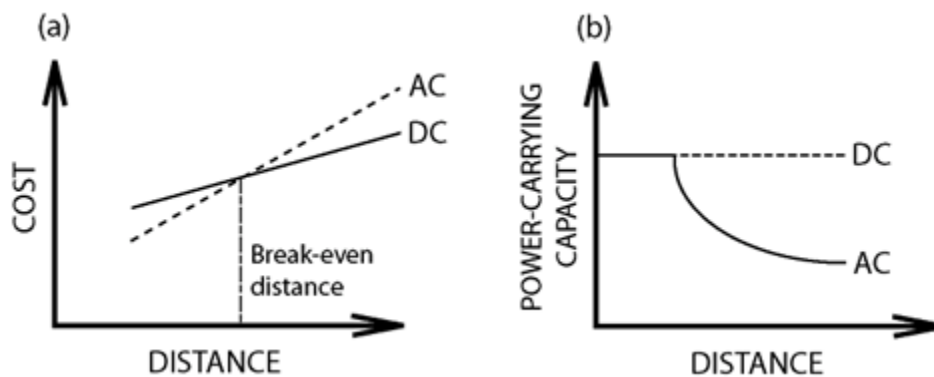


Fig. 1. Variations of cost and power transfer capacity with respect to transmission distance for AC and DC transmission system [1].

Compared with HVAC, other benefits of HVDC include: higher power-carrying capacity for very long distances (see Fig.1b)[1,3]; fewer transmission conducting wires and towers [1, 3, 4]; higher stability and reliability [1, 3, 5]; freedom from inductance compensation requirements [1, 3] and reactive power compensation [1]; asynchronous interconnections [1, 3, 5]; absence of skin effects that avoids localized surface heating [1]; reduced visual impact and right-of-way area [3,4, 5]; fewer environmental concerns [3, 4, 5]; and reduced corona effect [1]. The major obstacles to developing HVDC technology are the high cost of conversion equipment and the difficulty of breaking elevated DC currents [1]. Various attempts have been made to improve converter technology [1, 6, 7, 8], resulting in some cost reductions. Quite importantly, ABB Ltd., has recently announced its successful development of a new hybrid HVDC breaker, which makes it possible to establish massive, super-efficient interconnected supergrids instead of point-to-point power delivery [2]. This technology also reduces the possibility of catastrophic blackouts by disconnecting sections that are struck by lightning.

#### Development of conductors for power transmission

Numerous efforts have been made in recent years to develop new conductor materials with high strength and high conductivity for long distance overhead power transmission [8, 9]. Conventional “Aluminum Conductor Steel Reinforced” (ACSR) cables were designed with a strong steel core to support the combined weight of the dual-part cable and the annealed aluminum outer strands surrounding the core to conduct the current [10]. For AC transmission, ACSR has a high conductivity (61% IACS) due to the skin effect that concentrates current on the exterior Al strands. However, the heavy, poorly conducting steel

core contributes little to conductivity and worsens sag for long distance DC transmission [10]. The large mismatch of thermal expansion coefficient and elastic modulus between Al and steel poses problems with residual stresses and thermal fatigue. ACSR also suffers from fretting fatigue of internal aluminum layers by aeolian vibrations [11]. Fatigue cracks near the Al strand/steel core contact edge [12, 13] caused the blackout of the southern states of Brazil in 2002 [14]. The potential exists for severe corrosion of the dissimilar metals in ACSR, which can cause strand breakage and line failure [15]. Aqueous solutions containing chloride ions can penetrate between the aluminum strands and attack the steel core [15, 16], creating a galvanic corrosion cell in which the aluminum strands are the anode and corrode rapidly. This corrosion will degrade the current carrying capability and mechanical strength of the conductor [15]. AFL's Alumoweld (Aluminum Clad Steel) improved the design of ACSR by using consolidation of high purity aluminum powder as a continuous heavy jacket to encapsulate the steel core instead of the woven pattern of aluminum strands [17].

These problems in ACSR have not been fully solved, and new conductor materials are needed to improve conductor performance to better meet the rising electrical power demands of modern civilization. The "All Aluminum Alloy Conductor" (AAAC) was designed mainly to improve the galvanic corrosion performance of the transmission line [18]. AAAC is stronger and lighter than an ACSR conductor of the same diameter [18, 19]. However, the Mg, Si, and other alloying elements added to boost strength by precipitation hardening also degrade AAAC's conductivity to 52.5 to 53% IACS [18, 19]. Therefore, selecting a suitable aluminum alloy for AAAC is a compromise between mechanical properties, thermal stability (due to precipitate coarsening), and electrical conductivity. The high coefficient of thermal expansion of AAAC makes it more susceptible to thermal fatigue

in emergency overload situations [19]. The conductor oscillations due to wind movement may still cause fretting fatigue problem in suspension clamp regions, spacers or other fittings, which led to the failure after only 6 months in-service of a 400kV overhead transmission line in Touggourt Biskra, Algeria [20].

A cable design called “Aluminum Conductor Alloy Reinforced” (ACAR) consists of a mixture of 6201-T81 and 1350-H19 strands of the same diameter. It is another replacement for ACSR and has an excellent balance between mechanical properties and electrical conductivity [21]. A major advantage of ACAR is the flexibility to adjust the relative number of 6201 strands to satisfy the particular requirement of strength and conductivity [21, 22]. It also displays excellent corrosion resistance [21].

The “Aluminum Conductor Composite Reinforced” (ACCR) invented by 3M consists of a composite core of continuous polycrystalline  $\text{-Al}_2\text{O}_3$  fiber (about 50 vol.%) within a matrix of substantially pure elemental aluminum or an alloy of aluminum with up to 2% weight copper [23]. As with the ACSR cable, the outer (enhanced conductivity) region of ACCR is composed of pure Al strands. The composite core has very high strength, excellent sag resistance and high temperature performance (up to  $240^\circ\text{C}$ ) due to the high strength and high stiffness of its aluminum oxide fiber reinforcement phase, although it has relatively high density ( $\sim 4\text{g/cm}^3$ ). Also aluminum oxide is non-conductive, which means that 50 vol. % of the Al matrix composite core is non-conductive. Moreover, the large mismatch of thermal expansion coefficient and elastic modulus between Al and  $\text{Al}_2\text{O}_3$  in the composite core, and between this core and its exterior pure Al strands make ACCR susceptible to similar thermal fatigue, spooling, and erection problems that occur with ACSR. Alternatively, “Aluminum Conductor Composite Core” (ACCC) invented by CTC Cable Corporation has a polymer

matrix/carbon+glass fiber reinforced composite core surrounded by at least one layer of stranded aluminum conductor [24, 25]. The hybrid epoxy/carbon+glass composite core was designed to have a high tensile strength, low coefficient of thermal expansion and high temperature sag resistance [25]. The drawback of ACCC again is the large difference of thermal expansion coefficient and elastic modulus between outer aluminum and composite core. The essentially non-conductive nature of the epoxy/carbon+glass composite core makes it even less energy efficient for DC transmission than ACCR. Trapezoidal wire (TW) is a common modification to replace conventional circular Al strands with trapezoidal strands. This shape modification increases the compactness of outer aluminum strands around the core, allowing 20-25% additional aluminum to be added to increase the current carrying capacity of the same diameter conductor by 8-10% for DC transmission [21]. TW has been applied as an optional cable configuration to all conductors discussed above.

#### A novel deformation processed Al/Ca composite conductor

The novel conductor Al/Ca composite proposed in this paper belongs to a class of composites called “Deformation Processed Metal-Metal Composites” (DMMCs), which are produced by severe plastic deformation of two ductile metal phases [26]. In DMMCs, the high ductility of two metal phases allows the compacted powder mixture to achieve a deformation true strain of 13.9 (a million-fold reduction in cross sectional area) without intermediate stress-relief annealing and without cracking [26]. The reinforcing filament thickness can be as low as 50 nm after extreme deformation [26, 27]. DMMCs display an excellent combination of high strength (2.2GPa) and high conductivity (85% IACS) in ref [27]. The high strength comes from the fact that the many closely spaced interphase

boundaries act as barriers to dislocation motion and may serve as sources for geometrically necessary dislocations that work harden the material [28, 29]. Many experimental results confirmed that the strength of DMMCs increased exponentially with the deformation true strain [27, 28, 30-33]. The high electrical conductivity is due to two nano-scale pure metal continuous phases acting as parallel conductive pathways that display little interphase boundary scattering to electrons travelling parallel to the wire axis [26]. Therefore, deformation processed Al/Ca composite can combine the advantages of creating the interphase boundary for high strength and maintaining continuous pure metal phases parallel to the wire axis for high conductivity.

The Al/Ca composite conductor has the potential to reduce tower construction costs and energy losses while increasing service life due to reliable performance even during emergency overload. Unlike ACSR that uses a heavy steel core to increase its strength, the Al/Ca composite is inherently strong enough to support its own weight with long span length between towers. A combination of high strength and low density, for example (in an estimate described later in this paper) 660 MPa and 2.47 g/cm<sup>3</sup> respectively for Al/Ca (20 vol. %), could allow wider tower spacing, which substantially reduces tower construction cost. Alternatively, with standard tower spacing, the Al/Ca composite conductor lines will be more resistant to wind and ice loading. In terms of emergency current overload performance, Ca has near zero solid solubility in Al even at high temperature because the large atomic radius difference between Al and Ca impedes inter-diffusive mixing during high-temperature exposure, avoiding the appreciable decrease of the conductivity of Al/Ca composite. Moreover, the microstructural stability and mechanical properties of Al/Ca composite at



elevated temperature should actually be improved by a refractory, high-melting  $\text{Al}_2\text{Ca}$  intermetallic compound (interfacial layer) that forms at interfaces approaching  $300^\circ\text{C}$  [33].

The well-known reactivity of Ca metal with water and oxygen suggests that Al/Ca composite might corrode when exposed to air and water. Simple immersion tests in various aqueous solutions and prolonged exposure to air at  $100^\circ\text{C}$  showed no difference between the long-term corrosion of Al/Ca composite and that of pure Al control specimens. The overwhelming majority of Ca filaments lie entirely inside the Al matrix, isolated from air or moisture. Ca filaments exposed on the conductor surface corrode quickly, leaving a pure aluminum surface that protects the internal Ca filaments from further corrosion. Therefore, the long-term corrosion behavior of Al/Ca composite is the same as that of pure Al. The similar thermal expansion coefficients of Al ( $23.6 \mu\text{m/m}\cdot^\circ\text{C}$ ) and Ca ( $22.8 \mu\text{m/m}\cdot^\circ\text{C}$ ) nearly eliminates the thermal fatigue problem present in ACSR, ACCR, and ACCC.

In the following sections, we will discuss the design process, production methods, properties and potential economic benefits of the new Al/Ca composite conductor. An additional thermal analysis was done to evaluate the effect of conductivity and cross section area of conducting wires on power carrying capacity of transmission line. Comparison will be made with other previously discussed conductors to evaluate the application prospects of Al/Ca DMMC cables for overhead long distance HVDC power transmission.

#### Application of Al/Ca Composite Conductor in HVDC Transmission

A typical HVDC system consists of two converter stations and the DC line, which converts the electrical current from AC to DC (rectifier) at the transmitting end and from DC to AC (inverter) at the receiving end [3]. Three factors have to be considered to build a new

HVDC transmission system: cost; technical performance; and reliability [1]. The cost of overhead line construction, right of way and operation and maintenance are much lower for HVDC, although the investment cost of HVDC converter stations is higher than the cost of AC substations [4]. For long distance overhead transmission, development of new, high-performance conductors is critical to reduce construction and maintenance costs, to increase energy transmission efficiency, and to increase reliability and service life [34].

## Design

The idea of developing Al/Ca composite conductor came from previous research on DMMCs, which exhibit an excellent combination of high strength and high conductivity [26, 27]. For example, in the extensively studied Cu-Nb DMMC, its extraordinarily high strength is greatly underestimated by a rule-of-mixtures estimation (volumetric weighted average) because Nb is not an exceptionally strong metal and would not be an ideal reinforcement material if the Cu/Nb composite obeyed the rule-of-mixtures model. Therefore, when we choose the potential metal candidate for a high-strength, high-conductivity DMMC as a conductor, the strength of the metal itself is a less important factor than ductility, density, conductivity and cost. High ductility allows the metal phase to deform extensively without any intermediate annealing to obtain a nanoscale filamentary microstructure that creates a large area of interfaces to strengthen the composite. High ductility also saves the cost of performing intermediate heat treatments. Low cost, and high conductivity are important properties for any conductor material, while low density is most critical for overhead conductors. The conductivity of DMMC can be roughly estimated by the rule-of-mixtures because the matrix metal and the filament metal act as parallel pathways for current flow.

However, there is a small electron scattering effect from filament-matrix interfaces since filament thickness is not perfectly uniform in the transverse direction.

Based on the above criteria, a list of metals ranked by conductivity was used (Table 1) to compare their density, cost, and corrosion behavior. It can be easily concluded that aluminum and calcium are the top two choices in terms of conductivity, cost, and density. The poor corrosion resistance of Ca is overcome by distributing Ca throughout the Al matrix to isolate Ca from air or moisture, as mentioned above. Our initial studies showed that both Al and Ca are highly ductile metals that allow deformation true strain up to 13.9 without any intermediate heat treatment [33]. Therefore, deformation processed Al/Ca composite has many desirable features and should be an excellent candidate for long-distance HVDC power transmission.

Table 1. A comparison of cost, density and corrosion resistance of potential electrical conductors at 20 °C [35].

Element	Conductivity (IACS)	Cost	Density(g/cm <sup>3</sup> )	Corrosion Resistance
Silver	105%	High	10.5	Very good
Copper	100%	Medium	8.9	Very good
Gold	80%	Very high	19.3	Excellent
<b>Aluminum</b>	<b>62-62.9%</b>	<b>Low</b>	<b>2.7</b>	<b>Very good</b>
<b>Calcium</b>	<b>48.7%</b>	<b>Medium</b>	<b>1.5</b>	<b>Poor</b>
Beryllium	38.9-43.1%	High	1.8	Good
Sodium	42%	Low	0.9	Very poor
Rhodium	40%	Very high	12.4	Excellent
Magnesium	37%	Low	1.7	Mediocre
Molybdenum	34%	Medium	10.3	Good
Iridium	32%	Very high	22.6	Excellent
Iron	19%	Low	7.9	Mediocre

## Production methods

An Al-9 vol% Ca DMMC was produced by powder metallurgy methods followed by severe mechanical deformation. The powder metallurgy process included blending selected elemental metal powders, loading and pressing the powder mixture into an Al canister, evacuating and sealing the canister, and sintering to consolidate the powders. The high-purity (99.99%, 20-45  $\mu\text{m}$ ) Al powder used was produced by a Gas Atomization Reaction Synthesis (GARS) process in the Ames Laboratory of the USDOE. GARS uses ultrahigh purity nitrogen gas for atomization of the molten Al stream to partially suppress the oxidation kinetics by creating a protective nitrogen atmosphere [36]. The reaction between nitrogen gas and the aluminum molten stream proved to be negligible due to the rapid solidification of liquid aluminum. The GARS-produced aluminum powders exhibited powder characteristics superior to commercial air atomization (CAA) and commercial inert gas atomization (CIGA) powders [36]. The very thin oxide surface film on GARS aluminum powder may enhance the development of metallurgical bonds during sintering. Commercially available high-purity Ca granules with an average particle size 1.2mm were blended with aluminum powder at a volume fraction of 91% Al and 9% Ca. The powder mixture was then loaded into a commercial-purity (1100) Al alloy can for compaction with a pressure of 6.55 to 8.73 MPa. The Al alloy can was sealed in a vacuum chamber by electron beam welding to protect the specimen from atmospheric contamination during the following hot extrusion and room temperature swaging. The warm extrusion was performed at 285 °C to provide a temperature high enough for dynamic recovery of both Al and Ca ( $0.4 T_m$ ), but low enough to avoid the formation of Al/Ca intermetallic compounds that could initiate cracks during extrusion. A pressure of 26.2 MPa was used to extrude the compacted powder mixture + Al can assembly

through a conical die with an 81.23mm inlet diameter and a 22.1mm outlet diameter. The extruded Al/Ca composite rod was water cooled to room temperature. The deformation true strain  $\eta$  of the specimen was calculated by

$$\eta = 2 \ln\left(\frac{d_0}{d_f}\right) \quad (1)$$

where  $d_0$  and  $d_f$  are the initial and final specimen diameters, respectively. A correction was made to account for the presence of an estimated initial 30% porosity of the compacted powder, because collapsing that porosity does not contribute to deformation true strain. The extruded rod was swaged at room temperature to a diameter of 6.35mm ( $\eta=4.86$ ) and then wire drawn to a diameter of 1 mm ( $\eta=8.55$ ). Wires were cut to 35mm lengths so they could be bundled and packed into a fully annealed Cu tube with an inside diameter of 25.4 mm. The bundled specimens were swaged to a diameter of 6.8 mm and wire drawn to a diameter of 1.7 mm ( $\eta=13.76$ ).

As mentioned above, calcium granules (1.2mm diameter) were used to process the Al-9%Ca composite because finer Ca powder is not available from any commercial vendor. As a preliminary attempt to generate smaller Ca powders, we utilized a rudimentary atomization method based on Raleigh stream instability to produce high-purity Ca powders with some finer size particles ( $\sim 300\mu\text{m}$  or smaller) (Fig.2). In this method, induction heating was used to melt calcium that exited through an orifice (diameter 0.5mm) by an overpressure of Ar gas on the sealed steel crucible. The liquid Ca break-up stream descended through an argon-filled glass cylinder and was captured in a quench bath that contained FisherBrand D19 (hydrocarbon based) mechanical vacuum pump oil to rapidly cool and solidify the Ca particles. The resulting Ca powder was then given six rinses in hexane to remove the pump oil. Two random Ca powder samples cleaned in hexane were suspended in absolute ethanol

for particle size distribution testing using Microtrac™ S3500 laser diffraction. A bimodal distribution (see Fig 3.) was observed in both samples with the median particle sizes found to be 372  $\mu\text{m}$  and 334  $\mu\text{m}$ , respectively. The bimodal distribution could be the result of the mixture of spherical and non-spherical particle shapes.

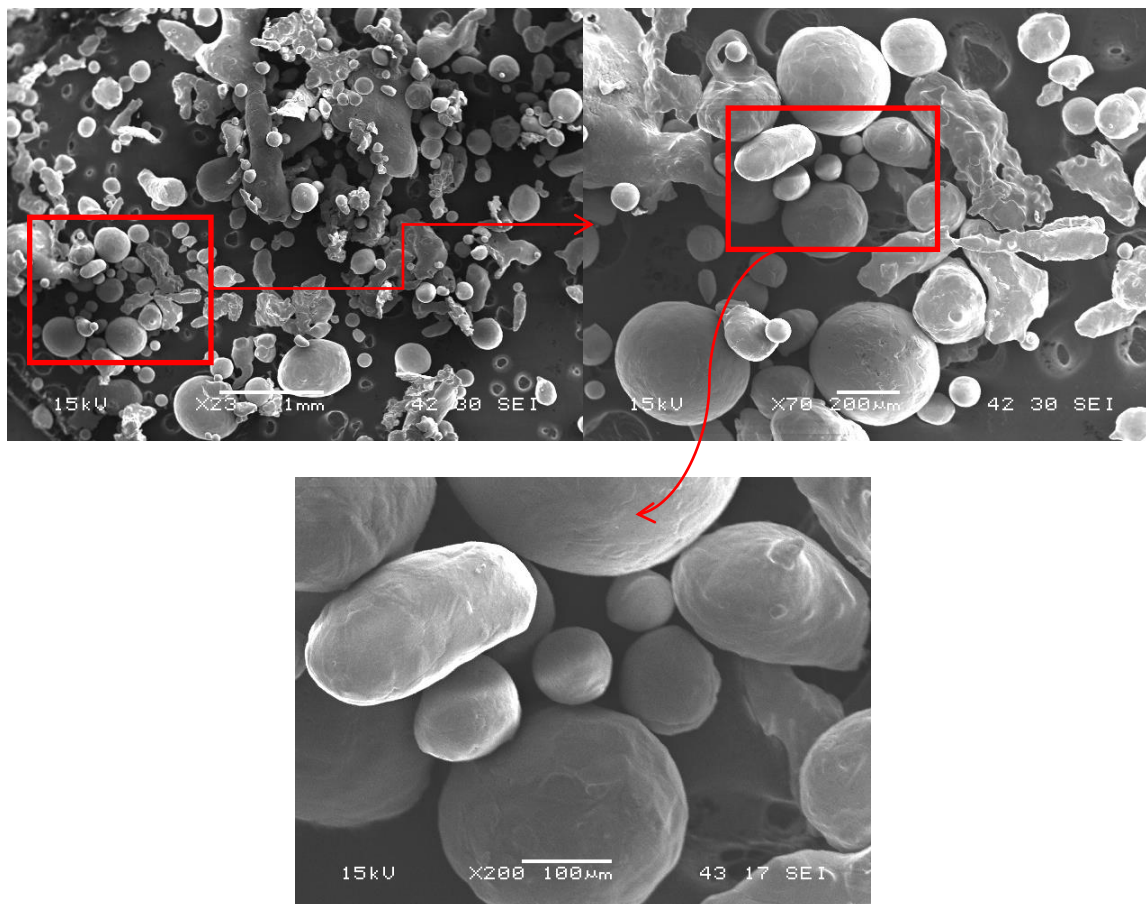


Fig 2. The scanning electron microscopy (SEM) micrographs of Ca powders produced by a Raleigh instability atomization method. The particle size distributions of these atomized Ca powders are shown in Fig. 3.

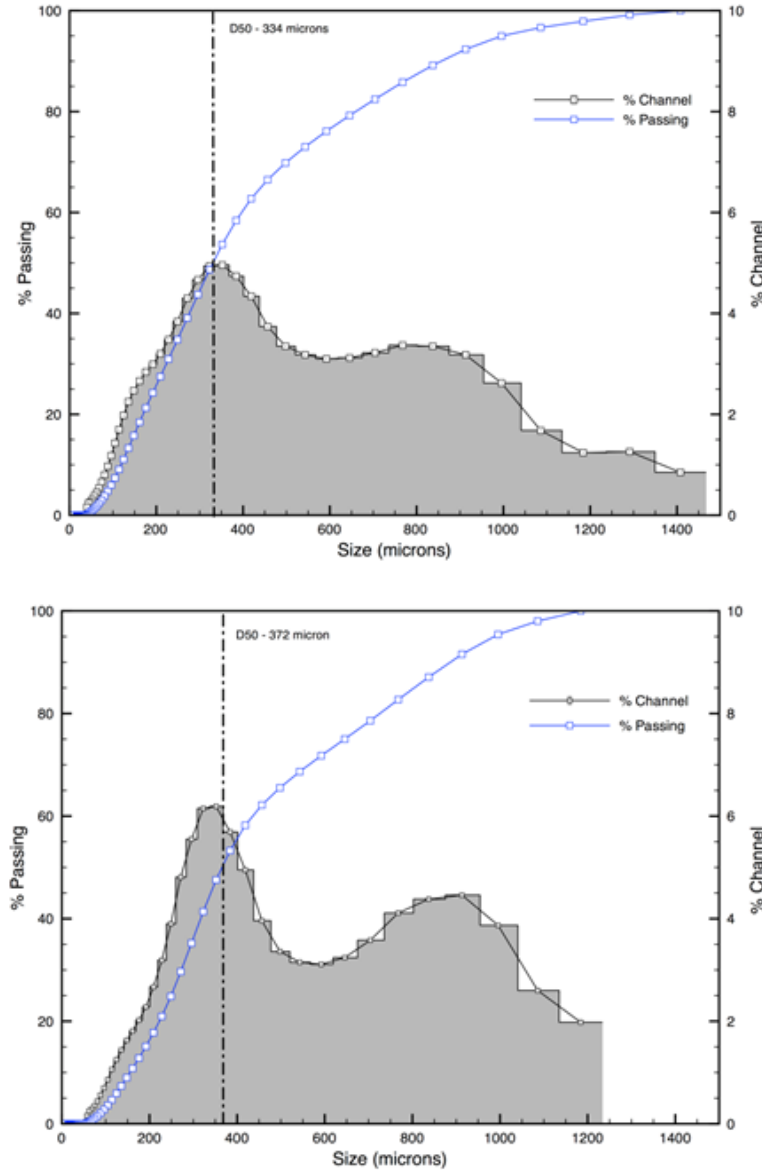


Fig. 3. The particle size distributions of two randomly sampled, as-atomized Ca powder samples measured by Microtrac<sup>TM</sup> S3500. The particle size medians of the two samples are 334  $\mu\text{m}$  and 372  $\mu\text{m}$ , respectively. The particles at the left of the vertical dashed lines are in the desired range for producing Al/Ca composites.

While these preliminary atomization trials demonstrated production of some Ca powder with the desired particle size range, we are also engaged in the fabrication of a rotating disk atomizer which uses a centrifugal atomization mechanism that should have the capability of generating much larger quantities of Ca powder with a more controlled particle

size. The new rotating disk atomizer will incorporate a rotating quench bath to allow it to be fairly compact. It is planned that we will utilize the same quench fluid and it is fortunate that we already have a procedure for cleaning this oil from the particles. Thus, larger quantities of Ca powders from this rotating disk atomizer with size less than about 300  $\mu\text{m}$  will be used to produce Al/Ca composite. This method is currently undergoing further development to optimize the atomization parameters and scale up quantities.

### Properties

Conductor material with superior mechanical and electrical properties would allow construction and operation of overhead HVDC power transmission line with reduced construction cost, reduced transmission losses, and extended service life [34]. The rule-of-mixture densities of Al-9 vol% Ca and Al-20 vol% Ca are 2.6  $\text{g/cm}^3$  and 2.47  $\text{g/cm}^3$ . Both of these values are much lower than ACSR (3.42  $\text{g/cm}^3$ ). Conductor strength and weight are both important factors in determining the maximum safe spacing of support towers for overhead power lines, as shown in the equation for the largest safe spacing ( $l$ ) for power line support towers:  $l = \frac{\sigma_y \sin(2\theta)}{\rho g}$ , where  $\sigma_y$  is the conductor's yield strength,  $\theta$  is the angle between the line tension vector and the horizontal,  $\rho$  is the conductor's density, and  $g$  is gravitational acceleration (9.81  $\text{m/s}^2$ ). This expression shows that tower spacing varies directly with conductor strength and inversely with conductor density. The best conductor to minimize construction costs (wide tower spacing) would possess high strength and low density.

A light, strong conductor also reduces sag, and improves resistance to wind or ice loading. In this section, the strength, electrical conductivity, and elevated temperature



performance of Al/Ca composite will be discussed; each factor plays a vital role in improving system energy efficiency, cost saving, and reliability.

### 1. Strength

The mechanical properties of deformation processed metal-metal composite are strongly dependent on the filament thickness  $t$  or spacing  $\lambda$ , which is determined by deformation true strain  $\eta$  [30-32]. In order to investigate this relation for Al-9 vol. % Ca, the Ca filament thickness of specimens with  $\eta=6.27, 8.55, 12.45, 13.76$  was measured from the microstructure images taken by a JOEL JSM-606LV scanning electron microscope. At least two tensile tests were performed on each specimen to get ultimate tensile strength (UTS) for each  $\eta$ . Table 2 shows the Ca filament thickness and UTS of Al-9 vol. % Ca at  $\eta=6.27, 8.55, 12.45, 13.76$ . Fig. 4 shows the relation between UTS and Ca filament thickness for Al-9 vol% Ca. It can be easily concluded that the UTS of Al-9 vol% Ca correlates well with Ca filament thickness  $t$  by a Hall-Petch relation:

$$UTS = 77.69 + \frac{181.6}{\sqrt{t}} \quad (2)$$

When filament thickness decreases into the nanometer regime, the UTS of the Al-9 vol% Ca composite would be expected to rise substantially. However, due to the large size (1.2mm) of the initial Ca granules used to make this composite, the Ca filament thickness is only in the micrometer regime after being subjected to a deformation true strain 13.76.

By using the rotating disk (centrifugal) atomization method to produce finer Ca powder (100 to 300  $\mu\text{m}$ ), Ca filament thickness between 100nm and 300nm should be obtained after a deformation true strain 13.76. In such an extrapolation, a UTS of approximately 484 MPa can be expected for an Al-9 vol% Ca composite that starts with fine

Ca powder. This intensive strengthening effect is due to the large interface area of ultrafine Ca filaments [28, 29]. These interfaces act as a barrier to dislocation motion [28] and as a source to generate geometrically necessary dislocations to accommodate strain incompatibility between fiber and matrix for hardening [29]. We can estimate the UTS of Al-20 vol% Ca with an average 200nm filament thickness by using Taylor's hardening law  $\sigma_Y = \sigma_0 + m\alpha Gb\sqrt{\rho}$ , where  $\sigma_y$  is the yield strength,  $m$  is Taylor orientation factor,  $\alpha$  is geometrical factor,  $G$  is shear modulus,  $b$  is Burgers vector, and  $\rho$  is the total dislocation density [37]. The interface area of Al-20 vol% Ca will be roughly 2.2 times that of Al-9vol% Ca with the same filament thickness. The incremental strength due to cold-worked Al or Ca is around 130 MPa, which should be the same in both Al-9 vol% Ca and Al-20 vol% Ca [38]. Under a reasonable assumption that the interface induced dislocation density is proportional to the interface area, the UTS of Al-20 vol% Ca with an average 200 nm filament thickness will be around 660 MPa. Further experimental work is needed to test the predictions from these models, but UTS values as high as 890 MPa have been observed in other Al-matrix nanocomposites, such as Al-20 vol% Ti [30].

Table 2. Experimentally measured mechanical properties and Ca filament thicknesses for Al-9 vol% Ca specimens at  $\eta=6.27, 8.55, 12.45, 13.76$  [39].

Deformation true strain $\eta$	Filament thickness $t$ ( $\mu m$ )	UTS (MPa)	Maximum strain before fracture (%)
6.27	60	93	13
8.55	9	145	18
12.45	4	179	16
13.76	2	197	16

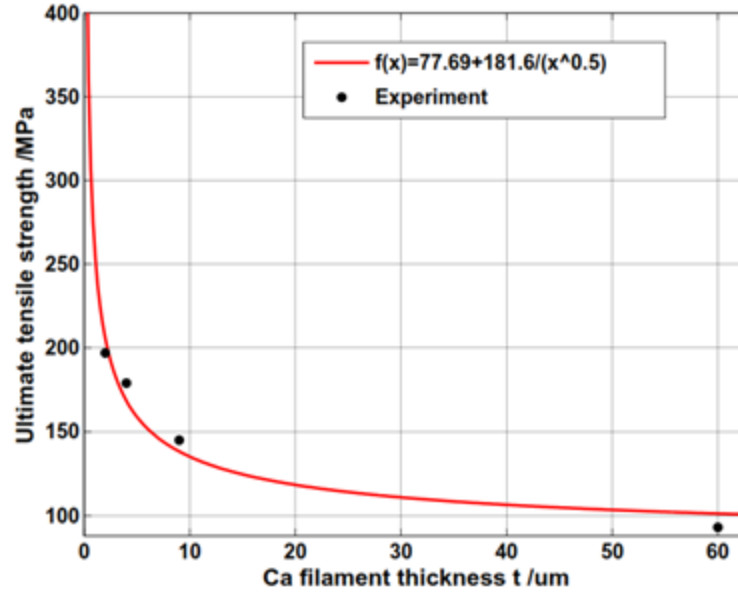


Fig. 4. Ultimate tensile strength as a function of Ca filament thickness  $t$  for Al-9 vol% Ca.

## 2. Electrical conductivity

Four-point resistivity measurements were performed by a Keithley Model 580 micro-ohmmeter with Model 5804 test leads to test the room temperature electrical conductivity of Al-9vol% Ca with  $\eta=8.55$  after heat treatment at  $300^\circ\text{C}$  for various lengths of time. Table 3 shows the conductivity of Al-9 vol% Ca with  $\eta=8.55$  heat-treated at different time. The conductivity of Al/Ca composite does not strongly depend on the deformation true strain as long as the Ca filament thickness is uniform in the longitudinal direction. The rule of mixture model can predict the conductivity of Al-9 vol% Ca very well. After heat treatment at  $300^\circ\text{C}$ , the conductivity of Al-9vol% Ca decreased slightly due to the formation of small amounts of  $\text{Al}_2\text{Ca}$  at the Al/Ca interfaces, which was confirmed later by X-ray diffraction analysis. The presence of hard  $\text{Al}_2\text{Ca}$  phase created a local stress field and slightly increased the scattering of electrons and hence increased resistivity. However, the formation of  $\text{Al}_2\text{Ca}$  would stabilize the filament shape against spheroidization and coarsening that would

otherwise substantially decrease the conductivity of Al/Ca composite after exposure to very high operating temperatures. On the whole, the formation of  $\text{Al}_2\text{Ca}$  in Al/Ca composite at elevated temperature is expected to bring more benefits than drawbacks, thereby making the Al/Ca composite a “smart” material with a favorable “defensive” response to high temperatures.

Table 3. The room temperature electrical conductivity of Al-9 vol% Ca at  $\eta=8.55$  after various heat treatment time at  $300^\circ\text{C}$ . For comparison, the electrical conductivity of pure Al is  $38 (\mu\Omega\cdot\text{m})^{-1}$ .

Heat treatment time (min) at $300^\circ\text{C}$	Electrical conductivity $((\mu\Omega\cdot\text{m})^{-1})$ at $22^\circ\text{C}$
0	36.6
5	36.6
15	34.8
30	34.8
60	33.3
180	33.3
720	33.3

### 3. Elevated temperature performance

The performance of conductor materials at elevated temperature is important when emergency overload situations occur. Unlike all previous conductors subject to loss of strength at elevated temperature [40], the elevated temperature strength of Al/Ca composite was improved by forming  $\text{Al}_2\text{Ca}$  intermetallic compound at the interfaces (see Fig. 5.(a)) [33]. The formation of  $\text{Al}_2\text{Ca}$  was verified by X-ray diffraction (see Fig. 5. (b)).  $\text{Al}_2\text{Ca}$  is a high-melting phase ( $1075^\circ\text{C}$ ) [41] and is more stable at elevated temperature than Ca, giving Al/Ca composite better hot strength and creep resistance. The formation of  $\text{Al}_2\text{Ca}$  at the interfaces is expected to stabilize the shape of the Ca filaments against spheroidization and coarsening, which can degrade the strength and conductivity of nanofilamentary metal-metal composites [32]. This smart response to elevated temperature will minimize damage to the

composite from emergency overload situations. The presence of  $\text{Al}_2\text{Ca}$  is expected to act as a stabilizing mechanism to retain the high strength and high conductivity of the composite at elevated temperature.

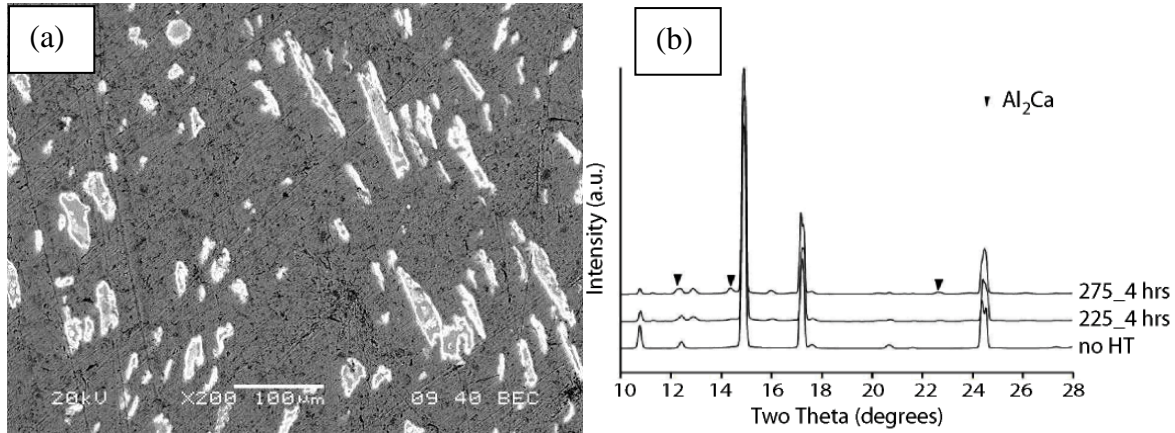


Fig. 5. (a) Back-scattered electron SEM micrograph of transverse section of Al-9 vol% Ca after heat treatment at 325°C for 1h. The Al matrix is dark. The Ca filaments are medium gray. The bright region surrounding the Ca filaments is comprised of  $\text{Al}_2\text{Ca}$ . (b) X-ray diffraction results of specimens at  $\eta=6.27$  after different heat treatment: non-heat treated (noHT), heat treated at 225°C for 4h (225\_4 hrs), heat treated at 275°C for 4h (275\_4 hrs).

#### Economic Analysis of Al/Ca Composite Conductor in Building HVDC Transmission System

The cost of a HVDC transmission line includes the initial investment costs and the operational costs [1]. The investment includes transmission towers, conductors, right of way and converter stations. The operational costs are mainly electrical energy losses on transmission lines but also include infrequent, unpredictable, and potentially expensive damage from wind or ice loading. In this section, we discuss how conductor materials' properties improvements could reduce tower construction cost, electrical energy losses and material cost by an increased service life. In addition, a thermal analysis was done to investigate the effect of material properties on the temperature increase during the emergency overload. A commonly used bipolar HVDC configuration in long distance bulk power transmission is used as an example to illustrate the economic benefits of Al/Ca composite

[3]. The HVDC system will still function properly if electrical outage occurs in only one pole by adopting the other half of bipolar configuration.

#### Comparison of properties Al/Ca with other conductors

Table 4 compares the anticipated density, strength and DC electrical conductivity of Al/Ca composite with four other commonly used conductors. Since there is no skin effect for DC transmission, the DC conductivities of ACSR and ACAR are lower than their AC conductivity. The presence of solute alloy atoms and possible precipitates increases electron scattering and lowers the conductivity of AAAC. The conductivity of ACCC/TW is relatively higher because only 12% of its cross sectional area is comprised of the very strong but poorly conductive composite core used to reinforce the conductor [25]. The strength of ACSR is good, but the heavy steel core places high demands on tower construction and transmission line installation. ACCC/TW has a good combination of mechanical and electrical properties. However, the polymer composite core at elevated temperature poses a high risk for degradation. The Al/Ca composite under development at Ames Laboratory is expected to be twice as strong as ACCC/TW, while pushing the DC conductivity higher than that of alternative conductors and lowering the density to 9% less than pure Al. The high strength at elevated temperature due to formation of  $\text{Al}_2\text{Ca}$  and nearly identical thermal expansion coefficients of Al and Ca will improve the mechanical and thermal fatigue resistance of Al/Ca composite even during overload. In the next 15 years, up to 1.5 trillion dollars could be spent on construction of new power transmission and distribution system in the U.S [42]. Successful development of Al/Ca composite could reduce construction costs and increase reliability of future power transmission grids.

Table 4. Comparison of the properties of Al/Ca composite with four commonly used conductors. Note: \* is estimated by rule of mixture. \*\* is estimated by the Hall-Petch model in the previous strength section.

Conductors	Density (g/cm <sup>3</sup> )	Strength (MPa)	DC Conductivity at 20°C (( $\mu\Omega \cdot m$ ) <sup>-1</sup> )	Elastic modulus (GPa)
ACSR	3.43 [22, 25]	304 [22]	28.1 [22]	85 <sup>a</sup>
AAAC	2.74 [22]	312 [22]	29.4 [22]	69 [44]
ACAR	2.74 [22]	251 [22]	31.7 [22]	69 [44]
ACCC/TW	2.612 [25]	345.1 [25]	34.8 [43]	57 [25]
Al-20vol.%Ca <sub>f</sub> Composite	2.47 <sup>a</sup>	660 <sup>b</sup>	36.2	60 <sup>a</sup>

#### Effect of conductor properties on cost of tower construction and energy loss

A simple model was used in this section to illustrate how conductor material properties would affect the construction cost and energy losses. Though we consider many key parameters that would affect the construction cost, this model is a rough estimation and not an accurate calculation of every related cost. What's more, our attention was focused on selecting the best conductor materials to reduce the cost for building HVDC transmission system. So the cost of converter stations should be irrelevant to the conductor material and treated as a constant. Though the conductor material may affect the cost of auxiliary systems, labor and maintenance, we do not consider these factors because these costs are only a small part of the total cost and are more dependent on geography than on the conductor material.

Suppose that we want to deliver electricity from point A to point B with an overhead 500kv, 1500km transmission line. After a simple mechanical analysis, the largest safe tower spacing distance  $l$  (see Fig. 6) is approximated by

$$l = \frac{\sigma_y \sin(2\theta)}{\rho g} \quad (3)$$

where  $\sigma_y$  is the yield strength of the conductor,  $\theta$  is the angle between line tension and horizontal,  $\rho$  is the density of the conductor and  $g$  is the gravitational acceleration.



Fig. 6. A schematic showing the safe tower spacing for an overhead power transmission line.

The current total length of the conducting wires is roughly  $\frac{2L}{\cos(\theta)}$  due to bipolar transmission. The initial total length  $L_0$  of the conducting wires is given by

$$L_0 = \frac{2L}{\cos(\theta)} \exp \frac{-\sigma_y}{E} \quad (4)$$

where  $L$  is the transmission distance between two cities,  $E$  is the elastic modulus of the conductor. The construction cost for each tower is  $M$ , assumed as a constant independent of conductor type. The material cost of conducting wire is  $W$  per meter for a fixed optimum cross sectional area. Therefore, the total construction cost for transmission towers and lines is given by

$$M * \frac{L}{l} + W * L_0 = \frac{\rho g L M}{\sigma_y \sin(2\theta)} + \frac{2LW \exp(\frac{-\sigma_y}{E})}{\cos(\theta)} \quad (5)$$

An optimum  $\theta$  can be found to minimize the total construction cost. A typical  $\theta$  can be calculated as  $33.68^\circ$  by the following setting:

$$L = 1500\text{km}, \sigma_y = 300\text{MPa}, E = 70\text{GPa}, g = 9.8 \frac{\text{m}}{\text{s}^2}, \rho = 2.7 \frac{\text{g}}{\text{cm}^3}, M = 200,000\$, W = 10 \$/\text{m}$$

The effect of strength, density and elastic modulus on the minimum construction cost was



investigated to verify the economic benefits of Al/Ca composite. Fig. 7. shows the variation of strength, density and elastic modulus on the minimum construction cost. The typical values chosen for calculation follow the same setting as above except that  $\sigma_y, \rho, E$  will be variables. It can be easily concluded that a high strength and low density conductor material can lower the total construction cost substantially, as shown in Fig. 7. The elastic modulus has negligible effect on the total construction cost, which matches the discussion in ref [34]. Life cycle costs are difficult to calculate with the data available today; obviously, for Al-Ca composite conductor, construction plus operating costs must be appreciably lower than those of ACSR if this new technology is to be competitive. Experiments being conducted in 2013-14 will provide information needed to develop reliable construction and life cycle cost estimates.

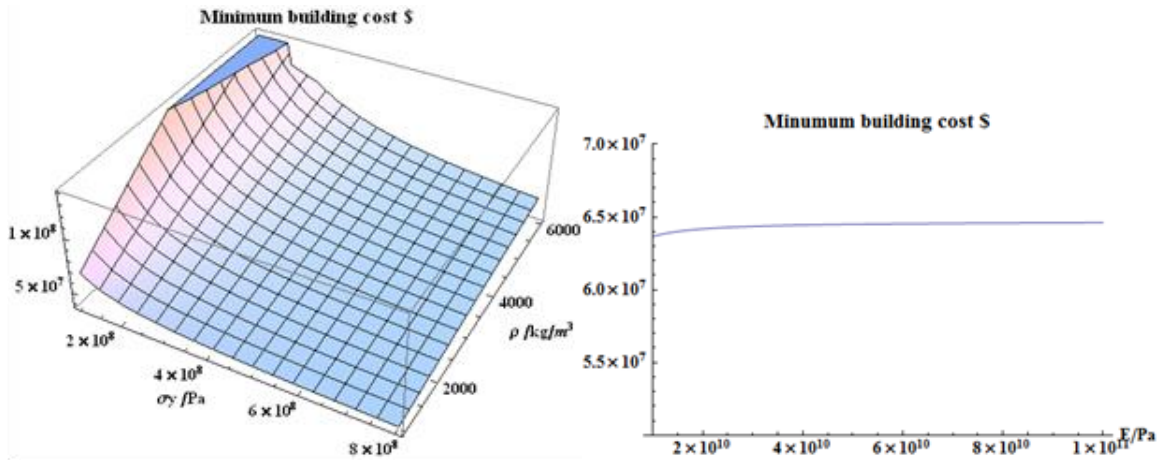


Fig. 7. The effect of density ( $\rho$ ), strength ( $\sigma_y$ ) and elastic modulus ( $E$ ) on the minimum construction costs of an HVDC system.

Table 5 gives a comparison of the total number of towers, total construction cost and annual electrical energy loss between Al/Ca composite conductor and four other conductors.

The calculation was done under a typical optimum  $\theta = 33.68^\circ$ . The calculation of total

number of towers and total construction cost is based on eq. (3) and (5), respectively. The total number of towers by using Al/Ca composite is almost 1/3 of that by using ACSR and 1/2 of that by using ACCC/TW, which would be a huge contribution to reduce the total construction cost as seen in Table 5. The relatively high cost of Al/Ca composite is easily compensated by the substantial reduction in tower construction. The electrical energy loss

power is calculated by  $I^2R = (\frac{P}{2U})^2 \frac{2L}{\sigma A \cos(\theta)}$ , where  $P$  is the total transmission power,  $U$  is the transmission voltage,  $\sigma$  is the conductivity of the conductor and  $A$  is the cross sectional area of the conductor. A conductor with large  $A$  is always expensive due to both the material consumption and the complex manufacturing process, which makes it hard to use a mathematical model to describe the cost variation with respect to  $A$ . The electrical energy loss will be reduced by using conductors with large cross sectional area. Therefore, there should be an optimum  $A$  depending on specific transmission requirements, conductor material properties, cost and the manufacturing process. A fixed  $A = 700\text{mm}^2$  is chosen to simplify calculation to compare the electrical energy loss of different conductors. Other values are set up as:  $P = 3000\text{MW}$ ,  $U = 500\text{kV}$ ,  $L = 1500\text{km}$ ,  $\theta = 33.68^\circ$ . The conductivity data are from Table 4. The results in Table 5 showed that the annual energy loss for Al/Ca composite conductor can be  $3.23 \times 10^9$  kWh less than that of ACSR. If the price of electricity is 8 cents/ kWh, the saving would be 258 million dollars. Therefore, it is easily seen that the Al/Ca composite conductor can bring great economic benefits by reducing construction cost and energy waste cost compared with all previously developed conductors.

Table 5. Comparison of material cost, total number of towers, total construction cost and annual electrical energy loss between Al/Ca composite conductor and four other conductors for a 500kv, 3000MW, 1500km overhead HVDC transmission line. Note: a and b are

estimated by 2 times and 2.5 times the cost of ACSR, respectively. The calculations are done based on the properties from Table 4.

Conductor	W Material cost \$/m	Total number of towers	Total construction cost (\$)	Annual electrical energy loss (kWh)
ACSR	10.3 [45]	179.712	$7.29417 \times 10^7$	$1.445 \times 10^{10}$
AAAC	7.5 [45]	139.879	$6.49717 \times 10^7$	$1.381 \times 10^{10}$
ACAR	8.4 [45]	173.873	$7.17971 \times 10^7$	$1.281 \times 10^{10}$
ACCC/TW	20.6 <sup>a</sup>	120.59	$6.10995 \times 10^7$	$1.167 \times 10^{10}$
Al-20 vol% Ca composite	25.7 <sup>b</sup>	59.6085	$4.87665 \times 10^7$	$1.122 \times 10^{10}$

#### Thermal considerations during emergency overload

During emergency overload situations, the Joule heating effect causes an obvious temperature increase in the conducting wire. This temperature increase should pose a constraint to the maximum power that can be transferred, which may depend on the conductivity and geometry of the conducting wires. It is our purpose in this section to investigate this relation by a simple heat balance model. This model neglects heat absorbed from solar radiation and heat released by the conductor's own radiation due to their unpredictability and small contribution to total heat transfer. Besides, thermal expansion is neglected in this model due to relatively small coefficient of thermal expansion of conductor wires. Therefore, this model is simplified to catch the main features affecting the thermal equilibrium of conducting wires, but it neglects the sag problem that accompanies conductor heating.

The heat generation rate by Joule heating is given by  $\left(\frac{P}{2U}\right)^2 \frac{l}{A} r_0 [1 + \alpha(T - T_0)]$ , where  $l$  is the current length of conducting wires,  $r_0$  is the resistivity of conductor at initial temperature  $T_0$ ,  $T$  is the current temperature,  $\alpha$  is the temperature coefficient of resistivity.

Here we assume that the temperature is homogeneous in the conducting wires. The heat dissipation includes two parts. The first part is used to increase temperature of the conductor wires, given as  $C_p \rho A l \frac{dT}{dt}$ , where  $C_p$  is the specific heat of the conductor material,  $\frac{dT}{dt}$  is the current temperature changing rate. The second part is natural convective heat transfer at the conductor surface, which is described by Newton's law of cooling as  $\beta * 2\sqrt{\pi A} * l * (T - T_0)$ , where  $\beta$  is the convective heat transfer coefficient,  $T_0$  is the atmosphere temperature or the initial temperature of the conductor before any Joule heating occurs. Heat balance requires that heat generation rate is equal to heat dissipation rate, given as

$$\left(\frac{P}{2U}\right)^2 \frac{l}{A} r_0 [1 + \alpha(T - T_0)] = C_p \rho A l \frac{dT}{dt} + \beta * 2\sqrt{\pi A} * l * (T - T_0) \quad (6)$$

Eq. (6) is a first-order ordinary differential equation. In order to reach an equilibrium temperature instead of rising to infinity, the following condition must be satisfied:

$$\left(\frac{P}{2U}\right)^2 * r_0 * \frac{\alpha}{A} - 2\beta * \sqrt{\pi A} < 0 \quad (7)$$

Obviously, inequality (7) poses a power transfer limit for different  $r_0$  and  $A$ . Satisfying inequality (7) guarantees only that the temperature of the conducting wires will reach equilibrium after a sufficient amount of time. However, it is also clear that for real power transmission, a restriction in maximum operation temperature or equilibrium temperature  $T_{eq}$  should pose a much lower power transfer limit. From Eq (6), we obtained

$$T_{eq} = T_0 + \frac{\left(\frac{P}{2U}\right)^2 \frac{r_0}{A}}{2\beta\sqrt{\pi A} - \alpha\left(\frac{P}{2U}\right)^2 \frac{r_0}{A}} \quad (8)$$

For most conductors, we require that maximum operation temperature  $T_{eq} \leq 100^\circ\text{C}$ . Fig. 8 gives the power transfer limit  $P_{max}$  ( $T_{eq}=100^\circ\text{C}$ ) or maximum operation temperature  $T_{eq}$  ( $P_{max}=3000\text{MW}$ ) as a function of  $r_0$  and  $A$  according to eq. (8). The numerical values setting is  $U=500\text{kV}$ ,  $\beta=25\text{ W}/(\text{m}^2*\text{K})$ ,  $\alpha=0.00429\text{ K}^{-1}$ ,  $T_0=20^\circ\text{C}$ . It can be easily concluded

that a high conductivity and large cross section area of conducting wires will increase the power carrying capacity. The low density and high strength of Al/Ca composite will allow a larger diameter stranded conductor to be installed. Therefore, a combination of superior conductivity and large cross section area of Al/Ca composite conductor will boost the power carrying capacity of HVDC transmission line under a specified maximum  $T_{eq}$  or conversely, lower the maximum  $T_{eq}$  under a specified amount of power transferred, which substantially reduces the risk of power failure from overload situations.

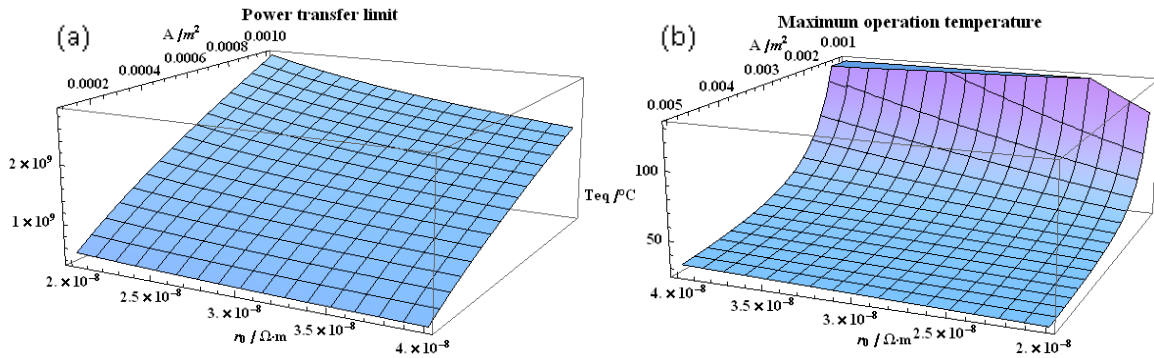


Fig. 8. (a) Power transfer limit  $P_{max}$  as a function of  $r_0$  and  $A$  under  $T_{eq} = 100^{\circ}C$ . (b) Maximum operation temperature  $T_{eq}$  as a function of  $r_0$  and  $A$  under  $P_{max} = 3000MW$ .

## Conclusions

In this paper, we introduced a novel lightweight, high strength, high conductivity Al/Ca composite, which may prove to be superior to any previously developed conductors. The Al/Ca composite is produced by powder metallurgy and severe plastic deformation. A simple Ca powder production method–Rayleigh atomization was adopted to obtain initial Ca powders with an average size of 300  $\mu m$ . After axisymmetric deformation to a true strain of

13.76, sufficient quantities of these fine Ca powders will deform to nanoscale filaments embedded inside Al matrix.

Underestimated by the conventional rule of mixture model, the strength of Al/Ca composite shows a Hall-Petch relation with filament thickness. The decreased filament thickness should create a large amount of interface area, which acts as the strengthening mechanism in DMMCs. The uniform Ca nanofilaments lying parallel to the wire axis act as parallel conductive pathways, and the interface plays a negligible role in the scattering of electrons, which should lead to the high conductivity of Al/Ca composite. Moreover, the excellent resistance to corrosion and fatigue (thermal and mechanical) of Al/Ca composite makes it a nearly ideal candidate for overhead HVDC power transmission. Besides, the formation of  $\text{Al}_2\text{Ca}$  observed at elevated temperature can stabilize the microstructure against filament spheroidization and coarsening and therefore retain both high strength and high conductivity during emergency overload. Additional research are needed to further investigate the fatigue and creep behavior of the composite, the strength and conductivity of the composite varying with Ca volume fraction, fracture toughness over the temperature range of  $-40\text{ }^{\circ}\text{C}$  to  $200\text{ }^{\circ}\text{C}$ , more complete characterization of the reaction kinetics of aluminum calcium intermetallics, the coronal discharge behavior of this material, etc.

The predicted superior properties of Al-Ca composites should lead to a substantial reduction in construction cost, energy loss cost and an increase in reliability and service life of the transmission line. A simple economic analysis was done to show how a low density, high strength, high conductivity conductor would reduce construction and energy loss cost. A thermal analysis was performed to show how high conductivity and large cross sectional area will be beneficial to lower the equilibrium temperature during emergency overload

situations or to increase the maximum power-carrying capacity under a specified maximum operation temperature. Therefore, in terms of economics, performance and reliability, the application prospects for Al/Ca composite wires are promising and deserves continued development work from both industrial partners and research institutions.

### References

1. Padiyar KR. HVDC Power Transmission Systems 2nd edi. Tunbridge Wells, Kent, UK: New Academic Science, 2011.
2. <http://news.nationalgeographic.com/news/energy/2012/12/121206-high-voltage-dc-breakthrough/>
3. Setreus J, Bertling L. Introduction to HVDC Technology for Reliable Electrical Power Systems. In: the 10th International Conference on Probabilistic Methods Applied to Power Systems. Rincon, May, 2008.
4. Cole S, Hertem DV, Meeus L, Belmans R. Technical Developments for the Future Transmission Grid. In: International Conference on Future Power Systems. Amsterdam, Nov, 2005.
5. Rudervall R, Charpentier JP, Sharma R. High Voltage Direct Current (HVDC) Transmission Systems Technology Review paper. In: Energy Week 2000. Washington, March, 2000.
6. Agelidis VG, Demetriades GD, Flourentzou N. Recent Advances in High-Voltage Direct-Current Power Transmission Systems. In: IEEE international conference on Industrial Technology. Mumbai, Dec, 2006. p.206-213.
7. Monsur N, Sood VK, Lopes L. Modeling a Hybrid Diode-Thyristor HVDC rectifier in EMTP-RV. In: Canadian Conference on Electrical and Computer Engineering. Ottawa, May, 2006. p.1258-1262.
8. Arrillaga J. High voltage direct current transmission. London, UK: Peter Peregrinus Ltd, 1983.
9. Adamson C, Hingorani NG. High Voltage Direct Current Power Transmission. London, England: Garraway, 1960.
10. Adams HW. Steel Supported Aluminum Overhead Conductors. U.S. Patent 3,813,481, Issued 1974.

11. Zhou ZR, Cardou A, Goudreau S, Fiset M. Fundamental investigations of electrical conductor fretting fatigue. *Tribolog Int* 1996;29(3):221–232.
12. Zhou ZR, Cardou A, Fiset M, Goudreau S. Fretting fatigue in electrical transmission lines. *Wear* 1994;173(1-2):179–188.
13. Azevedoa CRF, Henriquesb AMD, Pulino Filhoc AR, Ferreirab JLA, Araújo JA. Fretting fatigue in overhead conductors: Rig design and failure analysis of a Grosbeak aluminium cable steel reinforced conductor. *Eng Fail Anal* 2009;16(1):136–151.
14. Azevedoa CRF, Cescon T. Failure analysis of aluminum cable steel reinforced (ACSR) conductor of the transmission line crossing the Paraná River. *Eng Fail Anal* 2002; 9(6):645–664.
15. Aggarwal RK, Johns AT, Jayasinghe JASB, Su W. An overview of the condition monitoring of overhead lines. *Electr Pow Syst Res* 2000; 53(1):15–22.
16. Lyon SB, Thompson GE, Johnson JB, Wood GC, Ferguson JM. Accelerated Atmospheric Corrosion Testing Using a Cyclic Wet/Dry Exposure Test: Aluminum, Galvanized Steel, and Steel. *Corrosion* 1987; 43(12):719-726.
17. <http://www.aflglobal.com/Products/Aluminum-Clad-Steel.aspx>
18. Karabay S, Önder FK. An approach for analysis in refurbishment of existing conventional HV-ACSR transmission line with AAAC. *Electr Pow Syst Res* 2004; 72(2):179–185.
19. Karabay S. Influence of AlB<sub>2</sub> compound on elimination of incoherent precipitation in artificial aging of wires drawn from redraw rod extruded from billets cast of alloy AA-6101 by vertical direct chill casting. *Mater Design* 2008; 29(7):1364–1375.
20. Boniardi M, Cincera S, D'Errico F, Tagliabue C. Fretting fatigue phenomenon on an all Aluminium Alloy Conductor. *Key Eng Mat* 2007; 348-349: 5-8.
21. Hesterlee JM. Bare Overhead Transmission and Distribution Conductor Design Overview. *IEEE T Ind Appl* 1996; 32(3):709-713.
22. Kumar D, Jain GC, Agrawal VK. ACAR conductors-a techno-economic evaluation. In: *Symposium on Metallurgy of Substitute Ferrous & Non-Ferrous Alloys*. Jamshedpur, April, 1966. p. 214-220.
23. McCullough C et al. Fiber reinforced aluminum matrix composite wire. U.S. patent 6,544,645. Issued 2003.



24. Bryant D et al. Aluminum conductor composite core reinforced cable and method of manufacture. U.S. patent 7,438,971. Issued 2008.
25. Alawar A, Bosze EJ, Nutt SR. A composite core conductor for low sag at high temperature. *IEEE T Power Deliver* 2005;20(3):2193-2199.
26. Russell AM, Chumbley LS, Tian Y. Deformation Processed Metal-Metal Composites. *Adv Eng Mater* 2000;2(1-2):11-22.
27. Bevk J, Harbison JP, Bell JL. Anomalous increase in strength of in-situ formed Cu-Nb multifilamentary composites. *J Appl Phys* 1978; 49(12):6031-6038.
28. Spitzig WA, Pelton AR, Laabs FC. Characterization of the strength and microstructure of heavily cold worked Cu-Nb Composites. *Acta metall* 1987; 35(10):2427-2442.
29. Funkenbusch PD, Courtney TH. On the strength of heavily cold worked in situ composites. *Acta metall* 1985; 33(5):913-922.
30. Russell AM, Lund T, Chumbley LS, Laabs FA, Keehner LL, Harringa JL. A high-strength, high-conductivity Al-Ti deformation processed metal metal matrix composite. *Composites, Part A* 1999; 30(3):239-247.
31. Xu K, Russell AM, Chumbley LS, Laabs FC. Characterization of strength and microstructure in deformation processed Al-Mg composites. *J Mater Sci* 1999; 34(24):5955-5959.
32. Xu K, Wongpreedee K, Russell AM. Microstructure and strength of a deformation processed Al-20%Sn in situ composite. *J Mater Sci* 2002; 37(24): 5209-5214.
33. Tian L, Kim H, Anderson I, Russell AM. The microstructure-strength relationship in a deformation processed Al-Ca composite. *Mater Sci Eng A* 2013; 570: 106–113.
34. Douglass DA. Economic measures of bare overhead conductor characteristics. *IEEE T Power Deliver* 1988; 3(2): 754-761.
35. Ross RB. *Metallic Materials Specification Handbook*. New York: E. &F. N. Spon Ltd, 1980.
36. Flumerfelt JF. Aluminum powder metallurgy processing. In: PhD thesis submitted to Iowa State University. Ames, Feb, 1999. p.1-158.
37. Abu Al-Rub RK, Voyiadjis GZ. A physically based gradient plasticity theory. *Int J Plast* 2006; 22(4): 654–684.

38. ASM international Handbook Committee. Metals Handbook Tenth edition Volume 2 Properties and Selection: Nonferrous Alloys and Special-Purpose Materials Metals Park Ohio: ASM international, 1990.
39. Kim H. Al-Ca and Al-Fe Metal-metal Composite Strength, Conductivity, and Microstructure Relationships. In: PhD thesis submitted to Iowa State University. Ames, Jan, 2011.p.1-95.
40. Harvey JR. Effect of Elevated temperature operation on the strength of aluminum conductors. IEEE Trans Power Appar Syst 1972; 91(5):1769-1772.
41. Pzturk K, Zhong Y, Liu ZK, Luo AA. Creep Resistant Mg-Al-Ca Alloys: Computational Thermodynamics and Experimental Investigation. JOM 2003; 55(11): 40-44.
42. <http://www.brattle.com/newsevents/newsdetail.asp?recordid=568>
43. [http://www.midalcable.com/DataSheets/ACCCMidalData\(Eng\).pdf](http://www.midalcable.com/DataSheets/ACCCMidalData(Eng).pdf)
44. <http://www.matweb.com/>
45. [http://www.generalcable.com/NR/rdonlyres/26760444-32E6-4926-8C87-8A56B66CB5C0/0/USBarePriceSheets\\_Final010713.pdf](http://www.generalcable.com/NR/rdonlyres/26760444-32E6-4926-8C87-8A56B66CB5C0/0/USBarePriceSheets_Final010713.pdf)

CHAPTER 7 A LIGHTWEIGHT, HIGH STRENGTH, HIGH ELECTRICAL  
CONDUCTIVITY DEFORMATION PROCESSED AL MATRIX CA  
NANOFILAMENTARY COMPOSITE

A paper to be submitted to Acta Materialia

Liang Tian<sup>1</sup>, Trevor Riedemann<sup>2</sup>, Soren Muller<sup>3</sup>, Iver Anderson<sup>4</sup>, Alan Russell<sup>4</sup>

1. Primary researcher and author 2. Primary researcher. 3. Experimentalist 4. Project  
principal investigators

Abstract

Materials with light weight, high strength and high electrical conductivity are highly desired for many applications such as power transmission cables, fly-by-wire systems, downhole power feeds etc. However, it is difficult to get both high strength and high conductivity simultaneously. In this paper, an Al-20 vol% Ca nanofilamentary composite was produced by powder metallurgy and severe plastic deformation. The fine calcium metal powders (around 200  $\mu\text{m}$ ) were produced by a centrifugal atomization apparatus. After a deformation true strain more than 13, the calcium powder became fine calcium nanofilaments that reinforce the composite substantially by interface strengthening. The conductivity of the composite is slightly lower than the rule of mixture prediction due to minor quantities of impurity inclusions. The elevated temperature performance of this composite was also evaluated by differential scanning calorimetry and resistivity measurements.

## Introduction

Lightweight, high strength and high electrical conductivity are highly desired material properties for many applications such as power transmission cables, fly-by-wire control systems and downhole power feeds [1]. However, it is challenging to produce a material with both high strength and high electrical conductivity. Conventional strengthening methods such as strain hardening, second-phase hardening, precipitate hardening, or solid solution hardening significantly decrease material conductivity. A type of composite called deformation processed metal metal composites (DMMCs) has been found to exceed the rule-of-mixtures strength prediction and also delivers an electrical conductivity equal to the rule of mixtures predictions [2]. DMMCs are produced by powder metallurgy or by solidification of a liquid solution of two elements are mutually insoluble in the solid state, followed by severe plastic deformation [3]. The two ductile metal phases used for composite production can sustain a large deformation true strain as high as 16 without fracturing. The second (minority) phase deformed into fine filaments that reinforce the composite by interface strengthening, which means that the interfaces act as barriers to dislocation motion. DMMCs are essentially nanoscale bundles of two pure metals that have minimal electron scattering effect from solute impurities, interfaces, grain boundaries, and dislocations due to their unique microstructure [4].

Though many DMMCs systems have been studied in the past few decades [2], none possess densities and electrical conductivities close to those of pure Al. Al-Ca DMMCs has been invented by Russell et al [5] to produce a light, highly conductive, high-strength composite conductor. Both Al and Ca are low density, low cost, highly ductile fcc metals. They are the two most conductive metallic elements after the three Group 11 elements (Cu,

Ag, and Au). In Al/Ca DMMCs, highly reactive Ca filaments are embedded inside the Al matrix to be isolated from environmental air or moisture, which gives the composite excellent corrosion resistance. The first-generation Al-Ca (9 vol. %) composite was produced to prove this concept and study the microstructure-properties relationships [6]. However, the calcium metal used in producing that first-generation composite was commercially available calcium granules with average diameter around 1.2 mm. After a deformation true strain of 13.7, these granules were deformed into 2  $\mu\text{m}$  filaments, which were too coarse to reinforce the composite substantially from previous investigations on Al-Mg [7] and Al-Ti [8]. The investigations on Al-Mg and Al-Ti DMMCs demonstrated low densities and high strengths, but Mg and Ti are poor conductors, so those composites' conductivities were unexceptional.

In this study, we used fine calcium metal powders with average diameter around 200  $\mu\text{m}$  to produce second-generation composite, Al-Ca (20 vol. %), with finer calcium filaments for anticipated higher strength. Since no commercial vendors produce fine calcium metal powders, the fine Ca powders used in this experiment were produced by a centrifugal atomization device designed and fabricated at the Ames Laboratory of the U.S D.O.E. The processing, microstructure, and strength/conductivity relationship in Al-Ca (20 vol. %) composite has been studied and the results are reported here.

### Experimental Procedure

Al-Ca (20 vol. %) composite was produced by powder metallurgy and severe plastic deformation. High-purity (99.99 %) Al powders produced by Ames Laboratory gas atomization reaction synthesis (GARS) process (45-106  $\mu\text{m}$ ) were mixed with high-purity

(99.5%) fine calcium metal powder (106-212  $\mu\text{m}$ ) produced by the previously mentioned Ames Laboratory centrifugal atomization system. The mixed powders (80 vol. %, 157 g Al and 20 vol. %, 22.4 g Ca) were then die pressed into cylindrical powder compact (diameter 75mm and height 25.4 mm) under a pressing force of 20 tons (pressure 40.6 MPa). The powder compact has a density of 65%, which matched the compressibility curve for gas atomized aluminum powder [9]. The powder compacts were then loaded into a pure-Al (1100-H14) extrusion can (inside diameter 78 mm, outside diameter 90 mm and internal length 196.8 mm) and outgassed in vacuum chamber at a pressure of  $2.7 \times 10^{-5}$  Pa to remove air and moisture adsorbed on the powder particles. The can was then sealed by e-beam welding in vacuum with an end cap. Similar procedures were performed on pure Al powders with same size range to get pure Al powder compacts (64% dense) to serve as control specimens. One pure Al powder compact was made from GARS Al powders while the other seven compacts were made from commercial Al powders from Alfa Aesar Inc. The extrusion cans loaded with both Al/Ca powder compacts and pure Al powder compacts (the control sample) were sent for extrusion processing at the Extrusion Research & Development Center at the Technical University of Berlin, Germany to produce Al/Ca (20 vol. %) composite rod and pure Al rod. The indirect extrusions were done under 285 °C, which was thought to be hot enough to activate more slip systems and to promote recrystallization for easy deformation but cool enough to avoid formation of intermetallics. Extrusion was done with an extrusion force of 2 MN at a ram speed of 1.5 mm/s. The metal billet diameter reduced from 89 mm to 27.3 mm, which gives an extrusion ratio of 11 (The deformation true strain  $\eta$  of the specimen was calculated by  $\eta = 2\ln(d_0/d_f)$ , where  $d_0$  and  $d_f$  are the initial and final specimen diameters, respectively. Here, as-extruded composite specimen has a

deformation true strain 1.93 when accounting for its 35% porosity). Extrusion transforms spherical Ca metal particles into filaments that lie parallel to the rod axis. The pure Al skin from the pure Al extrusion can was removed from the Al/Ca composite rod with a lathe. After further deformation by swaging, the composite rod becomes composite wire of 2.95 mm diameter (deformation true strain 6.39). A short section of 2.95 mm composite wire was further swaged to 1mm (deformation true strain 8.52) for tensile tests and electrical conductivity measurements. All remaining 2.95 mm composite wires were then cut into several hundred 13 cm long segments, which were then cleaned with acetone and abraded by fine steel wool in an inert-atmosphere glove box to remove surface oil and oxide, which was intended to promote bonding between rods. The cleaned Al/Ca rod segments were then tightly packed into another similar pure Al extrusion can (packing density 72%), as were the pure 3.18 mm Al rods of the control specimen (packing density 68%). These e-beam sealed extrusion cans were sent again to Technical University of Berlin, Germany for the second and final extrusion. The second extrusion was done under 140 °C, which was chosen because differential scanning calorimetry testing on 2.95 mm Al/Ca composite wire (true strain 6.39) suggested that the formation of intermetallic compounds occurred at 186 °C, a considerably lower temperature than 295 °C reaction temperature measured in first generation Al/Ca composite with coarser Ca filaments. The fine Ca filaments seem to provide additional driving force to promote the reaction of Al and Ca to form intermetallic compounds  $\text{Al}_4\text{Ca}$  and  $\text{Al}_2\text{Ca}$  and decrease their formation temperatures. The second extrusion cold-welded the Al/Ca rods together into one 27.3 mm diameter monolithic mass (deformation true strain 8.42) that was immediately cooled by water after going through the die. This 27.3mm composite rod was swaged to 10.2 mm (deformation true strain 10.40), 3.5

mm (deformation true strain 12.53) and then 1.9 mm (deformation true strain 13.80). After a deformation true strain of 13.8, the Al/Ca composite was expected to contain Ca filaments with average diameter around 200 nm, which should be sufficiently fine for increasing strength while maintaining high electrical conductivity.

Microstructure, tensile strength, and electrical conductivity were measured at various deformation true strain levels. Microstructures were studied by Quanta 250 field emission-scanning electron microscopy. Each specimen was prepared by polishing on SiC grinding paper with hexane to 1200 grit; further polishing was then performed using 1  $\mu\text{m}$  glycol based diamond polishing fluid. Conventional polishing fluids like MetaDi or organic solvents can not be used because even the trace amount of water inside can etch the Ca filaments. Tensile tests were done by Instron 3367 under an elongation rate of 2mm/min to test the tensile strengths (average of three independent tests) of the Al/Ca (20 vol. %) sample and the pure Al control sample at various true strain levels. Differential scanning calorimetry (DSC) tests were done by Netzsch STA449 F1 under a heating rate 5  $^{\circ}\text{C}/\text{min}$  on Al/Ca samples with various deformation true strain levels to evaluate the microstructure evolution at elevated temperature. Electrical resistivity/conductivity data were measured by four-point probe method with a Keithley 224 constant current source 100 mA and a Keithley 614 electrometer for both as-deformed and annealed 1mm Al/Ca wire samples to understand how the annealing temperature and time affect the microstructure.



## Results and Discussions

## Microstructure characterization of Al/Ca (20 vol. %) composite

Fig.1 shows the as deformed microstructure of Al/Ca (20 vol. %) composite at different deformation true strains. The light gray Ca filaments adopted a ribbon-shaped morphology instead of the cylindrical morphology. According to the classic composite morphology theory [2], in a fcc matrix DMMC, a bcc metal filament tends to develop a  $\langle 110 \rangle$  fiber texture parallel to the deformation axis, which leads to a plain strain deformation mode that would form a ribbon like curling filamentary morphology. In contrast, fcc filaments tend to deform axisymmetrically to develop a cylindrical filament morphology due to the great number of slip planes in a textured fcc matrix. Therefore, the ribbon shaped Ca filaments could be related to a temporary temperature rise and large shear stress during extrusion causing a temporary crystal structure transformation from fcc Ca to bcc Ca (equilibrium transformation occurred at 728K) [10].

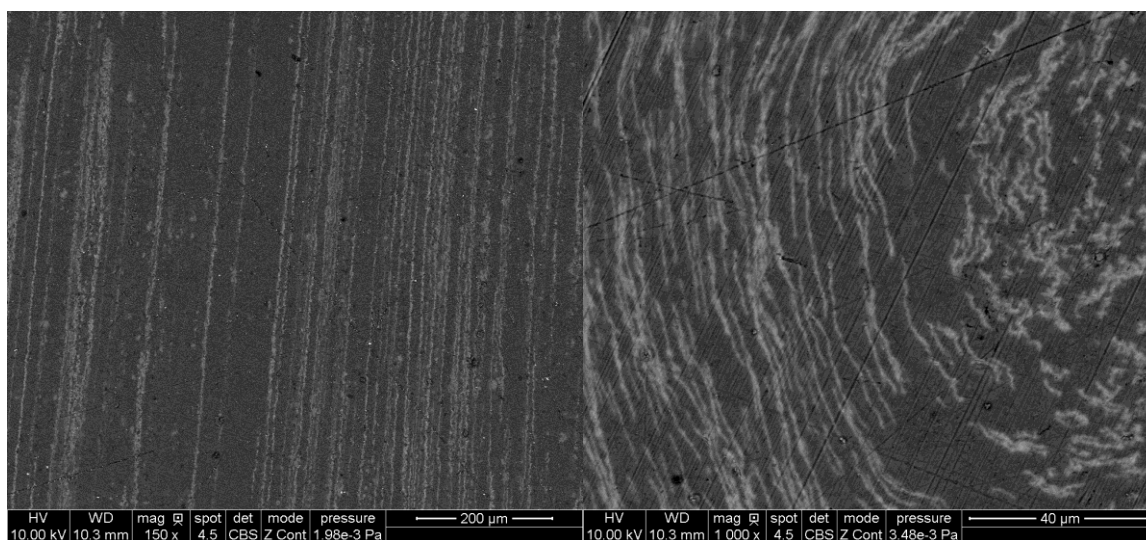


Fig 1. Back-scattered electron SEM (scanning electron microscopy) micrographs of Al-Ca (20 vol.%) composite: (a) longitudinal cross section at deformation true strain 6.39 (b) transverse cross section at deformation true strain 8.52. The Al matrix is dark gray, and the Ca filament is light gray in these images.

The Ca filament thickness can be measured from the SEM micrographs in Fig.1. Table 1 summarizes the Ca filament thicknesses at various deformation true strain levels. It can be easily seen that the filament thickness decreased sharply as deformation true strain increases. An exponential dependence of filament thickness on deformation true strain can be found to be  $111.6 \cdot \exp(-0.487 \cdot \eta)$  ( $\mu\text{m}$ ). This thickness dependence matched well with the ideal thickness dependence  $d_0 \cdot \exp(-0.5 \cdot \eta)$  ( $\mu\text{m}$ ), where  $d_0$  is between 100 and 200  $\mu\text{m}$ .

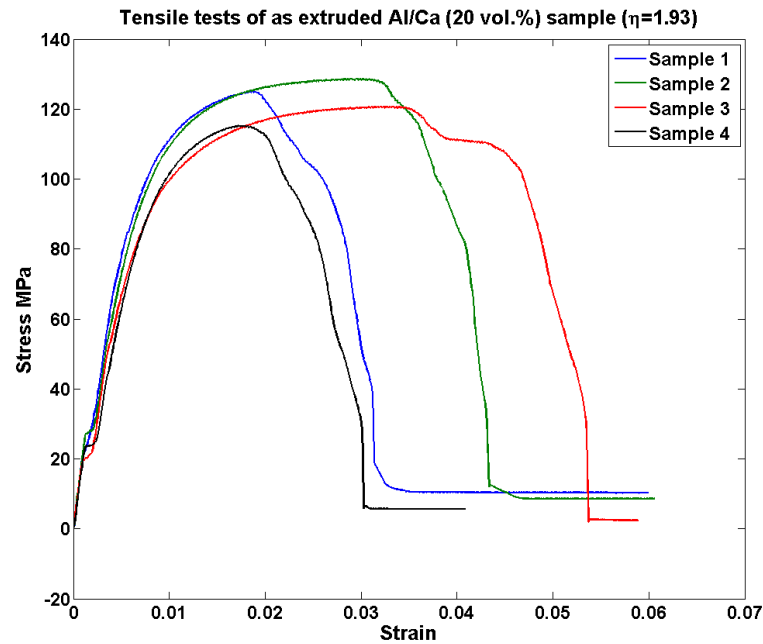
Table 1 The Ca filament thicknesses at different deformation true strains measured from the SEM micrographs from Fig. 1.

Deformation true strain $\eta$	Ca filament thickness ( $\mu\text{m}$ )
6.385	4.97
8.515	1.76

#### Strength of Al/Ca (20 vol. %) composite and pure Al

Fig.2 shows the tensile testing stress strain curves for as extruded ( $\eta=1.93$ ), 1mm as swaged ( $\eta=8.52$ ), 2.95 mm as swaged ( $\eta=6.39$ ) Al/Ca tensile specimens. The tensile strengths at various deformation true strain levels are summarized in Table 2, with the pure Al tensile strengths data at various deformation true strain levels in parentheses as a contrast. Fig 3 showed the experimental relationship between deformation true strain and tensile strength of Al/Ca composite and the fitting result by a Hall-Petch barrier model, which give the strength as  $102.8 + 139.3 / \sqrt{111.6 \cdot \exp(-0.487 \cdot \eta)}$  MPa. As these data show, the tensile strength increases as the deformation true strain increases for both Al/Ca (20 vol. %) composite and pure Al. At low deformation true strain level (e.g. below 8.5), the Al/Ca composite has no higher tensile strength than that of pure Al sample at the same strain level.

This suggests that the strengthening effect of Al/Ca composite is largely contributed by interface strengthening that is much less effective at low deformation true strain due to the small interface area from coarse Ca filament size, compared with the dominating strain hardening effect in pure Al sample. At high deformation true strains, the Ca filament thickness reduced to the submicron regime so that a large amount of interface area was created to strengthen the composite by acting as a barrier to dislocation motion.



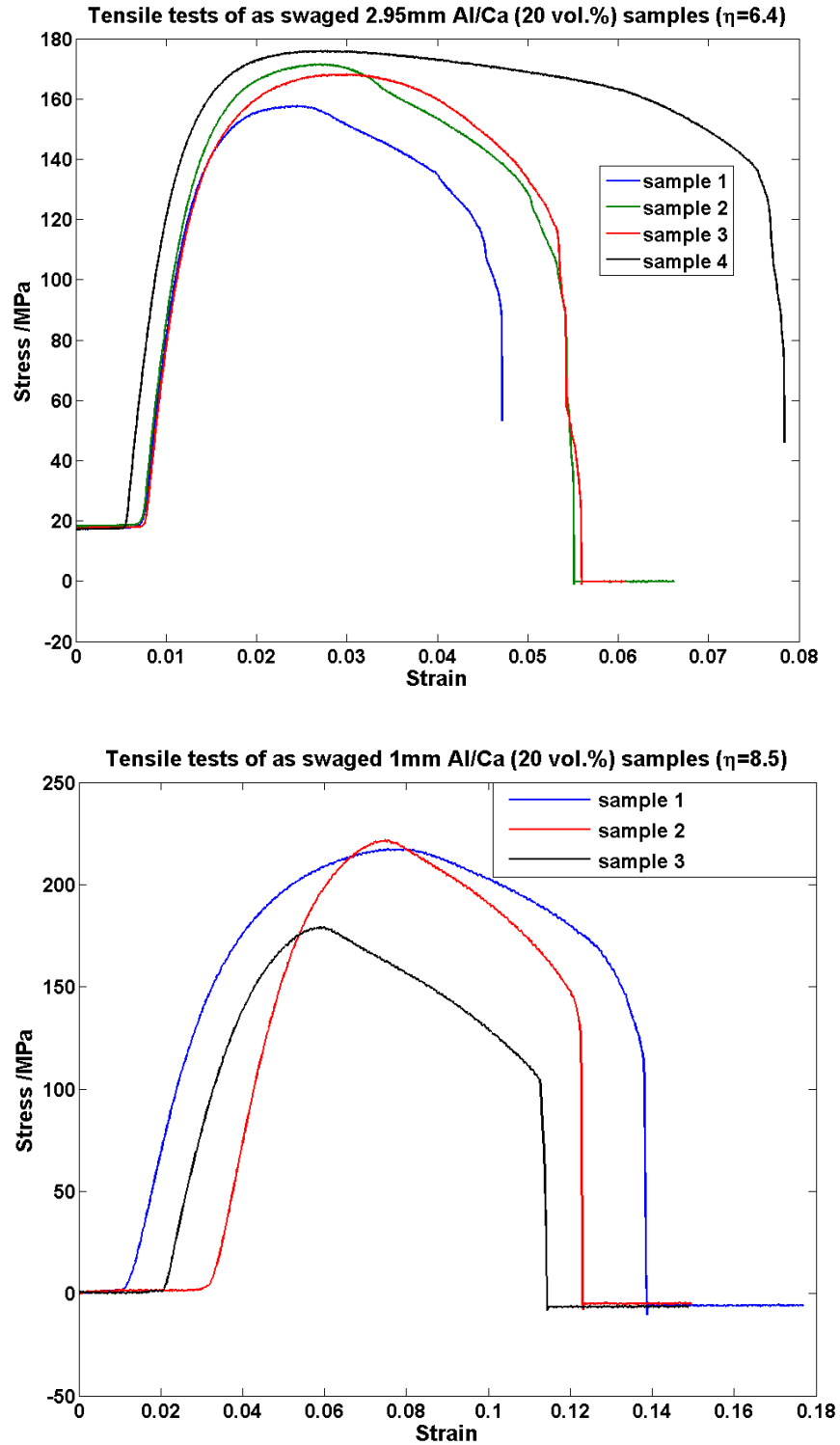


Fig. 2 Tensile tests of Al/Ca (20 vol.%) composite at various deformation true strain levels.

Table 2 The ultimate tensile strength of Al/Ca (20 vol.%) composites at various deformation true strains (the measured tensile strengths of pure Al at corresponding deformation true strain are included in parentheses).

Deformation true strain	Ultimate tensile strength (MPa)
1.93	122
6.39	168 (186)
8.52	206 (214)

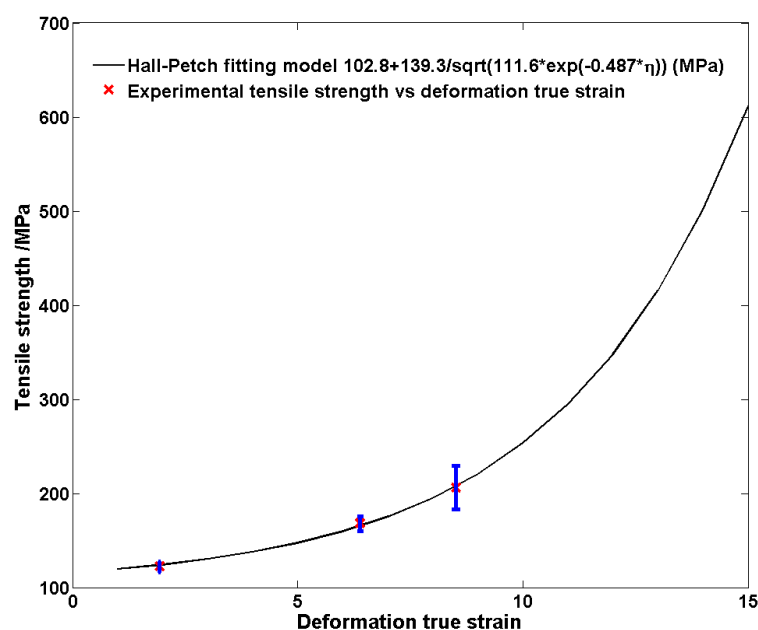
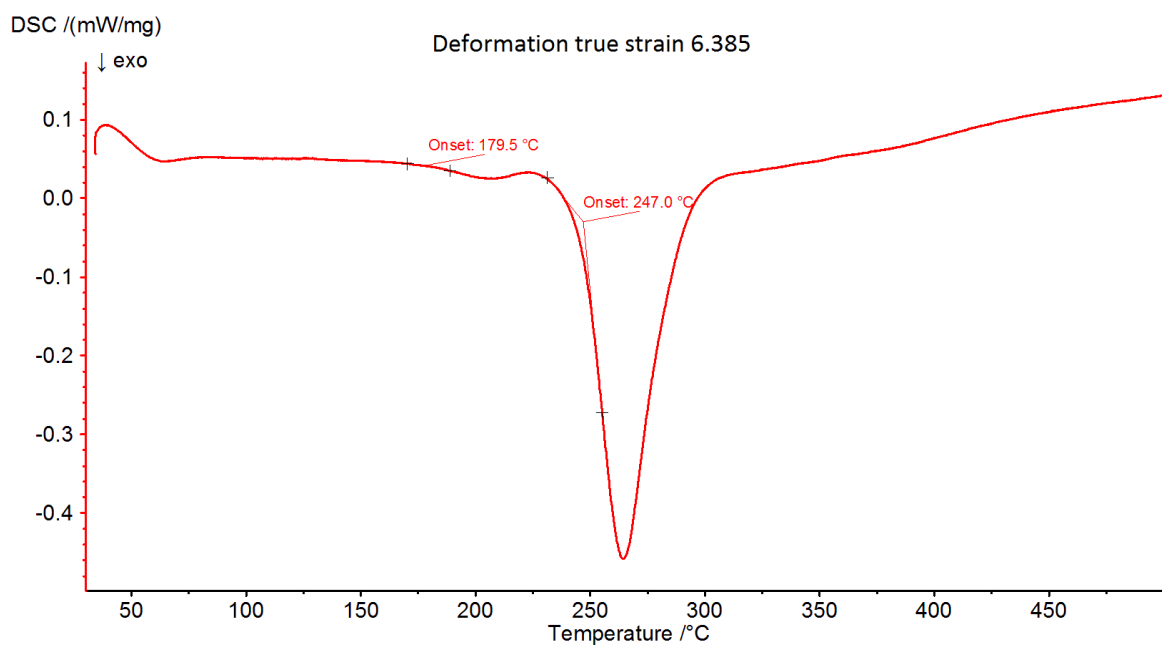
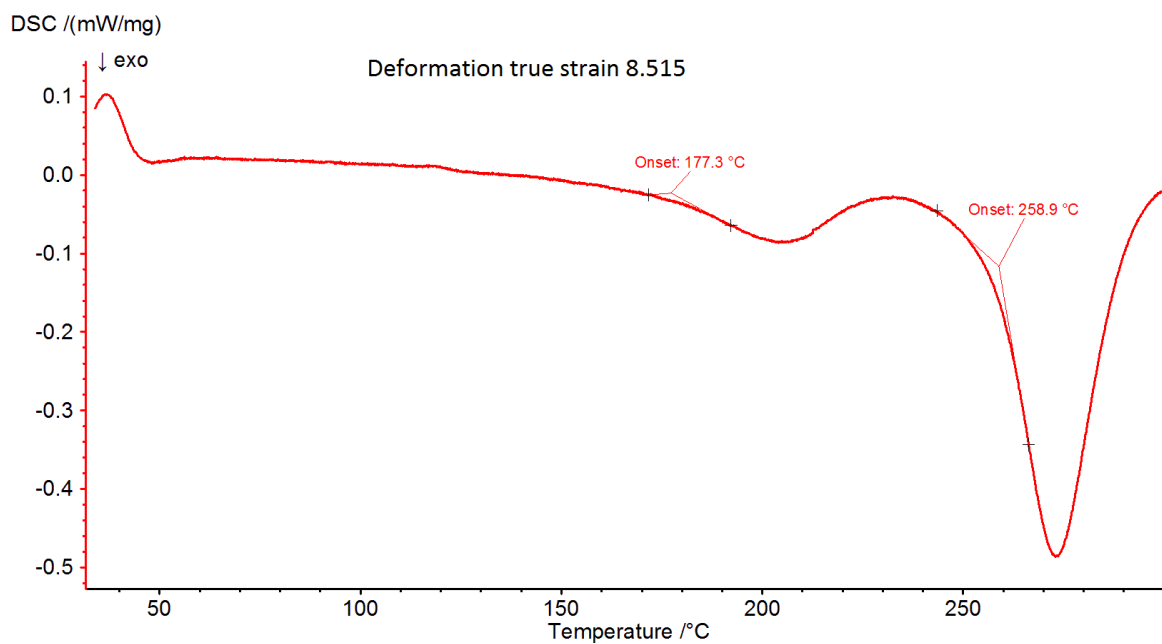


Fig.3. Tensile strength of Al/Ca (20 vol.%) composite as a function of deformation true strain. The experimental data are fitted by a Hall-Petch barrier model.

Differential scanning calorimetry (DSC) measurements on Al/Ca (20 vol.%) composite

DSC tests have been done on Al/Ca (20 vol. %) composite to further understand the microstructure transformation at elevated temperature. Previous investigation on Al/Ca (9 vol. %) composite [6] suggested that there are two exothermic reactions occurring during DSC testing. One is the formation of  $\text{Al}_4\text{Ca}$  at 225 °C and the other is the formation of  $\text{Al}_2\text{Ca}$  at 275 °C [6]. The formation of these intermetallic compounds has a great impact on the

performance of the Al/Ca composite conductor at elevated temperature during emergency overloading. Therefore, studying these reactions for Al/Ca (20 vol. %) composite at elevated temperature is important. Fig 4 shows the DSC curves for various Al/Ca (20 vol. %) composite samples at different deformation true strains under Argon atmosphere. It is clear that intermetallic formation begins at a higher temperature for as-extruded samples with low deformation true strain compared with that of further swaged samples with high deformation true strain. This should be due to the fact that the fine micron-size Ca filament size in as swaged samples can provide more driving force for the reaction due to the curvature driven atomic mixing by the Gibbs-Thompson effect. In as swaged samples, two exothermic events have been observed. The first event should be due to the  $\text{Al}_4\text{Ca}$  formation since the  $\text{Al}_4\text{Ca}$  formation has a much lower enthalpy of formation than that of  $\text{Al}_2\text{Ca}$  [11] and also  $\text{Al}_4\text{Ca}$  is highly unstable and will decompose into  $\text{Al}_2\text{Ca}$  quickly, which causes the first exothermic peak to be small. The second event should be due to the formation of  $\text{Al}_2\text{Ca}$ , which is a highly stable intermetallic compound with melting temperature 1087 °C; its formation enthalpy is more negative than that of  $\text{Al}_4\text{Ca}$ .



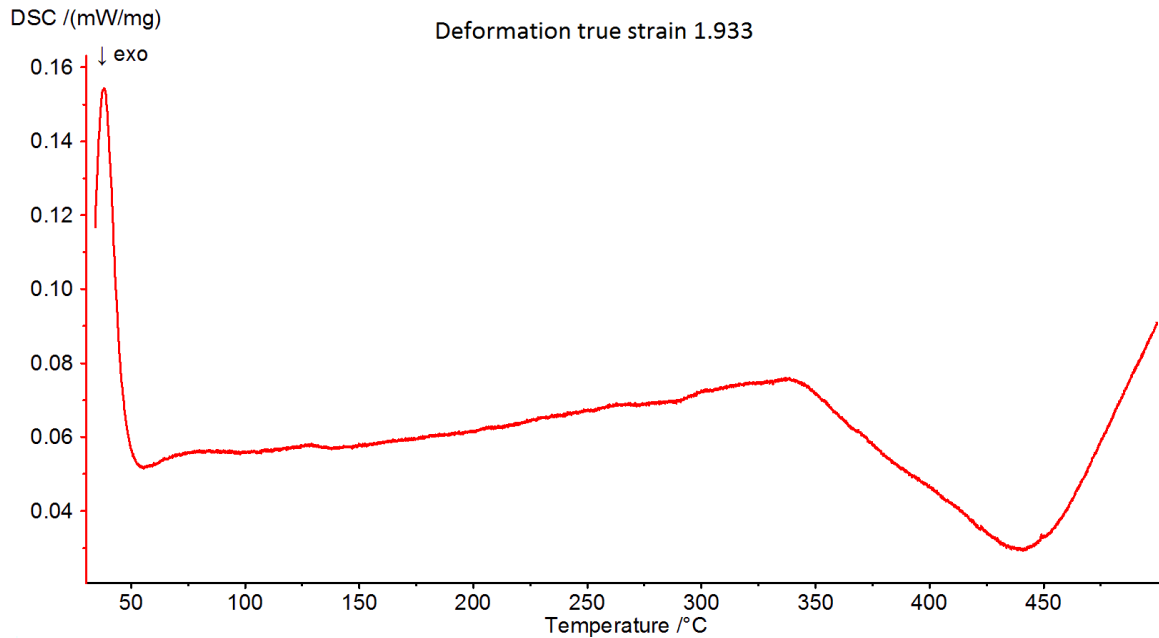


Fig. 4. The DSC curves for various Al/Ca (20 vol. %) composite samples at different deformation true strains under argon atmosphere. The as-swaged 1mm sample has deformation true strain 8.52. The as-swaged 3mm sample has deformation true strain 6.39. The as-extruded 2.54 cm sample has deformation true strain 1.93.

#### Electrical resistivity of Al/Ca (20 vol. %) composite and pure Al

The electrical resistivities of as-deformed 1mm Al/Ca composite wire and 1mm pure Al wire (deformation true strain 8.52) were measured by four-point probe resistivity measurement. The electrical resistivity of 1mm Al/Ca (20 vol. %) composite wire is  $0.0305 \mu\Omega \cdot \text{m}$  while the measured resistivity of 1mm pure Al wire is  $0.0283 \mu\Omega \cdot \text{m}$ . The resistivity of Al/Ca (20 vol. %) composite  $0.0305 \mu\Omega \cdot \text{m}$  is 3.4% higher than  $0.0295 \mu\Omega \cdot \text{m}$  predicted by the inverse rule of mixtures. This could be partially due to crystal defects such as powder particle oxide layer debris inclusions and from the increased dislocation density (both statistically stored dislocations (SSDs) and geometrically necessary dislocations (GNDs)) due to strain hardening and increased interface area. Our resistivity measurements on annealed pure Al wire suggested that the resistivity originated from increased dislocation



density by strain hardening is negligible. In the Al/Ca composite wire, the GNDs are generated to accommodate the Al/Ca interface area, which could be another contribution to resistivity when the Ca filaments are fine enough to reach submicron size. However, in this 1mm Al/Ca composite wire, the Ca filament size is close to 2  $\mu\text{m}$ , too coarse to generate strong interface scattering effect. It is also possible that this results from deformation induced chemical mixing to form localized solid solutions that increase the resistivity.

The electrical resistivities of Al/Ca composite wire and pure Al wire annealed at elevated temperature have been measured to evaluate the effect of high temperature annealing (emergency overloading of conducting cable) on the microstructure and resistivity of Al/Ca composite wire. Tables 3 and 4 summarize the resistivity of 1mm Al/Ca composite wire and 1mm pure Al wire annealed at 300 °C for various amount of time, respectively. From Table 4, we can see that the annealing of 1mm pure Al wire ( $\eta=8.5$ ) at 300 °C has no obvious effect on its resistivity. This suggested that the resistivity contribution from increased dislocation density of pure Al wire due to deformation is negligible, and the pure Al surface is quite resistant to oxidation to maintain its resistivity. The surface of Al/Ca composite rapidly becomes essentially pure Al following exposure to air, so the composite wire should be resistant to oxidation as well. From Table 3, we can see that the resistivity of Al/Ca (20 vol. %) composite has a significant increase after annealing at 300 °C for just 600 s. This resistivity increase could be due to the formation of  $\text{Al}_2\text{Ca}$  intermetallic compound as we have observed the  $\text{Al}_2\text{Ca}$  formation at 275 °C in Al/Ca (9 vol. %) composite ( $\eta=8.55$ ) [6] and our DSC test on 1mm Al/Ca (20 vol. %) composite wire ( $\eta=8.5$ ) in the previous section suggested that  $\text{Al}_2\text{Ca}$  formed at 258 °C. In order to verify this, the resistivity of arc-melted pure  $\text{Al}_2\text{Ca}$  specimens (confirmed by X-ray diffraction) has been measured to be 0.1115

$\mu\Omega\cdot\text{m}$ , roughly 4 times that of pure Al. If we assume that all Ca filaments had been fully converted into  $\text{Al}_2\text{Ca}$ , the volume fraction for Al and  $\text{Al}_2\text{Ca}$  would be 40% and 60%, respectively. By using an inverse rule of mixtures, the resistivity of Al/ $\text{Al}_2\text{Ca}$  (60 vol. %) composite is calculated to be  $0.0513 \mu\Omega\cdot\text{m}$ , which is close to the measured resistivity value of  $0.0515 \mu\Omega\cdot\text{m}$ . This suggests that the initial resistivity increase due to annealing for 10 mins could indeed be caused by the transformation of Ca filaments into  $\text{Al}_2\text{Ca}$ . The later resistivity drop could be caused by the decreased GNDs density due to annealing since the SSDs density from strain hardening is small by inferring from the resistivity of annealed pure Al wire. Another reason could be from the increased grain size of  $\text{Al}_2\text{Ca}$  during annealing, which reduces the grain boundary scattering effect when grain size increased from nanoscale to microscale [4]. The resulting slight increase of resistivity could be due to the thermal stress from the thermal expansion coefficient mismatch between Al and  $\text{Al}_2\text{Ca}$ .

Table 3. The electrical resistivities of 1mm Al/Ca (20 vol. %) composite wire (deformation true strain 8.5) annealed at 300 °C for different times.

Annealing time (mins)	0	10	20	30	40	50	60	70	140	160	1128
Electrical resistivity ( $10^{-4} \mu\Omega\cdot\text{m}$ )	305	515	515	505	505	507	510	510	515	514	518

Table 4. The electrical resistivities of 1mm pure Al wire (deformation true strain 8.5) annealed at 300 °C for different time.

Annealing time (mins)	0	10	20	30	40	50	175	360
Electrical resistivity ( $10^{-4} \mu\Omega\cdot\text{m}$ )	283	283	282	285	282	283	283	282

[illegible]

Electrical resistivity ( $10^{-4}\mu\Omega\cdot\text{m}$ )	328	356	368	368	370	372	380	384	384	389	413	450	456
---	-----	-----	-----	-----	-----	-----	-----	-----	-----	-----	-----	-----	-----

Table 6. The electrical resistivities of 1mm Al/Ca (20 vol. %) composite wire (deformation true strain 8.5) annealed at 125 °C for different time.

Annealing time (mins)	0	10	20	30	40	70	140	343	503	1326	1854
Electrical resistivity ( $10^{-4}\mu\Omega\cdot\text{m}$ )	304	307	310	311	312	317	321	321	321	327	329

From the equilibrium Al-Ca phase diagram [10], it is known that Al and Ca have essentially zero mutual solubility at thermodynamic equilibrium. Furthermore, a preliminary molecular dynamics simulation by reactive force field was done on an Al/Ca bicrystal with different interface structure and results suggested that the Al and Ca atoms tend to repel each other in most interface configurations (see Appendix A). Also  $\text{Al}_2\text{Ca}$  formation seems to require a pre-existing of an Al/Ca solution from both the phase diagram and the fact that the pure  $\text{Al}_2\text{Ca}$  sample was obtained by arc melting to get a liquid solution of Al and Ca. Therefore, there is a possibility that the contact between pure solid Al and pure solid Ca would not form  $\text{Al}_2\text{Ca}$  at the interface because Al and Ca have no mutual solubility and would not form Al/Ca solid solution. However, there is a phenomenon called deformation

induced chemical mixing that has been widely observed in heavily co-deformed metallic composites [12]. This phenomenon can cause the complete dissolution of a minority filament phase into the matrix phase. Several mechanisms of deformation induced mixing are mentioned. One of them is called the dislocation shuffle mechanism, which suggests that the shear transfer by multiple slips systems of two phases across the heterophase interface can lead to massive chemical mixing by shearing tiny embedded one-phase particles into another phase. These tiny particles would dissolve into their surround phase through curvature driven dissolution-Gibbs-Thomson effect due to the small size of particles, though the two phases are mutually insoluble under thermodynamic equilibrium. This mechanism would seem to be applicable to fcc Al and fcc Ca. Both shared the same multiple slip systems. One piece of evidence supporting this hypothesis is that from Table 3, we know that the resistivity after 10 mins annealing can be explained by the inverse rule of mixture of pure Al (40 vol.%) and pure  $\text{Al}_2\text{Ca}$  (60 vol.%), which suggests the complete dissolution of Ca to form Al/Ca solid solution that transforms into  $\text{Al}_2\text{Ca}$  during annealing. If the  $\text{Al}_2\text{Ca}$  formed by the reaction of Al and Ca at the interface, the diffusion barrier effect of  $\text{Al}_2\text{Ca}$  at the interface for Al into Ca or Ca into Al should slow the kinetics of its formation substantially, which seems to contrast with the fact that the  $\text{Al}_2\text{Ca}$  formation was complete within 10 mins.

### Conclusions

The 2<sup>nd</sup> generation Al/Ca (20 vol.%) composite was produced by powder metallurgy and severe plastic deformation. The fine Ca metal powders used in this experiment were produced by a centrifugal atomization device designed and fabricated at Ames Laboratory of

the U.S. D.O.E. After deformation processing, most Ca filaments adopted a ribbon-shaped morphology instead of cylindrical morphology. The strength of the composite increased with deformation true strain due to the stronger interfacial strengthening from finer Ca filaments, which can be described well by a Hall-Petch barrier model. The resistivity of the composite was slightly higher than the inverse rule of mixtures prediction due to some crystal defects such as oxide debris inclusions and dislocations. Both DSC tests and elevated temperature resistivity measurements suggested the formation of  $\text{Al}_4\text{Ca}$  and  $\text{Al}_2\text{Ca}$ . The kinetics of  $\text{Al}_4\text{Ca}$  formation and  $\text{Al}_4\text{Ca}$  decomposition into  $\text{Al}_2\text{Ca}$  vary drastically with temperature.

### References

- [1] Tian L, Anderson I, Riedemann T, Russell A, Kim H. *Electr Pow Syst Res* 2013;105:105.
- [2] Russell AM, Chumbley LS, Tian Y. *Adv Eng Mater* 2000;2:11.
- [3] Bevk J, Harbison JP, Bell JL. *J Appl Phys* 1978;49:6031.
- [4] Tian L, Anderson I, Riedemann T, Russell A. *Acta Mater* 2014;77:151.
- [5] Russell A.M., Anderson, I.E., Kim, H.J., and Frerichs, A.E. Aluminum/alkaline earth metal composites and method for producing. US 8,647,536 B2, 2014.
- [6] Tian L, Kim H, Anderson I, Russell A. *Mat Sci Eng a-Struct* 2013;570:106.
- [7] Xu K, Russell AM, Chumbley LS, Laabs FC, Gantovnik VB, Tian Y. *J Mater Sci* 1999;34:5955.
- [8] Russell AM, Lund T, Chumbley LS, Laabs FA, Keehner LL, Harringa JL. *Compos Part a-Appl S* 1999;30:239.
- [9] Neikov OD, Murashova IB, Yefimov NA, Naboychenko S. *Handbook of Non-Ferrous Metal Powders: Technologies and Applications*. Oxford: Elsevier; 2009.
- [10] ASM International, Materials Park, OH, USA. ASM Alloy Phase Diagram Database, accessed June 10, 2015. URL: <http://www1.asmiinternational.org/asmenterprise/apd/>.

- [11] Ozturk K, Chen LQ, Liu ZK. J Alloy Compd 2002;340:199.
- [12] Raabe D, Choi PP, Li YJ, Kostka A, Sauvage X, Lecouturier F, Hono K, Kirchheim R, Pippan R, Embury D. Mrs Bull 2010;35:982.

CHAPTER 8 PHASE FIELD STUDY OF INTERFACIAL DIFFUSION-DRIVEN  
SPHEROIDIZATION IN A COMPOSITE COMPRISED OF TWO MUTUALLY  
INSOLUBLE PHASES

A paper published in The Journal of Chemical Physics

Liang Tian<sup>1</sup>, Alan Russell<sup>2</sup>

1. Primary research and author 2. Project principal investigator

Abstract

The phase field approach is a powerful computational technique to simulate morphological and microstructural evolution at the mesoscale. Spheroidization is a frequently observed morphological change of mesoscale heterogeneous structures during annealing. In this study, we used the diffuse interface phase field method to investigate the interfacial diffusion-driven spheroidization of cylindrical rod structures in a composite comprised of two mutually insoluble phases in a two-dimensional case. Perturbation of rod radius along a cylinder's axis has long been known to cause the necessary chemical potential gradient that drives spheroidization of the rod by Lord Rayleigh's instability theory. This theory indicates that a radius perturbation wavelength larger than the initial rod circumference would lead to cylindrical spheroidization. We investigated the effect of perturbation wavelength, interfacial energy, volume diffusion, phase composition, and interfacial percentage on the kinetics of spheroidization. The results match well with both the Rayleigh's instability criterion and experimental observations.



## Introduction

Many two-phase composites consist of a cylindrical rod phase embedded inside a matrix phase [1-3]. These cylindrical rods tend to break up into spheres during annealing treatment [1, 3, 4]. Such spheroidization has a large effect on material properties [4-8]. For example, spheroidization of the filamentary phase in deformation processed metal-metal composites (e.g. Al-20%Sn composite [5]) lowers the strength and electrical conductivity [7] of the composite. The isothermal magnetization curve of Cu-Nb in-situ composites also depends on the spheroidization kinetics [7]. For metallic nanowires used in microelectronics, fragmentation of the nanowires into chains of nanospheres would affect its electrical, chemical and thermal properties [4]. In Al-Si alloys, the spheroidization of eutectic silicon resulted in outstanding fracture strain with good yield strength [6]. Thus, the stability of various properties of these materials depends on their morphological stability.

The first investigation of the break-up of rods into spheres was done by Plateau and Rayleigh when they studied the instability of jets of fluids [8]. Rayleigh introduced a tiny longitudinal perturbation of rod radius in a single harmonic form:  $r=R+\delta \cos(2\pi x/\lambda)$ , where  $R$  is the initial unperturbed rod radius,  $\delta$  is the amplitude of the perturbation,  $\lambda$  is the perturbation wavelength,  $x$  is the distance along the rod axis.  $\delta$  was assumed to be small to validate the small-surface-slope approximation [9]. Plateau and Rayleigh predicted that a cylinder with radius  $R$  would be unstable against the perturbation and would spheroidize when the perturbation wavelength  $\lambda$  is larger than the initial rod circumference  $2\pi R$  due to the minimization of surface free energy. The perturbation wavelength with the fastest spheroidization rate,  $\lambda_m$ , was predicted to be  $9.016 R$ . If the initial perturbation is multi-

harmonic, this fastest-growing perturbation will dominate and determine the final average spacing and sphere size [9].

In Rayleigh's theory, only surface diffusion is considered to drive the spheroidization due to volume conservation constraint so that surface free energy is the total free energy to be minimized. If the specific surface energy is independent of crystallographic orientation, the minimization of surface free energy is equivalent to the minimization of surface area of the phase (i.e., forming a spherical surface) [10]. This isotropic surface energy density assumption is a good approximation for amorphous and untextured polycrystalline materials. In the case of orientation-dependent specific surface energy (e.g. single-crystal materials), the equilibrium shape due to minimization of surface free energy can be determined by the well-known Wulff construction based on the Gibbs-Wulff theorem by using a polar plot of the surface energy density (gamma plot) [11]. From a mechanistic perspective, the driving force of surface diffusion for spheroidization is the chemical potential difference between surface atoms [5]. The chemical potential of an atom on a curved surface can be derived from the Gibbs-Thompson equation,  $\mu = \mu_0 + \gamma V \kappa$ , where  $\mu_0$  is the chemical potential of an atom on a flat surface,  $\gamma$  is the surface energy density,  $V$  is the atomic volume,  $\kappa$  is the surface curvature [5, 11].  $\kappa$  can be calculated by the direct sum of two principal curvatures  $\kappa_1$  and  $\kappa_2$ .  $\kappa_1$  is determined by perturbed rod radius, and  $\kappa_2$  is determined by the perturbation wavelength and amplitude. The total curvature determining the chemical potential is a competition between  $\kappa_1$  and  $\kappa_2$ , which can be mathematically simplified to be a competition between the unperturbed rod radius and the perturbation itself [5]. The competition between unperturbed radius and the perturbation itself can lead to the Rayleigh instability criterion. It clearly explains why radius perturbation is necessary to generate the chemical potential

gradient for the cylinder to spheroidize by surface diffusion. A similar explanation of this competition can be understood by the Young-Laplace equation utilizing the pressure-driving mechanism. Another way to understand the Rayleigh instability is that a critical intermediate perturbation stage exists so that before this stage, the growing of perturbation would increase the surface area of the system and would therefore be energetically unfavorable. After this stage, further growth of the perturbation would decrease the surface area substantially and lead to break-up of spheres even though spheres are initially more energetically favorable than rods [2].

The atomistic mechanism of spheroidization for the discussion above is a surface diffusion mediated kinetic process [12]. According to Ref [10], the available mechanisms for morphological change include surface diffusion, volume diffusion (e.g. Ostwald ripening), evaporation, and condensation. Nichols and Mullins investigated the contributions of both surface/interface and volume diffusion to the morphological changes and found that the surface diffusion is the dominating mechanism for shape change [13]. The influence of volume diffusion on morphological changes has attracted considerable attention recently [14-16]. It is our motivation in this paper to study the combined effect of both surface/interface diffusion and volume/bulk diffusion (i.e. compositional change driven by minimization of interfacial and bulk free energy, respectively) on the spheroidization of two insoluble phase systems. The diffuse interface phase field model is used to study diffusion-controlled phase morphology evolution by using a conserved compositional phase field variable. The temporal and spatial evolution of the compositional field is governed by the Cahn-Hilliard non-linear partial differential equation. The interface diffusion mechanism is explicitly implemented in the free energy functional as interfacial free energy. By setting the initial

interface microstructure, the interface related and bulk related chemical potential can be determined with time evolution to estimate the role of interface diffusion and volume diffusion to the kinetic spheroidization process. Though initially the interface diffusion is the only operating mechanism in our model, bulk diffusion (i.e. phase separation in insoluble systems) begins to play a role as time progresses. Our goal is to evaluate the effect of volume diffusion on spheroidization kinetics in these systems. The Rayleigh instability criterion for spheroidization will then be compared with our simulation results to verify its applicability in diffusion-controlled morphology change. The effect of phase composition, interface percentage, interface energy on the spheroidization kinetics were also investigated.

#### Diffuse Interface Phase Field Model

The phase field model is a powerful tool to study microstructural evolution at the mesoscale by using a set of conserved and non-conserved continuous phase field variables [17, 18]. The diffuse interface description of the phase field model uses the gradients of phase field variables to describe the interface, which allows one to avoid tracking the interface positions as moving boundary conditions and to predict the evolution of arbitrary morphologies and complex microstructures [17, 18]. In a sharp interface description, different microstructures are expressed as discrete regions separated by a zero-thickness interface [19]. Zhu et al found a good agreement of the kinetics of microstructural evolution between the diffuse interface and sharp interface descriptions [19]. The thermodynamic driving force for the field variables includes bulk and interface free energy, elastic, electrostatic, and magnetic energy [17]. The temporal and spatial evolution of phase field variables is described by the Allen-Cahn equation (time dependent Ginzburg-Landau

equation) for non-conserved field variables and the non-linear Cahn-Hilliard equation for conserved field variables [20]. The phase field model can at least qualitatively explain the experimental observations in the absence of a complete set of real thermodynamic and kinetic parameters, which can be difficult to obtain from experiments or more expensive atomistic simulations [19]. This approach has been widely used in modeling grain growth, spinodal decomposition, solidification, solid state phase transformations, etc [20].

The system in this study is the simplest isostructural two-phase system that needs only a single compositional field to describe the microstructure [21, 22]. In this system, the free energy dependence on structure-related field variables (grain boundaries, dislocations, etc.) is neglected because the driving force for the spheroidization is atomic diffusion. For untextured polycrystalline materials, these structure-related field variables would change only the kinetic parameters for atomic diffusion, which can be described well by atomic mobility, temperature, and the interfacial energy coefficient in our model. So the effects of these complex structural characteristics can be incorporated qualitatively in the above kinetic parameters. Isotropic interfacial energy coefficient and mobility will be assumed in our model to simplify the calculation. The effect of grain boundaries (i.e. grain growth) in two polycrystalline phase systems on the diffusion kinetics could be investigated in the future in both isotropic and anisotropic grain boundary energy cases.

In the diffuse interface phase field model, interfacial energy is incorporated by the gradients of phase field variables, so the total free energy,  $F$ , of our inhomogeneous system is given by [23]

$$F = \int_V \left[ f(c, T) + \frac{1}{2} \alpha (\nabla c)^2 \right] dV \quad (1)$$

where  $f(c,T)$  is the local free energy density,  $1/2 \alpha(\nabla c)^2$  is the interfacial free energy density,  $c$  is the compositional field,  $T$  is the temperature of the system,  $\alpha$  is the interfacial energy coefficient which substantially affects the kinetics of compositional evolution. We assume  $\alpha$  to be an isotropic constant. The local free energy density function of a two-phase binary system can be determined from real thermodynamic data. But since we are interested only in modeling the morphological evolution, a simple double well potential [21-23] can be used as

$$f(c,T) = \left(\frac{1}{4}c^4 - \frac{1}{2}c^2\right)\frac{T}{\tau} \quad (2)$$

where  $\tau$  is a phenomenological parameter introduced as a reference temperature, which characterizes the entropy of the system according to thermodynamics [24]. The local free energy density has two degenerate minima at 1 representing phase A and at -1 representing phase B. By adopting this form of local free energy density, the local free energy minimization tends to de-mix two phases, and the two-phase system has no mutual solubility. In this study, temperature is an input parameter that affects the kinetics of the system, chosen to be  $T=\tau$  when the temperature effect was not studied. Under this temperature setting, the potential well depth is 1/4 in eq. (2). The potential well depth is allowed to be changed independently of temperature in this study by adding a proportional constant in eq (2). It would also determine the relative role of bulk diffusion to the compositional evolution.

The local chemical potential of each molecule can be given by [20, 21]

$$\mu = \frac{1}{N_V} \frac{\delta F}{\delta c} = \frac{1}{N_V} \left( \frac{\partial f}{\partial c} - \alpha \nabla^2 c \right) \quad (3)$$

where  $N_V$  is the number density (number of molecules per unit volume),  $\frac{\delta F}{\delta c}$  is the functional derivative. The chemical potential is contributed by two parts: the first part,  $\frac{1}{N_V} \frac{\partial f}{\partial c}$ , depends only on local composition, which would be responsible for driving bulk diffusion; the second

part,  $\frac{\alpha}{N_V} \nabla^2 c$ , depends on both the local and neighboring composition fields, which drive interfacial diffusion. Under the small slope approximation (i.e. gradual compositional change across a diffuse interface), the second derivative of compositional field in space can be used to characterize the curvature of the interface. Therefore, the second part of the chemical potential,  $\frac{\alpha}{N_V} \nabla^2 c$ , is similar to the chemical potential on a curved surface,  $\gamma V \kappa$ , by the Gibbs-Thompson equation, where  $\alpha$  and  $\gamma$  stand for interfacial energy and  $\frac{1}{N_V} = V$ . The total chemical potential is a competition between interface and bulk-related chemical potential contribution. Our goal, therefore, is to investigate the dominating chemical potential gradient, contributed by either the bulk- or interface-related potential term, when spheroidization occurs.

The kinetics of diffusion can be described by Fick's First Law, which relates the diffusion flux  $J$  to the chemical potential gradient as

$$J = -N_V M \nabla \mu \quad (4)$$

where  $M$  is the atomic mobility, assumed to be constant. The mass conservation constraint for conserved field variables requires

$$\frac{\partial c}{\partial t} = -\nabla J \quad (5)$$

Therefore, the temporal and spatial evolution equation of the compositional field variable can be derived by combining eqs. (2)-(5) as

$$\frac{\partial c}{\partial t} = M \nabla^2 \left( \frac{\partial f}{\partial c} - \alpha \nabla^2 c \right) = M \nabla^2 \left[ (c^3 - c) \frac{T}{\tau} - \alpha \nabla^2 c \right] \quad (6)$$

Eq. (6) is called the Cahn-Hilliard equation. By numerically solving this non-linear partial differential equation, we can describe the diffusion-controlled morphological evolution of an

isostructural, two-phase system. Like most phase field simulations, we employ the second order finite difference discretization in space and explicit forward Euler method for time [23]. The temperature, interfacial energy coefficient and mobility in this equation are just parameters affecting the diffusion kinetics.

### Numerical Simulation Results

The numerical simulations are done in a two-dimensional (2D) square lattice with grid size  $a=1$ . The finite difference algorithm to evaluate the Laplacian in 2D is given by [20]

$$\nabla^2 c(i,j) = \frac{1}{2a^2} \left[ \sum_{NN} c(i,j) + \frac{1}{2} \sum_{NNN} c(i,j) - 6 * c(i,j) \right] \quad (7)$$

Where  $i,j$  indicates the position of the interested grid point, NN stands for nearest neighbor, NNN stands for next nearest neighbor. The time evolution of composition is given by the forward Euler method as

$$c(i,j,t+dt) = c(i,j,t) + \frac{\partial c}{\partial t}(i,j,t) * dt \quad (8)$$

The initial microstructures are set up as alternating complete phase A and phase B regions separated by single harmonic interfaces. Under this setting, the initial interfacial diffusion that drives mixing would be opposed against by the subsequent bulk diffusion that drives de-mixing. The cylindrical rod phase A would become rectangular in the longitudinal cross section for a 2D simulation. So if the perturbed rod radius of phase A is  $R_A + \delta \sin(2\pi \frac{x}{\lambda})$ , then the perturbed rod radius of phase B would be  $R_B - \delta \sin(2\pi \frac{x}{\lambda})$ . The effect of phase composition  $\frac{R_A}{R_B}$ , perturbation wavelength  $\lambda$  on shape change will be investigated in the following context. All simulations use periodic boundary conditions for all boundaries to eliminate the system-size effect.

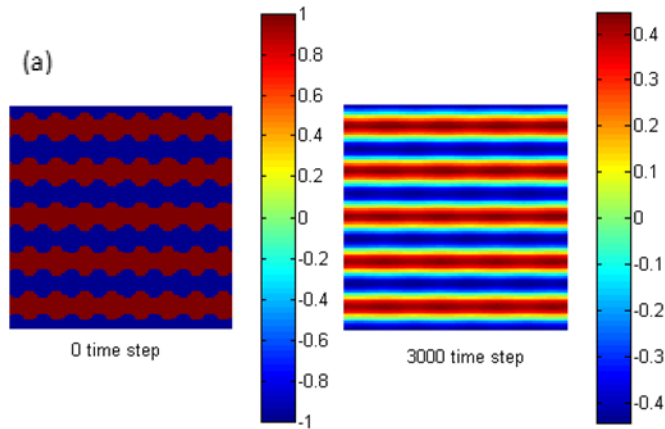


The effect of perturbation wavelength-applicability of Rayleigh instability criterion

The Rayleigh instability criterion claims that a rod would spheroidize if the perturbation wavelength  $\lambda$  is larger than the circumference of the unperturbed rod; otherwise it would smooth down. In a 2D case, the circumference of the unperturbed rod would be  $2R_A$ . In order to investigate if the combined diffusion-controlled morphology change satisfies this criterion, the following parameters are set up for the simulation:  $M = 1, T^* = \frac{\tau}{\tau} = 1, \text{ and } \alpha = 15$ . It is worthwhile to mention that in this study, we are only interested in qualitatively simulating the spheroidization phenomenon in two phase composites so that accurate input of all model parameters is not our concern. Therefore, the units of all input parameters and physical variables are neglected to avoid the wrong impression that the simulation is done quantitatively for a real physical system with input parameters coming from real thermodynamic and kinetic dataset. The system size is 100 by 100. Unperturbed rod radius  $R_A = R_B = 10$ , which suggests that the volume fraction of phase A is 50%, and the interfacial grid points account for 20% of the total grid points. The time step should be chosen small enough to maintain convergence and accuracy, large enough to reduce computational load and simulate long time duration. Here  $dt$  is chosen as  $4 * 10^{-3}$ . The perturbation amplitude  $\delta = 2$ . Three different perturbation wavelengths  $\lambda = 12.5, 20, 25$  are chosen to evaluate its effect on compositional evolution to determine if the Rayleigh instability criterion is applicable in this diffusion-controlled process.

The simulation results are given in Fig. 1. When the perturbation wavelength  $\lambda = 12.5$  (see Fig. 1. (a)) is less than the circumference  $2R_A$  of 2D unperturbed rod, the compositional profile flattens out. When  $\lambda = 20$  is equal to  $2R_A$ , the compositional field

begins to show some tendency toward spheroidization. When  $\lambda = 25$  is larger than  $2R_A$ , the compositional field become spheroidized. The simulation results show an obvious transition of compositional field from flattening to spheroidizing after a perturbation wavelength sweep from smaller than  $2R_A$  to larger than  $2R_A$ , which matches the description of Rayleigh instability criterion. From Fig. 1, it can also be concluded that the compositional field of a strongly curved interface (smaller  $\lambda$  in Fig. 1(a).) tends to become evenly distributed more quickly than that for a larger  $\lambda$  in Fig. 1(b) and (c). This can be explained by the fact that strongly curved interface has a larger initial chemical potential gradient, which acts as a larger driving force for diffusion to occur more rapidly. The experimental evidence of the applicability of Rayleigh instability criterion in spheroidization of two phase composites can be found in Ref [25, 26], which clearly showed that the spheroidized Nb rod had perturbation wavelength larger than the initial rod circumference.



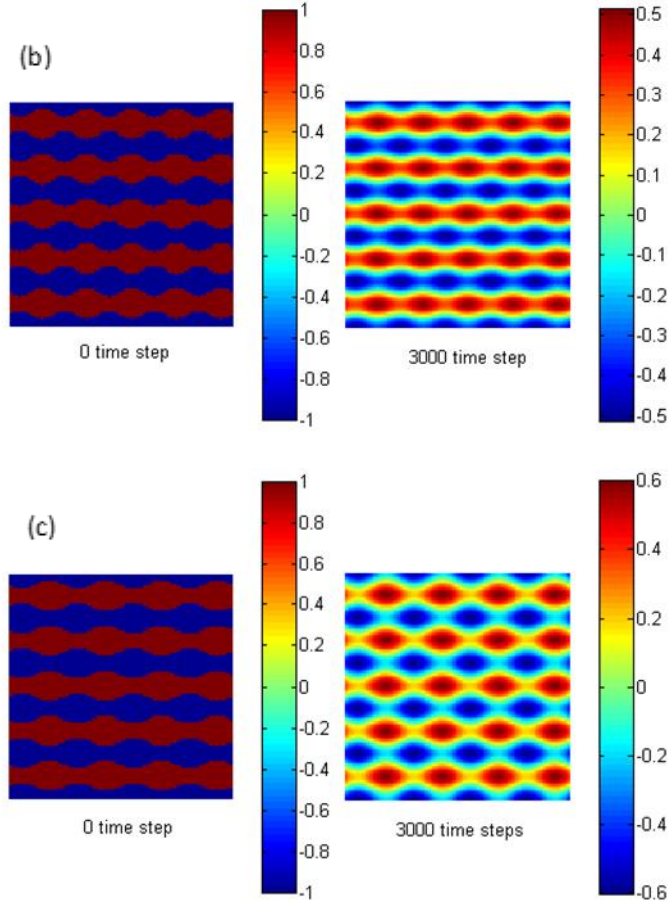


Fig. 1. The composition evolution in a two-phase system with size 100 by 100. The volume fraction of phase A (red) is 50%. The interface between phase A and phase B (blue) is a single harmonic perturbation with perturbation amplitude  $\delta = 2$ . Unperturbed rod radius  $R_A = R_B = 10$ . Time step  $dt = 4 * 10^{-3}$ . (a) Perturbation wavelength  $\lambda = 12.5$ ; (b) perturbation wavelength  $\lambda = 20$ ; (c) perturbation wavelength  $\lambda = 25$ .

The next thing to confirm is whether the interface-related chemical potential gradient in eq. (3) is the major driving force for the shape-change process. Therefore, the interface-related and bulk-related chemical potential distributions in the case of Fig. 1(c) at 1000, 3000 time steps are given in Fig. 2. The interface-related chemical potential gradient is roughly 2.8 and 2 times of its bulk-related counterpart at 1000 and 3000 time steps, respectively. Similar results can be obtained in the case of Fig. 1(a), but have not been included to reduce redundancy. This suggests that the interface-related chemical potential gradient is the major

driving force for the shape-reforming process, and it decreases more rapidly than the bulk-related chemical potential gradient as time progresses. This conclusion seems to match the previous statement in Ref [12, 13, 16] that the surface/interface diffusion is the dominating mechanism for the morphological change.

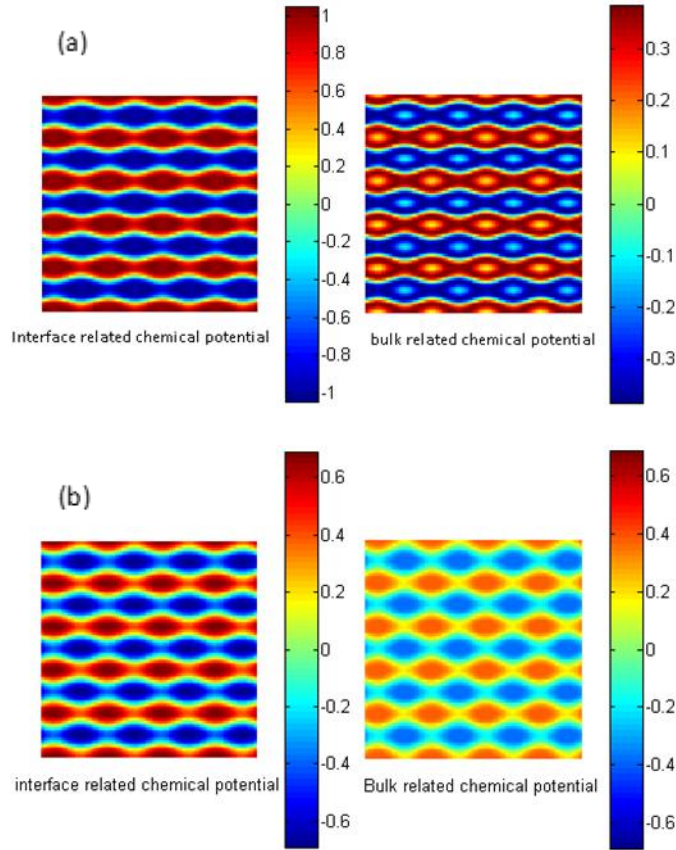


Fig. 2. The interface-related and bulk-related chemical potential distributions in the case of Fig. 1(c) at 1000 time steps (a) and 3000 time steps (b), respectively.

#### The effect of interfacial energy coefficient

In section 3.1, the interfacial energy coefficient,  $\alpha$ , is large so that compositional evolution is driven by a large interfacial chemical potential gradient to minimize the free energy as interpreted from eq. (6). The kinetics of the composition evolution should be directly affected by the value of  $\alpha$ . Therefore, three different  $\alpha$  values are chosen to compare

with the result in Fig 1(c) to investigate the effect of  $\alpha$  on spheroidization kinetics. The parameters are set up the same as in Fig. 1(c) except for the interfacial energy coefficient. The results of the compositional fields at 3000 time steps are given in Fig. 3, which clearly shows that a larger interfacial energy coefficient will yield a larger interfacial chemical potential (see eq. (6)) to drive the spheroidization of the compositional field faster.

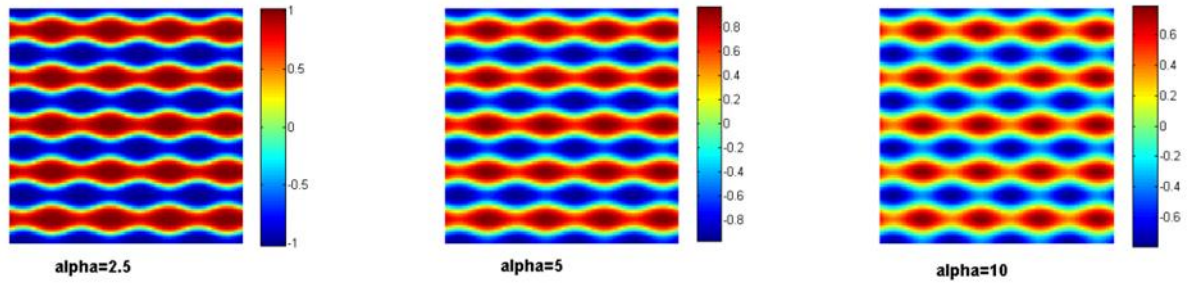
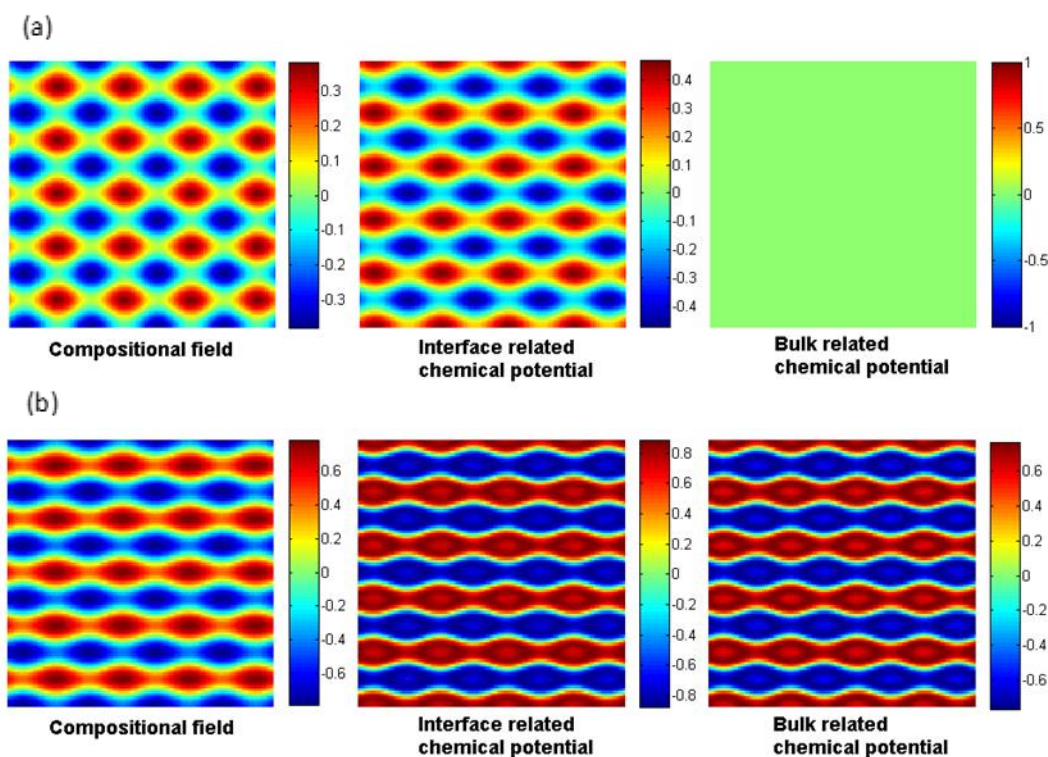


Fig. 3. The compositional field profiles at 3000 time steps for three different interfacial energy coefficients:  $\alpha = 2.5$  (left);  $\alpha = 5$  (middle); and  $\alpha = 10$  (right). The other parameters are the same as in Fig. 1(c). By comparing the composition evolution in Fig. 3 and Fig 1(c), it can be concluded that a larger interfacial energy coefficient yields faster spheroidization.

#### The effect of volume diffusion

From section 3.1, interfacial chemical potential is the major driving force for spheroidization. But the effect of volume diffusion on spheroidization is still unclear. In order to investigate the volume diffusion effect, we chose three double-well potentials with different potential well depths 0, 0.5, 1 to compare with the result in Fig. 1(c) with potential well depth  $\frac{1}{4}$ . The other parameters are the same as those in Fig. 1(c). The results from these three potential well depths at 3000 time steps are given in Fig. 4. Combining Fig. 4 and Fig. 1(c), it can be easily seen that as well depths increased from 0 to 1, the role of bulk free energy increased according to eq. (2); therefore, the bulk-related chemical potential will increase and become comparable with the interface-related chemical potential. The bulk

chemical potential tends toward de-mixing the two phases, which suppresses the compositional mixing driven by interfacial diffusion that favors a spheroidized compositional field. As a result, the spheroidization kinetics slows down substantially due to the less dominating role of interfacial diffusion. This is consistent with the previous conclusion that interface diffusion is the dominating mechanism for morphological change. For the case where well-depth is 0 (i.e. no volume diffusion, see Fig. 4(a)), the compositional spheroidization is much faster than that with a finite well-depth potential including the volume-diffusion effect. To summarize, the role of volume diffusion is to compete with interface diffusion to slow the spheroidization kinetics. If interfacial diffusion is dominating, the spheroidization occurs rapidly; otherwise, spheroidization will slow down substantially.





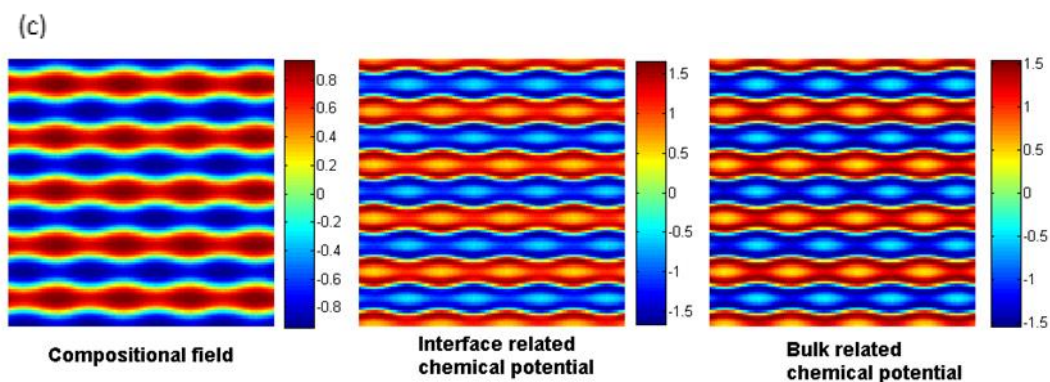


Fig. 4. The compositional field, interfacial chemical potential, and bulk chemical potential at 3000 time steps for three different potential well depths: (a) well depth=0; (b) well depth=0.5; and (c) well depth=1. The other parameters are the same as those in Fig. 1(c) where well depth was 0.25.

The effect of temperature on the spheroidization kinetics can be understood in a similar way as the effect of potential well depth when considering volume diffusion. According to eq. (2), increasing temperature would essentially have the same effect on increasing volume diffusion as increasing potential well depth by a linear temperature dependence of bulk free energy under a constant-entropy approximation. On the contrary, previous studies [27, 28] showed that increasing temperature would decrease the interfacial energy. The combined effect of these two would be unfavorable to spheroidization. It has been experimentally observed that coarsening is more favored than spheroidization at high temperature in Cu-Nb system [7]. Raabe et al [29] also observed that the initially heavily curled Cr filaments in Cu-Ag matrix undergo a morphological transition from spheroidization to competitive coarsening at 1273 K for 4 h. Since the temperature dependence of the interfacial energy is much more diverse and system-dependent [27, 28], there is some complexity and uncertainty when evaluating the temperature effect.

### The effect of phase composition

In previous discussions, the volume fraction of phase A was 50%. In order to investigate the effect of phase composition on the compositional spheroidization, two volume fractions of phase A, 40% and 30%, were chosen. The other parameters for calculation were the same as those in Fig 1(c). The results of compositional field, interface-related, and bulk-related chemical potentials at 3000 time steps are shown in Fig 5. By comparing Fig 1. (c), Fig 5. (a) and Fig 5. (b), it can be concluded that as the volume fraction of phase A decreases, the compositional spheroidization of phase A accelerates. The possible reason is that in all three cases, we have the same amount of interfacial grids (20% of the total), which yields the same initial interfacial diffusion driving forces. The less amount of phase A in Fig. 5(b) would subject its compositional field more to the interfacial diffusion. Therefore, interfacial diffusion plays a more dominating role on phase A in Fig. 5(b) than in Figs. 1(c) and 5(a). This can be directly verified by the relative ratio of interface-related chemical potential to bulk-related chemical potential in Fig. 5. The ratio of interface-related to bulk-related chemical potential of phase A region in Fig. 5(b) is roughly twice as much as that in Fig. 5(a). As a result, the more dominating interfacial diffusion in phase A of Fig. 5(b) would lead to faster compositional spheroidization of phase A as discussed in previous sections. This is consistent with the experimental observations that the minor filament phase is the spheroidized phase [5-7].



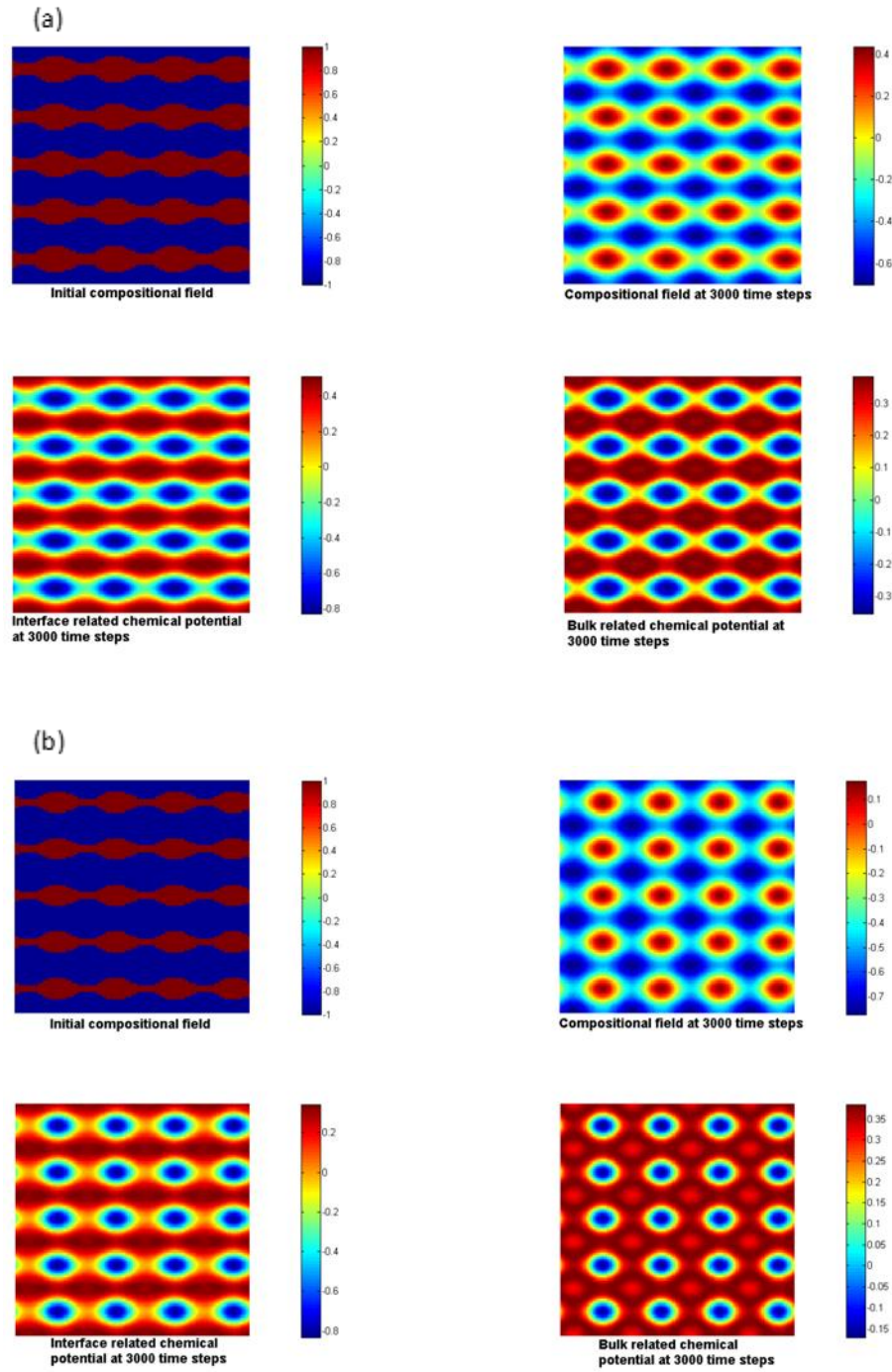


Fig. 5. Two initial compositional fields with different volume fractions of phase A are given to study the effect of phase composition on spheroidization. The other parameters are the same as those in Fig. 1(c). The compositional field, interface-related, and bulk-related chemical potential distributions at 3000 time steps are given: (a) 40 vol. % of phase A. (b) 30 vol. % of phase A.

### The effect of interface area

In the previous discussions (e.g. Fig. 1(c).), the lattice points at the interface account for 20% of the total lattice points in the system. Here, the interface area percentage is chosen to be 8% to be compared with the case in Fig. 1(c) to study the effect of interface area on the spheroidization kinetics. All other parameters for calculation are the same as those in Fig. 1(c). The results of compositional field, interface-, and bulk-related chemical potential distributions at 3000 time steps are given in Fig. 6. By comparing Fig. 6 with Fig. 1(c), it can be found that decreasing the interfacial area percentage from 20% to 8% would substantially decrease the spheroidization kinetics. The reason should be that the decreased interfacial area would lower the interfacial diffusion driving force, exerting less effect on the compositional evolution of both phases to be spheroidized. This can be verified by the ratio of interface- to bulk-related chemical potential of phase A in Fig. 2(b) and Fig. 6. This ratio in Fig. 6 is 1.5 compared with 2.2 in Fig. 2(b). This decreased interfacial driving force would slow down the compositional spheroidization. Generally, the interfacial area percentage is inversely proportional to the size of filament spacing and/or filament thickness in real systems. The large interfacial area percentage may be the reason why spheroidization is usually experimentally observed in sub-micron/nano-size composite systems [5, 7].

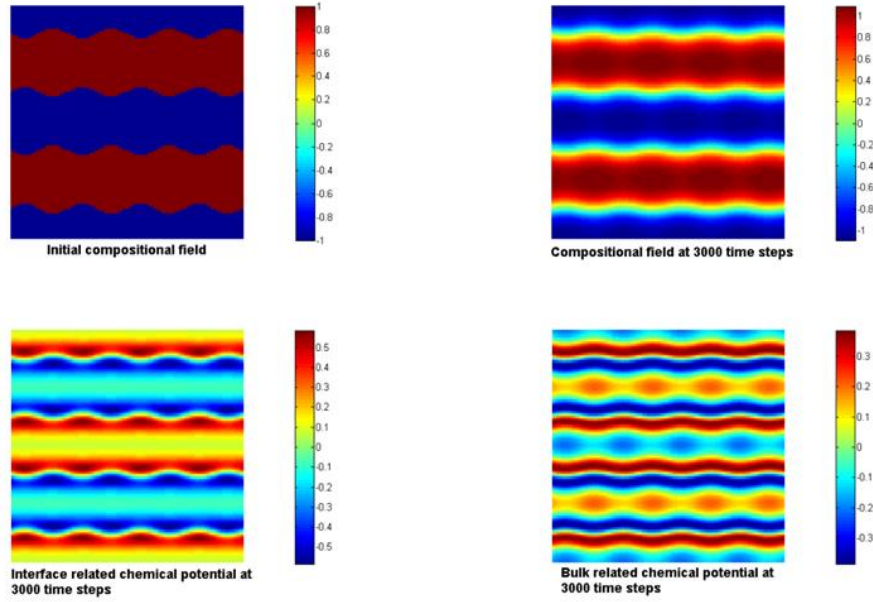


Fig. 6. The compositional field, interface-related, and bulk-related chemical potentials at 3000 time steps for a system with 8% interfacial area. The other parameters are the same as those in Fig. 1(c).

### Conclusions

In this paper, the interfacial diffusion-driven spheroidization of a two-phase system containing mutually insoluble phases was studied by the diffuse-interface phase field approach. A single conserved compositional field variable is used to describe the morphological change under an isostructural assumption to simplify calculation. The temporal and spatial evolution of the compositional field is described by the Cahn-Hilliard non-linear partial differential equations. Under a combined effect of interfacial diffusion and volume diffusion, the system would change its morphology if the interfacial diffusion is the dominating driving force for the compositional evolution. Perturbation of the cylindrical rod radius is a necessity to generate the initial interfacial chemical potential gradient to drive the morphology evolution. Whether the perturbed cylinder will spheroidize or smooth down would depend on the perturbation wavelength and the initial unperturbed rod

circumference. According to our simulations, the spheroidization for our system matches very well with the Rayleigh instability criterion. This is a reasonable result since interfacial diffusion is the dominating driving force for morphological evolution in both our study and Rayleigh's theory. Increasing the interfacial energy would enhance the interfacial diffusion contribution and accelerate the spheroidization kinetics. The bulk/volume diffusion driving de-mixing of the two phases seems to impede the spheroidization by competing with the interfacial diffusion. The volume fraction bias between two phases would favor the spheroidization of the minor phase, which has been observed in experiments [5-7]. A size effect also exists for spheroidization kinetics by changing the interfacial area percentage. Spheroidization has been frequently observed in experimental nano-scale composite systems [5, 7] because the large interfacial area provides a large driving force for interfacial diffusion.

#### References

1. H.P. Stuwe and O. Kolednik, *Acta metal.* 36, 1705 (1988).
2. E Werner, *Acta metal.* 37, 2047 (1989).
3. M. Mcleana, *Philos. Mag.* 27, 1253 (1973).
4. M.E. Toimil Molaes, A.G. Balogh, T.W. Cornelius, R. Neumann, C. Trautmann, *Appl. Phys. Lett.* 85, 5337 (2004).
5. X Kai, A.M. Russell, *J. Mater. Sci.* 37, 5209 (2002).
6. E. Ogris, A. Wahlen, H. Lüchinger, P.J. Uggowitzer, *J. Light Met.* 2, 263 (2002).
7. M.J.R. Sandim, H.R.Z. Sandim, D. Stamopoulos, R.A. Renzetti, M.G. Das Virgens, and L. Ghivelder *IEEE Trans. Appl. Supercond.* 16, 1692 (2006).
8. L. Rayleigh, *Proc. London Math. Soc.* 10, 4 (1878).
9. J. Choy, S.A. Hackney, and J.K. Lee, *J. Appl. Phys.* 77, 5647 (1995).

10. W. Mullins, J. Appl. Phys. 30, 77 (1959).
11. C.A. Johnson, Surf. Sci. 3, 429 (1965).
12. F.A. Nichols and W.W. Mullins, J. Appl. Phys. 36, 1826, (1965).
13. F.A. Nichols and W.W. Mullins, Trans. AIME 233, 1840 (1965).
14. E. Ho and G.C. Weatherly, Acta metal. 23, 1451, (1975).
15. T Courtney and J Kampe, Acta metal. 37, 1747, (1989).
16. H.L. Duan, IUTAM Symposium on Scaling in Solid Mechanics 10, 253, (2009).
17. L.Q. Chen, Annu. Rev. Mater. Res. 32, 113, (2002).
18. N. Moelans, B. Blanpain and P. Wollants, Comput Coupling Phase Diagr Thermochem 32, 268, (2008).
19. J.Z. Zhu, T. Wang, S.H. Zhou, Z.K. Liu, L.Q. Chen, Acta Mater. 52, 833 (2004).
20. R. Lesar, Introduction to Computational Materials Science: Fundamentals to Applications, (Cambridge University Press, NY, 2013).
21. J Zhu and L.Q. Chen, Phys. Rev. E 60, 3564, (1999).
22. N. Lecoq and H. Zapolsky, Discret Contin Dyn S 2011, 953, (2011).
23. D. Raabe, F. Roters, F. Barlat and L.Q. Chen, Continuum Scale Simulation of Engineering Materials, (Wiley-VCH, Weinheim, 2004).
24. D.R. Gaskell, Introduction to Metallurgical Thermodynamics, (Taylor & Francis, Bristol Pa, 1981).
25. H.R.Z. Sandim et al, Scripta Mater. 51, (2004).
26. D. Raabe, K. Miyake, H. Takahara, Mat Sci Eng A, 291 (2000).
27. H.M. Lu and Q. Jiang, J. Phys. Chem. B 109, 15463 (2005).
28. J.W. Cahn and J.E. Hilliard, J. Chem. Phys. 28, 258 (1957).
29. D. Raabe, J. Ge, Scripta Mater 51 (2004).

## CHAPTER 9 GENERAL CONCLUSIONS

### General Discussions

This study investigated the processing-microstructure-properties relationship in a deformation processed Al/Ca composite by developing both experimental and theoretical understandings to design next generation lightweight, high strength, high electrical conductivity Al/Ca composite conductor as high voltage power transmission cable. This research suggests that the Al/Ca (20 vol.%) composites show promise to replace the current high voltage power cables such as Aluminum Conductor Steel Reinforced (ACSR). The following is a summary of the results of each chapter and how they are contributing to the overall goal of developing a lightweight, high strength, high electrical conductivity Al/Ca composite conductor, as well as the recommendations for future research.

Chapter 2 experimentally studied the processing-microstructure-strength/conductivity relationship in 1<sup>st</sup> generation Al/Ca (9 vol. %) composites produced by power metallurgy and deformation processing. Most Ca filaments adopted a nearly cylindrical rod shape after deformation processing. Ca filament thickness decreased exponentially as deformation progressed, which created a large amount of interface area that acted as barrier to dislocation motion to strengthen the composite. The ultimate tensile strength of this Al/Ca composite increased substantially as deformation true strain increased, which can be quantified by a modified Hall–Petch barrier model. The commercially available Ca granules (diameter ~1.2 mm) used in producing this Al/Ca composite are deformed to 2  $\mu\text{m}$  filament size after a deformation true strain 13.8, which gives the composite a strength of 197 MPa. This 2  $\mu\text{m}$  filament size is insufficiently fine enough to create substantial strengthening effect based on

previous research on Al-Ti [1] and Al-Mg [2]. Therefore, fine Ca metal powders (around 200  $\mu\text{m}$ ) would be needed to produce next generation Al/Ca composite with higher strength. Filament coarsening and spheroidization were observed by SEM after heat treatment at 325 °C. Two intermetallic compounds  $\text{Al}_4\text{Ca}$  and  $\text{Al}_2\text{Ca}$  formed at elevated temperature 225 °C and 275 °C, as determined by SEM, DSC, and XRD. The resistivity of Al/Ca (9 vol. %) composite 0.027  $\mu\Omega\cdot\text{m}$  can be explained by the inverse rule of mixtures (ROMs) very well and increased to 0.030  $\mu\Omega\cdot\text{m}$  after heat treating at 300 °C for 1h due to the formation of  $\text{Al}_2\text{Ca}$  that can be explained well by inverse ROMs of 84 vol. % Al and 16 vol. %  $\text{Al}_2\text{Ca}$  with Ca fully converted.

Chapter 3 developed a dislocation density based, strain gradient strengthening model to predict the strength of deformation processed metal metal composites that Al/Ca composite belongs to. This model is based on the modified rule of mixtures in which the strength of each phase obeys the Taylor's dislocation hardening law with additional contribution from geometrically necessary dislocations (GNDs) emitted from the interface to accommodate the strain gradient. A physical link between the density of GNDs and the effective strain gradient has been established to incorporate the strain-gradient hardening effect. An intrinsic material length scale was introduced to compare with the characteristic microstructure length scale to evaluate the extent of the strain-gradient effect. Large deformation true strain leads to a small characteristic microstructure length, causing a strong strain-gradient effect when it is comparable with relatively large intrinsic material length. The dominating strain-gradient effect at large deformation true strain is responsible for the anomalous high strength of heavily cold-worked DMMCs, which deviates from the rule of mixtures prediction. This strain-gradient hardening model can predict the experimental

strengths of Cu/Nb, Cu/Ta, and Al/Ti DMMCs well over the entire deformation true strain range. We can apply this model to Al/Ca composite after obtaining a complete strain hardening curve of high purity Ca metal. This model also interprets that when the initial size of second phase approaches the intrinsic material length (usually around 100  $\mu\text{m}$ ), the strain gradient effect would be dominating at large deformation true strain and strengthen the composite substantially above the ROM predictions. This is the reason why we choose to produce fine Ca metal powders with size range from 100 to 300  $\mu\text{m}$  to get our next generation Al/Ca composite with higher strength. Comprehensive tests of high purity Ca tensile strengths at various deformation true strain levels should be performed in the future to obtain a complete strain hardening curve of Ca as input into our strain gradient strengthening model to predict the strength of Al/Ca composite.

Chapter 4 developed an approach to model the electrical resistivity of deformation processed metal-metal composites by a modified inverse rule of mixture that combines all the plausible scattering mechanisms such as interfaces, grain boundaries, impurities, phonons and dislocations. Interface and grain boundary scattering models are re-interpreted in DMMCs by considering filament morphological evolution during deformation processing. The role of grain boundary scattering are incorporated into our model by treating each metal phase as a single row of single crystals so that the grain boundary scattering would show a similar thickness dependence to interface scattering. This modeling approach has been successfully applied to the Cu-Nb, Au-Ag and Cu-Ag-Nb systems. We found that filament coarsening instead of dislocation annihilation is primarily responsible for the resistivity drop after annealing treatment or high temperature resistivity measurement in Cu-Nb DMMC. This is because the dislocation density has been confirmed by experiments to be sufficiently



low in as deformed DMMCs to have negligible scattering effect. The increasing resistivity with increased deformation is attributed to the reduced filament thickness and spacing that would increase the interface and grain boundary scattering. When applying this modeling approach to Al/Ca DMMCs, the major additional scattering mechanisms (i.e. interfaces and grain boundaries) is negligible for our expected Ca filament size around 200 nm that is much larger than the Ca's electron mean free path 27 nm determined by phonon scattering. This means that the electrical resistivity of Al/Ca DMMCs can be predicted by an inverse rule of mixtures of pure Al and pure Ca.

Chapter 5 developed a centrifugal atomization approach with rotating quench bath in inert atmosphere to produce fine Ca metal powders around 200  $\mu\text{m}$  for the production of 2<sup>nd</sup> generation Al/Ca composite with higher strength based on previous strengthening model while not degrading its conductivity based on previous electrical resistivity model. The powder characteristics such as mean particle size, particle size distribution, production yield and particle morphology was studied to evaluate the performance of the atomization condition. The mean particle size of atomized Ca powders from two atomization runs was about 150  $\mu\text{m}$ . The particle size distribution provided the evidence of a ligament disintegration atomization mode at the atomization disk edge, which is also supported by the solidified ligaments at disk edge after atomization. The production yield of fine Ca powders less than 250  $\mu\text{m}$  is as high as 83% of the total powders produced by the centrifugal atomizer. SEM micrographs showed that the larger Ca powders (i.e. 177-250  $\mu\text{m}$ ) tend to have irregular shapes, and the smaller Ca powders (i.e. 74-105  $\mu\text{m}$ ) tend to be spherical, which can be explained by a secondary atomization mechanism that distorted the particle morphology when partially liquid Ca droplets impinged upon the quench bath. This mechanism can be

supported by the morphology of the powders produced by filling the atomizer chamber with higher thermal conductivity helium gas. Helium gas cooled the in-flight liquid Ca droplets faster; thus a larger portion of droplets will fully solidify before reaching the quench bath, increasing the fraction of spherical particles that has been observed by our experiments. Spark testing and thermal gravimetric (TG) tests showed that these fine Ca powders were passivated well and posed no greater hazard than powders of other metals, thus should be safe to handle. The effects of processing parameters (e.g. disk rotational speed and radius, liquid flow rate, type of inert gas atmosphere and atomization disk material) on powder characteristics will be investigated independently in the future. Scale-up production of fine Ca metal powders are being planned with collaboration from industrial partners.

Chapter 6 evaluated the application prospects of Al/Ca composite as overhead high voltage power transmission cables by discussing its design process, production method, physical properties and economic benefits. The low density, high strength, high conductivity and good corrosion resistance of Al/Ca composite conductor would allow substantial reduction in construction cost, energy loss cost and an increase in reliability and service life of the transmission line. Additionally, a thermal analysis was performed to show how high conductivity and large cross sectional area will be beneficial to lower the equilibrium temperature during emergency overload situations or to increase the maximum power-carrying capacity under a specified maximum operation temperature. Therefore, in terms of economics, reliability and sustainability, the application prospects for Al/Ca composite conductors are very promising and deserves continued interests from both industrial partners and research institutions.

Chapter 7 studied the processing-microstructure-properties relationship in 2<sup>nd</sup> generation Al/Ca (20 vol. %) composite produced with initial fine Ca metal powders around 200  $\mu\text{m}$  diameter. As predicted by the Hall-Petch barrier model in Chapter 2, the strength of Al/Ca composite increased rapidly when Ca filament size reached submicron level. However, this filament size is still too coarse to generate obvious scattering effects from interfaces and grain boundaries, as mentioned in Chapter 4, so that the current experimental electrical conductivity of Al/Ca composite can be estimated by the rule of mixtures. DSC tests of these Al/Ca composite wires at high deformation true strain showed two exothermic events with low temperature event corresponding to the formation of  $\text{Al}_4\text{Ca}$  and high temperature event corresponding to the formation of  $\text{Al}_2\text{Ca}$ .  $\text{Al}_4\text{Ca}$  is highly unstable and will decompose into  $\text{Al}_2\text{Ca}$  quickly so that its formation was not observed at low deformation true strain wire due to small amount of formation and the rapid decomposition. Thus, a broad exothermic peak was observed. For high deformation true strain sample, the exothermic peak corresponding to the formation of  $\text{Al}_4\text{Ca}$  was observed due to the larger amount of  $\text{Al}_4\text{Ca}$  formation at greatly increased interface area of finer Ca filaments. This fact corresponds well with the resistivity measurements for Al/Ca wire annealed at elevated temperature for different durations. At low annealing temperature, the small resistivity increase initially was due to the formation of  $\text{Al}_4\text{Ca}$ . Then, the resistivity increased slowly due to the slow decomposition of  $\text{Al}_4\text{Ca}$  into  $\text{Al}_2\text{Ca}$  at low temperature. At high annealing temperature, the decomposition of  $\text{Al}_4\text{Ca}$  into  $\text{Al}_2\text{Ca}$  was so fast that the resistivity increased rapidly to the value determined by  $\text{Al}_2\text{Ca}$  and maintained relatively constant for further durations. Further work are needed to investigate the reaction kinetics of  $\text{Al}_4\text{Ca}$  and  $\text{Al}_2\text{Ca}$  at elevated temperature possibly by Advanced Photon Source (APS) at Argonne National

Laboratory or more comprehensive resistivity measurements after annealing at a set of temperatures for different durations. The strength of Al/Ca composite at various deformation true strains after annealed at different elevated temperature can also be studied in the near future. Additional research are also needed to investigate the fatigue strength, fracture toughness, creep behavior of the composite over the temperature range from  $-40^{\circ}\text{C}$  to  $200^{\circ}\text{C}$ , the strength and conductivity of the composite with varying Ca volume fraction, the coronal discharge behavior of this composite etc, in an actual outdoor field testing at the Oak Ridge National Laboratory Powerline Conductor Accelerated Testing facility.

Chapter 8 used diffuse interface phase field approach to simulate the cylindrical filament spheroidization in a composite comprised of two mutually insoluble phases in a two dimensional case. A single conserved compositional field variable is used to describe the morphological change under an isostructural assumption to simplify calculation. The filament spheroidization was believed to be driven by interfacial diffusion, which was caused by the chemical potential gradient due to the perturbation of rod radius. We found that the filament spheroidization criterion matched Lord Rayleigh's instability theory, which states that a radius perturbation wavelength larger than the initial rod circumference would lead to cylindrical spheroidization. Increasing the interfacial energy would enhance the interfacial diffusion contribution and accelerate the spheroidization kinetics. The bulk/volume diffusion driving de-mixing of the two phases seems to impede the spheroidization by competing with the interfacial diffusion. The volume fraction bias between two phases would favor the spheroidization of the minor phase. Spheroidization has been frequently observed in experimental nanoscale composite systems due to a larger interfacial area percentage. This interfacial diffusion driven phase morphological change should be able to be applied to

Al/Ca composite at elevated temperature since Al and Ca are mutually insoluble. Future research work are needed on Al/Ca interface to observe the intrinsic perturbation of interfaces by experiments so that we can decide if the filament spheroidization criterion would be satisfied in Al/Ca composite system. A preliminary study on Al/Ca interface at elevated temperature has been done in Appendix A whose supporting materials can be found in Appendix B.

#### References

1. AM Russell, T Lund, LS Chumbley, FA Laabs, LL Keehner, JL Harringa (1999) Compos Part a-Appl S 30: 239. Doi:Doi 10.1016/S1359-835x(98)00163-8
2. K Xu, AM Russell, LS Chumbley, FC Laabs, VB Gantovnik, Y Tian (1999) J Mater Sci 34: 5955. Doi:Doi 10.1023/A:1004772526480

## APPENDIX A. A PRELIMINARY STUDY OF THE AL/CA INTERFACE AT ELEVATED TEMPERATURE

Liang Tian<sup>1</sup>, Trevor Riedemann<sup>2</sup>, Iver Anderson<sup>3</sup>, Alan Russell<sup>3</sup>

1. Primary research and author 2. Primary experimentalist 3. Principal project  
investigators

### Abstract

Al/Ca composite is a type of deformation processed metal metal composite with light weight, high strength, and high electrical conductivity that has potential to be used as high voltage overhead power transmission conductor. The elevated temperature performance of Al/Ca composite is critical to the security of the power grid system under emergency overloading. In this paper, we did a preliminary study on the microstructure evolution at the Al/Ca interface under elevated temperature to evaluate its impact on the performance of Al/Ca composite by both experiment and simulation. Al/Ca diffusion couples have been produced by swaging high purity Ca filled pure Al cylinder and annealed at 356 °C for 2 weeks to inspect the microstructure at the interface by Auger electron spectroscopy. Selected physical properties of stable intermetallic compound  $\text{Al}_2\text{Ca}$  have been measured to evaluate the effect of its formation on the properties of Al/Ca composite. Finally, preliminary molecular dynamics simulations have been done by the Sandia LAMMPS molecular dynamics package with reactive force field on Al/Ca bicrystal interface to give some insights on how the microstructure changes at the interface.

## Introduction

Al/Ca composite is a type of metal-metal composite that is expected to have light weight, high strength, and high electrical conductivity. It may have future application as overhead high voltage power transmission cables [1]. Al/Ca composite is processed by powder metallurgy and severe plastic deformation to obtain two pure phases bonded by interfaces. The high strength of this type of composite comes from the large interface area acting as a barrier to dislocation motion while the high electrical conductivity can be attributed to the conductive pathways of two pure metal phases with minimal interphase boundary scattering [2]. The elevated temperature performance of Al/Ca composite is critical to the safety of power grids when power lines are overloaded under emergency. The microstructure evolution of Al/Ca composite at elevated temperature is controlled by the Al/Ca interface. Therefore, it was our purpose to study the Al/Ca interfaces at elevated temperature to understand how microstructure changes at the interface. Both experimental and computational approaches have been utilized to pursue this goal. Al/Ca diffusion couples were prepared by swaging high purity Ca filled Al cylinders and cutting them into small coupons by electrical discharge machining for Auger electron spectroscopy analysis of the interface microstructure. The physical properties of  $\text{Al}_2\text{Ca}$ , the most stable intermetallic compound in the Al-Ca binary system, have been tested to evaluate the effect of its formation at elevated temperature on the properties of Al/Ca composite. Molecular dynamics simulations have been done on an Al/Ca bicrystal using a reactive force field to provide some guidance on the microstructure evolution at the interface.

### Al/Ca Diffusion Couple Experiments

High-purity 99.999% electrolyzed Al from Tosoh SMD Inc was used by Materials Preparation Center (MPC) at Ames Laboratory to make an Al cylinder with an Al end plug (Fig.1). The Al cylinder was drilled a hole to be filled with high-purity distilled calcium. The Al cylinder and Al plug were soaked in 2% sodium hydroxide solution for about 3 mins to remove the surface oxide and then rinsed with methanol just before they are put into an argon-filled glove box. Small pieces calcium with total mass of 8.0 grams were loaded into the hollow part of the cylinder and packed tightly to produce a packing density of 53%. Then the Al/Ca cylinder assembly was electron-beam welded in vacuum, swaged at room temperature to 12.9 mm (0.51") diameter and cold-rolled at room temperature to 5.1 mm (0.2") thickness to break any possible oxide at the interface and to form a uniform and clean Al/Ca interface. Then the as-rolled sample was sheared into many pieces of 25 mm (1") long coupons with both ends cold welded by the crimping machine. A test in which two coupons were submerged in water showed no hydrogen bubble release, suggesting that both ends of the coupons were Al cold welded by the pinching machine, and the Ca was not exposed to the exterior environment. Two as-rolled coupons were chosen and cut into pieces 4.3 mm long by electrical discharge machining for metallographic sample preparation followed by Auger electron spectroscopy (AES) analysis to observe the microstructure across the interface. Since all coupons were cold welded and protected by Al, one coupon was chosen to be heat treated in air at 356 °C for 2 weeks to observe the possible microstructure change at elevated temperature. All the remaining coupons went through annealing at 150 °C for 1 hour in air to achieve recovery and recrystallization to eliminate the increased dislocation densities from cold working that would otherwise increase the self-diffusion of Al and Ca,



respectively. Two as-annealed coupons were cut into pieces for AES sample preparation to be compared with as-rolled samples and elevated temperature annealed samples.

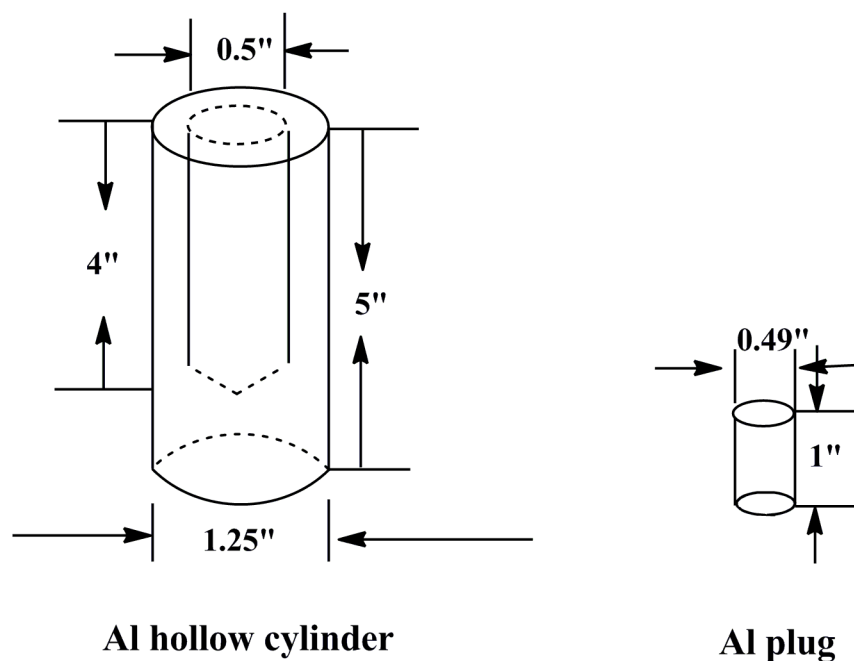
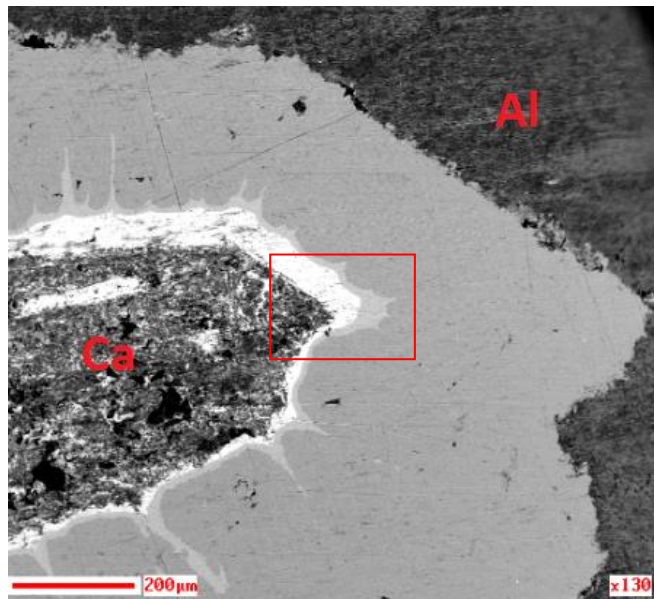


Fig.1. The schematic dimension of Al cylinder and Al plug prepared by Materials Preparation Center (MPC) at Ames Lab. Dimensions are in inches.

The Al/Ca coupon annealed for two weeks at 356 °C was cut by electrical discharge machining and mounted and polished with silicon carbide grit paper up to 1200 in kerosene medium and 1 micron glycol-based diamond suspension to minimize oxidation. The samples were then wiped with hexane just before inserting them into the Auger microprobe for surface analysis. A final fine polishing was done inside a glove bag containing an argon atmosphere. Fig 2. (a) shows the backscattering electron image of the Al/Ca interface after annealing at 356 °C for 2 weeks. It clearly showed that there are 3 different phases formed across the interface. Five points in these different areas across the interface were chosen for Auger surface composition analysis, as shown in Fig. 2(b). The results of these five composition analyses are given in Table 1. As these data show, from point 1 to point 5, the

Ca atom percentage decreases gradually, while Al content increases concomitantly, which is consistent with a diffuse interface condition. Despite efforts made to minimize oxidation, it is clear that oxidation did occur, and oxygen maintains a roughly constant percentage of about 40% on the surface layer. It is difficult to determine accurate stoichiometry of those three newly formed phases at the interface without removing the surface oxygen contained layer. These three different phases across the interface after elevated temperature annealing could be investigated further by higher vacuum instruments in the future. Similar work on as-rolled and as-annealed Al/Ca coupons could be done in future investigations.



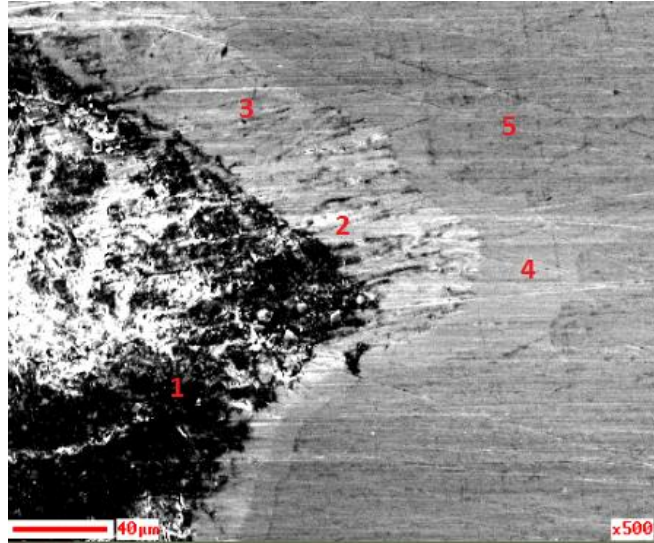


Fig. 2 (a) The backscattered electron image of the Al/Ca interface annealed at 356 °C for 2 weeks (1.21 million seconds). Image shows 3 different newly formed phases across the interface. (b) 5 points across the interface were chosen for Auger surface composition analysis (secondary electron imaging mode). Region shown in (b) is the highlighted area in (a). Accelerating voltage is 10 kV for all images.

Table 1. The surface composition analysis results of previously selected 5 points across the Al/Ca interface.

Point #	Al at. %	Ca at. %	O at. %	Al/Ca ratio
1	15	48.8	36.2	0.31
2	15.7	43.1	41.1	0.36
3	17.3	42.8	40	0.40
4	34.1	28.3	37.6	1.21
5	35.8	23.6	40.7	1.52

### Physical Properties of Al<sub>2</sub>Ca

High-purity Al (11.6 grams) and high-purity Ca (8.6 grams) were arc melted into a button and dropcast to form a 10mm diameter Al<sub>2</sub>Ca rod sample. Some part of the rod was filed into powders in a glove box and analyzed by X-ray diffraction. Fig. 3 shows the

experimental X-ray diffraction pattern of these filed powders compared with the  $\text{Al}_2\text{Ca}$  pattern calculated by the Rietveld method. The experimental peak positions and intensities matched well with those of the theoretically calculated  $\text{Al}_2\text{Ca}$ . This suggests that the sample produced by this method is indeed pure  $\text{Al}_2\text{Ca}$  without other phases present. Some peak broadening is visible in the pattern shown in Fig. 3, which result from elastic strain present in the filed pieces.

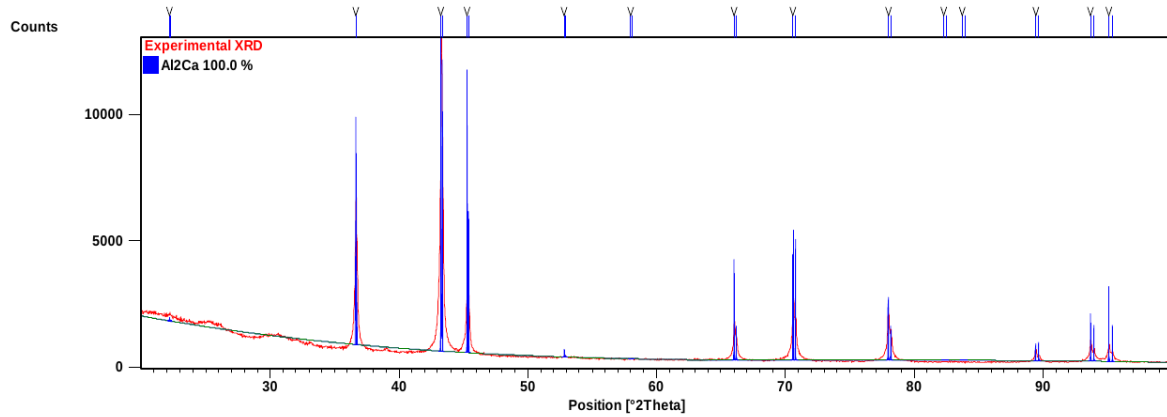


Fig.3. The experimental X-ray diffraction pattern of filed powders from arc-melted rod. As a contrast, the theoretically calculated  $\text{Al}_2\text{Ca}$  diffraction pattern was superimposed to confirm that these filed powders are pure  $\text{Al}_2\text{Ca}$ .

The arc-melted  $\text{Al}_2\text{Ca}$  rod sample was cut into small pieces with a square cross section roughly 1 mm by 1 mm using electrical discharge machining. Then the electrical resistivity of two short pieces of these samples was measured by four-point probe method. The results of two measurements are presented in Table 2. The accuracy of these measurements may not be high since it is difficult to obtain accurate resistance measurements on such short samples. From Table 2, the average resistivity from these two measurements is  $0.11 \mu\Omega\cdot\text{m}$ , which is roughly 4 times that of pure Al. Thus the formation of  $\text{Al}_2\text{Ca}$  at elevated temperature during emergency overloading would increase the resistivity of Al/Ca composite substantially, which would degrade power grid stability.

Table 2. The resistivity measurements of two independent Al<sub>2</sub>Ca samples by four point probe method

	Length (mm)	Cross section area (mm <sup>2</sup> )	Measured voltage (V)	Constant current (mA)	Resistivity ( $\mu\Omega \cdot m$ )
Sample 1	13.0	1.05	0.00012	100	0.097
Sample 2	23.3	1.09	0.00027	100	0.126

The thermal expansion coefficients of Al (23.6  $\mu m/m$  °C) and Ca (22.8  $\mu m/m$  °C) are nearly equal so no bi-metal thermal fatigue problem is anticipated. However, the coefficient of thermal expansion for the newly formed Al<sub>2</sub>Ca intermetallic compound has not been reported in the literature. The coefficient of thermal expansion for Al<sub>2</sub>Ca was measured in this study by a NETZSCH DIL 402 C dilatometer under He gas atmosphere with flow rate 100 mL/min. The sample length is 7.38 mm. The heating profile was from 25 °C to 300 °C with a heating rate of 5 °C/min. The measured length expansion fraction versus temperature is shown in Fig 4. This figure clearly shows a linear relation between length expansion and temperature, which gives a thermal expansion coefficient of 13  $\mu m/(m \cdot ^\circ C)$  for Al<sub>2</sub>Ca. This value is about half that of pure Al and pure Ca so that Al<sub>2</sub>Ca formation in Al/Ca composite wire at elevated temperature could possibly cause some long-cycle thermal fatigue problems but the intermetallic has the positive effect of reducing sag at elevated temperature.

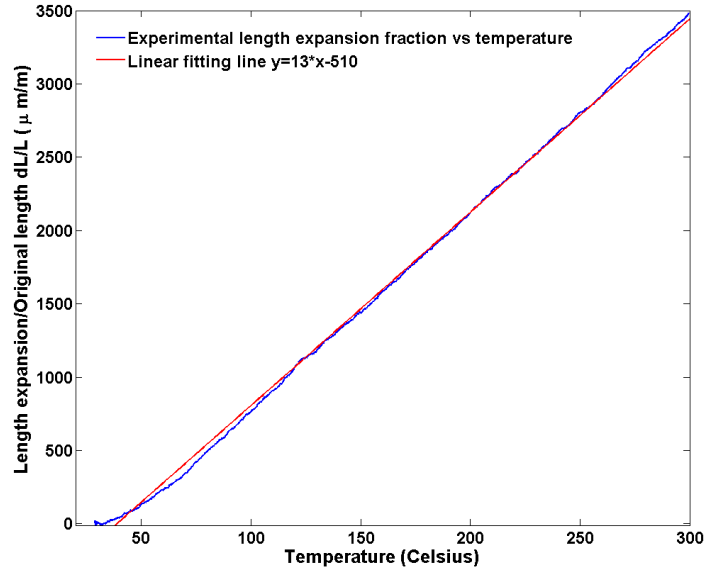


Fig. 4 The experimentally measured accumulated length expansion as a function of temperature. A linear fitting line is superimposed.

Compression tests were done on  $\text{Al}_2\text{Ca}$  specimens with a compression rate of 1mm/min. The dimension and compression strength values for three samples can be seen in Table 3. From Table 3, we can see that the average compression strength for  $\text{Al}_2\text{Ca}$  is 17.5 MPa. These low strength values probably result from the brittleness of  $\text{Al}_2\text{Ca}$  and the small dimensions of the compression test specimens. More accurate strength data could be obtained if a larger specimen were available for testing.

Table 3. The dimensions and compression strengths of three  $\text{Al}_2\text{Ca}$  samples subjected to compression tests.

	width 1 (mm)	width 2 (mm)	height (mm)	Max compression load (N)	Compression strength (MPa)
Sample 1	1.09	0.93	11.87	18.6	18.3
Sample 2	1.06	0.94	10.44	10.4	10.5
Sample 3	0.98	1.18	11.27	27.6	23.8

### Molecular Dynamics Simulation of Al/Ca Bicrystal Interface

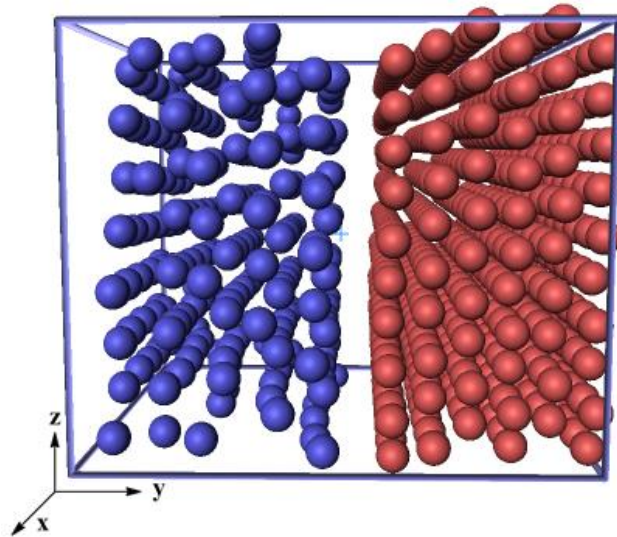
The Sandia LAMMPS molecular dynamics package [3] was used to model an Al/Ca bicrystal interface at elevated temperature. Since there is no available interatomic potential between Al and Ca, the reactive force field potential file from the reference [4] was adopted to model Al-Ca interaction. The guideline to build LAMMPS with reax user package and reax library has been given in Appendix B. It is worthwhile to mention that this reactive force field was used specially for the system being studied in reference [4] and may not be ideal for the Al-Ca system. Therefore, it is necessary to investigate the applicability of this potential in the Al-Ca system. We used this potential for calculating the equilibrium lattice constant of  $\text{Al}_2\text{Ca}$  intermetallic compound at 25 °C and obtained a value of 8.02 Å, a value that matched exactly with the published lattice constant of  $\text{Al}_2\text{Ca}$  [5]. However, the cohesive energy per atom calculated under this potential is -1.86 eV/atom, which is different from the experimental value of -3.28 eV/atom and the -3.53 eV/atom value calculated in this paper [6]. This suggests that the energetics of this reactive force field tend to underestimate the attraction between Al and Ca atom. The file for this calculation was also attached in Appendix B. Therefore, it seems that this reactive force field can reflect some feature of the potential interaction between Al and Ca atoms, and we did a trial study on Al/Ca interface using this potential. As a preliminary study, we start with the simplest Al-Ca bicrystal interface that has a much smaller system size than that of two polycrystalline Al and Ca phases separated by many incoherent interfaces since that case places much less demand on computational resources. The initial interface structure could be assumed as Al(111)/Ca(111) for an initial trial since the most densely packed planes have lowest surface energy.

Furthermore, since the atomic radius between Al and Ca is rather large (misfit strain is more than 25%), the interface could be assumed as purely incoherent, which would make the initial atomic arrangement across the interface easy to set up (i.e. the atomic arrangements of the two phases extend to the interface without relaxation by misfit dislocations), as described by Howe [7]. If there is some semicoherent nature in this heterophase interface, we could add misfit dislocations to relax the interface. As an initial trial, we can just neglect any semicoherent nature and check how the system responds under this potential. No tilt or twist was assumed between the two crystalline lattices. The input script for this interface simulation is attached in Appendix B.

As seen in Fig. 5, the simulation box y direction has free surface boundary condition while x and z direction has a periodic boundary condition. Minimization (molecular statics) was performed first on the bicrystal interface to get the lowest potential energy configuration. Then molecular dynamics was done at 356 °C under NPT ensemble. The current preliminary run of the simulation has been done up to 20,000 time steps with 1 femtosecond per time step. Fig. 5 shows the snapshot of initial atomistic configuration after minimization and the atomistic configuration at 20,000 dynamic time steps. The figure clearly shows no sign of Al and Ca atoms mixing into one another to form intermetallic compounds. Instead, the simulation box size increased a little in 3 directions and the total energy of the system did not decrease after 20,000 time steps. This suggests that the Al and Ca atoms tend to repel each other and demix under the current potential interaction, which seems to align with the fact that there is no mutual solubility between Al and Ca shown in the Al-Ca binary equilibrium phase diagram. Similar behavior has been observed in the Al(111)/Ca(110) interface case. This is probably due to the failure of this reactive force field in solving our current material



system, or it could be due to the initial set up of the atomistic configuration. There is a phenomenon called deformation induced chemical mixing in deformation processed metal metal composites like Cu-Nb composite [8]. This will form a non-equilibrium metastable solid solution of two insoluble phases. It is possible that the pre-existence of such metastable solid solution would be a prerequisite for the formation of intermetallic compounds. The transformation of a high energy state metastable solid solution into an intermediate energy state intermetallic compound could be easier than the direct de-mixing of metastable solid solution into two pure phases. However, this is speculative. Future work may be needed to see if extensive deformation can indeed induce atomic mixing in metal-metal composite by atomistic simulation. Furthermore, if deformation can indeed cause chemical mixing, we can start with this initial metastable solid solution configuration to run molecular dynamics to see if it will transform into an intermetallic compound. We may need to obtain a well behaved Al-Ca interatomic potential for these simulations by an *ab-initio* approach.



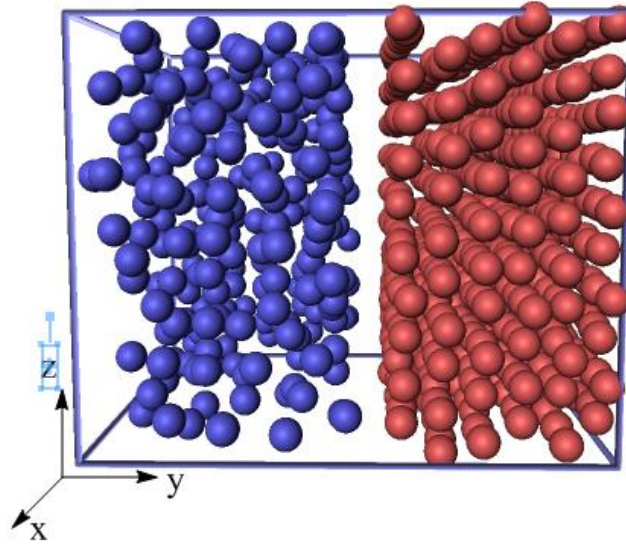


Fig. 5. Snapshots of Al/Ca interface atomistic configuration at 356 °C under NPT ensemble. Top image occurs at 0 dynamic time step after minimization. Bottom image occurs at 20,000 dynamic time steps with 1fs per time step. Ca atoms are blue and Al atoms are red. Boundary perpendicular to y direction has free surface condition while boundary perpendicular to x and z is periodic boundary condition.

### Conclusions

The microstructure evolution of Al/Ca interface at elevated temperature has been studied by a preliminary diffusion couple experiment and molecular dynamics simulation. Three different phases have been found across the Al/Ca interface after annealing at 356 °C for 2 weeks (1.21 million seconds). Oxygen was still found on the surface layer of Al/Ca interface even after polishing in an argon-filled glove bag connected to the Auger sample chamber. The physical properties of the most stable Al-Ca intermetallic compound  $\text{Al}_2\text{Ca}$  have been measured to evaluate the effect of its formation on the performance of Al/Ca composite conductor at elevated temperature. A much better Al-Ca interatomic potential would appear to be needed to accurately simulate the interaction between Al and Ca atoms at the interface.

## References

- [1] L Tian, I Anderson, T Riedemann, A Russell, H Kim (2013) *Electr Pow Syst Res* 105: 105. Doi:DOI 10.1016/j.epsr.2013.07.017
- [2] L Tian, H Kim, I Anderson, A Russell (2013) *Mat Sci Eng a-Struct* 570: 106. Doi:DOI 10.1016/j.msea.2013.01.062
- [3] S Plimpton (1995) *Journal of Computational Physics* 117: 1. Doi:DOI 10.1006/jcph.1995.1039
- [4] LC Liu, A Jaramillo-Botero, WA Goddard, H Sun (2012) *J Phys Chem A* 116: 3918. Doi:Doi 10.1021/Jp210135j
- [5] D Zhou, J Liu, P Peng, L Chen, Y Hu (2008) *Mater Lett* 62: 206.
- [6] D-W Zhou, J-s Liu, J Zhang, P Ping (2007) *Transactions of Nonferrous Metals Society of China* 17: 250.
- [7] JM Howe (1997) *Interfaces in materials: atomic structure, thermodynamics and kinetics of solid-vapor, solid-liquid and solid-solid interfaces*. Wiley-Interscience.
- [8] D Raabe, PP Choi, YJ Li, et al. (2010) *Mrs Bull* 35: 982. Doi:Doi 10.1557/Mrs2010.703

## APPENDIX B GUIDELINE TO USE LAMMPS MOLECULAR DYNAMIC PACKAGE WITH REAXX FORCE FIELD

Liang Tian<sup>1</sup>, Reza Mirzaeifar<sup>2</sup>

1. Primary researcher and author 2. Technical guide and reviser

### A Short Guide of Building LAMMPS with Reax Package and Library

Download the most stable version of LAMMPS source tarball written in C++ from LAMMPS website <http://lammps.sandia.gov/download.html#tar>. In Ubuntu terminal, change directory to the folder of source tarball and its subdirectory /src. Type command `make yes-reax` to install reax package. This will copy files from /src/reax folder to /src folder. Type `make ps` to check package installation status. Now we should build reax auxiliary library (see the /lib/reax/readme for instructions). Change directory to /lammpsversion/lib/reax. Type command `make -f Makefile.gfortran`, which uses Makefile.gfortran to make the reax library. This is because the reax is written in old fortran language. The output includes .a library file and `Make.lammps` that contains the setting from `Make.lammps.gfortran`. `Make.lammps.gfortran` is predefined make-files, which specify the location of gfortran compiler for the machine to find when building LAMMPS. Install gfortran compiler since it is not pre-installed. After making reax package and building auxiliary library for reax, it is ready to build lammps. Change directory to /lammps/src and type command `make serial`, an executable file called `Imp_serial` will be created after about 10mins. This is the file we are going to run LAMMPS input scripts containing our simulation details with. Copy this exe file to anywhere you want . Under its directory, run any input script by typing command

./lmp\_serial <file name. For multiple cores machine, it can be somewhat complicated and has to follow the strict guideline of making LAMMPS website.

#### Input Script File for Equilibrium Constant and Cohesive Energy Calculation of Al<sub>2</sub>Ca

# Al<sub>2</sub>Ca lattice parameter and cohesive energy calculation by reax potential

# ----- Initialize Simulation -----

clear

units real

dimension 3

boundary p p p

atom\_style full

atom\_modify map array

# ----- Create Atoms -----

# in LAMMPS, the lattice actually means crystal structure in solid state physics. In Al<sub>2</sub>Ca,

#there are total 24 atoms in unit cell. 6 atoms per basis (2 are Ca atoms and 4 are Al atoms).

#First defined 8 atoms are Ca, next 16 atoms are Al atoms

lattice custom 7.0 a1 1 0 0 a2 0 1 0 a3 0 0 1 basis 0 0 0 basis 0.25 0.25 0.25 basis 0.5 0.5 0 &  
basis 0.75 0.75 0.25 basis 0.5 0 0.5 basis 0.75 0.25 0.75 basis 0 0.5 0.5 basis 0.25 0.75 0.75&  
basis 0.625 0.625 0.625 basis 0.875 0.875 0.625 basis 0.625 0.875 0.875 basis 0.875 0.625&  
0.875 basis 0.125 0.125 0.625 basis 0.375 0.375 0.625 basis 0.125 0.375 0.875 basis 0.375&  
0.125 0.875 basis 0.125 0.625 0.125 basis 0.375 0.875 0.125 basis 0.125 0.875 0.375 basis&

0.375 0.625 0.375 basis 0.625 0.125 0.125 basis 0.875 0.375 0.125 basis 0.625 0.375 0.375 &  
basis 0.875 0.125 0.375

#  $0 \leq x, y, z < 1$  due to pbc. Theoretical equilibrium lattice constant should be 8.02Å

region cell block 0 1 0 1 0 1 units lattice

create\_box 2 cell

create\_atoms 1 box basis 1 1 basis 2 1 basis 3 1 basis 4 1 basis 5 1 basis 6 1 basis 7 1 basis &  
8 1 basis 9 2 basis 10 2 basis 11 2 basis 12 2 basis 13 2 basis 14 2 basis 15 2 basis 16 2 &  
basis 17 2 basis 18 2 basis 19 2 basis 20 2 basis 21 2 basis 22 2 basis 23 2 basis 24 2

replicate 1 1 1

#----define mass-----

mass 1 40

mass 2 27

# atom type 1 is Ca, atom type 2 is Al

# ----- Define Interatomic Potential -----

pair\_style reax

pair\_coeff \* \*ffield.reax 4 6

# atom type 1 Ca is the 4<sup>th</sup> place in the atom list in reax potential file

neighbor 2.0 bin

neigh\_modify delay 10 check yes

# ----- Define Settings -----

compute eng all pe/atom

compute eatoms all reduce sum c\_eng

# ----- Run Minimization -----

reset\_timestep 0

fix 1 all box/relax iso 1.0 vmax 0.001

thermo 10

thermo\_style custom step pe lx ly lz press pxx pyy pzz c\_eatoms fmax

dump 1 all custom 20 EMin.Al2Ca.cfg mass type xs ys zs c\_eng fx fy fz

dump\_modify 1 element Ca Al

min\_style cg

minimize 1e-25 1e-25 5000 10000

undump 1

unfix 1

#----run dynamics-----

reset\_timestep 0

timestep 1

velocity all create 298 12345 mom yes rot no

# temperature 25 C

fix 1 all npt temp 298 298 100 iso 1 1 1000

dump 1 all custom 1000 Al2Ca\_Dyn.cfg mass type xs ys zs c\_eng fx fy fz

dump\_modify 1 element Ca Al

```

thermo 1000

thermo_style custom step pe vol lx ly lz press pxx pyy pzz c_eatoms temp ke fmax

run 20000

write_restart restart.Al2Ca20000

print "All done!"

```

Lattice constant is the lx or ly or lz (unit Angstrom) and cohesive energy is calculated by the  $c\_atoms * 0.043/24$  (unit eV/atom) at the end of 20,000 time steps.

#### Input Script for Al/Ca Bicrystal Interface Simulation

```

# LAMMPS Input File for Al/Ca bicrystal interface

# This file will generate an initial Al(111)/Ca(111) incoherent interface and minimize

# and run dynamics using reax potential

# ----- Initialize Simulation -----

clear

units real

dimension 3

boundary p s p

atom_style full

# ----- Create Atomistic Structure -----

lattice fcc 4.05

```



region whole block 0 25 -14 14 0 25 units box

create\_box 2 whole

region upper block INF INF 0 14 INF INF units box

lattice fcc 4.05 orient x -1 0 1 orient y 1 1 1 orient z -1 2 -1

create\_atoms 1 region upper

region lower block INF INF -14 0 INF INF units box

lattice fcc 5.58 orient x -1 0 1 orient y 1 1 1 orient z -1 2 -1

create\_atoms 2 region lower

group upper type 1

group lower type 2

#---define Mass----

mass 1 27

mass 2 40

# ----- Define Interatomic Potential -----

pair\_style reax

pair\_coeff \* \*ffield.reax 6 4

neighbor 2.0 bin

neigh\_modify delay 10 check yes

# ----- Displace atoms and delete overlapping atoms -----

displace\_atoms upper move 0 0.05 0 units lattice

```
delete_atoms overlap 0.25 lower upper
```

```
# ----- Define Settings -----
```

```
compute csym all centro/atom fcc
```

```
compute eng all pe/atom
```

```
compute eatoms all reduce sum c_eng
```

```
# ----- Run Minimization -----
```

```
reset_timestep 0
```

```
thermo 20
```

```
thermo_style custom step pe lx ly lz press pxx pyy pzz c_eatoms fmax
```

```
dump 1 all custom 20 EnMin.AlCa.cfg mass type xs ys zs c_csym c_eng fx fy fz
```

```
dump_modify 1 element Al Ca
```

```
min_style cg
```

```
minimize 1e-15 1e-15 5000 5000
```

```
undump 1
```

```
# ----- Run Minimization 2-----
```

```
# Now allow the box to expand/contract in x and z directions (perpendicular to the interface),
```

```
#fix box/relax command only works for periodic dimension
```

```
reset_timestep 0
```

```
thermo 20
```

```
thermo_style custom step pe lx ly lz press pxx pyy pzz c_eatoms fmax
```

```
fix 1 all box/relax x 1.0 z 1.0 couple xz vmax 0.001
```

```
# 1 atmosphere pressure in x and z directions
```

```
min_style cg
```

```
minimize 1e-15 1e-15 5000 5000
```

```
# ----- Calculate AlCa interface Energy -----
```

```
variable Almineng equal -3.360000
```

```
variable Camineng equal -1.840000
```

```
variable esum equal "v_Almineng * count(upper)+ v_Camineng * count(lower)"
```

```
variable xseng equal "c_eatoms*0.043 - v_esum"
```

```
variable intarea equal "lx * lz * 2"
```

```
variable inteng equal "v_xseng/v_intarea"
```

```
variable inteng_mJm2 equal "${inteng}*16021.7733
```

```
variable inteng_rnd equal round("${inteng_mJm2})
```

```
print "Al/Ca incoherent interface energy is ${inteng_mJm2} mJ/m^2"
```

```
# ----- Dump data into Data file -----
```

```
reset_timestep 0
```

```
dump 1 all custom 10000 AlCa_final.cfg mass type xs ys zs c_csym c_eng fx fy fz
```

```
dump_modify 1 element Al Ca
```

```
minimize 1e-15 1e-15 5000 5000
```

```
undump 1
```

```
unfix 1
```

```
write_restart restart.AlCa
```

```
#-----begin dynamics-----
```

```
reset_timestep 0
```

```
timestep 1
```

```
velocity all create 629 12345 mom yes rot no
```

```
#temperature 356 C
```

```
fix 1 all npt temp 629 629 100 x 1 1 1000 z 1 1 1000
```

```
dump          2 all custom 1000 AlCa_Dyn.cfg mass type xs ys zs c_csym c_eng fx fy fz
```

```
dump_modify   2 element Al Ca
```

```
thermo 1000
```

```
thermo_style custom step pe vol lx ly lz press pxx pyy pzz temp ke
```

```
run 20000
```

```
write_restart restart.AlCa10000
```

```
print "All done"
```